Young Massive Clusters Near the Galactic Center: Initial Mass Function and Stellar Evolution

A DISSERTATION SUBMITTED TO THE GRADUATE DIVISION OF THE UNIVERSITY OF HAWAIʻI AT MĀNOA IN PARTIAL FULFILLMENT OF THE REQUIREMENTS FOR THE DEGREE OF

DOCTOR OF PHILOSOPHY

IN

ASTRONOMY

August 2018

By
Matthew Hosek Jr

Dissertation Committee:

J. Lu, Chairperson
R. Kudritzki
M. Liu
M. Morris
B. Reipurth
N. Santhanam

Acknowledgements

There are many people whose support have made this dissertation possible. First off, I'd like to acknowledge my advisor Jessica Lu, who has been a wonderful role model and mentor for me since we first started working together. I cannot thank her enough for her steady encouragement and enthusiasm for this project. I'd also like to thank the rest of my thesis committee for their guidance and support: Rolf Kudritzki, Michael Liu, Mark Morris, Bo Reipurth, and Narayana Santhanam. I'd like to give an additional shout-out to Rolf, who was my first 699 advisor and taught me how to conduct grad-level research.

I have been fortunate to work with a wonderful group of collaborators who have provided much insight into the results presented in this manuscript: Jay Anderson, Will Clarkson, Tuan Do, Andrea Ghez, Eddie Schlafly, Francisco Najarro, and Nicholas Rui. I look forward to continuing to work with them in future projects. I'd also like to thank the past and present members of Jessica's research group, with whom I've had many scientific discussions and have learned a lot from: Fatima Abdurrahman, Siyao Jia, Dongwon Kim, Casey Law, Kelly Lockhart, Max Service, and Paolo Turri.

I'd also like to thank the administrative staff of the IfA and UC Berkeley, who have helped me deal with the logistical challenge of working at Berkeley while being enrolled at IfA. In particular I'd like to thank Diane Tokumura for helping me with travel arrangements, Kristin Prada for handling the financial side of things, and Bill Unruh for going above and beyond to set up my office at IfA.

I have had the pleasure of being part of both the IfA and UC Berkeley grad student communities, which have been incredibly welcoming and supportive. I'd like to especially thank my cohort: Laurie Chu, BJ Fulton, Sean Goebel, Michael Kotson, Ehsan Kourkchi, and Evan Sinukoff, as well as the various housemates who have put up with me over the years: Dani Atkinson, Ben Boe, Ali Farzad,

Bon Haung, Greg Hoover, Thomas de Jaeger, Alana Ju, Kelly Lockhart, Erik Petigura, Louis Scuderi, and Lauren Zuckerberg. You guys are awesome!

I'd like to give a special shout-out to Kimberly Aller for her constant support throughout this entire process, even though I may have scheduled my dissertation defense on her birthday...

Finally, I would not be here without the love and support of my friends and family, especially my parents who have encouraged my interest in astronomy from the start. I'd like to give a special thanks to my Grandma, who sends me clippings of astronomy newspaper articles to this day.

Abstract

With projected distances of just ∼30 pc from Sgr A*, the Arches and Quintuplet clusters are valuable probes of star formation in the extreme Galactic Center (GC) environment. Of particular interest is the Initial Mass Function (IMF), which yields critical insight into the physics driving star formation and is a vital ingredient in many areas of astronomy. We use multi-epoch Hubble Space Telescope (HST) observations to obtain high-precision proper motions of stars beyond the central 25" of these clusters for the first time, calculating cluster membership probabilities down to ∼2 $M_\odot$. We achieve significantly cleaner cluster samples than is possible through photometric methods due to severe differential extinction in the field. For the Arches cluster, we 1) measure the stellar radial density profile out to 3 pc for the first time, finding no evidence of a tidal radius and demonstrating that the cluster is much larger than predicted; 2) combine this sample with HST observations of Westerlund 1 to measure the extinction law of highly reddened stars in the Galactic plane between 0.8 μm – 2.2 μm, revealing it to be inconsistent with a single power-law (contrary to long-held assumptions) and significantly steeper than commonly-used extinction laws; and 3) use these observations with K-band spectroscopy to make the first proper motion-based IMF measurement of the cluster, finding significant deviations from the local IMF and suggesting that the IMF of the GC is non-standard. In addition, we show current progress on the analysis of the Quintuplet cluster along with a science case for future studies of both clusters with the James Webb Space Telescope.

Table of Contents

List of Tables

List of Figures

Chapter 1

Introduction

1.1 The Galactic Center: An Extreme Star Formation Environment

The Galactic Center (GC) environment is significantly different than that of the solar neighborhood, exhibiting high gas temperatures and densities, UV radiation fields, turbulence, magnetic fields, intense cosmic rays, and tidal shear (Morris & Serabyn 1996). Spanning a galactocentric radius of ∼200 pc and host to the most massive molecular clouds in the galaxy, the Central Molecular Zone (CMZ) has a star formation rate density nearly 2 orders of magnitude higher than the galactic disk, evidenced by the stellar luminosity functions of the region (Figer et al. 2004), large numbers of isolated massive evolved stars (Mauerhan et al. 2010; Dong et al. 2012), and the presence of several young massive clusters (YMCs) with masses of $\sim 10^4$ $M_\odot$ (Figer et al. 1999). However, it has been noted that the star formation rate at the CMZ is still an order of magnitude lower than predicted by extrapolations of standard star formation rate indicators, perhaps due to the extreme conditions (Longmore et al. 2013a; Kruijssen et al. 2014).

One particularly striking feature of the CMZ is a large and twisted molecular ring structure with a galactocentric radius of ∼100 pc (Molinari et al. 2011; Kruijssen et al. 2014), which contains the Sgr B2 and Sgr C star forming regions as well several possible YMC progenitors (Longmore et al. 2013b). One proposed mechanism for star formation in the CMZ is the collision of gas clouds along the galactic *X1* and *X2* orbit families (Binney et al. 1991), which follow the semi-major and semi-minor axes of the Galactic bar, respectively. This is consistent with the locations of the Sgr B2 and

Sgr C regions, which appear to fall at the intersection points between the molecular ring (thought to be part of the *X2* orbit system) and *X1* orbit system (Molinari et al. 2011). Alternatively, star formation events may be triggered by the tidal compression of molecular clouds at their closest approach to the GC, evidenced by the fact that massive clouds appear to show progressively more star formation "downstream" from their peri-center passage (Longmore et al. 2013b).

The Arches and Quintuplet Clusters are YMCs with projected distances of just ∼30 pc from the central supermassive black hole (Figure 1.1). The Arches is younger than the Quintuplet, with an age of 2-4 Myr (Najarro et al. 2004; Martins et al. 2008) compared to 4-6 Myr (Figer et al. 1999; Liermann et al. 2009), and is the more compact of the two clusters. Given their close proximity (projected separation: ∼12 pc) and similar orbital motion, it has been suggested that the Arches and Quintuplet formed at a similar location (Stolte et al. 2014; Kruijssen et al. 2015). However, the exact birthplace and formation mechanism of these clusters is unknown due to the uncertainty in their orbits, as their line-of-sight distances and absolute ages are poorly constrained. Nonetheless, the extinction of the clusters as well as their observed interactions with surrounding molecular clouds place them within the CMZ (Lang et al. 2001).

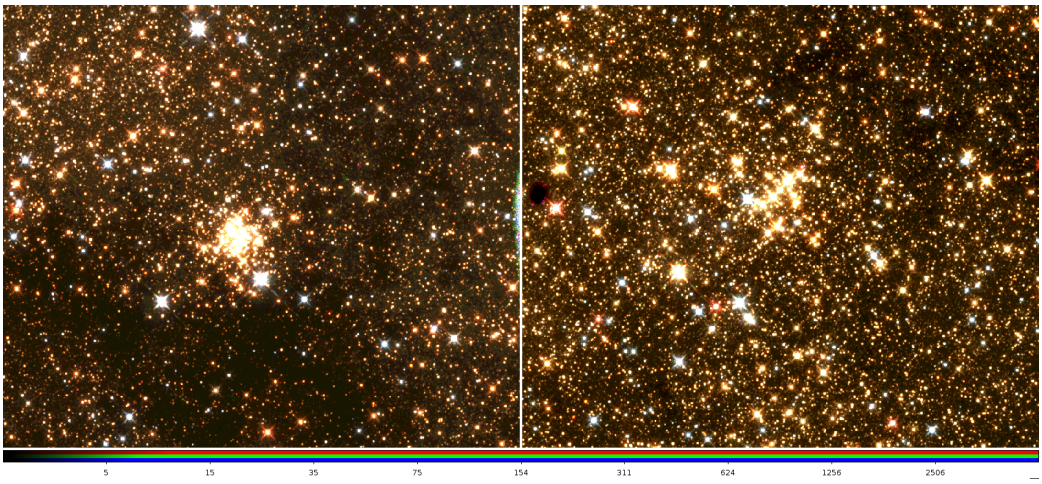

Figure 1.1 Three color *HST* image of the Arches (left) and Quintuplet (right) clusters, with F127M (1.27 μm) = blue, F139M (1.39 μm) = green, and F153M (1.53 μm) = red. Significant differential reddening is evident from the changing density of the field stars. Each image is ∼120" x 120", which at distance of 8 kpc corresponds to 4.8 x 4.8 pc.

The Arches and Quintuplet clusters provide a unique opportunity to study star formation and cluster evolution in the extreme environment of the GC. Due to their youth and high mass these

stellar populations sample the full stellar mass range, making them ideal for measuring the Initial Mass Function as discussed below. In addition, the clusters provide a snapshot of star cluster evolution at different ages in the presence of strong tidal fields.

1.2 The Initial Mass Function

A fundamental quantity of star formation is the Initial Mass Function (IMF), which describes the distribution of stellar masses created during a star-forming event. The properties of the IMF and how it behaves in different environments yields critical insight into the physics controlling star formation (e.g. Krumholz 2014; Offner et al. 2014) and is a vital ingredient in many areas of astronomy such as star formation over cosmic time (e.g. Narayanan & Davé 2012; Clauwens et al. 2016), the mass assembly and chemical evolution of galaxies (e.g. Davé 2008; Vincenzo et al. 2015), and stellar feedback (e.g. Dale 2015). In a seminal paper, Salpeter (1955) measured the IMF of nearby field stars to be a single power law: $dN/dm \propto \mathrm{m}^{-\alpha}$, where $\alpha = 2.35$. Today, the local IMF is often described by a set of power laws that are nearly equal to the Salpter IMF at high masses but turns over at low masses (Kroupa 2001; Kroupa et al. 2013):

$$\Phi(m) = dN/dm \propto \begin{cases} m^{-0.3\pm0.4}, & \text{for } 0.01 < m/M_\odot \lesssim 0.08 \\ m^{-1.3\pm0.3}, & \text{for } 0.08 < m/M_\odot \leq 0.5 \\ m^{-2.3\pm0.36}, & \text{for } 0.5 < m/M_\odot \leq 150 \end{cases} \tag{1.1}$$

Alternatively, the local IMF can be described as a log-normal function below 1 $\mathrm{M}_\odot$ (critical mass: $0.08^{+0.21}_{-0.016}$ $\mathrm{M}_\odot$, variance: $0.7^{+0.05}_{-0.1}$ $\mathrm{M}_\odot$) and a single power law above 1 $\mathrm{M}_\odot$ with a slope of -2.3 $\pm$ 0.3 (Chabrier 2003, 2005). However, these parameterizations are similar to each other and so it has not yet been established which is a better description of the IMF (Figure 1.2).

Stellar populations across the Milky Way and nearby galaxies have been found to be consistent with the local IMF (see reviews by Bastian et al. 2010; Offner et al. 2014). At the high-mass end ($\mathrm{M} \gtrsim 1$ $\mathrm{M}_\odot$), the IMFs of open clusters in the Milky Way (e.g. Carraro et al. 2005; Maciejewski & Niedzielski 2007; Bonatto & Bica 2007) as well as star clusters in the LMC (e.g. Selman & Melnick 2005; Kerber & Santiago 2006; Da Rio et al. 2009), SMC (e.g. Massey 2003; Sabbi et al. 2008), and

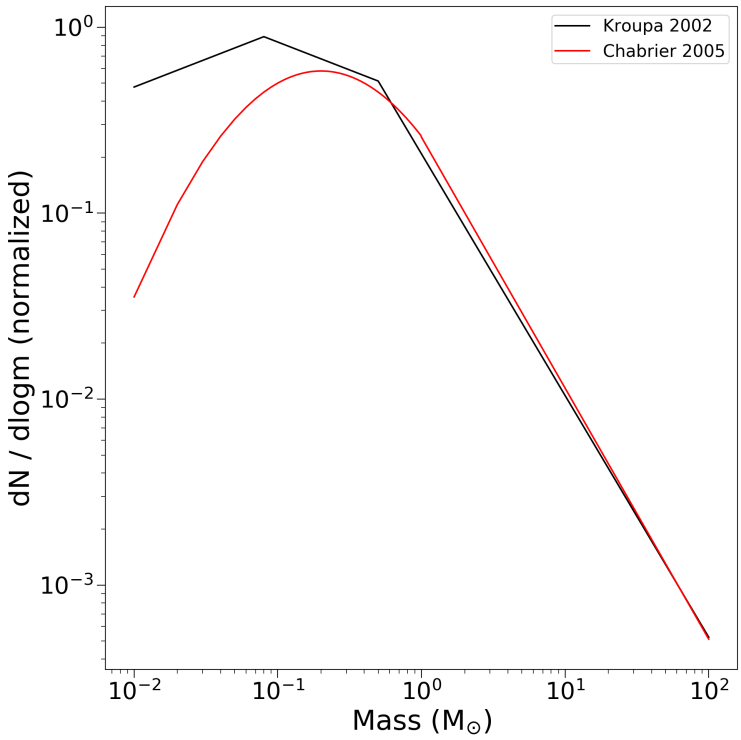

Figure 1.2 Comparison of the Kroupa (2002) (black) and Chabrier (2005) (red) formulations of the local IMF. The mass functions are similar to very low stellar masses, making it difficult to distinguish between the two.

M31 (Weisz et al. 2015) have been found to generally agree with the local IMF within uncertainties. At the low mass end ($0.15 \lesssim$ m / $M_\odot \lesssim 1.0$), the mass functions of young nearby clusters such as the Pleiades (Lodieu et al. 2012a), Orion Nuclear Cluster (Da Rio et al. 2012), α Perseus (Lodieu et al. 2012b), and Praesape (Boudreault et al. 2012) have been found to be very similar to the local field population, as well. The IMFs in the lowest mass regime ($M \lesssim 0.15\ M_\odot$) show less agreement, though these measurements are extremely difficult due to sample incompleteness and uncertainties in stellar models. A (non-exhaustive!) plot of recent mass function measurements in the Milky Way, LMC, SMC, and M31 is shown in Figure 1.3.

Studies of YMCs in the Milky Way disk have also been found to be consistent with the local IMF, although potential discrepancies exist. The high-mass IMF slopes of Westerlund 2 (Zeidler et al. 2017), Trumpers 14 and 16 (Hur et al. 2012), and h and χ Persei (Slesnick et al. 2002) have been reported to be consistent with other clusters, but NGC 3603 has been found to be potentially top-heavy ($\alpha = 1.74^{+0.62}_{-0.47}$, 1.88 ± 0.15; Harayama et al. 2008; Pang et al. 2013, respectively). The

NGC 3603 result may be biased due to mass segregation, which has been found to be significant within the cluster. Indeed, the uncertainty in the Harayama et al. (2008) measurement is quite large in order to account for this (as well as other) systematic uncertainties, while Pang et al. (2013) acknowledge that their measurement is restricted to the inner 60" of the cluster and thus is prone to mass segregation effects. The IMF of Westerlund 1 is also possibly discrepant, as both a standard IMF ($\alpha = 2.44^{+0.08}_{-0.20}$; Gennaro et al. 2011, via near-infrared photometry) and and top-heavy IMF ($\alpha = 1.8 \pm 0.1$; Lim et al. 2013, via optical photometry) have been reported over similar mass ranges. This highlights the difficulty of making these measurements, as differences in cluster membership selection, stellar models, and methodology can significantly impact the results.

1.2.1 Does the IMF Change in Starburst Environments?

As a result of its success in describing local stellar populations, the local IMF is commonly adopted to describe stellar populations across a wide range of astrophysical situations. However, the range of environments probed by IMF studies are limited to those typically found in galactic disks in the present-day universe (e.g. Fukui & Kawamura 2010). Whether the local IMF can be extended to more extreme star formation environments is unknown. Of particular interest are starburst environments, which are thought to be common in galaxies in the early universe (z$\sim$2) where the majority of star formation is thought to have occurred (Madau & Dickinson 2014). Molecular clouds in these environments have been found to have significantly higher velocity dispersions, temperatures, densities, and external pressures than those in the Milky Way disk (e.g. Smith et al. 2006; Swinbank et al. 2011).

Several competing predictions have been offered for how the IMF should behave in starburst-like environments. Some authors argue that the increased gas temperature, which is a consequence of higher dust temperatures and/or cosmic ray flux due to the high star formation rate, raises the thermal Jeans mass of a molecular cloud. This in turn raises the characteristic stellar mass, leading to an overabundance of higher-mass stars and a "top-heavy" IMF (e.g. Larson 2005; Bonnell et al. 2006; Klessen et al. 2007; Bonnell & Rice 2008; Papadopoulos et al. 2011; Narayanan & Davé 2013). Others contend that the stellar mass distribution is set primarily by the turbulent properties of the molecular cloud. In highly turbulent starburst regions, the increased fragmentation outweighs the impact of higher gas temperatures, favoring the formation of lower-mass stars and leading to

a "bottom-heavy" IMF (e.g. Padoan & Nordlund 2002; Hopkins 2012, 2013; Chabrier et al. 2014). However, recent numerical simulations suggest that turbulence may not have a significant impact on proto-stellar scales (Bertelli Motta et al. 2016; Liptai et al. 2017), and some studies predict that the IMF is set by local processes such as radiative feedback and thus is largely independent of environment (e.g. Bate 2009; Offner et al. 2009; Krumholz 2011; Krumholz et al. 2012; Guszejnov et al. 2016).

Observationally, there is some evidence that the IMF does vary in starburst-like environments, though these results are debated. Spectroscopic studies of massive elliptical galaxies suggest that the IMF becomes increasingly bottom-heavy with increasing velocity dispersion and/or α-element enhancement, conditions that reflect starburst-like conditions (e.g. Conroy & van Dokkum 2012; La Barbera et al. 2013; Spiniello et al. 2014). Further studies suggest that the IMF varies as a function of galactocentric radius within an elliptical galaxy, with bottom-heavy IMFs reported in the dense core regions (e.g. Martín-Navarro et al. 2015; van Dokkum et al. 2017; Conroy et al. 2017; Parikh et al. 2018), which are thought to have formed rapidly in starburst-like environments at high redshift (e.g. Oser et al. 2010). However, these results rely on the proper modeling of unresolved stellar spectra, which is prone to systematic effects such as elemental abundance gradients (e.g. McConnell et al. 2016; Zieleniewski et al. 2015, 2017; Vaughan et al. 2018). In addition, the lower number of high-mass stars predicted by a bottom-heavy IMF makes it difficult for galactic chemical evolution models to reproduce the high metallicities observed in elliptical galaxies (Weidner et al. 2013; Ferreras et al. 2015). It is also inconsistent with the observed number of low-mass X-ray binary systems, which are found to be nearly constant as a function of galaxy velocity dispersion (Peacock et al. 2014; Coulter et al. 2017), unless the IMF variations are limited to the inner $\sim$0.2 - 0.3 effective radii of the galaxy (Peacock et al. 2017).

Additional methods for measuring the IMF in distant galaxies include modeling galaxy masses using stellar kinematics (e.g. Cappellari et al. 2012, 2013; Li et al. 2017) or gravitational lensing (e.g. Treu et al. 2010). These studies also suggest a bottom-heavy IMF in the cores of elliptical galaxies, though these trends are debated due to the difficulty of modeling the matter distribution of the systems involved (e.g. Smith et al. 2015; Leier et al. 2016). Overall, the consistency of IMF determinations for a single galaxy using spectroscopic, kinematic, and lensing methods has not yet been established, with some galaxies showing agreement and others showing significant variations

(Lyubenova et al. 2016; Newman et al. 2017). This highlights the difficulty of measuring the IMF from unresolved and complex stellar populations.

At more recent cosmological times, massive clusters in starburst galaxies (also known as Super Star clusters or Starburst clusters) also probe starburst environments. These clusters can only be partially resolved with current observing facilities, and so their mass functions are inferred from light-to-mass ratios (e.g. Ho & Filippenko 1996). This analysis also faces many challenges, including the assumption of virial equilibrium, uncertainties in stellar models and extinction corrections, the impact of mass segregation and multiplicity, and velocity dispersion anisotropy (Larsen et al. 2004). In general, Starburst clusters older than $\sim$100 Myr have been found to be consistent with the local IMF, though younger clusters have been reported to exhibit a range of both bottom-heavy and top-heavy IMFs, perhaps as a result of these difficulties (e.g. McCrady et al. 2005; Bastian et al. 2006, 2007).

A more direct approach to measure the IMF is to use direct star counts from star clusters. The GC has been identified as a nearby analog for starburst environments, with molecular clouds exhibiting compositions, kinematics, and densities similar to those in high-redshift galaxies (Kruijssen & Longmore 2013; Ginsburg et al. 2016). Thus, the GC presents a unique opportunity to study the IMF of starburst-like environments in a resolved manner. Within the inner parsec of the Galaxies lies the Young Nuclear Cluster (YNC), where the luminosity function for $M > 10\ M_{\odot}$ indicates that the cluster has a top-heavy IMF ($\alpha = 1.7 \pm 0.2$; Lu et al. 2013, see also Figure 1.3). By studying the Arches and Quintuplet clusters, we can determine if such variation is limited to this cluster or if it extends throughout the CMZ.

1.2.2 The IMF of the Arches and Quintuplet Clusters: Previous Work

While there have been several studies of the IMF of the Arches and Quintuplet clusters, it is not yet clear whether they are consistent with the local IMF. For the Arches, the *present-day* mass function (PDMF) of the inner region ($r \lesssim 0.5$ pc) has been measured to be top-heavy (Figer et al. 1999; Stolte et al. 2002, 2005; Kim et al. 2006), while the outer regions have been found to be Salpeter-like or bottom-heavy (Espinoza et al. 2009; Habibi et al. 2013). This indicates that there is significant mass segregation within the cluster (Figure 1.4). Dynamical modeling is required to determine whether the PDMF is consistent with the IMF (e.g. Kim et al. 2000; Harfst et al. 2010;

Park et al. 2018), though the uncertainty in cluster orbit means that a large parameter space must be explored (Stolte et al. 2008). The inner region of the Quintuplet cluster has also been found to be top-heavy ($\alpha = 1.68^{+0.13}_{-0.09}$ for r < 0.5 pc; Hußmann et al. 2012), though presumably mass segregation significantly impacts this measurement as well. Similar to the Arches, a suite of orbits are possible for the Quintuplet, making dynamical modeling difficult (Stolte et al. 2014).

Even with an accurate dynamical model, determining whether the PDMF is consistent with the local IMF heavily depends on the behavior of the PDMF at large cluster radii, where the discrepancies between dynamical models with different IMFs are the largest (see Figure 13 of Harfst et al. 2010). This raises a major challenge when studying these clusters: the significant amount of differential extinction across the field ($\Delta A_V \sim 15$ mag; Habibi et al. 2013) blends the photometric cluster sequence with the background field population, thus compromising the ability to separate cluster members from field stars via photometry. The resulting field contamination can significantly bias mass function measurements at large cluster radii. For example, Stolte et al. (2005) showed that the field can account for as much as 50% of an uncorrected mass function for Arches cluster at less than $\sim$15 $M_\odot$ beyond a cluster radius of 0.5 pc. In addition, the differential extinction undermines the ability to statistically subtract the field population via a control field away from the cluster, since the photometric distribution of the field stars will change. Thus, an alternative method of separating the cluster and field populations must be used to accurately measure the Arches and Quintuplet IMFs.

Currently, the strongest evidence that the Arches cluster has an unusual IMF comes from Clarkson et al. (2012), who find the photometric mass of the cluster inferred from a local IMF is inconsistent with dynamical mass estimates based on the internal velocity dispersion of high-mass stars ($M > 10$ $M_\odot$) at the cluster core (r < 0.2 pc). They conclude that the mass function is either top-heavy and/or truncated at low masses (i.e., "bottom light"). We will test these claims using direct star counts down to $\sim$2 $M_\odot$.

1.3 Dissertation Overview

We use multi-epoch *Hubble Space Telescope* (HST) observations of the Arches and Quintuplet clusters to measure their IMFs, measuring proper motions for stars down to $\sim$2 $M_\odot$ out to large radii

($r \leq 3$ pc). Since proper motions are not affected by differential extinction, we obtain significantly better cluster membership probabilities than is possible through photometry alone. With the large field-of-view we encompass a large fraction of the clusters in our analysis, allowing us to measure the dynamical structure of the clusters in order to account for mass segregation. This dissertation is organized as follows:

- **Chapter 2: The Arches Cluster: Extended Structure and Tidal Radius**

  We present the first measurement of the radial profile of the Arches cluster out to large cluster radii (3 pc), revealing that the cluster does not exhibit a tidal radius to at least 2.8 pc (3σ lower limit). A detailed description of the proper motion extraction and cluster membership analysis is presented, which are used in future chapters.

- **Chapter 3: The Optical/Near-Infrared Extinction Law in Highly Reddened Regions**

  We derive a precise extinction law toward the Arches cluster and Westerlund 1 between 0.8 μm – 2.2 μm using a new methodology that makes minimal assumptions regarding the underlying functional form of the law. We find that the extinction law is inconsistent with a single power law over this wavelength regime and is significantly steeper than many commonly-used laws in the literature.

- **Chapter 4: The Unusual Initial Mass Function of the Arches Cluster**

  We find that the Arches IMF is best described by a single power law that is significantly top-heavy ($\alpha = 1.76 \pm 0.03 \pm 0.05$, where $dN/dm \propto m^{-\alpha}$), though we cannot discount a 2-segment power law IMF with a break mass at $5.16^{+1.25}_{-0.65}$ $M_\odot$ and a high-mass slope generally consistent with the local IMF (e.g., a "bottom-light" IMF due to the deficit of low mass stars rather than overabundance of high-mass stars). We discuss this result in the context of other young massive clusters in the Milky Way disk and the Galactic Center.

- **Chapter 5: Moving Forward**

  Current progress on the IMF analysis of the Quintuplet Cluster is presented, as well as an avenue for future studies of the Arches and Quintuplet clusters in the age of the *James Webb Space Telescope* (JWST).

- **Chapter 6: Conclusions**

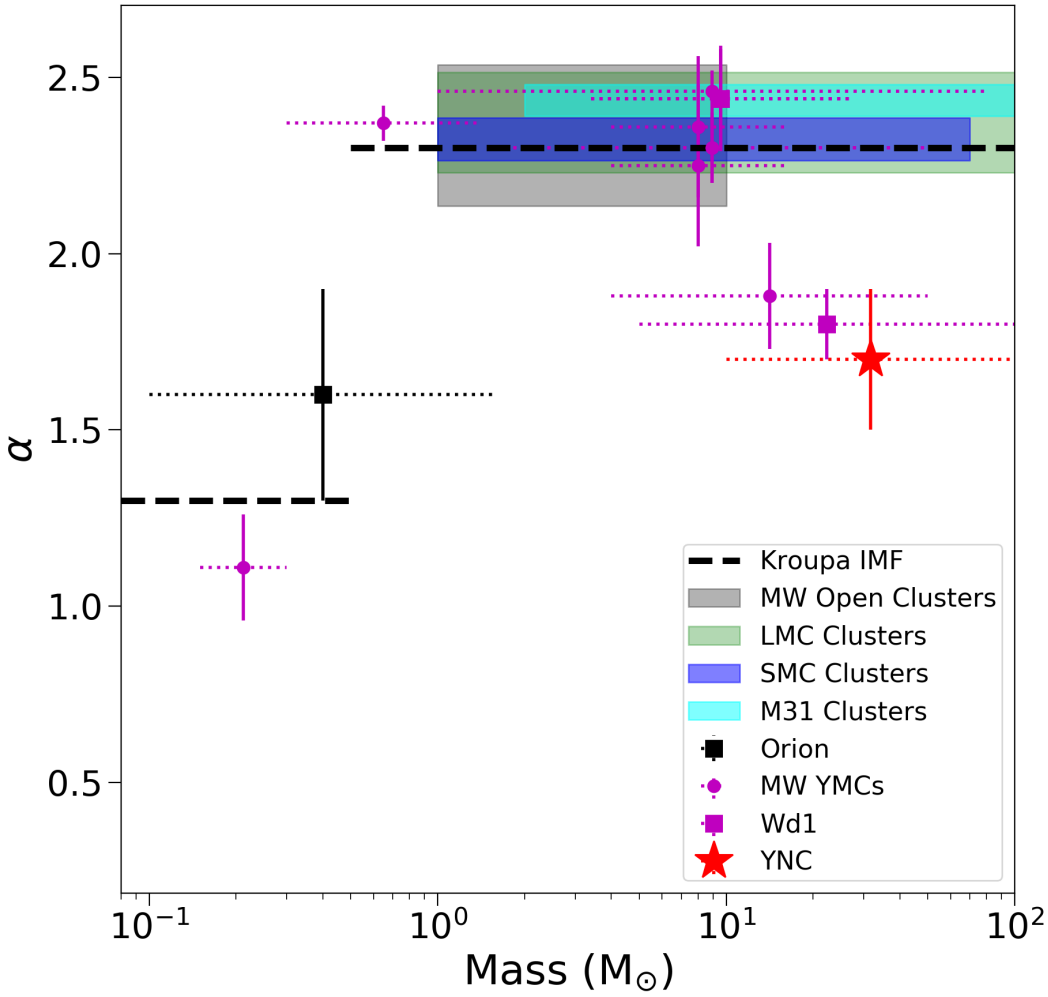

Figure 1.3 Recent measurements of the IMF power-law slope α as a function of stellar mass. The local IMF is shown as the black dashed lines, with the weighted averages taken across samples of clusters in the Milky Way, LMC, SMC, and M31 are shown by the black, green, blue, and cyan shaded boxes, respectively. The magenta circles show IMF measurements of YMCs in the Milky Way disk except for Wd1, where both high-mass IMF measurements from the literature are shown as magenta squares. Also plotted is the mass function of the Orion Nebula (black square) and the Young Nuclear Cluster (YNC; red star). The YNC indicates that the IMF at the GC might be Associated references for these measurements are given in the text.

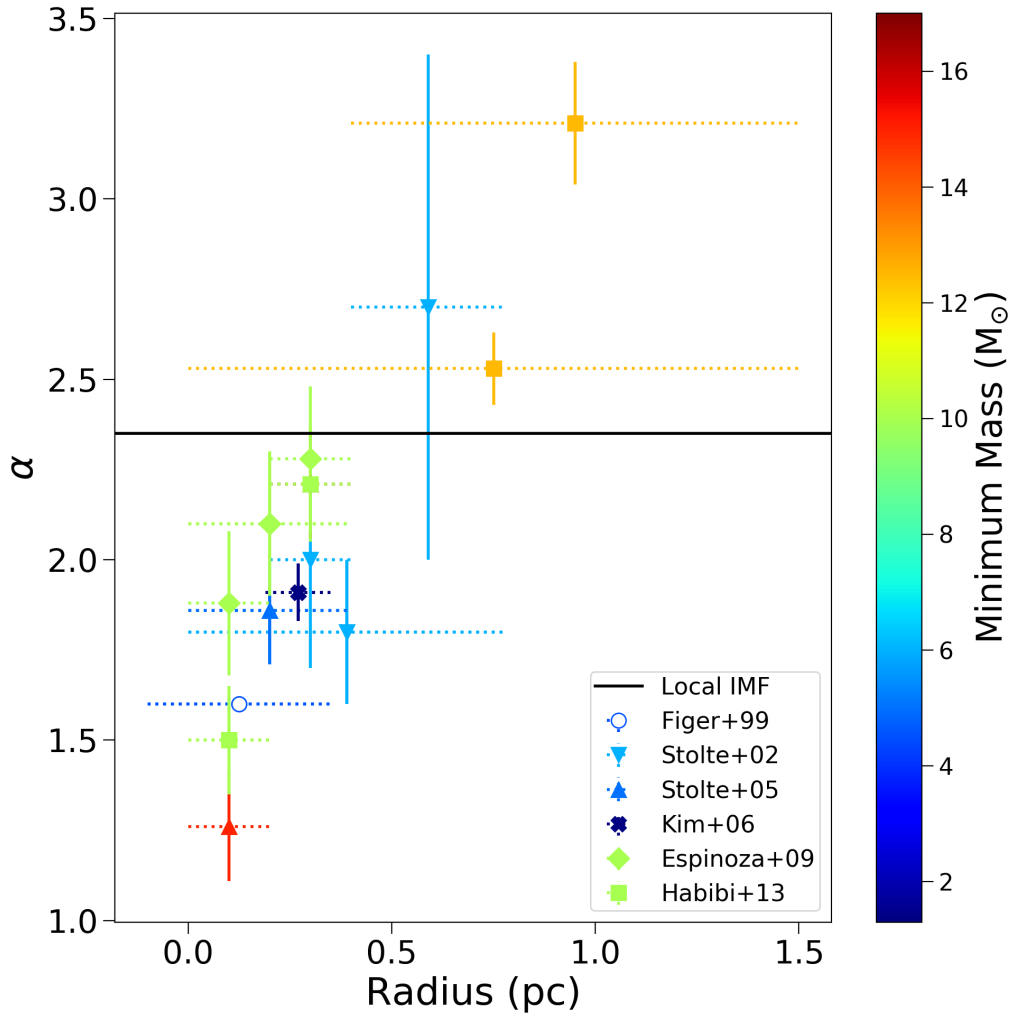

Figure 1.4 Previous measurements of the Arches mass function as a function of radius. For each point, the x-direction error bar corresponds to the radius range of the measurement while the y-direction error bar shows the uncertainty in α. The color of each point corresponds to the depth of the sample. If no uncertainty is reported, then the symbol is unfilled. The mass function is found to increase (e.g., become steeper) as a function of radius, indicating the presence of mass segregation.

References

Bastian, N., Covey, K. R., & Meyer, M. R. 2010, ARA&A, 48, 339

Bastian, N., Konstantopoulos, I., Smith, L. J., et al. 2007, MNRAS, 379, 1333

Bastian, N., Saglia, R. P., Goudfrooij, P., et al. 2006, A&A, 448, 881

Bate, M. R. 2009, MNRAS, 392, 1363

Bertelli Motta, C., Clark, P. C., Glover, S. C. O., Klessen, R. S., & Pasquali, A. 2016, MNRAS, 462, 4171

Binney, J., Gerhard, O. E., Stark, A. A., Bally, J., & Uchida, K. I. 1991, MNRAS, 252, 210

Bonatto, C., & Bica, E. 2007, MNRAS, 377, 1301

Bonnell, I. A., Clarke, C. J., & Bate, M. R. 2006, MNRAS, 368, 1296

Bonnell, I. A., & Rice, W. K. M. 2008, Science, 321, 1060

Boudreault, S., Lodieu, N., Deacon, N. R., & Hambly, N. C. 2012, MNRAS, 426, 3419

Cappellari, M., McDermid, R. M., Alatalo, K., et al. 2012, Nature, 484, 485

—. 2013, MNRAS, 432, 1862

Carraro, G., Baume, G., Piotto, G., Méndez, R. A., & Schmidtobreick, L. 2005, A&A, 436, 527

Chabrier, G. 2003, PASP, 115, 763

Chabrier, G. 2005, in Astrophysics and Space Science Library, Vol. 327, The Initial Mass Function 50 Years Later, ed. E. Corbelli, F. Palla, & H. Zinnecker, 41

Chabrier, G., Hennebelle, P., & Charlot, S. 2014, ApJ, 796, 75

Clarkson, W. I., Ghez, A. M., Morris, M. R., et al. 2012, ApJ, 751, 132

Clauwens, B., Schaye, J., & Franx, M. 2016, MNRAS, 462, 2832

Conroy, C., & van Dokkum, P. G. 2012, ApJ, 760, 71

Conroy, C., van Dokkum, P. G., & Villaume, A. 2017, ApJ, 837, 166

Coulter, D. A., Lehmer, B. D., Eufrasio, R. T., et al. 2017, ApJ, 835, 183

Da Rio, N., Gouliermis, D. A., & Henning, T. 2009, ApJ, 696, 528

Da Rio, N., Robberto, M., Hillenbrand, L. A., Henning, T., & Stassun, K. G. 2012, ApJ, 748, 14

Dale, J. E. 2015, , 68, 1

Davé, R. 2008, MNRAS, 385, 147

Dong, H., Wang, Q. D., & Morris, M. R. 2012, MNRAS, 425, 884

Espinoza, P., Selman, F. J., & Melnick, J. 2009, A&A, 501, 563

Ferreras, I., Weidner, C., Vazdekis, A., & La Barbera, F. 2015, MNRAS, 448, L82

Figer, D. F., Kim, S. S., Morris, M., et al. 1999, ApJ, 525, 750

Figer, D. F., Rich, R. M., Kim, S. S., Morris, M., & Serabyn, E. 2004, ApJ, 601, 319

Fukui, Y., & Kawamura, A. 2010, ARA&A, 48, 547

Gennaro, M., Brandner, W., Stolte, A., & Henning, T. 2011, MNRAS, 412, 2469

Ginsburg, A., Henkel, C., Ao, Y., et al. 2016, A&A, 586, A50

Guszejnov, D., Krumholz, M. R., & Hopkins, P. F. 2016, MNRAS, 458, 673

Habibi, M., Stolte, A., Brandner, W., Hußmann, B., & Motohara, K. 2013, A&A, 556, A26

Harayama, Y., Eisenhauer, F., & Martins, F. 2008, ApJ, 675, 1319

Harfst, S., Portegies Zwart, S., & Stolte, A. 2010, MNRAS, 409, 628

Ho, L. C., & Filippenko, A. V. 1996, ApJ, 472, 600

Hopkins, P. F. 2012, MNRAS, 423, 2037

—. 2013, MNRAS, 433, 170

Hur, H., Sung, H., & Bessell, M. S. 2012, AJ, 143, 41

Hußmann, B., Stolte, A., Brandner, W., Gennaro, M., & Liermann, A. 2012, A&A, 540, A57

Kerber, L. O., & Santiago, B. X. 2006, A&A, 452, 155

Kim, S. S., Figer, D. F., Kudritzki, R. P., & Najarro, F. 2006, ApJ, 653, L113

Kim, S. S., Figer, D. F., Lee, H. M., & Morris, M. 2000, ApJ, 545, 301

Klessen, R. S., Spaans, M., & Jappsen, A.-K. 2007, MNRAS, 374, L29

Kroupa, P. 2001, in Astronomical Society of the Pacific Conference Series, Vol. 228, Dynamics of Star Clusters and the Milky Way, ed. S. Deiters, B. Fuchs, A. Just, R. Spurzem, & R. Wielen, 187

Kroupa, P. 2002, Science, 295, 82

Kroupa, P., Weidner, C., Pflamm-Altenburg, J., et al. 2013, The Stellar and Sub-Stellar Initial Mass Function of Simple and Composite Populations, ed. T. D. Oswalt & G. Gilmore, 115

Kruijssen, J. M. D., Dale, J. E., & Longmore, S. N. 2015, MNRAS, 447, 1059

Kruijssen, J. M. D., & Longmore, S. N. 2013, MNRAS, 435, 2598

Kruijssen, J. M. D., Longmore, S. N., Elmegreen, B. G., et al. 2014, MNRAS, 440, 3370

Krumholz, M. R. 2011, ApJ, 743, 110

—. 2014, Phys. Rep., 539, 49

Krumholz, M. R., Klein, R. I., & McKee, C. F. 2012, ApJ, 754, 71

La Barbera, F., Ferreras, I., Vazdekis, A., et al. 2013, MNRAS, 433, 3017

Lang, C. C., Goss, W. M., & Morris, M. 2001, AJ, 121, 2681

Larsen, S. S., Brodie, J. P., & Hunter, D. A. 2004, AJ, 128, 2295

Larson, R. B. 2005, MNRAS, 359, 211

Leier, D., Ferreras, I., Saha, P., et al. 2016, MNRAS, 459, 3677

Li, H., Ge, J., Mao, S., et al. 2017, ApJ, 838, 77

Liermann, A., Hamann, W.-R., & Oskinova, L. M. 2009, A&A, 494, 1137

Lim, B., Chun, M.-Y., Sung, H., et al. 2013, AJ, 145, 46

Liptai, D., Price, D. J., Wurster, J., & Bate, M. R. 2017, MNRAS, 465, 105

Lodieu, N., Deacon, N. R., & Hambly, N. C. 2012a, MNRAS, 422, 1495

Lodieu, N., Deacon, N. R., Hambly, N. C., & Boudreault, S. 2012b, MNRAS, 426, 3403

Longmore, S. N., Bally, J., Testi, L., et al. 2013a, MNRAS, 429, 987

Longmore, S. N., Kruijssen, J. M. D., Bally, J., et al. 2013b, MNRAS, 433, L15

Lu, J. R., Do, T., Ghez, A. M., et al. 2013, ApJ, 764, 155

Lyubenova, M., Martín-Navarro, I., van de Ven, G., et al. 2016, MNRAS, 463, 3220

Maciejewski, G., & Niedzielski, A. 2007, A&A, 467, 1065

Madau, P., & Dickinson, M. 2014, ARA&A, 52, 415

Martín-Navarro, I., Barbera, F. L., Vazdekis, A., Falcón-Barroso, J., & Ferreras, I. 2015, MNRAS, 447, 1033

Martins, F., Hillier, D. J., Paumard, T., et al. 2008, A&A, 478, 219

Massey, P. 2003, ARA&A, 41, 15

Mauerhan, J. C., Cotera, A., Dong, H., et al. 2010, ApJ, 725, 188

McConnell, N. J., Lu, J. R., & Mann, A. W. 2016, ApJ, 821, 39

McCrady, N., Graham, J. R., & Vacca, W. D. 2005, ApJ, 621, 278

Molinari, S., Bally, J., Noriega-Crespo, A., et al. 2011, ApJ, 735, L33

Morris, M., & Serabyn, E. 1996, ARA&A, 34, 645

Najarro, F., Figer, D. F., Hillier, D. J., & Kudritzki, R. P. 2004, ApJ, 611, L105

Narayanan, D., & Davé, R. 2012, MNRAS, 423, 3601

—. 2013, MNRAS, 436, 2892

Newman, A. B., Smith, R. J., Conroy, C., Villaume, A., & van Dokkum, P. 2017, ApJ, 845, 157

Offner, S. S. R., Clark, P. C., Hennebelle, P., et al. 2014, Protostars and Planets VI, 53

Offner, S. S. R., Klein, R. I., McKee, C. F., & Krumholz, M. R. 2009, ApJ, 703, 131

Oser, L., Ostriker, J. P., Naab, T., Johansson, P. H., & Burkert, A. 2010, ApJ, 725, 2312

Padoan, P., & Nordlund, Å. 2002, ApJ, 576, 870

Pang, X., Grebel, E. K., Allison, R. J., et al. 2013, ApJ, 764, 73

Papadopoulos, P. P., Thi, W.-F., Miniati, F., & Viti, S. 2011, MNRAS, 414, 1705

Parikh, T., Thomas, D., Maraston, C., et al. 2018, MNRAS, arXiv:1803.08515

Park, S.-M., Goodwin, S. P., & Kim, S. S. 2018, ArXiv e-prints, arXiv:1804.08869

Peacock, M. B., Zepf, S. E., Maccarone, T. J., et al. 2014, ApJ, 784, 162

Peacock, M. B., Zepf, S. E., Kundu, A., et al. 2017, ArXiv e-prints, arXiv:1705.01115

Sabbi, E., Sirianni, M., Nota, A., et al. 2008, AJ, 135, 173

Salpeter, E. E. 1955, ApJ, 121, 161

Selman, F. J., & Melnick, J. 2005, A&A, 443, 851

Slesnick, C. L., Hillenbrand, L. A., & Massey, P. 2002, ApJ, 576, 880

Smith, L. J., Westmoquette, M. S., Gallagher, J. S., et al. 2006, MNRAS, 370, 513

Smith, R. J., Lucey, J. R., & Conroy, C. 2015, MNRAS, 449, 3441

Spiniello, C., Trager, S., Koopmans, L. V. E., & Conroy, C. 2014, MNRAS, 438, 1483

Stolte, A., Brandner, W., Grebel, E. K., Lenzen, R., & Lagrange, A.-M. 2005, ApJ, 628, L113

Stolte, A., Ghez, A. M., Morris, M., et al. 2008, ApJ, 675, 1278

Stolte, A., Grebel, E. K., Brandner, W., & Figer, D. F. 2002, A&A, 394, 459

Stolte, A., Hußmann, B., Morris, M. R., et al. 2014, ApJ, 789, 115

Swinbank, A. M., Papadopoulos, P. P., Cox, P., et al. 2011, ApJ, 742, 11

Treu, T., Auger, M. W., Koopmans, L. V. E., et al. 2010, ApJ, 709, 1195

van Dokkum, P., Conroy, C., Villaume, A., Brodie, J., & Romanowsky, A. J. 2017, ApJ, 841, 68

Vaughan, S. P., Davies, R. L., Zieleniewski, S., & Houghton, R. C. W. 2018, MNRAS, 475, 1073

Vincenzo, F., Matteucci, F., Recchi, S., et al. 2015, MNRAS, 449, 1327

Weidner, C., Kroupa, P., Pflamm-Altenburg, J., & Vazdekis, A. 2013, MNRAS, 436, 3309

Weisz, D. R., Johnson, L. C., Foreman-Mackey, D., et al. 2015, ArXiv e-prints, arXiv:1502.06621

Zeidler, P., Nota, A., Grebel, E. K., et al. 2017, AJ, 153, 122

Zieleniewski, S., Houghton, R. C. W., Thatte, N., & Davies, R. L. 2015, MNRAS, 452, 597

Zieleniewski, S., Houghton, R. C. W., Thatte, N., Davies, R. L., & Vaughan, S. P. 2017, MNRAS, 465, 192

Chapter 2

The Arches Cluster: Extended Structure and Tidal Radius

Note: This chapter originally appeared as Hosek et al. (2015), with co-authors Jessica R. Lu, Jay Anderson, Andrea M. Ghez, Mark R. Morris, and William I. Clarkson

Abstract

At a projected distance of ∼26 pc from Sgr A*, the Arches cluster provides insight to star formation in the extreme Galactic Center (GC) environment. Despite its importance, many key properties such as the cluster's internal structure and orbital history are not well known. We present an astrometric and photometric study of the outer region of the Arches cluster (R > 6.25") using *HST* WFC3IR. Using proper motions we calculate membership probabilities for stars down to F153M = 20 mag (∼2.5 $M_\odot$) over a 120" x 120" field of view, an area 144 times larger than previous astrometric studies of the cluster. We construct the radial profile of the Arches to a radius of 75" (∼3 pc at 8 kpc), which can be well described by a single power law. From this profile we place a 3σ lower limit of 2.8 pc on the observed tidal radius, which is larger than the predicted tidal radius (1 – 2.5 pc). Evidence of mass segregation is observed throughout the cluster and no tidal tail structures are apparent along the orbital path. The absence of breaks in the profile suggests that the Arches has not likely experienced its closest approach to the GC between ∼0.2 – 1 Myr ago. If accurate, this constraint indicates that the cluster is on a prograde orbit and is located front of the sky plane that intersects Sgr A*. However, further simulations of clusters in the GC potential are required to interpret the observed profile with more confidence.

2.1 Introduction

The Arches cluster is a young (2-4 Myr; Najarro et al. 2004, Martins et al. 2008) massive (∼4–6 x 10^4 $M_\odot$; Clarkson et al. 2012) star cluster near the center of the Milky Way. It has a projected distance of just ∼26 pc from the supermassive black hole (SMBH) and is one of the most centrally concentrated star clusters in the Galaxy. Old enough to be free of its natal gas cloud and yet young enough to sample the full stellar mass range, the Arches cluster provides a unique opportunity to probe star formation and cluster evolution in the extreme Galactic Center (GC) environment. However, studies of the cluster are complicated by stellar crowding and the high level of extinction which varies significantly across the field (1.6 mag $< A_{Ks} <$ 3.3 mag; Habibi et al. 2013). This effectively smears out the photometric properties of the cluster population, making it difficult to separate cluster members from field stars through photometry alone. As a result, important questions about the cluster's structure, initial mass function, and orbital history remain.

The Arches is one of the closest examples of a young massive cluster (YMC) in a strong tidal field. Such objects are not predicted to have long lifetimes, as simulated clusters near the GC show complete tidal disruption on the order of ∼10 Myr (Kim et al. 1999, 2000) or shorter when interactions with giant molecular clouds are considered (Kruijssen et al. 2014). Since the effects of tidal perturbations are most significant for stars on the outskirts of their clusters (Gnedin et al. 1999; Küpper et al. 2010), measuring the structure of the outer region of the Arches offers insight to its past interactions. For example, it was long thought that the observed tidal radius (i.e., limiting radius) of a cluster, where the stellar density drops to zero, should correspond to its theoretical tidal radius (i.e., Jacobi radius), where the gravitational acceleration of the cluster equals the tidal acceleration of its parent galaxy (von Hoerner 1957). Early Fokker-Planck simulations of clusters on eccentric orbits further suggested that the tidal radius imposed by the strongest tides at perigalacticon should persist to later times (Oh & Lin 1992). However, more recent N-body simulations show that perigalacticon passage does not cleanly truncate a cluster, but rather results in an extended radial profile that approaches a power law (Oh et al. 1995; Johnston et al. 1999; Peñarrubia et al. 2009; Küpper et al. 2010). The "extratidal" stars can have a different profile slope than the rest of the cluster, creating a break in the profile at a radius which may be related to the time since perigalacticon passage (Peñarrubia et al. 2009; Łokas et al. 2013).

Measurements of globular cluster profiles have revealed the presence of extratidal stars, often associated with tidal tail structures (Odenkirchen et al. 2001; Siegel et al. 2001; Odenkirchen et al. 2003; Belokurov et al. 2006; Sollima et al. 2011; Chun et al. 2015). However, as discussed by Küpper et al. (2010) and Carballo-Bello et al. (2012), even clusters that are not exposed to varying external tidal fields can also form extratidal structures through two-body relaxation, as stars which become energetically unbound from the cluster do not escape instantaneously but rather on a time-scale which is dependent on their orbital parameters (Fukushige & Heggie 2000; Baumgardt & Makino 2003; Zotos 2015). Both of these mechanisms affect the radial profile of globular clusters, which have ages larger than their relaxation times. On the other hand, two-body relaxation is negligible for YMCs that are much younger than than their relaxation times, and so the impact of tidal perturbations on their profiles should be easier to isolate. Given the high likelihood of strong tidal interactions with the GC, the Arches offers a promising opportunity to measure such a feature. In addition, a detailed understanding of the Arches cluster profile is necessary for assessing the impact of dynamical effects on the present-day mass function (i.e. mass segregation and tidal stripping).

Insight into the past tidal interactions of the Arches cluster also provides valuable information about its orbit. While its bulk proper motion (Stolte et al. 2008; Clarkson et al. 2012) and doppler velocity (Figer et al. 2002) have been measured, the line-of-sight distance is unknown, preventing a unique orbital solution. As a result, the birth environment of the cluster and its relation to the nearby Quintuplet cluster are not well understood. For example, it has been suggested that both the Arches and Quintuplet formed in a collision between gas clouds along the X_1 and X_2 orbit families in the Galactic bar, which may be a region of highly efficient star formation (Binney et al. 1991; Stolte et al. 2014). Alternatively, the Arches may be the end product of a cluster formation sequence identified by Longmore et al. (2013) and Kruijssen et al. (2014), where starburst clusters form from the tidal compression of gas clouds that pass close to the GC. It has also been suggested that the Arches may be a possible source of the isolated massive stars observed near the GC, depending on its orbit and how much tidal stripping has occurred (Mauerhan et al. 2010; Habibi et al. 2014). If the time since the last tidal perturbation (presumably occurring at the closest approach to the GC) can be established, the set of possible orbits for the Arches calculated by Stolte et al. (2008) can be significantly restricted.

We present the radial profile of the Arches cluster out to large cluster radii (∼75", or ∼3 pc at 8 kpc[1]) and investigate the structure of the outer region of the cluster for the first time. We use stellar proper motions rather than photometry to calculate cluster membership probabilities, avoiding many of the difficulties introduced by differential reddening. The effectiveness of this method on the Arches cluster was demonstrated by Stolte et al. (2008) and Clarkson et al. (2012), who used ground-based adaptive optics (AO) observations to measure the cluster's bulk proper motion and identify members in the central 10" x 10" region. In this paper, we conduct an astrometric study of the Arches cluster using the *Hubble Space Telescope* (HST), which provides high astrometric precision over a field of view 144 times larger than these previous studies. This allows us to measure the radial profile to beyond the predicted tidal radius (25" - 60"; Kim et al. 2000; Portegies Zwart et al. 2002). In addition, we examine the degree of mass segregation throughout the cluster and search for the presence of tidal tails. The consequences of our results are discussed in relation to the orbital history of the Arches cluster.

2.2 Methods

2.2.1 Observations and Measurements

We observed the Arches cluster with the *Hubble Space Telescope* (HST) WFC3IR camera using the F127M, F139M, and F153M filters (1.27 μm, 1.39 μm, and 1.53 μm, respectively; PI: Ghez, ID: 11671, 12318, 12667). A summary of the observations is provided in Table 2.1. These observations have a field of view of 120" x 120" and are centered at α(J2000) = 266.4604, δ(J2000) = -28.8222 with a position angle of -45° (Figure 2.1). Astrometry is performed on the F153M observations, which were obtained in three epochs over a two year baseline between 2010 – 2012. Of this filter set, F153M was chosen for astrometry because it provides the optimal combination of limited saturation and a well-sampled point spread function (PSF) with a FWHM ∼0.17" (1.4 pix, scale = 0.121" pix^{-1}). High astrometric and photometric precision is achieved by observing at the same position angle and pixel position across epochs and using a dense, sub-pixel spiral dithering pattern within each epoch. F127M and F139M observations were only obtained in 2010 using a simpler dither pattern for the purpose of color information to derive extinction.

[1]All distances throughout this paper assume a distance of 8 kpc to the Arches cluster.

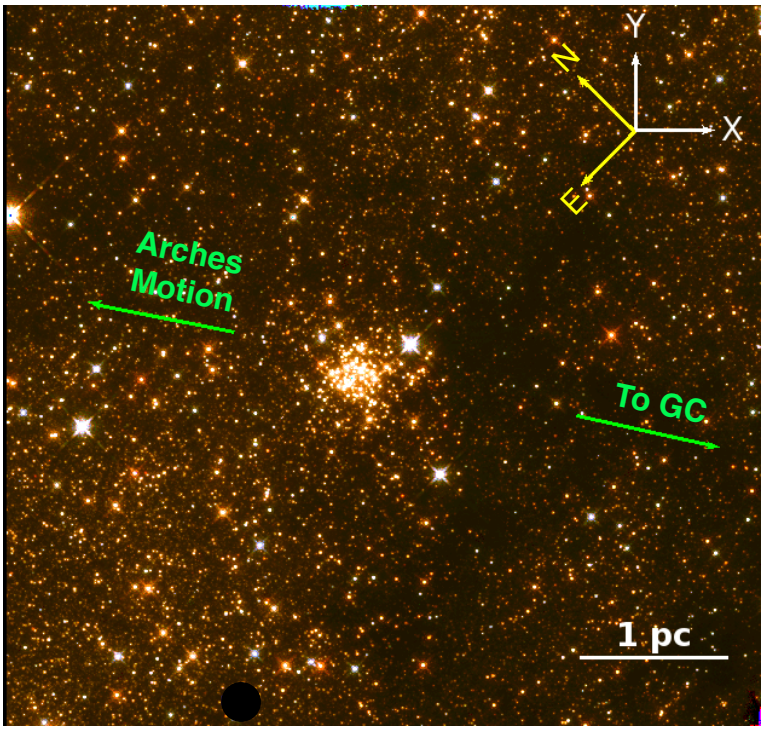

Figure 2.1 Three color image of the Arches Cluster, with F127M = blue, F139M = green, and F153M = red. Significant differential extinction is apparent from the changing density of the field stars. The hole in the lower left side of the image is due to a known defect in the WFC3IR chip. The proper motion of the cluster (labeled with green arrow) is very nearly parallel to the Galactic plane.

Table 2.1. HST WFC3IR Observations

Date	Filter	N_{images}	Exp. Time (s)	Depth (mag)[b]	Pos Error (mas)[a]	Phot Error (mag)[a]
2010.6150	F127M	12	7200	23.63	0.60	0.02
2010.6148	F139M	10	3500	23.29	0.90	0.03
2010.6043	F153M	21	7350	23.31	0.88	0.05
2011.6829	F153M	21	7350	23.32	0.88	0.05
2012.6156	F153M	21	7350	23.31	0.88	0.05

[a]Median value at mag = 20 in respective filter

[b]Estimated from 95th percentile of extracted stellar magnitudes.

Each frame is processed using the standard *HST* pipeline, which produces a `flt` image which has been flat-fielded and bias-subtracted. We use a combination of public and custom software to extract high-precision astrometry and photometry via PSF-fitting with a variable PSF model. While this method has been previously implemented on HST optical observations of Globular Clusters, this is the first time it has been applied to WFC3IR observations. We produce a list of individual stellar measurements for each filter/epoch using the program *KS2*, a generalization of the software developed to reduce the Globular-Cluster Treasury Program (Anderson et al. 2008). Star positions are transformed to an arbitrary astrometric reference frame where the net motion of the cluster plus field is 0 mas yr^{-1} using general 6-parameter linear transformations that can be described as a 2D translation, rotation, plate scale, and shear for each image. Approximately ∼50,000 stars are measured in each filter/epoch. The photometry is calibrated to the standard Vega magnitude system using the zero points derived for the WFC3IR camera[2]. A detailed description of the data reduction and measurement process, as well as an analysis of the astrometric and photometric errors, is provided in Appendix 2.6.

We calculate proper motions for the stars that are detected in all three F153M epochs, using linear fits weighted by the individual astrometric errors. Proper motion uncertainty as a function of observed F153M magnitude is presented in Figure 2.2. Several tests were conducted to confirm the validity of these errors (see Appendix 2.6). Previous studies of the bulk proper motion of the Arches cluster relative to the field population by Stolte et al. (2008) and Clarkson et al. (2012) revealed that a precision of ∼0.8 mas yr^{-1} is needed in order to reliably separate cluster members from field stars. As a conservative error cut, we restrict the forthcoming analysis to stars with a proper motion precision of 0.65 mas yr^{-1} or better, which we achieve down to F153M ≈ 20 mag. At the average distance and reddening of the Arches cluster this corresponds to roughly 2.5 $M_\odot$. We additionally require a minimum photometric precision of 0.06 mags in each F153M epoch to ensure high-quality results. We measure ∼26,000 proper motions, ∼6000 of which pass these error cuts. The kinematic distinction between cluster and field stars is clearly seen in a vector point diagram (VPD; Figure 2.3). Note that the proper motions have been rotated from image coordinates into projected equatorial coordinates where the two-dimensional proper motion vector of any star is $\boldsymbol{\mu} = [\mu_\alpha \cos\delta,\ \mu_\delta]$. Proper motions are also shifted into a reference frame where the cluster is at

[2]As of August 2014; http://www.stsci.edu/hst/wfc3/phot_zp_lbn

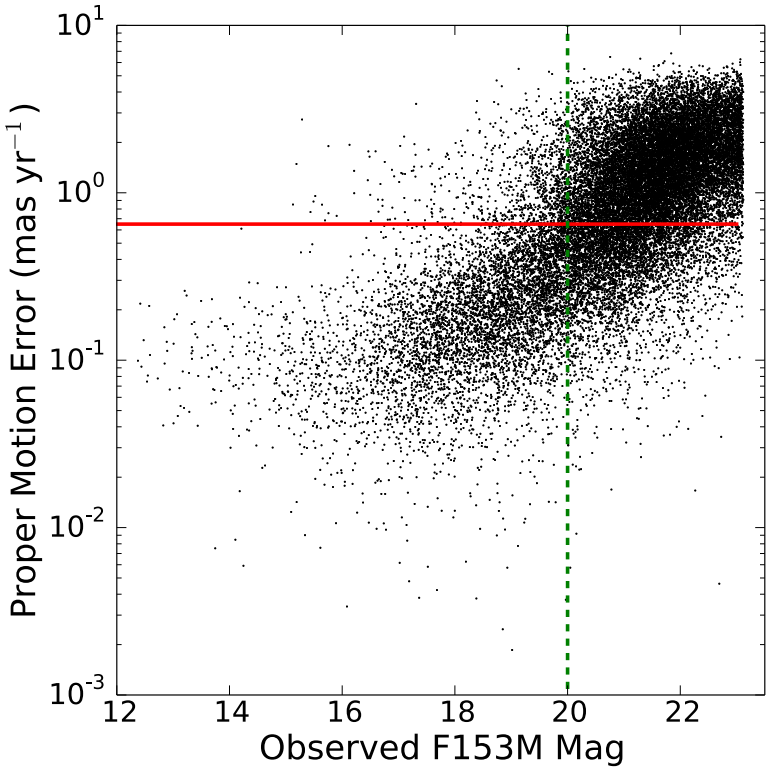

Figure 2.2 Proper Motion error vs. F153M magnitude. The red line marks our proper motion error cut of 0.65 mas yr^{-1}. Only stars below this cut are included in our analysis. The green line denotes F153M = 20 mag, which corresponds to $\sim$2.5 $M_{\odot}$ at the approximate distance and average reddening of the Arches cluster.

rest, estimated from the mean motion of stars within the central 10"x10" region of the cluster. This sample is an order of magnitude larger than the sample analyzed by Clarkson et al. (2012), who had a much smaller field of view.

2.2.2 Cluster and Field Populations

In order to calculate cluster membership probabilities we must first characterize the kinematic distributions of the cluster and field star populations. Previous studies of the Arches cluster have assumed that the field kinematics can be modeled as a single elliptical Gaussian distribution (Clarkson et al. 2012). The field kinematic distribution is elliptical because it is primarily composed of stars in the Galactic bulge that exhibit a larger velocity dispersion along the Galactic plane than

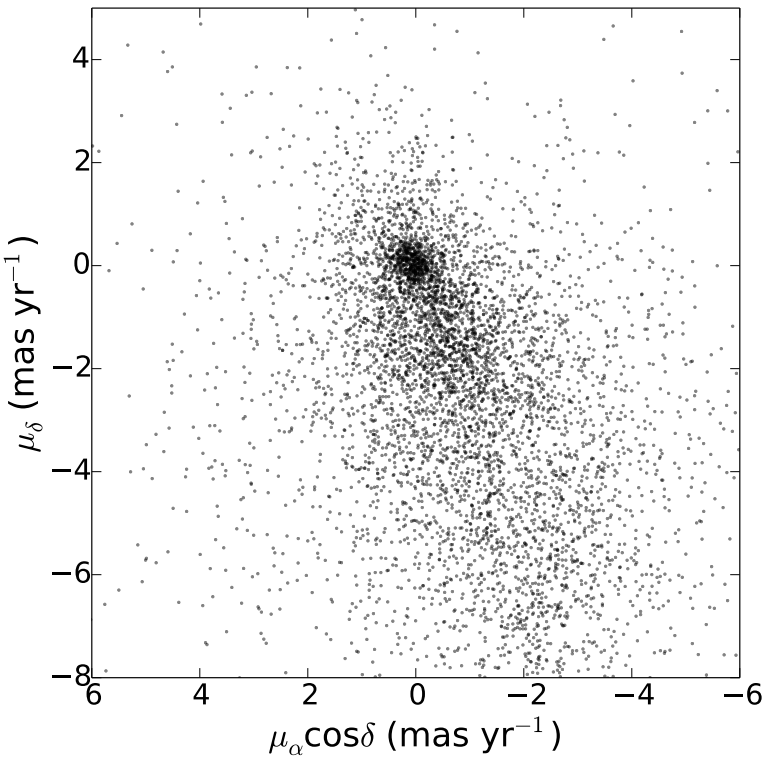

Figure 2.3 Vector point diagram of the ∼6000 stars included in our analysis. Proper motions are in the reference frame of the cluster. Cluster members appear as a distinct clump of stars at ($\mu_\alpha$cosδ, μ_δ) = (0, 0), while the field stars are spread along the Galactic plane.

perpendicular to it, a consequence of coherent rotation (Clarkson et al. 2008; Howard et al. 2009; Kunder et al. 2012). However, close inspection of Figure 2.3 reveals that the field population cannot be described by a single Gaussian function. To account for this complexity, we adopt a Normal Mixture Model (McLaughlin & Peel 2000) to simultaneously fit multiple Gaussians to the observed VPD. A more complete description of the field requires modeling the stellar density, kinematics, and reddening at all distances along our line of sight towards the Arches. Such analysis would be valuable for exploring Galactic structure but is beyond the scope of this paper.

We construct a likelihood function for each star in the sample from from the sum of K Gaussian components:

$$L(\boldsymbol{\mu}_i) = \sum_{k=0}^{K} \pi_k \frac{1}{2\pi|\boldsymbol{\Sigma}_{ki}|^{1/2}} exp\left(-\frac{1}{2}(\boldsymbol{\mu}_i - \overline{\boldsymbol{\mu}}_k)^T \boldsymbol{\Sigma}_{ki}^{-1}(\boldsymbol{\mu}_i - \overline{\boldsymbol{\mu}}_k)\right) \tag{2.1}$$

$$\mathcal{L} = \prod_{i}^{N} L(\boldsymbol{\mu}_i)$$

where $\boldsymbol{\mu}_i$ is the proper motion of the ith star, π_k is the fraction of total stars in the kth Gaussian such that $\sum_{k=0}^{K} \pi_k = 1$, $\overline{\boldsymbol{\mu}}_k$ is the velocity centroid of the kth Gaussian, and $\boldsymbol{\Sigma}_{ki}$ is the covariance of the kth Gaussian and ith star. The total likelihood over the sample of N stars is $\mathcal{L}$. Following Clarkson et al. (2012), we add the covariance matrices of the population model and stellar proper motion uncertainties such that $\boldsymbol{\Sigma}_{ki} = \boldsymbol{S}_i + \boldsymbol{Z}_k$, where $\boldsymbol{S}_i$ is the velocity error matrix (assumed to be diagonal with velocity error components $\sigma^2_{\mu_{\alpha cos\delta}}$ and $\sigma^2_{\mu_\delta}$) and $\boldsymbol{Z}_k$ is the covariance matrix of the kth Gaussian fit.

With the likelihood function defined, we can determine the global kinematic parameters of the cluster and field populations through Bayesian inference using Bayes' theorem:

$$P(\boldsymbol{\pi}, \overline{\boldsymbol{\mu}}, \boldsymbol{Z}|\boldsymbol{\mu}, \boldsymbol{S}) = \frac{P(\boldsymbol{\mu}, \boldsymbol{S}|\boldsymbol{\pi}, \overline{\boldsymbol{\mu}}, \boldsymbol{Z}) P(\boldsymbol{\pi}, \overline{\boldsymbol{\mu}}, \boldsymbol{Z})}{P(\boldsymbol{\mu}, \boldsymbol{S})} \tag{2.2}$$

where $P(\boldsymbol{\pi}, \overline{\boldsymbol{\mu}}, \boldsymbol{Z}|\boldsymbol{\mu}, \boldsymbol{S})$ is the posterior probability of our model parameters $\boldsymbol{\pi}$, the set of π_k values; $\overline{\boldsymbol{\mu}}$, the set of Gaussian velocity centroids; and $\boldsymbol{Z}$, the set of Gaussian covariance matrices given the observed stellar velocities $\boldsymbol{\mu}$ and velocity error matrix $\boldsymbol{S}$. $P(\boldsymbol{\mu}, \boldsymbol{S}|\boldsymbol{\pi}, \overline{\boldsymbol{\mu}}, \boldsymbol{Z})$ is the probability of the

observed stellar velocity distribution given the model, and $P(\boldsymbol{\pi}, \overline{\boldsymbol{\mu}}, \boldsymbol{Z})$ is the prior probability of the model. In this case, $P(\boldsymbol{\mu}, \boldsymbol{S}|\boldsymbol{\pi}, \overline{\boldsymbol{\mu}}, \boldsymbol{Z})$ is the total likelihood $\mathcal{L}$ defined in Equation 2.1.

To find the posterior probability distribution we use *Multinest*, a publicly available nested sampling algorithm which serves as an alternative to Markov Chain Monte Carlo (MCMC) algorithms when exploring multi-modal parameter spaces (Feroz et al. 2009). This iterative technique calculates the posterior probability at a fixed number of points in the parameter space and identifies possible peaks, restricting subsequent sampling to the regions around these peaks until the change in evidence drops below a user-defined tolerance level. Multiple peaks can be identified and evaluated, resulting in increased sampling efficiency with complicated parameter spaces. We run the algorithm using the python module *PyMultinest* (Buchner et al. 2014).

We find that the cluster and field populations can be well described with a 4-Gaussian mixture model, with one Gaussian describing the cluster and the other three describing the field (Figure 2.4). The use of this model is justified by the Bayesian Information Criterion (Schwarz 1978), which is minimized compared to less complicated (3-Gaussian) or more complicated (5-Gaussian) mixture models. We require the cluster Gaussian to be circular, consistent with the results of Clarkson et al. (2012), and adopt a prior to roughly constrain its location around (v_x, v_y) = (0,0). The parameters for the field Gaussians as well as the remaining parameters for the cluster Gaussian are unconstrained. The one-dimensional posterior distributions are well described by a Gaussian function, which is used to determine the best-fit value and error for that parameter. A summary of the parameter priors, best-fit results, and errors is provided in Table 4.6.

These results can be compared with those of Clarkson et al. (2012), who examine the kinematics of the inner 10" x 10" of the cluster using ground-based AO observations. Their measurements have a higher precision but much smaller field of view than our observations. We obtain a velocity dispersion of 0.18 $\pm$ 0.02 mas yr^{-1} for the cluster, which is consistent with the measurement of 0.15 $\pm$ 0.01 mas yr^{-1} by Clarkson et al. (2012) within errors. This agreement comes despite using fully independent data sets which focus on different regions of the cluster.

However, there is less agreement on the bulk motion of the Arches relative to the field population. Clarkson et al. (2012) model the field using a single elliptical Gaussian distribution with a velocity center offset by 4.39 $\pm$ 0.38 mas yr^{-1} from the cluster. In this study we model the field using 3 elliptical Gaussians, and our fits indicate that all have smaller motions relative to the cluster than

the Clarkson et al. (2012) result (see Table 4.6). If we calculate the average motion of the field from the average sum of the 3 field Gaussians, then we get an overall field motion of 2.83 $\pm$ 0.33 mas yr^{-1} relative to the cluster, which is substantially and significantly lower than the Clarkson et al. (2012) result. We discuss this discrepancy further in §2.4.1.

Table 2.2. Cluster and Field Population Model: Free Parameters, Priors, and Results

	Cluster Gaussian		Field Gaussian 1		Field Gaussian 2		Field Gaussian 3	
Parameter[a]	Prior[b]	Result	Prior	Result	Prior	Result	Prior	Result
π_k	U(0, 1)	0.08 ± 0.01	U(0, 1)	0.25 ± 0.03	U(0, 1)	0.42 ± 0.04	U(0, 1)	0.25 ± 0.03
$\mu_{\alpha,k}$ (mas yr^{-1})	G(0, 0.2)	0.06 ± 0.03	U(-4, 12)	-0.26 ± 0.06	U(-4, 12)	-1.19 ± 0.11	U(-4, 12)	-1.15 ± 0.15
$\mu_{\delta,k}$ (mas yr^{-1})	G(0, 0.2)	0.06 ± 0.02	U(-4, 12)	-0.77 ± 0.09	U(-4, 12)	-3.40 ± 0.25	U(-4, 12)	-3.05 ± 0.20
$\sigma_{a,k}$ (mas yr^{-1})	U(0, 8)	0.18 ± 0.02	U(0, 8)	1.27 ± 0.09	U(0, 8)	2.73 ± 0.12	U(0, 8)	3.20 ± 0.13
$\sigma_{b,k}$ (mas yr^{-1})	$\sigma_b = \sigma_a$	0.18 ± 0.02	U(0, 4)	0.60 ± 0.05	U(0, 4)	1.30 ± 0.08	U(0, 4)	3.05 ± 0.13
θ_k (rad)	—	0	U(0, π)	1.16 ± 0.05	U(0, π)	1.20 ± 0.03	U(0, π)	0

[a]Description of parameters: π_k = fraction of stars in Gaussian; $\mu_{\alpha,k}$ = RA-velocity centroid of Gaussian; $\mu_{\delta,k}$ = DEC-velocity centroid of Gaussian; $\sigma_{a,k}$ = semi-major axis of Gaussian; $\sigma_{b,k}$ = semi-minor axis of Gaussian; θ_k = angle between $\sigma_{a,k}$ and the RA-axis

[b]Uniform distributions: U(min, max), where min and max are bounds of the distribution; Gaussian distributions: G(μ, σ), where μ is the mean and σ is the standard deviation

2.2.3 Extinction Map Using Red Clump Stars

Taking advantage of the high photometric precision of HST, we use red clump (RC) stars in the Galactic bulge to measure the extinction across the Arches cluster field. This provides an alternative to "sliding" apparent cluster members along their reddening vector in a color-magnitude diagram (CMD) to a theoretical cluster isochrone to measure extinction, as has been done in previous studies of the Arches cluster (Kim et al. 2006; Espinoza et al. 2009; Habibi et al. 2013). This CMD sliding method is prone to field contamination and isochrone uncertainties, especially for the pre-main sequence at low to intermediate masses. On the other hand, stellar evolution theory and observations show that RC stars exhibit well-defined luminosities and colors which do not vary significantly with age or metallicity (Castellani et al. 1992; Paczynski & Stanek 1998; Stanek et al. 2000), making them useful calibrators to measure extinction. This is especially true near the GC, where the relatively high density of RC stars in the bulge population makes it possible to create reddening maps of different regions (Sumi 2004; Schödel et al. 2010). Though the line-of-sight position of the Arches with respect to the bulge RC stars is uncertain, we assume that all of the extinction is caused by foreground material and so the RC population exhibits similar extinction as the cluster members themselves. With this approach we create the first RC-based extinction map of the Arches cluster.

Bulge RC stars are readily identified as a narrow population spread along the reddening vector in the F127M vs. F127M - F153M color-magnitude diagram (Figure 2.5). The spread of this population is primarily caused by differential reddening, which smears out what would normally be a tight clump of stars. In order to isolate RC stars, we use a PHOENIX model atmosphere (Allard et al. 2011) with typical RC parameters at solar metallicity (T_{eff} = 4700 K, log g = 2.40; Mishenina et al. 2006) to calculate the F127 vs. F127M - F153M reddening vector using the GC extinction law of Nishiyama et al. (2009). Keeping the slope of the reddening vector fixed, the y-intercept is fit to stars which fall within a broad area in the CMD around the RC population. We identify RC stars as those within a rectangle with the long axis centered on the reddening vector with the length of the short axis defined by the least crowded section of the RC bar (F127M - F153M $\approx$ 2.7). This corresponds to a width of constant value ΔF127M = 0.7 mag. Identified

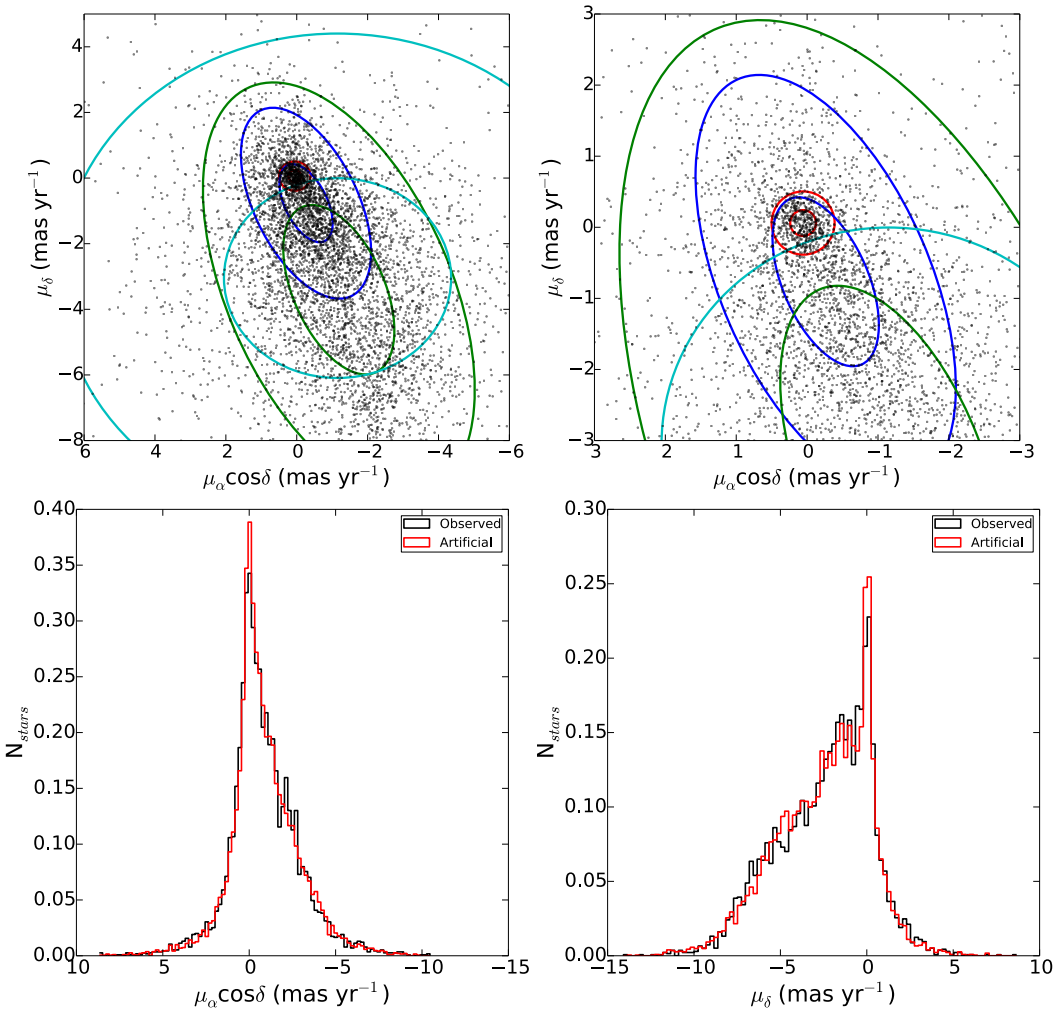

Figure 2.4 *Top:* Vector point diagram of our sample with the fitted 1- and 2σ distributions of the cluster Gaussian (red) and field Gaussians (blue, green, cyan corresponding to field Gaussians 1, 2, and 3 in Table 4.6, respectively). The *left* plot shows all stars in the field, demonstrating the extension of the field populations in the direction of the Galactic plane. The *right* plot is a zoomed-in view of the cluster population, readily apparent as a tight clump of stars moving with a common motion relative to the field. *Bottom:* Proper motion distribution of the stars in projected equatorial coordinates (*left*: RA, *right*: Dec). The predicted distribution of the Normal Mixture Model (red) is found to be a good match to the observed stars (black).

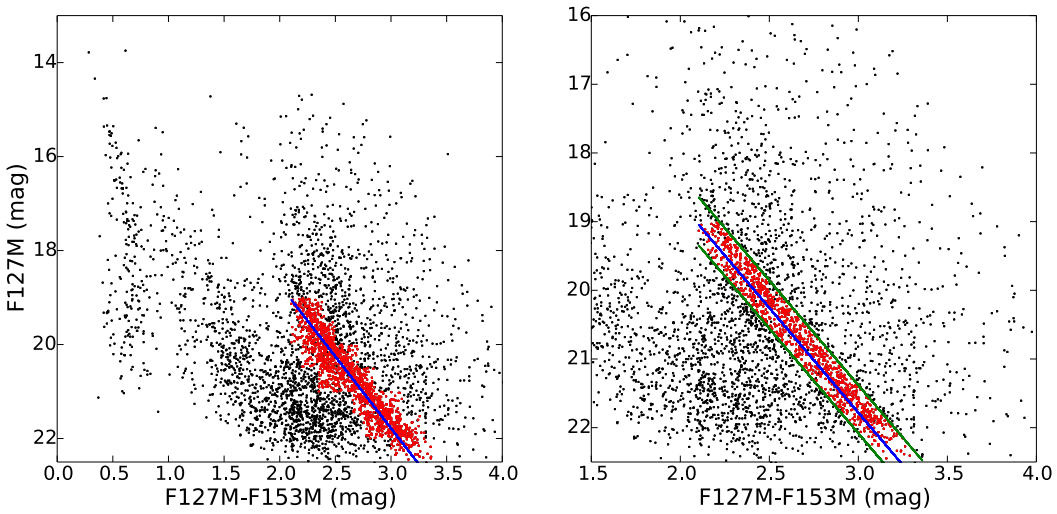

Figure 2.5 The identification of Red Clump (RC) stars in the F127M vs. F127M - F153M color-magnitude diagram, as described in § 2.2.3. *Left*: The full field CMD, with the stars used in the initial fit of the RC reddening vector in red and the reddening vector itself in blue. *Right*: A zoomed-in view of the RC population, with the RC reddening vector and final identification criterion shown with blue and green lines, respectively. Stars falling between the green lines (red points) are identified as RC stars and are used to make the extinction map.

cluster members (§ 4.3.1) are removed from this sample. The extinction of each identified RC star is taken from the nearest point on the reddening vector in color-magnitude space.

We measure the extinction for 1027 RC stars identified across the field. These values are spatially interpolated using a 5th order bivariate spline to map the extinction at every position (Figure 2.6). The typical error is $\sigma_{A_{Ks}} = 0.10$ mags, as derived in §4.3.1. Extinction values range from $1.8 < \mathrm{A}_{Ks} < 3.0$ with a median of $\mathrm{A}_{Ks} = 2.4$ for cluster members. This range is in agreement with the reddening map of Habibi et al. (2013), who find $1.6 < \mathrm{A}_{Ks} < 3.3$ also using a Nishiyama et al. (2009) reddening law.

2.2.4 Completeness Analysis

In order to accurately measure the radial density profile of the Arches Cluster we must conduct an extensive completeness analysis on our astrometry pipeline. In addition to the sensitivity threshold of our observations, stars may be missed due to source confusion and proximity to bright and/or saturated stars. These effects are especially relevant for the dense central region of the cluster. To

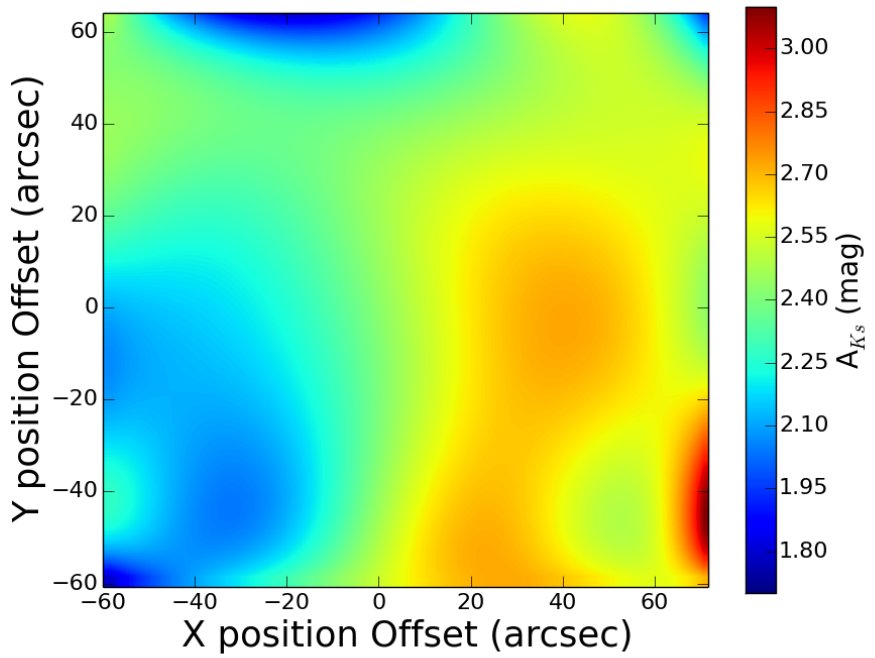

Figure 2.6 The extinction map created via the spatial interpolation of the Red Clump extinction values as described in the text. The IR reddening law of Nishiyama et al. (2009) is used to calculate A_λ at different wavelengths. Positions are given with respect to the cluster center located at (x, y) = (0, 0), and the axes are oriented same manner as Figure 2.1. Strong cluster candidates ($P_{member} > 0.7$) have an average reddening of $A_{Ks} = 2.4$ mag.

quantify our completeness we perform an artificial star injection and recovery test, planting 400,000 stars in each image and determining which are recovered to sufficient accuracy and precision as a function of spatial position and magnitude. The magnitudes of the artificial stars are drawn from the observed CMD of the field in order to best simulate the photometric properties of the observed stars. These magnitudes are then perturbed by a random amount reflecting the photometric uncertainty (assumed to be Gaussian distributed) of the real star they are simulating. The same set of artificial stars is applied to all observations. This analysis assumes that the artificial star measurement errors match those of the observed stars, which we test in Appendix 2.7.

The conditions an artificial star must fulfill in order to be considered as recovered matches the criteria applied to the real data. Within a given epoch, a recovered artificial star must: 1) be detected in at least 75% of the images within that epoch; 2) have position and magnitude errors less than 1.5 mas (required for a proper motion precision better than or equal to 0.65 mas yr^{-1}) and 0.06 mag, respectively; and 3) have a measured position and magnitude within 0.5 pix (60 mas) and 0.5 mag of the planted values to guard against misidentification. In addition, artificial stars must be recovered in all 3 F153M epochs, which is required of the observed stars in order to derive their proper motions (§ 3.2). After detection/non-detection, the extinction map is used to differentially de-redden the artificial stars to the mean extinction of the cluster (A_{Ks} = 2.4 mag). The fraction of recovered artificial stars to the total number of planted artificial stars represents the completeness fraction as a function of position and differentially de-reddened magnitude.

The resulting completeness curves as a function of differentially de-reddened magnitude and of radius are presented in Figure 2.7. Over the full field we achieve greater than 50% completeness down to F153M = 20 mag. However, the completeness in the inner 6.25" (∼0.25 pc) of the cluster is significantly lower due to stellar crowding, falling to 30% by F153M = 18.5 mag. As a result, we restrict the following analysis to observed stars with R > 6.25" and differentially de-reddened magnitudes brighter than F153M = 20 mag.

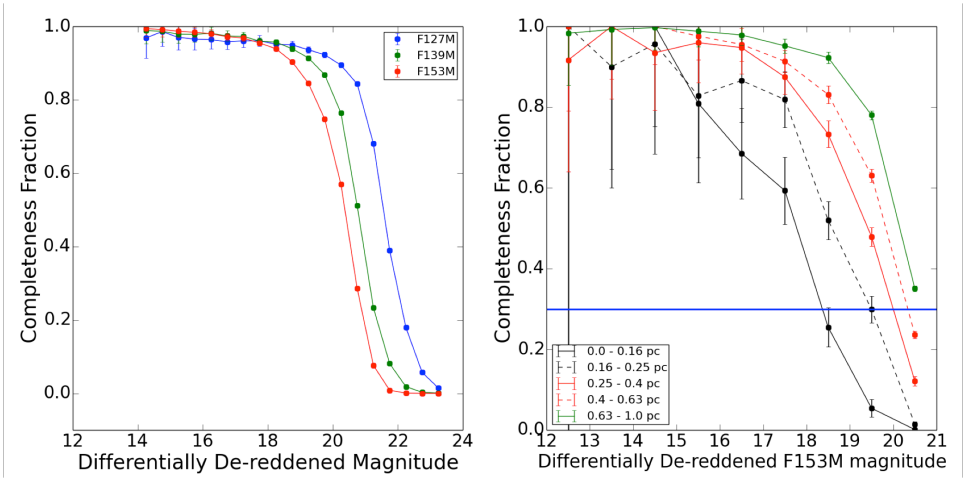

Figure 2.7 Completeness as a function of observed magnitude and radius. *Left*: Completeness as a function of differentially de-reddened magnitude (A_{Ks} = 2.4 mag) for the F127M, F139M, and F153M filters. These completeness values are calculated over the entire field. *Right*: The F153M completeness as a function of differentially de-reddened magnitude in different radius bins. The blue line marks a minimum completeness of 30%, which is achieved down to F153M = 20 mag for R > 0.25 pc. This sets the faint-end magnitude limit and inner radius limit for the radial profile.

2.3 Results

2.3.1 Cluster Membership

With the kinematic properties of the cluster and field populations determined (§ 2.2.2), we calculate the probability of cluster membership for each star based on its proper motion:

$$P^i_{member} = \frac{\pi_c P^i_c}{\pi_c P^i_c + \sum_k^K \pi_k P^i_k} \tag{2.3}$$

where π_c and π_k are the fraction of total stars in the cluster and kth field Gaussian, respectively, and P^i_c and P^i_k are the probability of ith star being part of the cluster and kth field Gaussian, respectively. A histogram of the resulting cluster membership probabilities is shown in Figure 2.8. In the following analysis we include all stars with $P_{member} > 0.3$, weighted by their individual membership probabilities. This criteria selects 701 stars which represent 446.8 "cluster members" based on the sum of the cluster membership probabilities. We consider stars with $P_{member} > 0.7$ as strong cluster candidates, whose distributions in position and velocity space are shown in Figure 2.9.

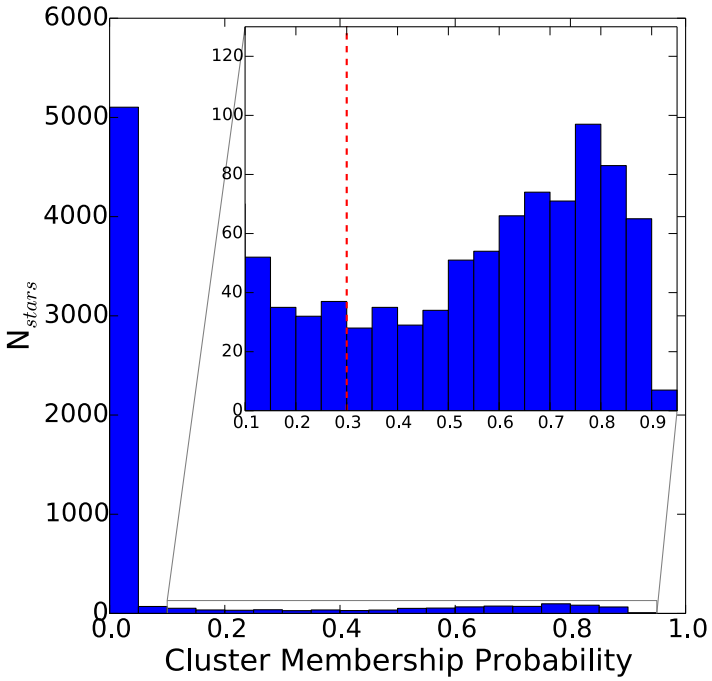

Figure 2.8 A histogram of the membership probabilities obtained for the sample. All objects with $P_{cluster} \geq 0.3$ (red line, inset plot) are considered in the profile analysis, weighted by their membership probability. Of ∼6000 stars examined, 701 meet this criterion, with membership probabilities that sum to 446.8.

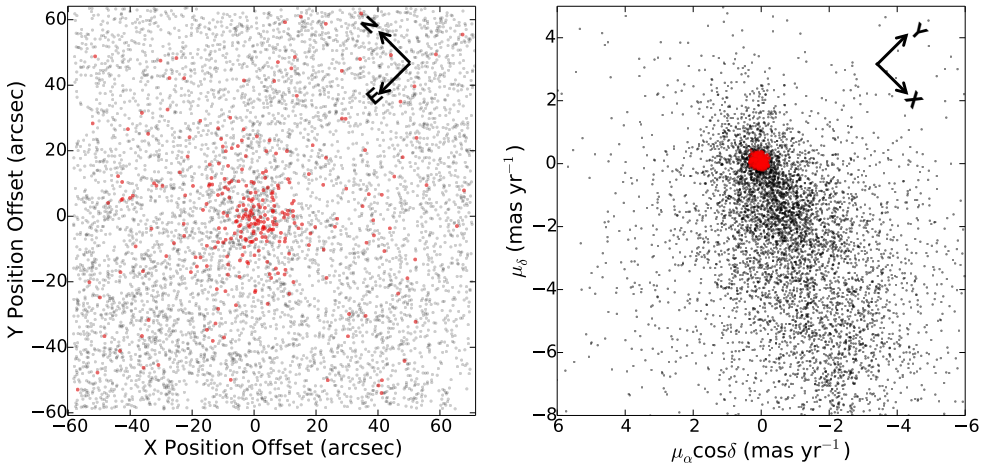

Figure 2.9 The spatial (*left*) and kinematic (*right*) positions of strong cluster candidates ($P_{member} > 0.7$), marked as red points, compared to the rest of the sample in black points. The spatial positions are plotted in arcseconds relative to the cluster center and are in image coordinates (same orientation as Figure 2.1). Proper motions are plotted in projected equatorial coordinates. The radial profile of the Arches includes all stars with $P_{member} > 0.3$, a larger sample than is shown here.

By applying the extinction map derived in §2.2.3 to the strong cluster candidates we create a differentially de-reddened F127M vs F127M - F153M CMD of the cluster (Figure 2.10). The improvement relative to the uncorrected CMD is noticeable in both the overall color dispersion and definition of the blue edge. Stars with colors more blue than the blue edge are very likely field contaminants, while the the scatter along the redward edge of the cluster may be caused by intrinsic reddening of the objects themselves, perhaps due to circumstellar disks (Stolte et al. 2010).

The remaining color dispersion of the differentially de-reddened CMD provides an estimate of the uncertainties of the extinction map. Between $16 < \mathrm{F127M} < 21$ mag the median color dispersion is 0.36 mags. Assuming that the photometric uncertainties in each filter are negligible and adopting the Nishiyama et al. (2009) extinction law, this color dispersion corresponds to an extinction error of $\sigma_{A_{F153M}} = 0.18$ mags ($\sigma_{AKs} = 0.10$ mags).

The mean extinction of the strong cluster candidates is $A_{Ks} = 2.42 \pm 0.14$ mag. The inner region of the cluster ($R < 0.4$ pc) exhibits a tight range of reddening values from $2.33 < A_{Ks} < 2.53$ mag, while the outer region of the cluster ($R > 0.4$ pc) exhibits a much wider range from $2.04 < A_{Ks} < 2.76$ mag. In the literature, there are variations in the measured extinction for the

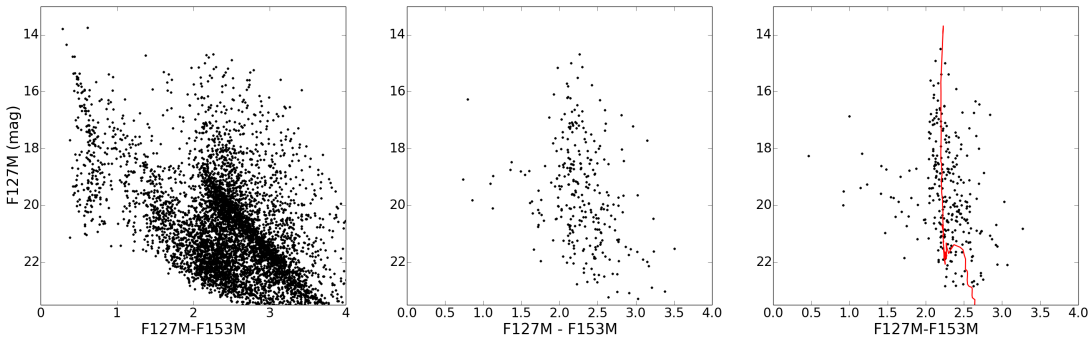

Figure 2.10 The F127M vs. F127M - F153M color-magnitude diagram for the full sample (*left*), strong cluster candidates ($P_{member} > 0.7$, *middle*), and strong cluster candidates after being differentially de-reddened using the extinction map (*right*). The reddening correction noticeably tightens the color dispersion and blue edge of the population. The differentially de-reddened CMD is consistent with a theoretical 2.5 Myr cluster isochrone at 8000 pc with $A_{Ks} = 2.4$ mag, overlaid in red. The isochrone is created using the pre-main sequence evolutionary models of Siess et al. (2000) for M < 7 $M_\odot$ and the main sequence models with rotation of Meynet & Maeder (2003) for M > 9 $M_\odot$, with an interpolation between the models over the missing mass range.

Arches due to different methodologies and reddening laws. Using the same Nishiyama et al. (2009) extinction law with the CMD sliding method, Habibi et al. (2013) find $A_{Ks} = 2.6 \pm 0.2$ mag for 0.2 pc < R < 0.4 pc and $A_{Ks} = 2.6 \pm 0.3$ mag for 0.4 pc< R < 1.5 pc. Also using the CMD sliding method, Espinoza et al. (2009) and Kim et al. (2006) find higher values of $A_{Ks} = 2.97$ and 3.1 for R < 0.4 pc using the extinction laws of Fitzpatrick (2004) and Rieke et al. (1989), respectively. Our measurements are consistent with previous measurements made using the same extinction law.

2.3.2 Radial Density Profile

Using stars with $P_{member} > 0.3$, we construct the radial profile of the Arches Cluster using the Bayesian methodology described by Do et al. (2013). This allows us to construct an un-binned profile that simultaneously incorporates cluster membership probabilities, image completeness, and geometric area corrections at large radii to account for incomplete area coverage. As discussed in §2.2.4, only stars with differentially de-reddened magnitudes of F153M ≤ 20 mag and R > 6.25" (0.25 pc) are considered. We adopt a single power law as our likelihood function:

$$L_i(r, \Gamma, b) = A_0 r_i^{-\Gamma} + b \tag{2.4}$$

where r_i is the radius of the ith star and the field contamination b is assumed to be constant across the image. The profile amplitude A_0 is calculated such that the integral of the radial profile yields the total number of cluster members observed after membership probability, completeness, and area corrections.

The total likelihood $\mathcal{L}$ is then the product of the individual likelihoods for N total stars:

$$log\mathcal{L} = \sum_{i}^{N} w_i(r) \log L_i(r, \Gamma, b) \tag{2.5}$$

$$w_i(r) = \frac{P_i}{A_i(r)C_i(r)}$$

where P_i is the membership probability of the ith star, A_i(r) is the relative fraction of observed area at the star's radius relative to an infinite field of view ($A_i = 1.0$ for $0 <$ r ≤ 60", $A_i < 1.0$ for r > 60"), and C_i(r) is the completeness at that star's radius. A summary of our best-fit model and subsequent results are presented in Table 2.3 and Figure 2.11. A binned profile is included for comparison, with errors calculated from the Poisson uncertainties in the completeness correction and observed profile as well as the uncertainties in the extinction map. These are captured by recalculating the stellar density in each radius bin using a magnitude cut brighter or fainter than F153M = 20 mag by the map error value ($\sigma_{A_{F153M}} = 0.18$ mag). The half-light radius of the profile is 0.48 pc, largely consistent with previous studies (0.4 pc, Figer et al. 1999). The bivariate posterior distributions for these parameters are presented in Appendix 2.8.

Included in the right panel of Figure 2.11 is the radial profile for the inner part of the Arches from Espinoza et al. (2009), which spans a stellar mass range of 10 $M_\odot$ < M < 120 $M_\odot$ out to R = 0.4 pc. There is good agreement between the shape of the two profiles, though the absolute values of the Espinoza et al. (2009) profile must be scaled. This is necessary due to differences in sensitivity and treatment of cluster membership. We note that our profile spans far beyond the limits of previous astrometric studies of the Arches cluster, which are restricted to R < 0.2 pc. We leave the combination of these astrometric data sets and the presented data set to a future paper.

Table 2.3. Power-Law Profile Fit Results

	Bin	N_{stars} [a]	Power-law slope Γ	Field Contamination b (stars / pc^2)	Normalization Constant A_0 (stars / pc^2)
Full Cluster		451.0	2.06 ± 0.17	2.52 ± 1.32	23.09 ± 3.5
Split by Mass (2-bin)	High Mass[b]	106.5	2.70 ± 0.35	0.64 ± 0.48	3.50 ± 1.22
	Low Mass[c]	354.5	1.75 ± 0.15	0.78 ± 1.37	20.33 ± 2.75
Split by Mass (3-bin)	High Mass[d]	129.6	2.75 ± 0.37	1.47 ± 0.48	3.36 ± 1.26
	Intermediate Mass[e]	163.6	2.00 ± 0.28	2.04 ± 0.56	6.38 ± 1.46
	Low Mass[f]	165.7	2.29 ± 0.30	2.09 ± 0.53	6.47 ± 1.48
Split by Direction[g]	Parallel	225.7	1.86 ± 0.17	2.32 ± 0.88	22.57 ± 1.9
	Perpendicular	226.0	2.19 ± 0.18	2.29 ± 0.82	21.35 ± 2.43
Prior[h]			U(0.5, 4.5)	U(0,8), G(2.52,1.32)[i]	—

[a]Weighted by membership probability and corrected for completeness.

[b]F153M $<$ 17 mag (M $>$ $\sim$13 $M_\odot$)

[c]17 $<$ F153M $<$ 20.0 mag ($\sim$2.5 $M_\odot$ $<$ M $<$ $\sim$13 $M_\odot$)

[d]F153M $<$ 17.3 mag (M $>$ $\sim$12 $M_\odot$)

[e]17.3 $<$ F153M $<$ 18.8 mag ($\sim$6 $M_\odot$ $<$ M $<$ $\sim$12 $M_\odot$)

[f]18.8 $<$ F153M $<$ 20.0 mag ($\sim$2.5 $M_\odot$ $<$ M $<$ $\sim$6 $M_\odot$)

[g]Relative to the direction of the Arches cluster orbit

[h]Uniform distributions: U(min, max), where min and max are bounds of the distribution; Gaussian distributions: G(μ, σ), where μ is the mean and σ is the standard deviation

[i]Adopted U(0,8) for the full cluster profile fit, G(2.52, 1.32) for the directional profile fit

To quantitatively assess whether the power-law model is an appropriate one for the observed profile, we conduct a posterior predictive analysis using χ^2 as the test statistic (Gelman et al. 2013). We randomly select 1000 sets of model parameters from the joint posterior distribution and generate artificial binned profiles from these models. Each data point within the artificial profiles is shifted by an offset randomly drawn from a normal distribution with a width equal to the uncertainty in that value, determined from the combination of the poisson uncertainty and the uncertainty in the completeness correction. We then calculate a χ^2 value for each binned profile with respect to the best-fit model to the observations:

$$\chi^2(\Gamma, b) = \sum_{j=1}^{n} \frac{(P_j^{bin} - P_j^{model})^2}{\sigma_j^2} \tag{2.6}$$

where P_j^{bin} is the jth point in the binned profile with uncertainty σ_j and P_j^{model} is the value predicted for the jth bin by the best-fit model. We find that only 1% of these χ^2 values are lower than the χ^2 value for the observed binned profile and conclude that a power-law model is a good fit to the data. We emphasize that this χ^2 statistic and binned profiles are used to test the validity of the model, not to fit the model itself.

Previous studies of other YMCs have shown that these objects often appear to have extended radial profiles without signs of tidal truncation (Elson et al. 1987; Mackey & Gilmore 2003a,b; McLaughlin & van der Marel 2005). These studies fit the profiles using a model defined by Elson et al. (1987), hereafter referred to as an EFF87 profile model. We fit our profile with this model, adding a constant term b for field contamination:

$$\Sigma(r) = \Sigma_0 \left(1 + \frac{r^2}{a^2}\right)^{-\gamma/2} + b \tag{2.7}$$

where a is related to the core radius r_c of the cluster:

$$r_c = a \left(2^{2/\gamma} - 1\right)^{1/2} \tag{2.8}$$

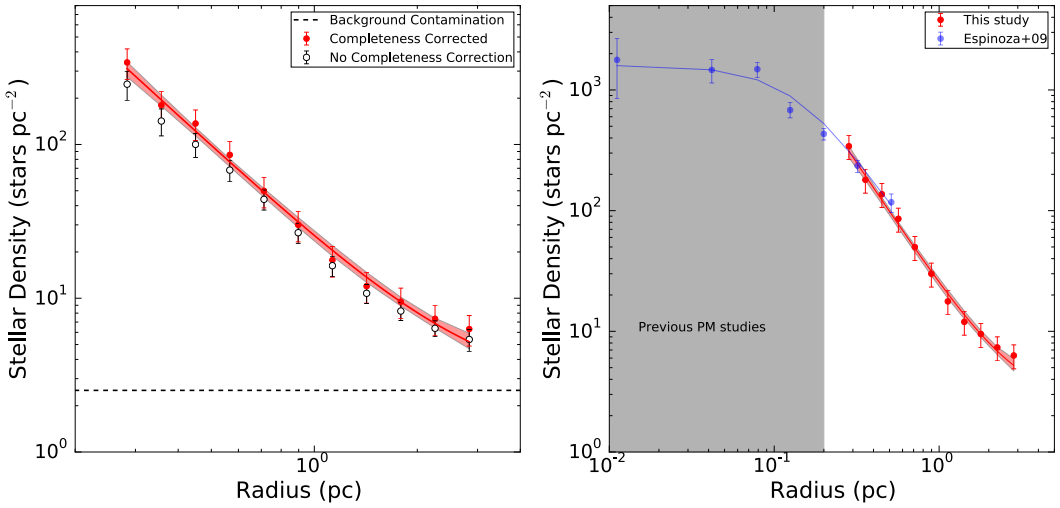

Figure 2.11 The radial profile of the Arches Cluster. *Left*: The best-fit power law model as described in the text and Table 2.3. The red line represents the power-law fit to the unbinned data and the black dotted line the residual field contamination value. A binned profile is included to guide the eye; the black open points are the binned profile before completeness correction and the red solid points the binned profile after completeness correction. Uncertainty in the fit (1σ) is captured by the red shaded region, which spans the standard deviation of 1000 profiles randomly drawn from the joint posterior distribution. Note that the binned profile is presented only for comparison and does not affect the fit. *Right*: Same as left, but with the inner cluster profile from Espinoza et al. (2009) added in blue (10 $M_\odot$ < M < 120 $M_\odot$) and scaled to our profile. The radius range probed the previous proper motion study of Clarkson et al. (2012) is shaded in grey.

We use the same Bayesian framework as described above, only with this profile as the likelihood function. Since incompleteness prevents our profile from stretching into the core region of the Arches we adopt the core radius r_c determined by Espinoza et al. (2009) of 0.14 ± 0.05 pc in our model. The consequent fit is nearly identical to the single power law model fit. We obtain $\gamma = 2.3 \pm 0.2$, which is consistent with the range and median values of 2.01 – 3.79 and 2.59 determined from a sample of LMC and SMC YMCs by Mackey & Gilmore (2003a,b). Given that we have no information about r_c from our profile and the marginal difference between this profile and the power-law fit, we proceed with the single power-law model.

Mass Segregation

Evidence for mass segregation in the Arches cluster has been found in the flattening of the mass function toward the cluster center (Figer et al. 1999a; Stolte et al. 2002; Espinoza et al. 2009;

Habibi et al. 2013) and a shallower radial profile for stars between ∼10 - 30 $M_\odot$ compared to stars between ∼30 - 120 $M_\odot$ (Espinoza et al. 2009). However, in addition to being dependent on photometric cluster membership, these results rely on measurements in the dense innermost regions of the cluster (R < 15") where completeness is lowest for low-mass stars due to stellar crowding (Ascenso et al. 2009). We avoid this inner region and instead examine mass segregation in the less-dense outer regions of the cluster.

Following Espinoza et al. (2009), we separate our radial profile as a function of differentially de-reddened magnitude to test for mass segregation. These magnitudes are a good proxy for stellar mass, as only a small fraction of stars in the Arches (∼6%) have been found to exhibit IR excess emission from circumstellar disks which could bias the photometry (Stolte et al. 2010). Adopting the single power-law model described above (Equations 2.4, 2.5), we find the power-law slope of stars brighter than F153M = 17 mag (M >∼13 $M_\odot$) to be notably steeper than the slope of stars between F153M = 17 – 20 mag (∼2.5 $M_\odot$< M <∼13 $M_\odot$). A Kolmogorov-Smirnov test finds the probability of these profiles being drawn from the same parent distribution to be <0.05%, demonstrating that mass segregation is present throughout the spatial extent of the cluster. The profiles in these different magnitude bins are shown in Figure 2.12, with the fit summarized in Table 2.3 and accompanying bivariate posterior distributions in Appendix 2.8.

The adopted magnitude separation is an optimization between obtaining a large enough sample for good statistics in the bright-star profile and showing the mass segregation, which become less evident with fainter magnitude cuts. To demonstrate this, we split the sample into three subsets by magnitude such that each magnitude bin contains ∼130 cluster members before completeness corrections in Figure 2.12. These magnitude bins correspond to F153M < 17.3 mag (M >∼12 $M_\odot$), F153M = 17.3 – 18.8 mag (∼6 $M_\odot$< M <∼12 $M_\odot$), and F153M = 18.8 – 20 mag (∼2.5 $M_\odot$< M <∼6 $M_\odot$). Mass segregation remains evident with the brightest (thus highest mass) profile being noticeably steeper than the other two profiles, while the intermediate and faint-star profiles are more similar to one another.

We caution that the conversion from observed magnitude to mass is highly uncertain due to uncertainties in evolutionary models, especially in the pre-main sequence. To determine the stellar masses at the magnitudes presented above, we adopt a cluster isochrone with the nominal properties of the Arches cluster (age = 2.5 Myr, distance = 8000 pc, A_{Ks} = 2.4 mag) constructed using a

combination of Geneva models with initial rotation speed of 300 km s^{-1} (Meynet & Maeder 2003) and Siess et al. (2000) pre-main sequence models, as discussed in Lu et al. (2013). However, a more accurate conversion from magnitude to mass (and a more detailed examination of cluster mass segregation) will be the focus of a future paper.

The Search for Tidal Tails

Given the strong gravitational fields near the GC, the Arches cluster is expected to have tidal tails leading and trailing its orbit. Such structures have been observed for globular clusters and have yielded insight to the object's orbit and the gravitational potential of the Galaxy (e.g., Odenkirchen et al. 2001, 2003; Grillmair & Johnson 2006). Adopting the model of the initial conditions of the Arches from Harfst et al. (2010), the 3D velocity from Clarkson et al. (2012), and assuming a current position 100 pc in front of the GC, Habibi et al. (2014) predict that the Arches should have tidal tails extending 20 pc (∼500") along the Galactic plane. To search for these structures we compare the radial profiles parallel and perpendicular to the cluster's bulk velocity, which is consistent with the direction of the Galactic plane (Clarkson et al. 2012).

Tidal tails would cause an asymmetry in these profiles, either as a steepening or truncation of the perpendicular profile relative to the parallel profile as the cluster is stretched and sheared by the Galactic tidal field (i.e. Figure 5 of Odenkirchen et al. 2003). Using the single power-law model, we do not find evidence of a significant difference between the parallel and perpendicular profile slopes (Table 2.3, Figure 2.13). Bivariate posterior distributions for these profiles are are presented in Appendix 2.8. While the binned profiles might appear to be discrepant at ∼1 – 1.5 pc, a Kolmogorov-Smirnov test of these profiles in the region of highest completeness (0.5 pc $<$ R $<$ 3.0 pc) concludes that the profiles are drawn from the same distribution with a probability of ∼16%. Thus, we cannot conclude that profiles are statistically different. This conclusion does not change when different cluster membership probability cuts are adopted (P $>$ 0.7, for example). Further observations of the Arches cluster at large radii are needed to detect the presence of tidal tails.

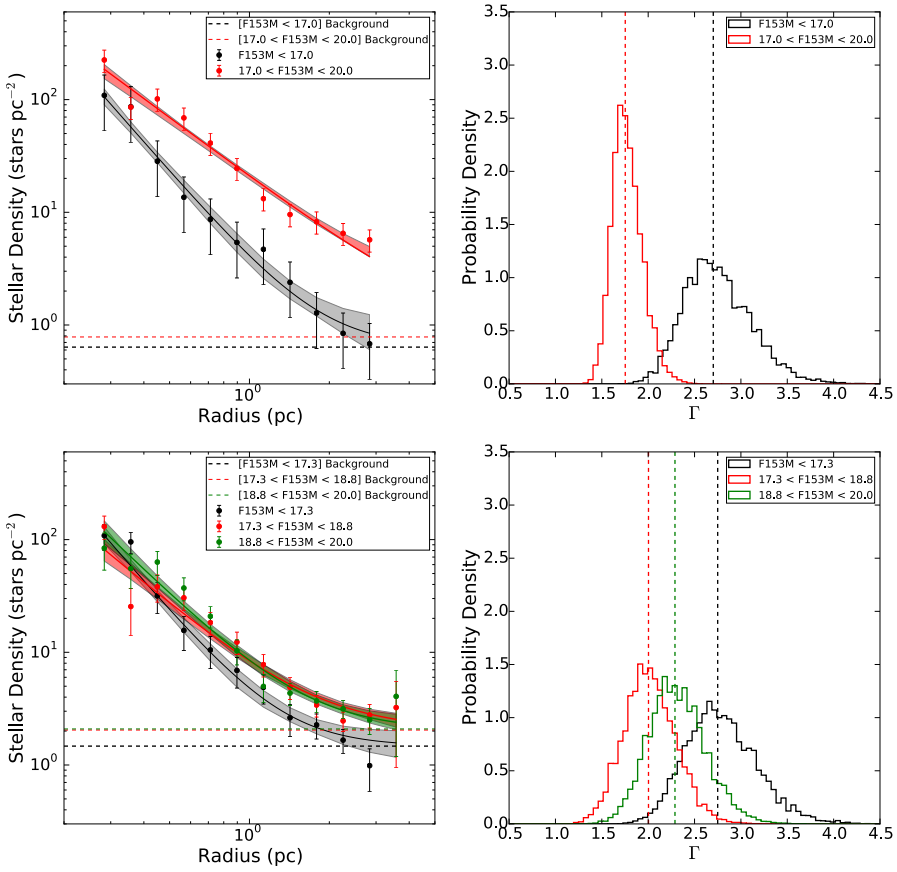

Figure 2.12 Mass segregation in the Arches cluster. *Top:* The clearest evidence for mass segregation is found in the steepening of the profile for high-mass stars (black; F153M $\leq$17 mag, or M $\geq\sim$13 $M_\odot$) compared to low-mass stars (red; F153M >17 mag, or M $<\sim$13 $M_\odot$). On the *left*, the solid lines show the power law profile fit to the unbinned data, the dotted lines show the residual field contamination values, and the data points show the binned profiles after completeness correction. 1σ model uncertainties are shown as the shaded regions. The posterior distributions of the power-law slope Γ are shown to the *right*. The slopes differ by 2.5σ, and a Kolmogorov-Smirnov test rejects the hypothesis that the profiles are drawn from the same parent distribution. *Bottom:* Similar to above, but splitting the sample into three subsamples by magnitude such that each magnitude bin contains $\sim$130 stars before completeness correction. Mass segregation remains evident in the steepening of the brightest profile compared to the other two profiles. The best parameter values for all fits are presented in Table 2.3.

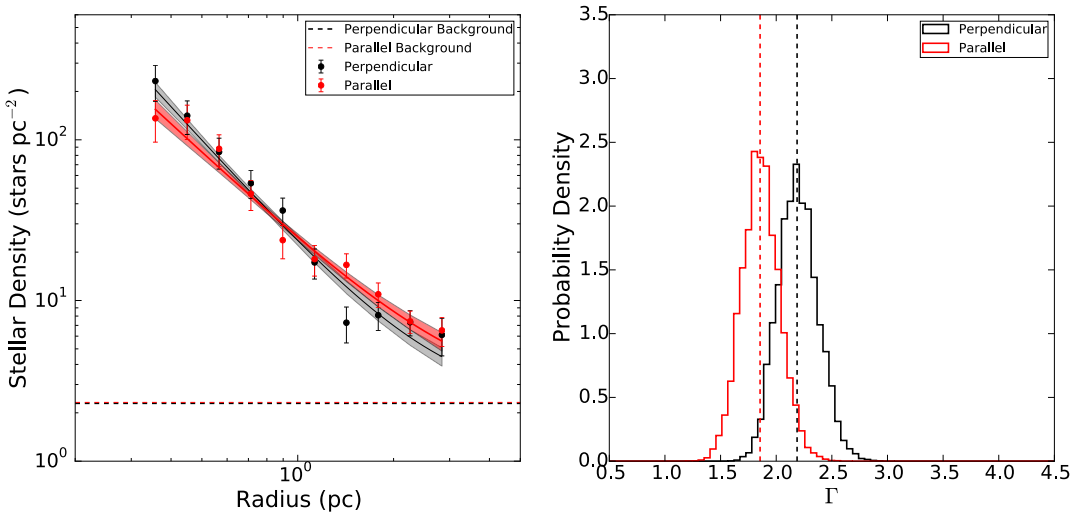

Figure 2.13 The search for tidal tails in the Arches cluster. *Left:* No significant asymmetries suggesting the presence of tidal tails are found in a comparison of the profile parallel (red) and perpendicular (black) to the cluster's orbit. Power-law fits, residual field contamination, and 1σ uncertainties are shown in the same manner as Figure 2.11, while the best-fit parameter values are presented in Table 2.3. *Right:* The posterior distributions for the power-law slope Γ of the fitted profiles. The black and red dotted lines show the best-fit slopes for the perpendicular and parallel profiles, respectively, and which only differ by $\sim 1.4\sigma$. A Kolmogorov-Smirnov test cannot reject the hypothesis that these profiles were drawn from the same parent distribution.

2.3.3 Observed Tidal Radius

Utilizing the large field of view, we can directly constrain the spatial extent of the Arches cluster for the first time. This is a significant improvement over previous studies which were forced to estimate the tidal radius based on observations of the inner region of the cluster. For example, Kim et al. (2000) compared the radial profile of massive stars in the Arches ($M > 20\ M_{\odot}$) out to 0.8 pc (Figer et al. 1999a) to the radial profiles of similarly massive stars in N-body simulations of the cluster and found an expected tidal radius between 1 – 1.2 pc. A second estimate by Portegies Zwart et al. (2002) placed the tidal radius at 1.6 – 2.5 pc, based on a highly model-dependent analysis of the mass segregation observed in the same Figer et al. (1999a) profile. However, our study shows that the Arches profile extends well beyond these predictions, with no evidence of King-like tidal radius out to ∼3 pc (Figure 2.14).

To place a quantitative lower limit on the observed tidal radius, we use the Bayesian framework described above to fit our profile with a King (1962) model:

$$\Sigma(r) = k * \left(\frac{1}{[1 + (r/r_c)^2]^{1/2}} - \frac{1}{[1 + (r_t/r_c)^2]^{1/2}} \right)^2 + b \tag{2.9}$$

where k is a normalization constant, b is a constant background term, and r_c and r_t are the core and tidal radii of the cluster, respectively. We adopt the core radius of 0.14 ± 0.05 pc measured by Espinoza et al. (2009) as a prior for r_c, though our profile provides no additional information at $R \leq 0.25$ pc. An uninformed prior is used for r_t, and k is calculated such that the integral of the fitted profile yields the total number of cluster members observed after membership probability, completeness, and area corrections.

The result of the fit is summarized in Table 2.4 and marginalized posterior distributions presented in Appendix 2.8. We obtain a 3σ lower limit of 2.8 pc on a King-like tidal radius for the cluster. Of course, it is quite possible that the Arches profile is not truncated at all, and may behave as a power law throughout the full cluster extent. Regardless, it is clear that the cluster extends beyond its predicted tidal radius of 2.5 pc.

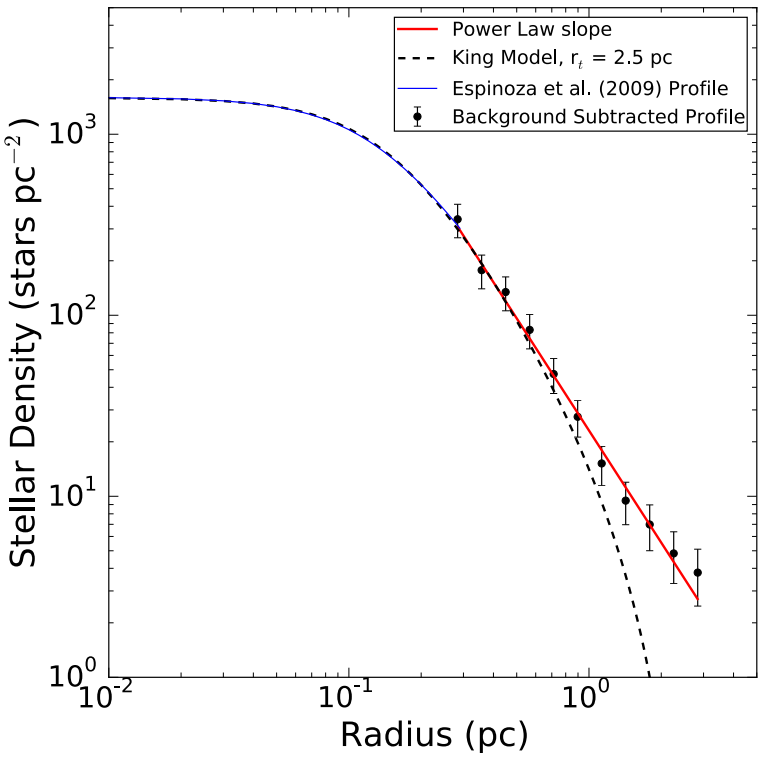

Figure 2.14 The background-subtracted profile of the Arches cluster compared to a King profile with a tidal radius of $r_t = 2.5$ pc. The Arches profile is composed of the best-fit power law slope (red line) and binned profile (black points) from this study, and the profile for the inner 0.4 pc measured by Espinoza et al. (2009) scaled to our profile (blue line). The King profile model (black dotted line) is clearly discrepant with this profile at large radii. We place a 3σ lower limit of 2.8 pc on the location of a King-like tidal radius in the Arches cluster.

Table 2.4. King Profile Fit Results

Parameter[a]	Prior[b]	Result
r_t (pc)	U(1, 15)	2.8[c]
r_c (pc)	G(0.14, 0.05)[d]	0.13 ± 0.03
b (stars pc^{-2})	U(0,15)	3.46 ± 0.94
k (stars pc^{-2})	—	1729 ± 643

[a]Description of parameters: r_t = tidal radius; r_c = core radius; b = field contamination; k Normalization factor

[b]Uniform distributions: U(min, max), where min and max are bounds of the distribution; Gaussian distributions: G(mean, standard deviation)

[c]3σ lower limit

[d]Source: Espinoza et al. (2009)

2.3.4 Tidal Breaks in the Radial Profile

We examine our profile for the presence of breaks which would be indicative of significant tidal interactions. The profile is remarkably consistent with a single power law from 0.25 pc $<$ R $<$ 1 pc, though beyond 1 pc the profile appears to exhibit slightly higher stellar densities than expected. This feature is adequately modeled as a constant field contamination term in Equation 2.5. However, we must confirm that this feature can indeed be attributed to residual field contamination rather than a true over-density of cluster stars.

Field contamination may arise from the uncertainties in the cluster membership probabilities, which in turn are a result of uncertainties in the fits of the cluster and field kinematic distributions. To estimate the impact of these uncertainties, we perform a Monte-Carlo experiment where we randomly draw 1000 kinematic models from the joint posterior distribution obtained in § 2.2.2 and calculate the stellar cluster membership probabilities for each. We then determine the number of cluster members for each model from the sum of membership probabilities for all stars with $P_{member} > 0.3$, the same calculation we do for the best-fit kinematic model in § 4.3.1. The standard deviation in the number of cluster members across the kinematic models is 34.32, centered around a median very nearly equal to the number of members identified by the best-fit kinematic model.

We therefore adopt 34.32 as the uncertainty in the number of cluster members due to imperfect cluster membership probabilities.

The cluster membership uncertainty provides an estimate on the number of field contaminants potentially among our sample of cluster members. Spread evenly across the field, this would result in a field surface density of 1.49 stars pc^{-2} in the profile. This is consistent with the background of the single power law fit (2.52 ± 1.32) to 1σ. In addition, Figure 1 of Peñarrubia et al. (2009) shows that a tidal event may cause an asymmetry in the parallel and perpendicular profiles, with the stellar over-density dominating the parallel profile relative to the perpendicular one. That no such asymmetry is observed (§2.3.2) is further evidence that there is no tidal break in the Arches profile between 0.25 - 3.0 pc.

2.4 Discussion

In order to interpret the Arches cluster profile in terms of its tidal history, we require theoretical/numerical studies of YMCs on moderately eccentric orbits in the inner Milky Way potential that examine the evolution of the outer radial profile. If it exists, the observable King-like tidal radius of the cluster is significantly larger than predicted by previous studies, though these assume a spherically symmetric potential for the Galaxy or assume the cluster is on a circular orbit (Kim et al. 2000; Portegies Zwart et al. 2002). Given the high gas densities toward the GC, the effect of interactions with Giant Molecular Clouds on the radial profile may also need to be considered. Unfortunately there are no such studies currently available in the literature; while there are many N-body simulations of clusters in varying tidal fields, very few discuss the corresponding evolution of the outer cluster profile. As a result, in §2.4.1 we consider the implications of simulation results by Peñarrubia et al. (2009, hereafter P09), which model the response of dwarf spheroidal galaxies to tidal perturbations at perigalacticon. We discuss other simulations which more closely reflect the Arches cluster and its environment but do not examine the evolution of the radial profile in sufficient detail in §2.4.2.

2.4.1 Time Since Last Pericenter Passage

Modeling the effects of tidal stripping on dwarf spheroidal galaxies, P09 find a relation between the location of a tidal break in a radial profile and the time elapsed since perigalacticon. Here we apply this relation to the Arches cluster to place limits on the time elapsed since its closest approach to the GC. However, there is a major caveat in this analysis: the orbits examined by P09 are significantly different than what is expected for the Arches. These authors simulate dwarf spheroidal galaxies on highly eccentric orbits ($\epsilon = 0.96 - 0.99$) with a closest approach of 900 pc from the GC, where the Arches is likely on an orbit with $\epsilon = 0.25 - 0.38$ and a closest approach between 50 – 200 pc from the GC (Stolte et al. 2008; Kruijssen et al. 2014). Assuming the Milky Way potential model described in Bovy (2015), the radial force felt by the Arches is ∼6 times larger than that of the innermost P09 orbit. A similar formation and evolution of a tidal break in response to perigalacticon is found in N-body simulations of dwarf galaxies on more moderately-eccentric orbits ($0.23 < \epsilon < 0.9$) by Łokas et al. (2013), though these models also probe weaker tidal fields than is experienced by the Arches (smallest pericenter: 12.5 kpc). N-body studies of star clusters on eccentric orbits show the formation of a tidal break at large radii, as well (Küpper et al. 2010; Johnston et al. 1999; Lee et al. 2006). Given the supporting evidence from multiple studies and the lack of alternative studies in stronger tidal fields that examine the outer radial profile (see §2.4.2), we move forward with the results from the P09 simulations.

After perigalacticon, the radial profiles of P09 develop a tidal break that initially forms at small radii and moves outward over time. Normalizing by core radius R_c and core crossing time $t_{cr} \equiv R_c / \sigma_0$, they obtain the following relation:

$$R_b/R_c = 0.55(t - t_p)/t_{cr} \tag{2.10}$$

where R_b is the radius of the tidal break and $(t - t_p)$ is the time elapsed since perigalacticon. Given that no break is observed in the Arches profile between 0.25 pc – 3.0 pc and adopting a velocity dispersion of 5.4 km s^{-1} (Clarkson et al. 2012), this relation indicates that the Arches has not had a significant tidal perturbation between ∼0.08 Myr and ∼1 Myr ago. However, P09 note that while their relation describes all models well at large break radii, it tends to underestimate the time since

perigalacticon passage for break radii close to the core radius ($R_b \leq 4\ R_c$). Restricting the lower boundary to the innermost radius that is well described by this relation (0.6 pc for the Arches), we find that it is likely that the Arches has not experienced perigalacticon between ∼0.2 Myr and ∼1 Myr ago.

This result, which suggests that the cluster may either be nearly at or long past closest approach, places a limit on the set of potential orbits calculated for the Arches cluster (Stolte et al. 2008). Restricting the orbits to those which place the Arches within the Central Molecular Zone (highly likely given its interactions with surrounding gas clouds, cf. Wang et al. 2010), this constraint rejects the viability of retrograde orbits since these place the cluster's closest approach within the timeframe in which we would expect to observe a tidal break. This provides further evidence that the cluster is on a prograde orbit and thus is located in front of the sky plane which passes through Sgr A*. However, we cannot significantly constrain the prograde orbits, which place the cluster very near closest approach. The allowed orbits are consistent with both cluster formation mechanisms discussed in §3.1, and so no additional insight regarding the birth of the Arches cluster can be obtained.

Additional astrometric observations of the Arches are needed to provide higher precision proper motions from which the velocity dispersion profile of the cluster can be measured. Combined with the radial profile, the velocity dispersion profile is a sensitive tracer of cluster's tidal interaction history and current dynamical state, and may lead to the measurement of current Jacobi radius of the cluster (Küpper et al. 2010). This can yield the present distance between the Arches and Sgr A*, the last bit of information required for a full orbital solution. The different formation mechanisms for the Arches can then be distinguished, as they differ in predictions of the current distance between the cluster and SMBH (∼50 pc for the tidal compression scenario versus ∼100 - 200 pc for the cloud collision scenario).

It is important to note that the orbit calculations of the Arches cluster rely on the accurate measurement of the cluster's bulk motion relative to Sgr A*. This is not a trivial task due to an observational bias towards stars on the near side of the GC. Limited by their field of view, Stolte et al. (2008) model the kinematics of 67 identified field stars using a single circular Gaussian distribution, taking the bulk motion of the Arches to be the difference between the kinematic centers of the Arches and field distributions (5.6 ± 0.5 mas yr^{-1}). This is the value used in the

currently published orbits. Using 210 field stars and a more sophisticated elliptical Gaussian model for the field population, Clarkson et al. (2012) obtain a slightly lower field motion of 4.39 ± 0.38 mas yr^{-1} relative to the cluster. However, with a much larger field of view and more available field stars (∼5322 stars with $P_{member} < 0.3$), our study shows that the field has a complex kinematic structure that must be modeled with multiple Gaussians. Great care must be taken to properly interpret these structures in the context of a Galactic model and measure the bulk motion of the Arches with respect to Sgr A*, which is left to a future paper.

2.4.2 Applicability of Other Theoretical Studies

Despite the significant caveats in applying the P09 results to the Arches cluster, it is the most applicable theoretical study currently available that examines the detailed evolution of the outer radial profile of a stellar system as it passes through perigalacticon. N-body simulations of dwarf galaxies on orbits with moderate eccentricities by Łokas et al. (2013) exhibit tidal breaks that behave similarly as those in the P09 models, though the relation between the location of the break radius and the time since perigalacticon passage is not assessed quantitively. Alternatively, N-body simulations by Küpper et al. (2010) examine objects more similar to the Arches, studying the behavior of 10^4 $M_\odot$ star clusters on elliptical orbits with $0.25 < \epsilon < 0.70$ (smallest pericenter: 600 pc). The resulting cluster profiles show that extratidal stars form power-law extensions at large cluster radii, though the detailed evolution of the profile after perigalacticon is not explored in detail. Additional simulations of clusters on elliptical orbits by Johnston et al. (1999) and Lee et al. (2006) also show extratidal stars forming a break in the cluster profile, though neither study examines how this break evolves as a function of orbital phase.

There is a large body of additional literature studying the dynamical evolution of star clusters in tidal fields, though these do not show the evolution of the outer radial profile. N-body simulations of clusters on eccentric orbits by Baumgardt & Makino (2003), Lamers et al. (2010), and Webb et al. (2014) primarily focus on the evolution of the mass-loss rate and mass function, while Webb et al. (2013) examines the half-mass radius, tidal radius, and cluster size rather than the morphology of the radial profile at large. Many other studies examine clusters on circular orbits, though these are limited to old (>10 Gyr) globular clusters (Trenti et al. 2010; Gieles et al. 2011), or do not present detailed radial profiles of their models (Ernst et al. 2009; Madrid et al. 2012).

It is worthwhile to note that none of the studies discussed above examine the evolution clusters within the central regions of the Milky Way. There have been several studies of Arches-like young compact clusters within the inner 200 pc of the Galaxy, but these similarly do not examine the evolution of the outer radial profile. N-body simulations by Kim et al. (2000) and Portegies Zwart et al. (2002) make predictions regarding expected cluster lifetimes and the evolution of the radial profile out to the half-mass radius. Portegies Zwart et al. (2004) focus on the evolution of the mass function of Arches-like clusters, concluding that the mass function of the inner region of the Arches reported by Figer et al. (2002) could be explained by dynamical mass segregation. Several other studies model the effects of dynamical friction on compact clusters, predicting in-spiral towards the GC and their subsequent evolution, though the cluster profile during this process is not presented (Kim & Morris 2003; Portegies Zwart et al. 2003; Gürkan & Rasio 2005). Additional studies of the behavior of the radial profiles of Arches-like clusters near the GC are required to draw more conclusive interpretations from the observations presented here.

2.5 Conclusions

We have conducted a multi-epoch photometric and astrometric study of the Arches cluster using the *Hubble Space Telescope* WFC3IR camera at 1.27, 1.39, and 1.53 μm. Using a sophisticated astrometric pipeline we extract individual stellar proper motions to an accuracy of at least 0.65 mas yr^{-1} down to F153M $\approx$ 20 mag ($\sim$2.5$_{\odot}$), reaching a precision of $\sim$0.1 mas yr^{-1} for the brightest stars. Taking advantage of the distinct kinematic properties of the cluster, we use a 4-Gaussian mixture model to simultaneously fit the cluster and field proper motion distributions and calculate cluster membership probabilities. This is a substantial improvement over photometrically-determined cluster membership due to the large degree of differential reddening across the field. The field of view in this study is 144 times larger than previous astrometric studies of the Arches cluster, allowing for the identification of high-probability cluster members out to a cluster radius of 75" ($\sim$3 pc at 8 kpc).

Combining the cluster membership probabilities, an extinction map derived from red clump (RC) stars, and an extensive completeness analysis, we construct the stellar radial density profile for the Arches cluster between 6.25" $<$ R $<$ 75" (0.25 pc $<$ R $<$ 3.0 pc) down to a differentially

de-reddened magnitude of F153M = 20 mag. This profile is well fit by a single power-law of slope Γ = 2.06 ± 0.17 with a constant field contamination density of 2.52 ± 1.32 stars pc^{-1}. Surprisingly, no evidence of a tidal radius is observed. Adopting a King profile as a model, we obtain a 3σ lower limit of 2.8 pc for the observed tidal radius of the Arches cluster. This shows that the cluster extends beyond its largest predicted theoretical tidal radius of 2.5 pc.

Additionally, we examine the Arches cluster profile for evidence of mass segregation and tidal tails. We find the cluster to exhibit mass segregation at all observed radii, with the radial profile of bright stars (F153M < 17 mag, or M> ∼13 $M_\odot$) being notably steeper than the profile of fainter (17 < F153M < 20 mag) stars. A KS test reveals the differences between these profiles to be significant. We leave a careful conversion from brightness to mass for a future paper. Similarly, we search for evidence of tidal tails by comparing the profile parallel to the direction of orbit to the profile perpendicular to it. No statistically significant asymmetries are observed in these profiles, as would be expected from tidal tail structures. Further observations, perhaps at larger cluster radii, are needed to continue to search for tidal tails.

No evidence of a tidal break is observed in the radial profile, as might be expected if the Arches has experienced a tidal perturbation in its recent past. Assuming that the results of dynamical simulations of dwarf spheroidal galaxies on highly eccentric orbits by Peñarrubia et al. (2009) can be applied to the Arches, this suggests that the Arches not likely experienced its closest approach to the GC within 0.2 – 1 Myr ago. This constraint would reject all possible retrograde orbits of the cluster, providing further evidence that the Arches is on a prograde orbit and located in front of the sky plane which intersects Sgr A*. However, additional simulations studying the profile of Arches-like clusters on mildly-eccentric orbits in the inner Milky Way potential are required to interpret the observed profile with higher confidence.

Further astrometric observations of the Arches to obtain its velocity dispersion profile are needed to better constrain its orbit and distinguish between different possible cluster formation scenarios. It is important to note that an accurate determination of the cluster's orbit requires measuring its bulk motion with respect to Sgr A*, which is a difficult task given the complex kinematic structure of the field population revealed in this study. A revised measurement of the Arches proper motion, along with a new calculation of possible orbits, is left to a future paper.

Acknowledgments

The authors thank the anonymous referee for insightful comments which improved this paper and acknowledge support from HST GO-13809. A.M.G. is supported by the NSF grants AST-0909218 and AST-1412615, and the Lauren Leichtman & Arthur Levine Chair in Astrophysics. This work is based on observations made with the NASA/ESA Hubble Space Telescope, obtained at the Space Telescope Science Institute, which is operated by the Association of Universities for Research in Astronomy, Inc., under NASA contract NAS 5-26555. These observations are associated with programs #11671, 12318, and 12667. This research has made extensive use of NASA's Astrophysical Data System. MWH would also like to acknowledge the SWOOP writing retreat and its participants for useful feedback.

2.6 Appendix A: WFC3IR Measurements and Proper Motions

In this appendix we describe the methods and software used to extract high precision astrometry, photometry, and proper motions from the WFC3IR observations. This is the first application of this methodology on WFC3IR observations. Stars are first detected and measured in the `flt` images using the FORTRAN program *img2xym_wfc3ir_stdpsf* developed by Jay Anderson. Similar to the code *img2xym_WFC.09x10* documented in Anderson & King (2006), this performs PSF-fitting measurements using a library of spatially-variable PSF models it derives for the WFC3IR camera. This library contains a 3x3 grid of PSFs that spans the camera's field, where the PSF at any point can be derived from a spatial interpolation of these models. Since this routine operates on one image at a time in a single pass, it is not designed to deal with overlapping stars. It reduces each star as if it is the only contribution to the 5x5 pixels centered on its brightest pixel.

Each image is run through this program twice. The first iteration extracts the bright high S/N stars in the field ($\sim$400 stars per image), simultaneously measuring the residuals between the observed PSF and the library PSF. New image-specific PSF models are created in order to minimize these residuals and make them uniform across the field. The second iteration then uses the modified PSF library to accurately measure both bright and faint sources, producing a star list with fluxes and positions for $\sim$13,000 sources in each image extending down to F127M = 22.45

mag, F139M = 22.09 mag, and F153M = 21.71 mag. A small number of stars (∼200) with F153M ≤∼15 are saturated and are thus measured using the outer part of the PSF.

Next, we cross-identify stars from each exposure with a master list for the filter/epoch set, initially taken to be the first image in the set. Common stars found in at least 75% of the images are used to transform positions from the distortion-corrected frame of each exposure into the master list reference frame using general 6-parameter linear transformations. This gives ∼N observations for each star, where N is the number of images in the filter/epoch set, which allows us to find a robust average position and flux. These averaged measurements produce an overall star catalog for the filter/epoch. We then adopt these catalogs as the new reference-frame positions and repeat the procedure, improving the transformations. The improvement in the second iteration is considerable, decreasing astrometric residuals by nearly a factor of 2. Finally, the new star catalogs for each filter/epoch are then transformed to an arbitrary astrometric reference frame where the net motion of the cluster plus field stars is 0 mas yr^{-1}. This produces what we will call the "one-pass" catalogs, because they are limited to the stars which can be detected in a single image.

In principle, we could continue our analysis of the Arches Cluster using the one-pass catalogs. However, by stacking the images in each filter/epoch we significantly increase the detection depth, important because signal from otherwise undetected faint stars can be mistakenly associated with brighter stars and introduce biases in the measurements. With the image transformations, PSF models, and one-pass catalogs as input, we use the program *KS2* to stack the images, make stellar detections to significantly fainter magnitudes, and then redo the astrometric and photometric measurements in each individual image at the positions found in the stacked image. The measurements for the individual images are then averaged together to produce the final catalogs for each epoch/filter. We emphasize that we don't use the measurements of the stacked image, but only those of the individual images. This iterative multiple-finding strategy increases the number of stars detected to ∼50,000 per filter (nearly five times as many as the one-pass analysis), reaching F127M = 23.63 mag, F139M = 23.29 mag, and F153M = 23.31 mag as noted in § 3.2. To ensure the accuracy of our transformation we again combine the individual star lists into star catalogs for each filter/epoch and re-align to the common astrometric reference frame using a first-order bi-variate polynomial (see Ghez et al. 2005 and references therein). Higher order fits were found to

introduce artificial structure in the astrometry. Astrometric and photometric errors as a function of magnitude are presented in Figure 2.15.

The *KS2* code returns a final star catalog with the root-mean-square errors (σ_{RMS}) for the astrometric and photometric measurements for each star in the filter/epoch. Theoretically the errors should be quantified by the error on the mean (σ_{RMS} / $\sqrt{N_{obs}}$, where N_{obs} is the number of images in the filter/epoch). To test this, we compare the *KS2* errors to quantities measured across the F153M epochs that are directly caused by these errors: the standard deviation of the magnitude of each star (assuming no stellar variability) and the residuals between the measured position and position predicted by the star's proper motion. This comparison reveals the error on the mean to better capture the astrometric errors and the RMS error to better capture the photometric errors, and so we adopt these for the individual star measurements throughout (Figure 2.16). This choice does not significantly affect the proper motion errors described below, which are dominated by the position residuals rather than the astrometric errors themselves.

Proper motions are derived independently for the X and Y directions (in the image coordinate system) using a linear fit to the change in position over the F153M epochs:

$$x = x_0 + v_x(t - t_0) \tag{2.11}$$

$$y = y_0 + v_y(t - t_0)$$

where t_0 is the astrometric error-weighted average time of observations, (v_x, v_y) are the X and Y proper motions, and (x_0, y_0) and (x, y) are the star positions at t_0 and t, respectively. To test the validity of these errors, we apply the derived proper motions to their respective stars and examine the residuals between the predicted and the observed positions. The distributions of the X and Y position residuals are approximately Gaussian, though more power is present in the wings than expected (Figure 2.18). This is a consequence of stellar crowding distorting our measurements, as these wings are dominated by faint stars (F153M $<$ 20 mag) which are more prone to this effect. Given the high stellar density of near the center of the cluster this is not unexpected. The distribution of χ^2 values for the proper motion fits follows the expected distribution for 1 degree of freedom, appropriate as we constrain 2 parameters with 3 measurements.

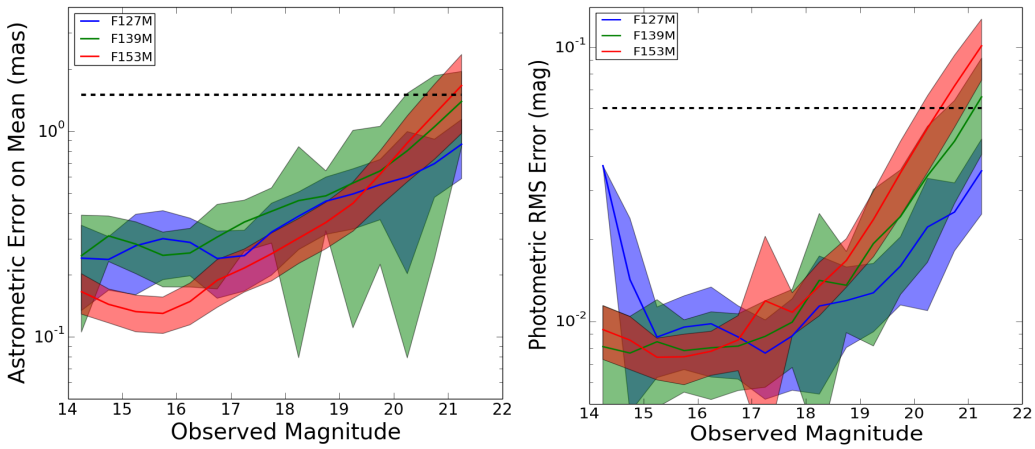

Figure 2.15 Astrometric error on the mean and photometric RMS error vs. observed magnitude for the F127M (blue), F139M (green), and F153M (red) filters. The solid lines show the median errors and the shaded regions cover one standard deviation. Stars with astrometric errors above 1.5 mas (and thus proper motion errors above 0.65 mas yr^{-1}) or photometric errors above 0.06 mag in the F153M filter are not included in the analysis. These cuts are shown by the black dotted lines.

Photometry is calibrated to the standard Vega magnitude system by deriving the filter-dependent offset between *KS2* magnitudes and 0.4" aperture photometry magnitudes. Aperture photometry is performed using *DAOPHOT* (Stetson 1987) on the `drz` image for each epoch/filter, a composite image of all exposures in the same filter/epoch produced by the *HST* pipeline. This offset is then combined with the appropriate 0.4" zeropoint derived for the WFC3IR camera (see § 3.2 for reference) to determine the overall zeropoint for the *KS2* observations. For stars with F153M $\leq$ 20 (consistent with our proper motion precision cut, § 3.2), the median F153M astrometric and photometric errors are 0.34 mas and 0.018 mags, respectively, with evidence of higher errors in regions of increased stellar density (Figure 2.17). Within this sample the median F127M and F139 photometric errors are 0.033 mag and 0.025 mag, respectively.

2.7 Appendix B: Artificial Star and Observed Star Errors

The completeness analysis described in § 2.2.4 assumes that the measured artificial star errors match the observed star errors. A direct comparison of the errors reveals that the observed astrometric and photometric errors have an error floor that is not reproduced by the artificial star tests (Fig. 2.19). A possible explanation for this feature is residual PSF variations which are not captured

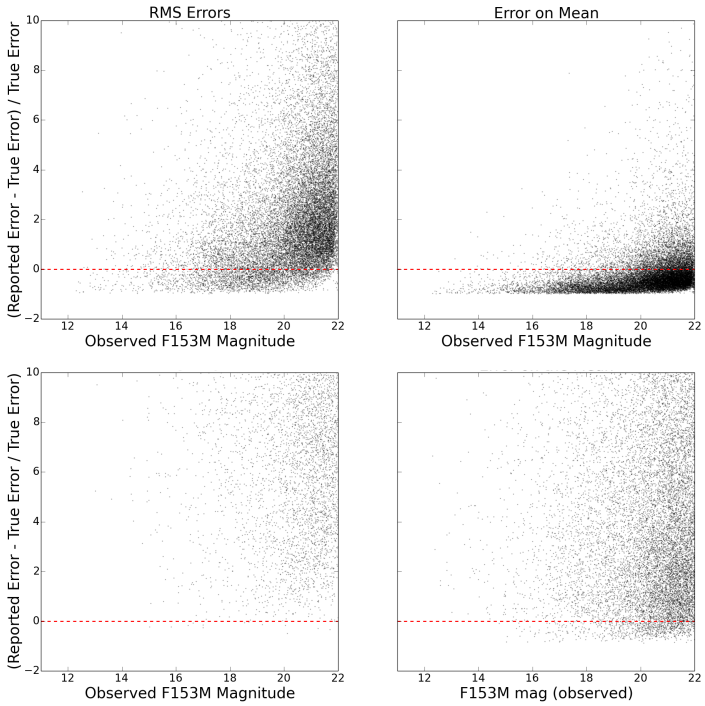

Figure 2.16 *Top:* The fractional difference between the RMS error (*left*) and error on the mean (*right*) and the "true" errors for the photometric measurements. The "true" photometric error for each star is taken to be the standard deviation of the observed magnitude across the F153M epochs. *Bottom:* Similar to above, the fractional difference between the RMS error (*left*) and error on the mean (*right*) and the "true" errors for the astrometric measurements. The "true" errors are taken to be the RMS residuals between the fitted proper motion and the observed position of each star in the F153M epochs. For the photometry, the mean is found to underestimate the true error, and so the photometric RMS error is adopted for individual measurements. For the astrometry, the RMS error is found to strongly overestimate the true error, and so the astrometric error on the mean is adopted for individual measurements.

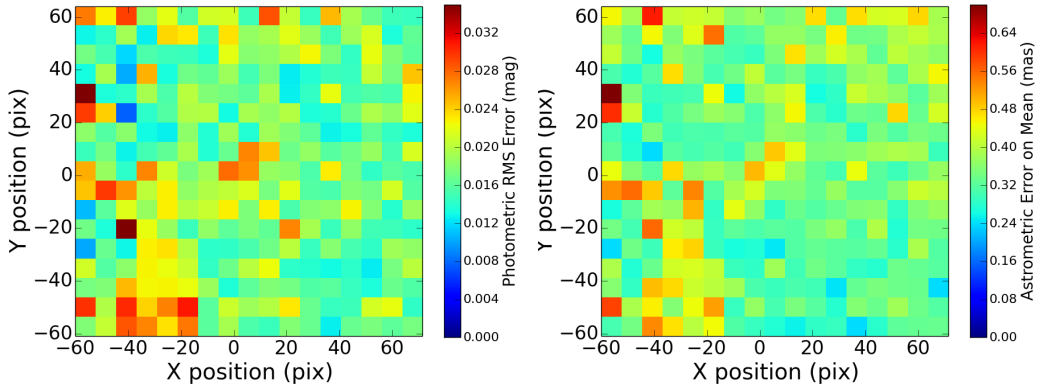

Figure 2.17 Average astrometric error (*left*) and F153M photometric error (*right*) as a function of position on the camera for all stars with F153M < 20 mag. Average error values are calculated in 7" bins and are plotted relative to the cluster center. Axes are oriented in the same manner as Figure 2.1. Higher errors are observed in the low reddening regions and the cluster center due to stellar crowding.

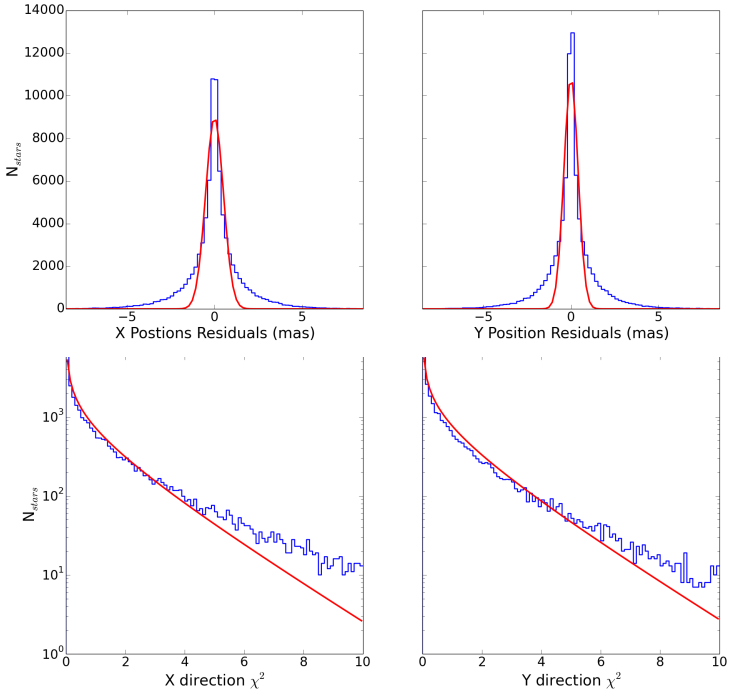

Figure 2.18 Position residuals between the observed positions and those predicted from the fitted proper motions. *Top:* A histogram of the X (*left*) and Y (*right*) residuals (blue line). Ideally these distributions would be Gaussian (red line), but stellar crowding results in more power in the wings of the distribution. *Bottom:* The distribution of χ^2 values for the proper motion fits in both X (*left*) and Y (*right*), where we adopt the error on the mean as the proper motion error (blue line). These values match the expected χ^2 distribution with 1 degree of freedom (red line), validating our reported errors.

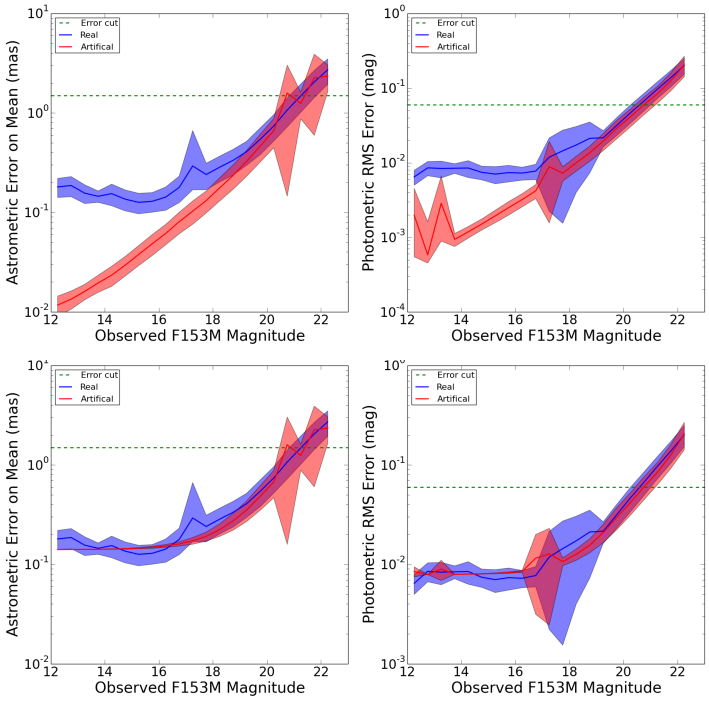

Figure 2.19 Comparison of the astrometric (*left*) and photometric (*right*) errors for the observed and artificial stars in blue and red, respectively. The *top* plots show the initial artificial star errors and the *bottom* plots show the artificial star errors after a constant error term has been added. The solid line and filled area represents the median and standard deviation of the errors. The additional error terms reflect the error floor seen in the observed star measurements, and are measured to be of 0.14 mas and 0.008 mag for the astrometry and photometry, respectively. After this adjustment the error distributions match well. The green dotted line shows the error cuts used in this study.

by our spatially-varying PSF model, as the artificial stars are planted using this model and thus wouldn't reflect this error. A constant error correction term of 0.14 mas and 0.008 mag is added to the artificial star position and magnitude uncertainties, after which the artificial star errors are found to closely follow those of the observed stars. This error correction does not have a noticeable effect on the completeness analysis as only stars far below the error cuts are significantly affected.

2.8 Appendix C: Posteriors of Profile Fits

In this appendix we present the bivariate posterior distributions for the different power law profile fits described in §2.3.2 and the marginalized and bivariate posterior distributions for the King profile fit described in §2.3.3. The bivariate posterior distributions show the correlations between

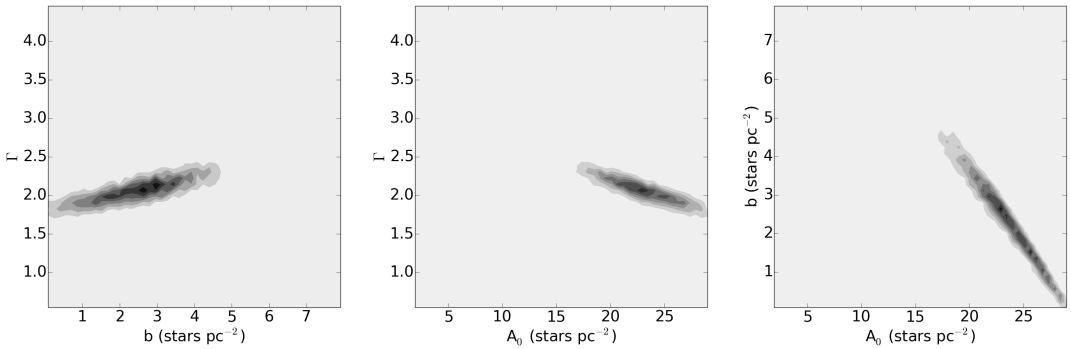

Figure 2.20 The bivariate posterior distributions for the power law model fit to the full cluster sample.

the power law slope (Γ), background level (b) and profile amplitude (A_0) for the profile fits to the full cluster (Figure 2.20), high-mass/low-mass members (Figure 2.21), and the parallel/perpendicular members (Figure 2.22). The marginalized posteriors of these parameters (not shown) are well described by Gaussians, which provide the best fit parameter values and errors reported in Table 2.3.

For the King model fit, the marginalized posterior distribution for the tidal radius (r_t), core radius (r_c), background (b), and normalization factor (k) are shown in Figure 2.23, while the bivariate posterior distributions are shown in Figure 2.24. The significance of the 3σ lower limit on the tidal radius is discussed in §2.3.3. The best fit parameter values and errors are reported in Table 2.4.

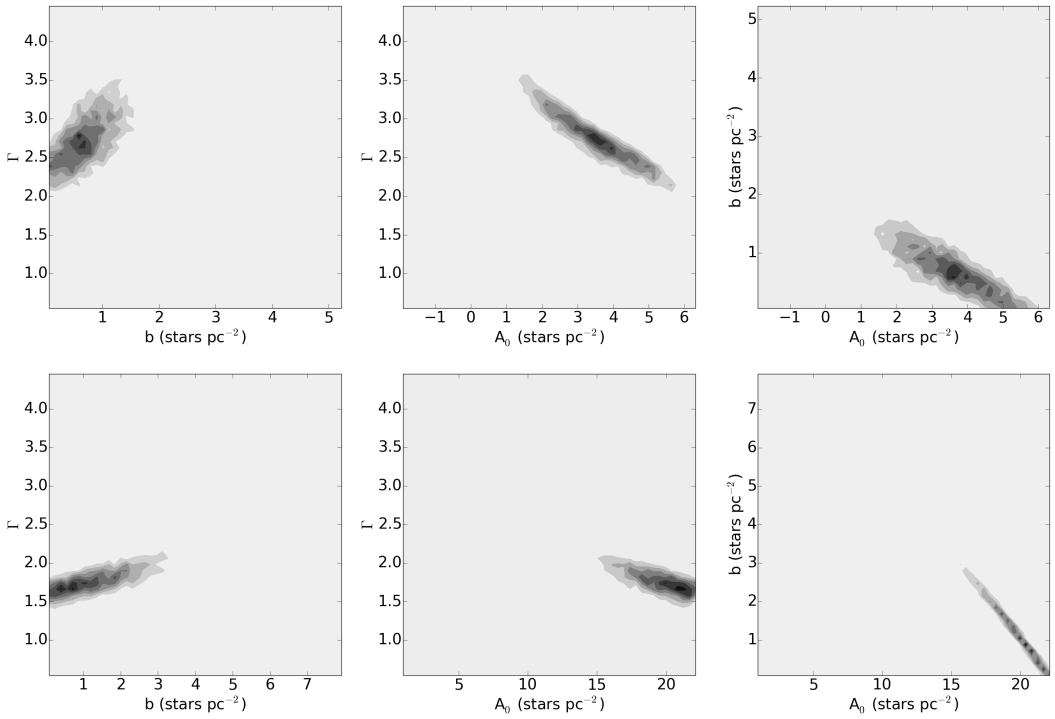

Figure 2.21 The bivariate posterior distributions for the power law model fits to the high-mass (*top*, F153M < 17 mag) and low-mass (*bottom*, F153M > 17 mag) cluster members. That the high-mass stars have a steeper power law slope Γ is an indication of mass segregation in the Arches cluster.

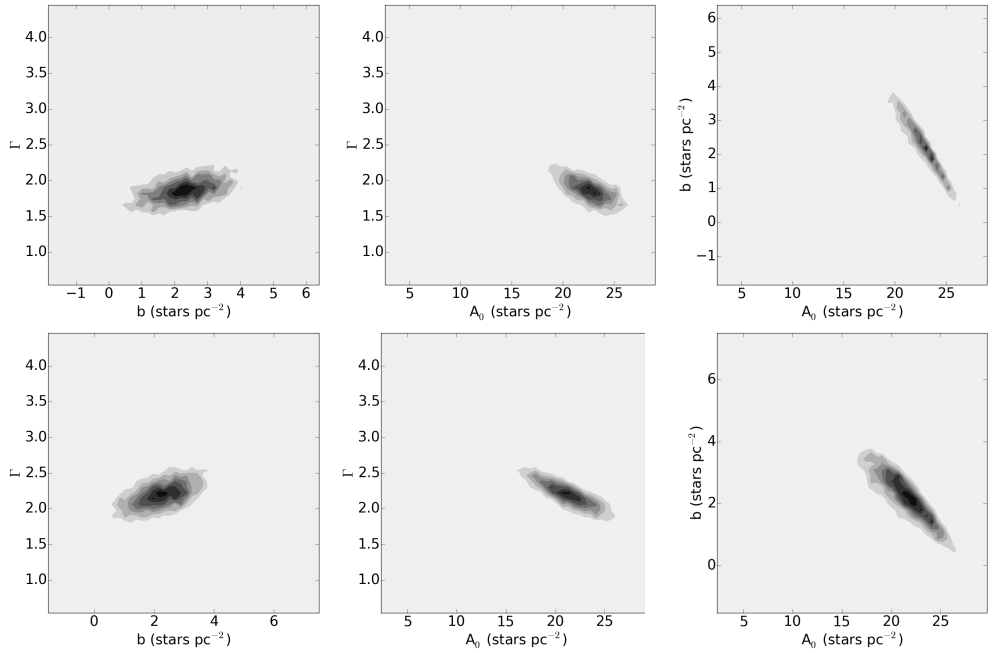

Figure 2.22 The bivariate posterior distributions for the power law model fits to the cluster members parallel (*top*) and perpendicular (*bottom*) to the bulk cluster orbit. The existence of tidal tails would cause asymmetries in these profiles such as a difference in the power law slope Γ of these profiles. No significant evidence for tidal tails are found.

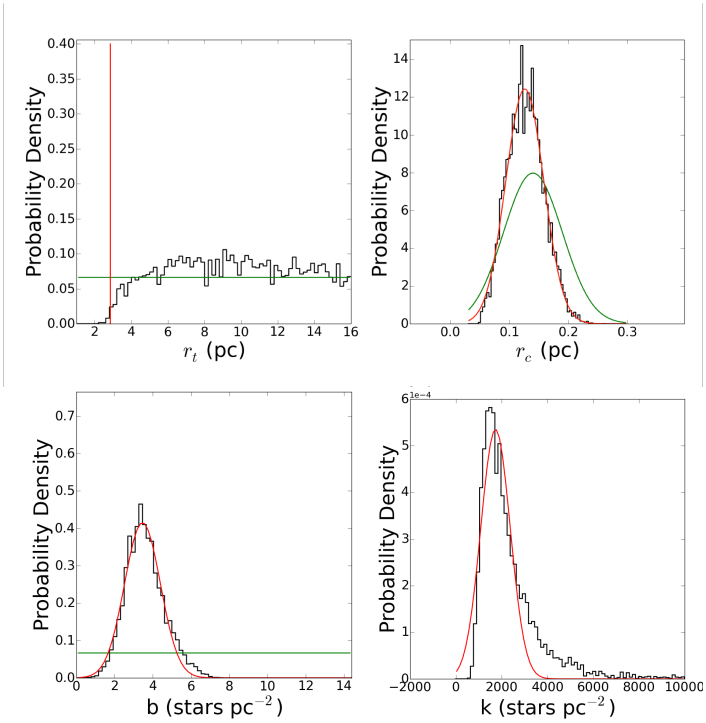

Figure 2.23 The 1D marginalized posterior distributions for the King model fit. The output of the *Multinest* sampling is in black, the corresponding Gaussian fit in red, and the input prior in green (if applicable). The 3σ limit to the tidal radius r_t (2.8 pc) is indicated by the red line, where 99.7% of the best-fit models fall above this value.

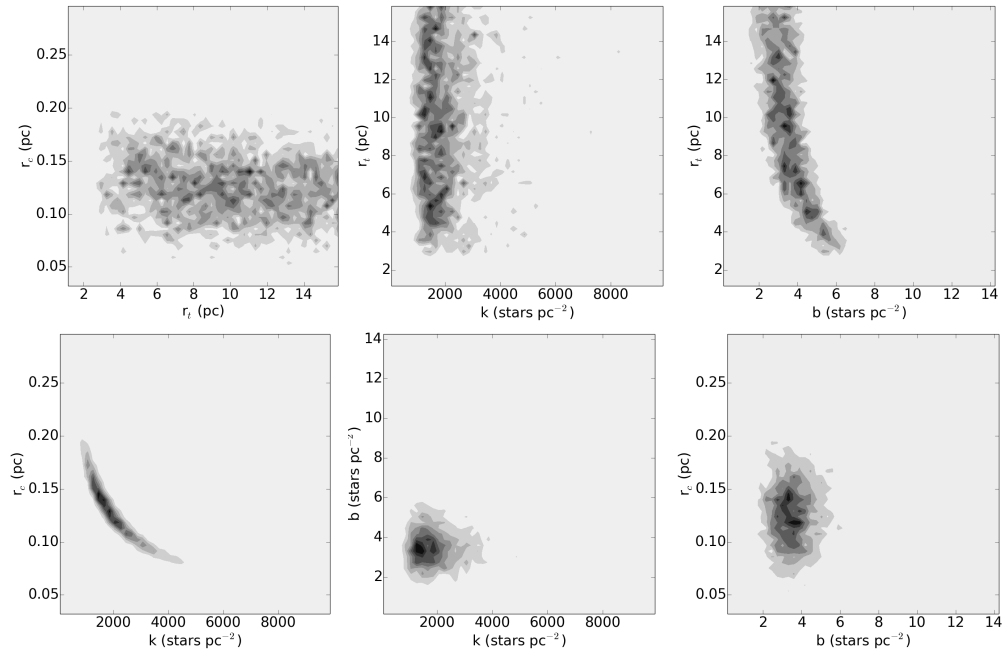

Figure 2.24 The bivariate posterior distributions for the King model fit.

References

Allard, F., Homeier, D., & Freytag, B. 2011, in Astronomical Society of the Pacific Conference Series, Vol. 448, 16th Cambridge Workshop on Cool Stars, Stellar Systems, and the Sun, ed. C. Johns-Krull, M. K. Browning, & A. A. West, 91

Anderson, J., & King, I. R. 2006, PSFs, Photometry, and Astronomy for the ACS/WFC, Tech. rep.

Anderson, J., Sarajedini, A., Bedin, L. R., et al. 2008, AJ, 135, 2055

Ascenso, J., Alves, J., & Lago, M. T. V. T. 2009, A&A, 495, 147

Baumgardt, H., & Makino, J. 2003, MNRAS, 340, 227

Belokurov, V., Evans, N. W., Irwin, M. J., Hewett, P. C., & Wilkinson, M. I. 2006, ApJ, 637, L29

Binney, J., Gerhard, O. E., Stark, A. A., Bally, J., & Uchida, K. I. 1991, MNRAS, 252, 210

Bovy, J. 2015, ApJS, 216, 29

Buchner, J., Georgakakis, A., Nandra, K., et al. 2014, A&A, 564, A125

Carballo-Bello, J. A., Gieles, M., Sollima, A., et al. 2012, MNRAS, 419, 14

Castellani, V., Chieffi, A., & Straniero, O. 1992, ApJS, 78, 517

Chun, S.-H., Kang, M., Jung, D., & Sohn, Y.-J. 2015, AJ, 149, 29

Clarkson, W., Sahu, K., Anderson, J., et al. 2008, ApJ, 684, 1110

Clarkson, W. I., Ghez, A. M., Morris, M. R., et al. 2012, ApJ, 751, 132

Do, T., Lu, J. R., Ghez, A. M., et al. 2013, ApJ, 764, 154

Elson, R. A. W., Fall, S. M., & Freeman, K. C. 1987, ApJ, 323, 54

Ernst, A., Just, A., & Spurzem, R. 2009, MNRAS, 399, 141

Espinoza, P., Selman, F. J., & Melnick, J. 2009, A&A, 501, 563

Feroz, F., Hobson, M. P., & Bridges, M. 2009, MNRAS, 398, 1601

Figer, D. F., Kim, S. S., Morris, M., et al. 1999a, ApJ, 525, 750

Figer, D. F., McLean, I. S., & Morris, M. 1999b, ApJ, 514, 202

Figer, D. F., Najarro, F., Gilmore, D., et al. 2002, ApJ, 581, 258

Fitzpatrick, E. L. 2004, in Astronomical Society of the Pacific Conference Series, Vol. 309, Astrophysics of Dust, ed. A. N. Witt, G. C. Clayton, & B. T. Draine, 33

Fukushige, T., & Heggie, D. C. 2000, MNRAS, 318, 753

Gelman, A., Carlin, J. B., Stern, H. S., Dunson, D. B., & Vehari, V. 2013, Bayesian Data Analysis: Third Edition (Taylor & Francis)

Ghez, A. M., Salim, S., Hornstein, S. D., et al. 2005, ApJ, 620, 744

Gieles, M., Heggie, D. C., & Zhao, H. 2011, MNRAS, 413, 2509

Gnedin, O. Y., Lee, H. M., & Ostriker, J. P. 1999, ApJ, 522, 935

Grillmair, C. J., & Johnson, R. 2006, ApJ, 639, L17

Gürkan, M. A., & Rasio, F. A. 2005, ApJ, 628, 236

Habibi, M., Stolte, A., Brandner, W., Hußmann, B., & Motohara, K. 2013, A&A, 556, A26

Habibi, M., Stolte, A., & Harfst, S. 2014, A&A, 566, A6

Harfst, S., Portegies Zwart, S., & Stolte, A. 2010, MNRAS, 409, 628

Hosek, Jr., M. W., Lu, J. R., Anderson, J., et al. 2015, ApJ, 813, 27

Howard, C. D., Rich, R. M., Clarkson, W., et al. 2009, ApJ, 702, L153

Johnston, K. V., Sigurdsson, S., & Hernquist, L. 1999, MNRAS, 302, 771

Kim, S. S., Figer, D. F., Kudritzki, R. P., & Najarro, F. 2006, ApJ, 653, L113

Kim, S. S., Figer, D. F., Lee, H. M., & Morris, M. 2000, ApJ, 545, 301

Kim, S. S., & Morris, M. 2003, ApJ, 597, 312

Kim, S. S., Morris, M., & Lee, H. M. 1999, ApJ, 525, 228

King, I. 1962, AJ, 67, 471

Kruijssen, J. M. D., Longmore, S. N., Elmegreen, B. G., et al. 2014, MNRAS, 440, 3370

Kunder, A., Koch, A., Rich, R. M., et al. 2012, AJ, 143, 57

Küpper, A. H. W., Kroupa, P., Baumgardt, H., & Heggie, D. C. 2010, MNRAS, 407, 2241

Lamers, H. J. G. L. M., Baumgardt, H., & Gieles, M. 2010, MNRAS, 409, 305

Lee, K. H., Lee, H. M., & Sung, H. 2006, MNRAS, 367, 646

Łokas, E. L., Gajda, G., & Kazantzidis, S. 2013, MNRAS, 433, 878

Longmore, S. N., Kruijssen, J. M. D., Bally, J., et al. 2013, MNRAS, 433, L15

Lu, J. R., Do, T., Ghez, A. M., et al. 2013, ApJ, 764, 155

Mackey, A. D., & Gilmore, G. F. 2003a, MNRAS, 338, 120

—. 2003b, MNRAS, 338, 85

Madrid, J. P., Hurley, J. R., & Sippel, A. C. 2012, ApJ, 756, 167

Martins, F., Hillier, D. J., Paumard, T., et al. 2008, A&A, 478, 219

Mauerhan, J. C., Cotera, A., Dong, H., et al. 2010, ApJ, 725, 188

McLaughlin, D. E., & van der Marel, R. P. 2005, ApJS, 161, 304

McLaughlin, G., & Peel, D. 2000, Finite Mixture Models (Wiley-Interscience)

Meynet, G., & Maeder, A. 2003, A&A, 404, 975

Mishenina, T. V., Bienaymé, O., Gorbaneva, T. I., et al. 2006, A&A, 456, 1109

Najarro, F., Figer, D. F., Hillier, D. J., & Kudritzki, R. P. 2004, ApJ, 611, L105

Nishiyama, S., Tamura, M., Hatano, H., et al. 2009, ApJ, 696, 1407

Odenkirchen, M., Grebel, E. K., Rockosi, C. M., et al. 2001, ApJ, 548, L165

Odenkirchen, M., Grebel, E. K., Dehnen, W., et al. 2003, AJ, 126, 2385

Oh, K. S., & Lin, D. N. C. 1992, ApJ, 386, 519

Oh, K. S., Lin, D. N. C., & Aarseth, S. J. 1995, ApJ, 442, 142

Paczynski, B., & Stanek, K. Z. 1998, ApJ, 494, L219

Peñarrubia, J., Navarro, J. F., McConnachie, A. W., & Martin, N. F. 2009, ApJ, 698, 222

Portegies Zwart, S. F., Makino, J., McMillan, S. L. W., & Hut, P. 2002, ApJ, 565, 265

Portegies Zwart, S. F., McMillan, S. L. W., & Baumgardt, H. 2004, in Astronomical Society of the Pacific Conference Series, Vol. 322, The Formation and Evolution of Massive Young Star Clusters, ed. H. J. G. L. M. Lamers, L. J. Smith, & A. Nota, 439

Portegies Zwart, S. F., McMillan, S. L. W., & Gerhard, O. 2003, ApJ, 593, 352

Rieke, G. H., Rieke, M. J., & Paul, A. E. 1989, ApJ, 336, 752

Schödel, R., Najarro, F., Muzic, K., & Eckart, A. 2010, A&A, 511, A18

Schwarz, G. 1978, The Annals of Statistics, 6, 461

Siegel, M. H., Majewski, S. R., Cudworth, K. M., & Takamiya, M. 2001, AJ, 121, 935

Siess, L., Dufour, E., & Forestini, M. 2000, A&A, 358, 593

Sollima, A., Martínez-Delgado, D., Valls-Gabaud, D., & Peñarrubia, J. 2011, ApJ, 726, 47

Stanek, K. Z., Kaluzny, J., Wysocka, A., & Thompson, I. 2000, ACTAA, 50, 191

Stetson, P. B. 1987, PASP, 99, 191

Stolte, A., Ghez, A. M., Morris, M., et al. 2008, ApJ, 675, 1278

Stolte, A., Grebel, E. K., Brandner, W., & Figer, D. F. 2002, A&A, 394, 459

Stolte, A., Morris, M. R., Ghez, A. M., et al. 2010, ApJ, 718, 810

Stolte, A., Hußmann, B., Morris, M. R., et al. 2014, ApJ, 789, 115

Sumi, T. 2004, MNRAS, 349, 193

Trenti, M., Vesperini, E., & Pasquato, M. 2010, ApJ, 708, 1598

von Hoerner, S. 1957, ApJ, 125, 451

Wang, Q. D., Dong, H., Cotera, A., et al. 2010, MNRAS, 402, 895

Webb, J. J., Harris, W. E., Sills, A., & Hurley, J. R. 2013, ApJ, 764, 124

Webb, J. J., Leigh, N., Sills, A., Harris, W. E., & Hurley, J. R. 2014, MNRAS, 442, 1569

Zotos, E. E. 2015, MNRAS, 446, 770

Chapter 3

The Optical/Near-Infrared Extinction Law in Highly Reddened Regions

Note: This chapter originally appeared as Hosek et al. (2018), with co-authors Jessica R. Lu, Jay Anderson, Tuan Do, Edward F. Schlafly, Andrea M. Ghez, William I. Clarkson, Mark R. Morris, and Saundra M. Albers.

Abstract

A precise extinction law is a critical input when interpreting observations of highly reddened sources such as young star clusters and the Galactic Center (GC). We use Hubble Space Telescope observations of a region of moderate extinction and a region of high extinction to measure the optical and near-infrared extinction law (0.8 μm – 2.2 μm). The moderate extinction region is the young massive cluster Westerlund 1 (Wd1; $A_{Ks} \sim 0.6$ mag), where 453 proper motion-selected main-sequence stars are used to measure the shape of the extinction law. To quantify the shape we define the parameter $\mathcal{S}_{1/\lambda}$, which behaves similarly to a color excess ratio but is continuous as a function of wavelength. The high extinction region is the GC ($A_{Ks} \sim 2.5$ mag), where 819 red clump stars are used to determine the normalization of the law. The best-fit extinction law is able to reproduce the Wd1 main sequence colors, which previous laws misestimate by 10% – 30%. The law is inconsistent with a single power law, even when only the near-infrared filters are considered, and has A_{F125W} / A_{Ks} and A_{F814W} / A_{Ks} values that are 18% and 24% larger than the commonly used Nishiyama et al. (2009) law, respectively. Using the law we recalculate the Wd1 distance to

be 3905 ± 422 pc from published observations of eclipsing binary W13. This new extinction law should be used for highly reddened populations in the Milky Way, such as the Quintuplet cluster and Young Nuclear Cluster. A python code is provided to generate the law for future use.

3.1 Introduction

Understanding the optical through near-infrared (OIR; I–K band; 0.8 μm – 2.2 μm) extinction law is critically important for studying objects beyond the solar neighborhood. For example, measurements of the stellar initial mass function in extinguished clusters (e.g. Habibi et al. 2013), studies of stellar populations at the Galactic Center (e.g. Feldmeier-Krause et al. 2015), and mapping the Milky Way's structure (e.g. Bovy et al. 2016) all depend on precise and accurate knowledge of the extinction law. In addition, the shape of the extinction law depends on the underlying dust grain properties along the line of sight, and so measuring the extinction law provides insight into grain characteristics across different interstellar environments (e.g. Draine 2003; Voshchinnikov et al. 2017). Commonly used extinction laws such as Cardelli et al. (1989) and Fitzpatrick (1999) describe the OIR extinction as a power law ($A_\lambda \propto \lambda^{-\beta}$) with $\beta = 1.6$, derived from photometry of a small sample of stars along different sightlines. Additional studies at that time obtained similar results with β values of $\sim$1.7 – 1.8 (e.g. Draine 1989; Martin & Whittet 1990), and so this description of the OIR extinction law has been widely adopted.

More recent studies have used large-scale photometric surveys to refine the measurement of the OIR extinction law. A power law has been found to be a good fit in the NIR regime (J–K; 1.25 μm – 2.2 μm), though with a generally steeper exponent than was found in earlier work. Studies such as Indebetouw et al. (2005), Messineo et al. (2005), and Nishiyama et al. (2009) use Two-Micron All Sky Survey (2MASS) JHK photometry of red giant stars (often red clump stars) to measure extinction, reporting $\beta = 1.7$, 1.9, and 2.0 respectively. The steeper slopes of Messineo et al. (2005) and Nishiyama et al. (2009) were derived for fields toward the Galactic Bulge, while the shallower slope of Indebetouw et al. (2005) was found for fields at Galactic longitudes of $\ell = 42°$ and $\ell = 284°$, hinting at a variation in the law with Galactic longitude. However, spectroscopic studies of red clump stars in the APOGEE (Wang & Jiang 2014) and *Gaia*-ESO surveys (Schultheis et al. 2015) show no evidence of NIR law variability as a function of either total extinction or angle relative to

the Galactic center. These studies find slopes of 1.95 and 2.12, respectively, supporting a steeper NIR extinction law.

A more complicated function is required for the extinction law when observations shortward of J-band are included. The Cardelli et al. (1989) law has a single free parameter, R_V (the ratio of absolute to selective extinction in V-band), which begins to significantly impact the steepness of the law shortward of I-band. Fitzpatrick & Massa (2009) adopt a two-parameter model model that behaves as a power law whose exponent increases with wavelength in order to reproduce Hubble Space Telescope (*HST*) spectrophotometry (0.75 μm – 1 μm) and ground-based JHK photometry for a sample of OB-type stars. A study of red clump (RC) stars in the OGLE-III and VVV surveys by Nataf et al. (2016) similarly concluded that a law with multiple free parameters is required to reproduce the observed colors in VJHK (0.5 – 2.14 μm), finding the Cardelli et al. (1989) law to be inconsistent regardless of how R_V is varied. However, Schlafly et al. (2016) present a one-parameter law where variations in R_V can explain Pan-STARRS, 2MASS, and WISE photometry (0.5 μm – 4.5 μm) of APOGEE stars in the galactic disk, though this law is most similar to the Fitzpatrick & Massa (2009) law.

While able to utilize large samples across many lines of sight, a disadvantage of survey-based extinction studies is that they are limited by the photometric depth of the surveys used and are dominated by low-extinction stars. The Galactic Center (GC) presents an opportunity to measure the extinction law at high extinctions ($A_{Ks} \sim 2.5$ mag), where small variations in the law can have a large effect on observations. Previous studies of the GC extinction law include Schödel et al. (2010), who use photometry of RC stars in the central parsec region to measure a power law slope of $\beta = 2.21 \pm 0.24$ between H- and K-band, and Fritz et al. (2011), who measure $\beta = 2.11 \pm 0.06$ from analysis of gaseous emission lines ($\lambda \geq 1$ μm) from the minispiral structure near Sgr A*. Most recently, Nogueras-Lara et al. (2017) obtain $\beta = 2.31 \pm 0.03$ for JHK observations of RC stars in the wide-field (7.95' x 3.43') GALACTICNUCLEUS survey, finding no dependence on field location or total extinction. However, the trade-off for observing at such high reddening is the rapid loss of starlight shortward of J-band, and so the optical portion of the GC extinction law remains largely unexplored.

In this paper, we combine *HST* observations of a region of moderate extinction with a region of high extinction in order to constrain the shape and normalization of the extinction law between

0.8 μm – 2.2 μm. The moderate extinction region is Westerlund 1 (Wd1), a young massive cluster with an extinction of $A_{Ks} \sim 0.7$ mags (Damineli et al. 2016, hereafter D16) located in the Galactic plane (ℓ = -20.451°, b = -0.404°). While these observations allow us to sensitively probe the shape of the extinction law through the I-band, the uncertainty in the cluster distance prevents a tight constraint on the normalization of the law. To overcome this, we incorporate NIR *HST* observations of red clump (RC) stars found in the line-of-sight (LOS) toward the Arches cluster, a similar young massive cluster near the GC (ℓ = 0.121°, b = 0.0168°). The average distance of these stars is much better constrained and thus the normalization of the law can be determined. We use a forward-modeling Bayesian technique to simultaneously fit the extinction law and global properties of both populations without assuming a functional form for the law.

3.2 Observations and Measurements

We combine observations of Wd1 and RC stars in the Arches cluster field to measure the OIR extinction law (Figure 3.1). For Wd1, we use *HST* observations in the F814W, F125W, and F160W filters combined with VISTA K_s observations obtained through the *VISTA Variables in the Via Lactea* (*VVV*) survey (Minniti et al. 2010). For the RC stars, we use *HST* observations obtained in the F127M and F153M filters (1.27 μm, and 1.53 μm, respectively). These filters provide photometry from 0.8 μm – 2.2 μm with the throughputs shown in Figure 3.2. An overview of the observations is provided in Table 3.1.

3.2.1 HST Observations: Wd1

HST observations of Wd1 were obtained over an 8 year period between 2005 - 2013. The earliest observations were made in 2005 with the Advanced Camera for Surveys Wide Field Camera (ACS-WFC, GO-10172, PI: R. De Grijs) in the F814W filter. The total exposure time was 2407 s, comprised of 3 slightly dithered images covering a 211" x 218" field of view (0".05 pix^{-1}). A second set of observations was obtained in 2010 with the infrared channel of the Wide Field Camera 3 (WFC3-IR) in the F125W and F160W filters (GO-11708, PI: M. Andersen)[1]. The final observations

[1]Observations were also obtained in the F139M filter, but a comparison between the output photometry and stellar SED models indicated either a problem with the photometry (perhaps an incorrect zeropoint) or stellar models at these wavelengths (1.35 μm – 1.41 μm). As a result, F139M is not considered in this analysis.

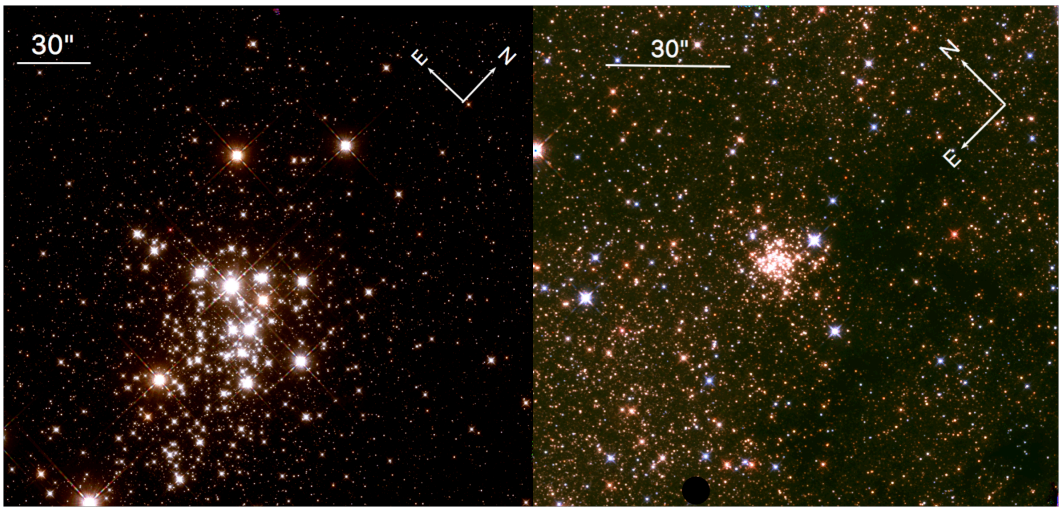

Figure 3.1 *HST* three-color images of Wd1 (left) and the Arches cluster field (right). The Wd1 image is a 2 x 2 mosaic created with the WFC3-IR camera, with F125W as blue, F139M as green, and F160W as red. The Arches image is a single WFC3-IR field with F127M as blue, F139M as green, and F153M as red. The F139M observations are not used in the extinction law analysis.

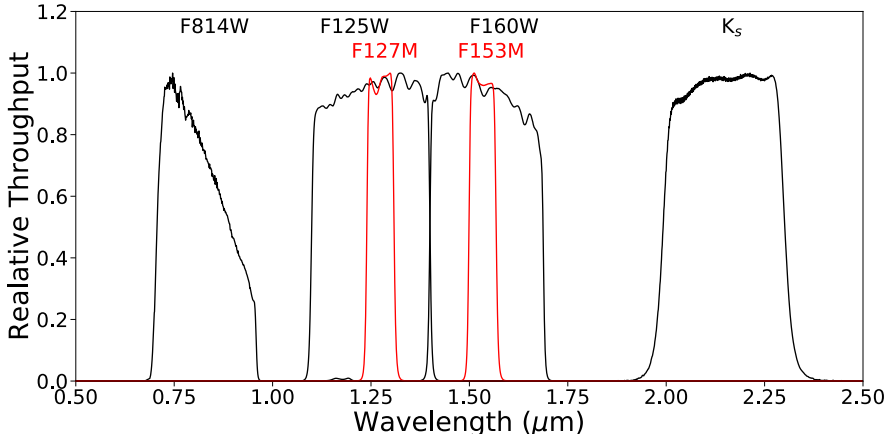

Figure 3.2 Filters used to constrain the Wd1 and Arches field RC star extinction law. The F125W, F127M, F153M, and F160W filters are from *HST* WFC3-IR, the F814W filter from *HST* ACS-WFC3, and the K_s filter from the *VISTA* VVV survey.

were obtained in 2013 with WFC3-IR in the F160W filter to provide a third positional epoch (GO-13044, PI: J. R. Lu). These observations mimicked the 2010 F160W observations, though a different position angle was used due to new *HST* guide star restrictions. Since the field of view for WFC3-IR is ∼130" (0".12 pix^{-1}), a 2 x 2 mosaic was used to cover the entire 2005 ACS-WFC field of view. Each pointing had 7 images per filter, for total exposure times of 2443 s and 2093 s in F125W and F160W, respectively.

The *HST* observations were reduced using the standard online HST data reduction pipeline and the resulting "FLT" images were downloaded from the HST archive on 2011 Dec 14. High-quality astrometric and photometric measurements were extracted from the individual FLT images using *KS2*, an expansion of the software developed for the Globular Cluster Treasury Program (Anderson et al. 2008). With this software, the measurements are combined to produce a single starlist for each filter. The sources are matched across epochs and positions transformed into a common astrometric reference frame where proper motions can be calculated. A detailed explanation of this process is given in H15.

To calculate the KS2 photometric zeropoints, we compared the KS2 starlists with calibrated photometry obtained using DOLPHOT, a version of HSTPHOT (Dolphin 2000) with specific modules for ACS and WFC3-IR. We used Tiny Tim (Krist et al. 2011) point spread functions and the general procedure and recommendations (e.g., DOLPHOT input parameters) outlined in Williams et al. (2014). The DOLPHOT output was culled to eliminate spurious and overly crowded sources using sharpness, crowding, and SNR cuts of <1, <0.55, and >5, respectively. The remaining sources were cross-matched with the KS2 starlists, and the KS2 zeropoints calculated from the average difference between the DOLPHOT and KS2 magnitudes over a magnitude range selected to omit bright saturated stars and faint noisy stars (Figure 3.3). The uncertainty on the average difference is less than 0.1% for all filters, and so the KS2 zeropoint uncertainty in dominated by the reported HST zeropoint uncertainty of 1% (Kalirai et al. 2009). The final zeropoints (in magnitudes) are 32.6783, 25.2305, 23.566, 23.088, and 24.5698 for the F814W, F125W, F127M, F153M, and F160W filters, respectively.

The proper motions provide a reliable method to separate likely cluster members from field stars. Following H15, a Gaussian Mixture model was used to describe the kinematic distributions of the cluster and field, from which a cluster membership probability is calculated for each star. The

Table 3.1. Observations

Date	Target	Filter	Telescope/Inst	P.A. (deg)	t_{exp}[a] (s)	N_{img}[b]	N_{mosaic}[c]	N_{stars}	Depth[d] (mag)
2005.485	Wd1	F814W	*HST* ACS-WFC	46.43	802	3	1	10,056	24.3
2010.652	Wd1	F125W	*HST* WFC3-IR	-45.87	349	7	2×2	10,029	22.1
2010.652	Wd1	F160W	*HST* WFC3-IR	-45.87	299	7	2×2	10,056	20.8
2013.199	Wd1	F160W	*HST* WFC3-IR	134.67	299	14	2×2	10,056	20.8
2010.351[e]	Wd1	K_s	*VISTA* VVV	49.5	4	4		5990	15.8
2010.615	Arches	F127M	*HST* WFC3-IR	-45.33	600	12	1	30,530	21.8
2010.604	Arches	F153M	*HST* WFC3-IR	-45.33	350	21	1	30,530	20.5
2011.683	Arches	F153M	*HST* WFC3-IR	-45.33	350	21	1	30,530	20.5
2012.616	Arches	F153M	*HST* WFC3-IR	-45.33	350	21	1	30,530	20.5

[a]Exposure time for a single image

[b]Number of images at each dither position

[c]Mosaic pattern used in observations

[d]Magnitude at which median error is 0.05 mags

[e]File: ADP.2014-11-25T14:28:20.543.fits

resulting proper motion catalog contains 9922 stars with membership probabilities and is presented in detail in Lu et al., in prep.

3.2.2 VISTA Observations: Wd 1

Using the 4m *VISTA* telescope at Cerro Paranal, the *VVV* survey mapped 520 deg^2 of the Milky Way bulge and disk in the K_s-band (Minniti et al. 2010). This area was observed in 1.64 deg^2 tiles, each composed of 6 individual pointings dithered such that each pixel (except for those at the extreme edges of the tile) was covered by at least 4 images. The *VVV* photometric catalog for the tile containing Wd1 was downloaded from Data Release 2 using the ESO Phase 3 Archive Interface[2]. However, the positions in the catalog revealed that there were only limited detections near Wd1, likely due to significant stellar crowding in the field. In addition, the *VVV* catalog contains aperture photometry, which can be compromised in crowded regions such as Wd1. As a result, we performed point spread function (PSF) photometry on the *VISTA* tile directly to improve the measurements in the Wd1 field.

[2]http://archive.eso.org/wdb/wdb/adp/phase3_vircam/form

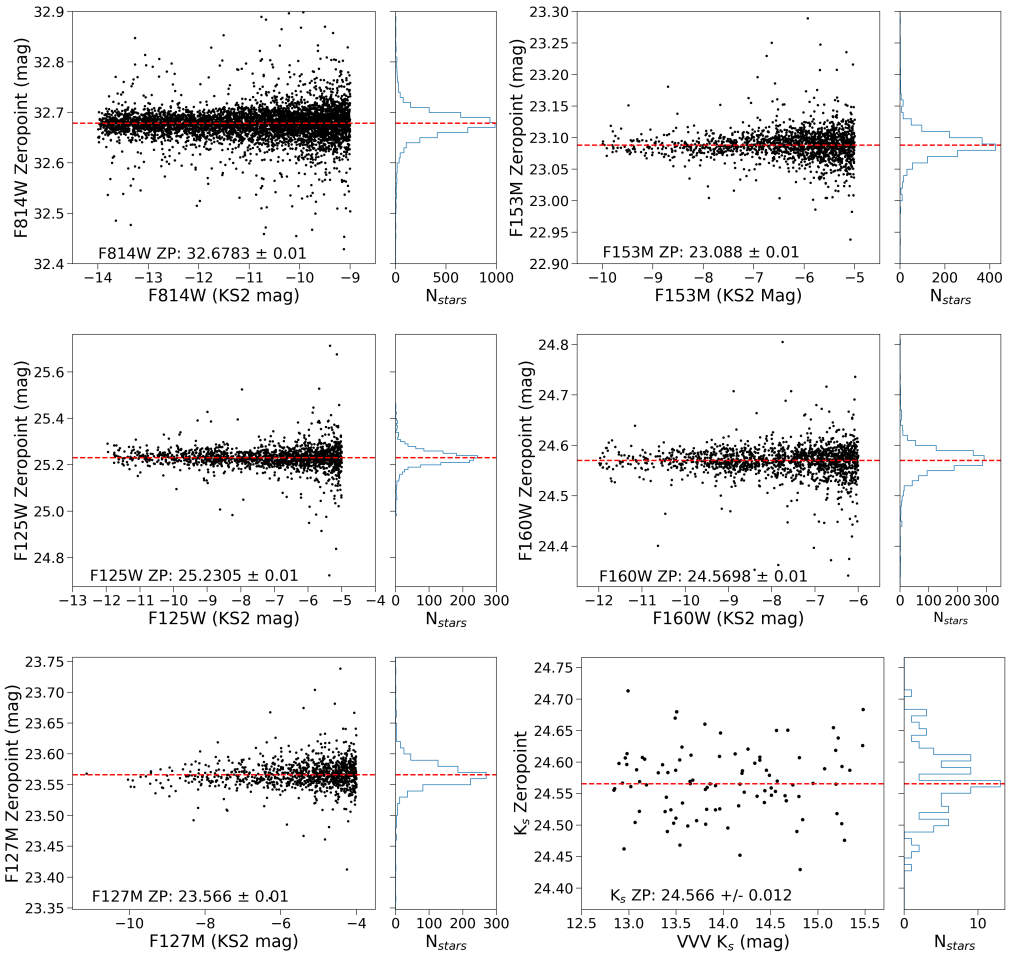

Figure 3.3 The photometric zeropoints derived for the filters used in this study. The *HST* filter zeropoints are for the *KS2* photometry and the *VISTA* K_s zeropoint is for the *AIROPA* photometry. The *KS2* zeropoints have uncertainties of 0.01 mags and the *AIROPA* zeropoint has a statistical uncertainty of 0.012 mags.

After downloading the VISTA K_s tile image using the Phase 3 Archive Interface, we trimmed the tile to a manageable region (4.2' x 4.2') that overlaps our *HST* observations. To perform PSF photometry we used *AIROPA*, an expansion of the *Starfinder* code (Diolaiti et al. 2000), in the legacy mode (Witzel et al. 2016). In this mode, *AIROPA* behaves identically to *Starfinder* v1.6. Briefly, an empirical PSF is derived from a subset of user-identified stars and then cross-correlated with the image to detect stars above a user-defined threshold. We carefully selected 27 relatively isolated and non-saturated stars in the tile to define the model PSF and set the minimum correlation coefficient of 0.7. This results in the detection of ∼6000 stars in the image.

We calibrate the PSF photometry by matching sources between the PSF and *VVV* catalogs. A two-dimensional first-order polynomial is used to transform the *VVV* positions into the PSF catalog astrometric reference frame, obtaining 1300 stars with positions matched within 1" (the FWHM of the image). Only stars with photometric errors less than 0.05 mags in both catalogs and fainter than the saturation limit are considered. Further, we require each star's *VVV* 1" aperture diameter magnitude ("APERMAG1") be consistent with its 2" aperture diameter magnitude ("APERMAG3") to within 0.05 mags, in an effort to eliminate stars with close neighbors affecting the aperture photometry. After these cuts 136 stars remain. The photometric zeropoint for the PSF catalog is calculated from the median difference between the *VVV* magnitude and the instrumental PSF magnitude (Figure 3.3). The final K_s zeropoint is 24.566 ± 0.012 mags, where the uncertainty is the median difference error (0.005 mags) combined in quadrature with the *VVV* zeropoint error reported for the tile image (0.011 mags).

It has been shown that the photometric errors reported by *Starfinder* (and thus *AIROPA* in single-PSF mode) are systematically underestimated because they do not capture errors in the PSF model itself (Schödel 2010). This PSF uncertainty is largely constant with magnitude, usually dominating the error budget for bright stars where the photon noise is very low. We derive this additional error term from the same sample of matched stars used to derive the photometric zeropoint. We assume that the standard deviation of the difference between the PSF and *VVV* catalog magnitudes (σ_Δ) is a combination of the *VVV* catalog error (σ_{VVV}), PSF error reported by *AIROPA* (σ_A), and the constant PSF error term (σ_{PSF}):

$$\sigma_\Delta^2 = \sigma_{VVV}(m)^2 + \sigma_A(m)^2 + \sigma_{PSF}^2 \tag{3.1}$$

where σ_{VVV} and σ_A are both functions of the magnitude m. We find $\sigma_{PSF} = 0.058$ mag, which is added in quadrature with the reported *AIROPA* errors to produce the final photometric errors for the PSF catalog.

3.2.3 HST Observations: Arches Cluster

The Arches cluster was observed with *HST* WFC3-IR using the F127M and F153M filters in 2010 (GO-11671; PI: A.M. Ghez), and then repeat observations in F153M were obtained in 2011 and 2012 for astrometric purposes (GO-12318, GO-12667; PI: A.M. Ghez). These observations, along with the photometric and astrometric measurements extracted using KS2, and are presented in H15. The photometric zeropoints are derived in the same manner as the Wd1 *HST* observations and are also shown in Figure 3.3. We use the same catalog presented in H15, which contains ∼26,000 stars.

3.3 Methods

We forward-model the Wd1 stars and Arches field RC photometry, simultaneously allowing the extinction law, Wd1 total extinction and distance, and RC star average distance and magnitude spread to vary in order to achieve the best-fit. The extinction law can be divided into two components: the wavelength-dependent extinction law shape and the wavelength-independent normalization factors (see Appendix 3.7). This analysis assumes that both components of the NIR extinction law (JHK) are the same along the Wd1 (ℓ = -20.451°, b = -0.404°) and Arches cluster (ℓ = 0.121°, b = 0.0168°) lines of sight (LOS).

While the extinction law shape is known to vary across different sightlines in the optical and UV (e.g. Cardelli et al. 1989), the NIR shape has been observed to be relatively constant as a function of total extinction and galactic longitude (Wang & Jiang 2014; Schultheis et al. 2015; Majaess et al. 2016). A notable exception is the extinction law of Fitzpatrick & Massa (2009), which exhibits significant variations in the NIR for a small sample of targets. However, Schlafly et al. (2016) derive a law for a large set of sightlines that calls for minimal variation in the NIR, supporting the case for a similar NIR shape for the Wd1 and Arches LOS. We confirm this assumption by comparing the shape of Wd1-data only and Wd1+RC extinction law fit in §3.4.3.

The normalization of the extinction law is more challenging to measure since it requires knowledge of the distance to the source object. As a result, how the normalization might change for different LOS is not well studied. However, the extinction along the Wd1 and Arches LOS are dominated by similar material, namely dust from foreground spiral arms in the Galactic Plane. Further, it is not clear why the normalization of the law would be different if the shape is the same. We move forward assuming that the normalization factors are the same for both clusters, though this will require future verification (§3.5.5).

A Bayesian analysis is used to compare a given extinction law model to the observations. The likelihood function contains a component for the Wd1 MS stars and a component for the RC stars, which are combined in the final analysis. In this section, §3.3.1 describes the stellar models used to simulate the observed populations, §3.3.2 and §3.3.3 describe the observed Wd1 and Arches RC samples, and §3.3.4 describes the extinction law model, likelihood equation, and subsequent tests of the analysis.

3.3.1 Stellar Models and Synthetic Photometry

To model the Wd1 and RC observations, we use stellar models to represent the stellar population, apply extinction to their spectra using a generated extinction law, and then calculate synthetic photometry in the observed filters. To generate the Wd1 stars we must first adopt a cluster age. Spectroscopic studies of the evolved star population suggest a cluster age between 4 – 6 Myr, based on the properties of the O-type supergiants (Negueruela et al. 2010) and the observed ratio of different populations of supergiants to Wolf-Rayet stars (Crowther et al. 2006). Analysis of the pre-main sequence (pre-MS) turn-on feature in the CMD has found cluster ages between 3 – 5 Myr (Brandner et al. 2008; Gennaro et al. 2011), but the age is degenerate with the cluster distance (e.g. Andersen et al. 2017), which is uncertain to ± 700 pc (∼18%; Kothes & Dougherty 2007). None of these studies find evidence of an age spread in the cluster, and Clark et al. (2005) point out that the large number of massive stars would be expected to remove excess gas in the cluster within a crossing time. We thus assume the cluster is coeval and adopt an age of 5 Myr. We will perform separate analyses assuming ages of 4 Myr and 6 Myr to assess the impact of the age uncertainty on the extinction law.

A theoretical Wd1 cluster isochrone is generated with the adopted age and assuming solar metallicity using Geneva evolution models with rotation ($\Omega = 0.4$; Ekström et al. 2012) for the main sequence/evolved stars and Pisa evolution models (Tognelli et al. 2011) for the pre-MS. For each star in the isochrone, the effective temperature, T_{eff}, and surface gravity, $\log(g)$, from the stellar evolution model are used to select a model atmosphere. The atmospheres are drawn from a combined library of ATLAS9 (Castelli & Kurucz 2004) and PHOENIX (version 16; Husser et al. 2013) synthetic spectra. ATLAS9 spectra are used for $T_{eff} > 5500$ K and PHOENIX spectra are used for $T_{eff} < 5000$ K, with a linear interpolation of the two model sets between 5000 – 5500 K. The spectra are then reddened using a custom-built extinction law (§3.3.4) and total extinction using *Pysynphot* (STScI Development Team 2013). The reddened spectra are convolved with the desired filter functions to produce synthetic photometry. The output magnitudes can then be scaled to any cluster distance (a free parameter in our model) for a direct comparison to the observations.

As discussed in §3.3.2, we limit the observed Wd1 sample to only stars that fall on the main sequence (MS). These stars represent an ideal sample to examine the extinction law because their intrinsic colors are well understood and are only slightly dependent on mass in the filters used in this study. We restrict the stellar mass range of the theoretical isochrone to match the selection criterion imposed on the observed sample, selecting stars between 0.5 and 3.0 mags brighter than the pre-MS bridge in F160W (Figure 3.4). The pre-MS bridge, which connects the MS and pre-MS sequences in a color-magnitude diagram (CMD), is only dependent on the cluster age. Thus, no assumptions regarding the cluster distance, extinction law, or total extinction are required in order to appropriately set the isochrone mass range. For a 5 Myr cluster this mass range is 4.41 $M_\odot$ – 14.0 $M_\odot$. To test whether the ATLAS9 atmospheres (which assume local thermodynamic equilibrium) are appropriate for the high-mass stars in our sample, we compare the synthetic magnitudes for a 9 $M_\odot$, 12 $M_\odot$, and 15 $M_\odot$ main sequence star with those calculated using non-local thermodynamic equilibrium CMFGEN atmospheres from Fierro et al. (2015). We find that the synthetic magnitudes agree to within the photometric errors, and so we move forward with the ATLAS9 models in our analysis.

A similar procedure is used to model the Arches field RC stars. We select the RC star model from a 10 Gyr PARSEC stellar isochrone (Bressan et al. 2012) at solar metallicity, which represents the average stellar population in the Galactic bulge (Zoccali et al. 2003; Clarkson et al. 2008).

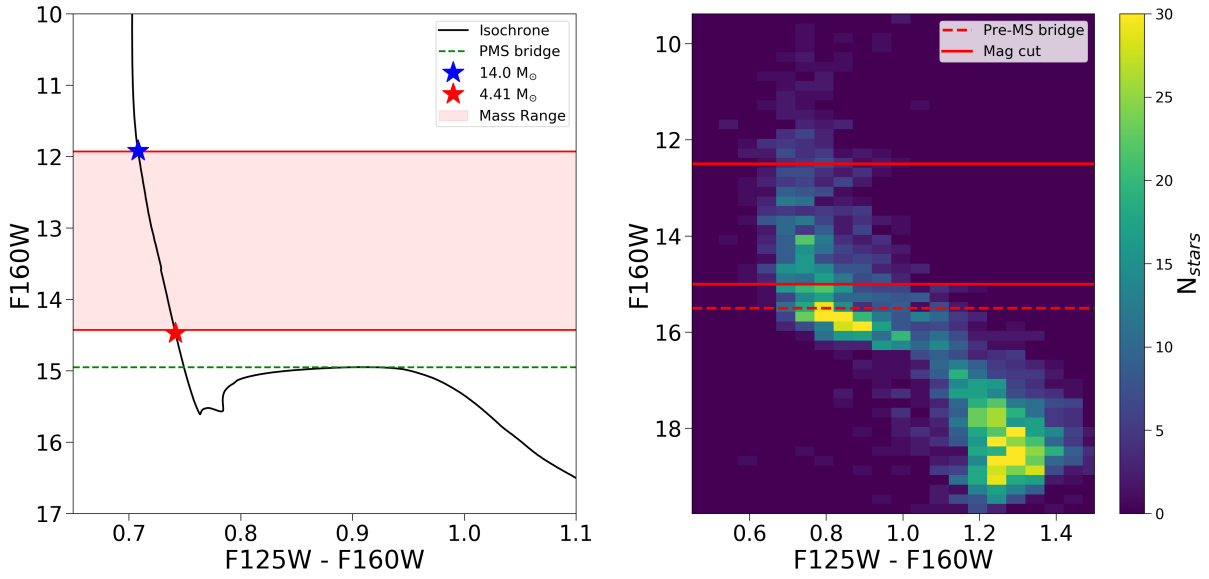

Figure 3.4 The criteria used to select main-sequence cluster members based on a theoretical isochrone. *Left:* The mass range for a 5 Myr isochrone, which is selected based on magnitude relative to the pre-MS bridge (green dashed line). These criteria match those imposed on the observed sample. *Right:* Color-magnitude diagram of proper-motion selected Wd1 members (cluster membership probability $P_{clust} \geq 0.6$). We identify MS stars in our Wd1 sample as those between 0.5 mags brighter and 3 mags brighter (red lines) than the pre-MS bridge (red dotted line) in F160W.

The chosen model matches the average effective temperature (T_{eff}) and surface gravity ($\log(g)$) measured for solar-metallicity RC stars in the *Hipparcos* catalog (T_{eff} = 4700 K, $\log g$ = 2.40 cgs; Mishenina et al. 2006). The synthetic photometry is then scaled to the average distance of the RC population, which is a free parameter in our model.

3.3.2 Wd1 Sample: Main Sequence Stars

We select a sample of high-probability Wd1 members that fall on the MS, are not saturated, and have small photometric errors. Each star in the sample has photometry in each *HST* filter, and a subset of the stars have *VISTA* K_s photometry as well. The steps used to create the sample are described below.

The sample is created directly from the *HST* proper motion catalog described in §3.2.1 and Lu et al., in prep. First, we restrict the catalog to stars with cluster membership probabilities greater than 0.6 and photometric errors less than 0.05 mags in each filter. MS stars are identified as those 0.5 mags brighter than the pre-MS bridge in F160W, corresponding to F160W $\leq$ 15.0 mags (Figure 3.4). This conservative criterion is adopted to minimize contamination from pre-MS stars scattered into the MS by differential reddening. At the bright end, we adopt a magnitude cut of F160W $\geq$12.5 mag in order to eliminate saturated sources in the *VISTA* K_s observations. After these cuts, 537 of the original 9922 stars remain in the sample.

To eliminate photometric outliers (such as field stars or binary systems with unusual colors), we apply an iterative 3-sigma cut in a two-color diagram (2CD) across the HST filters: F814W - F125W vs. F814W - F160W. We fit a line to the sample (via orthogonal regression) and calculate the root-mean-squared (RMS) residual relative to the fit in 0.25 magnitude bins. Stars with residuals larger than 3 times the RMS value in their magnitude bin are removed. This process is repeated until no further stars are eliminated. A total of 53 stars are rejected by this criterion.

A final cut is required to eliminate cluster stars that would otherwise be outside the adopted F160W magnitude range but have been scattered into the sample by differential extinction. For example, a high-mass star intrinsically brighter than the F160W magnitude limit can scatter into the sample if it is located in a region of higher extinction. This star would appear redward of the average main-sequence population. Similarly, a low-mass star could scatter into the sample if it is in a region of lower extinction, placing it blueward of the average main sequence population. To

Table 3.2. Wd1 Sample Selection

Selection Description	Selection Criterion	N_{stars} (HST)	N_{stars} (HST–VISTA)
Original Sample		**9922**	**1071**
		Cut from Sample	
Membership	$P_{clust} \geq 0.6$	7007	426
Phot Error	≤ 0.05 mag	826	15
Phot Range	$12.5 \leq$ F160W ≤ 15.0	1552	272
Isolation	4.5", $\geq$ star mag + 3	—	229
Sigma-clipping	3σ, iterative	42	12
Differential Extinction	see §3.3.2	42	11
Final Sample		**453**	**106**

eliminate these stars we make a cut in F160W vs. F814W - F160W CMD space, where the median color is taken to represent the MS. Two lines with a slope of 1 that intersect the bright and faint ends of the MS are used to identify and remove potentially scattered stars (Figure 3.5). This slope is a conservative estimate of the steepest possible reddening vector in the CMD, corresponding to A_{F814W} / $A_{F160W} \sim 2$. A steeper reddening vector would require A_{F814W} / $A_{F160W} < 2$, which is much lower than any law reported in the literature. An additional 42 stars are removed by this criterion, resulting in a final sample size of 453 stars.

To construct the *HST*-*VISTA* subsample, we iteratively match the *HST* proper motion catalog with the *VISTA* catalog using a 0.25 ($\sim$2 *HST* HST pixels) matching radius. An additional "isolation cut" is imposed to reduce the impact of stellar crowding on the seeing-limited *VISTA* photometry: stars lying within 4.5" of another star that has a brightness within 3 magnitudes of the star itself (as identified from the *HST* catalog) are rejected. All of the same cuts are applied for a final *HST*-*VISTA* subsample of 106 stars.

A summary of the adopted cuts and sample size is provided in Table 4.3.4. These stars form well-defined reddening vectors in the *HST*-only and *HST*-*VISTA* 2CDs, which are used in the extinction law analysis (Figure 3.6). The typical photometric uncertainty is $\sim$0.02 mag for the *HST* filters and $\sim$0.07 mag for *VISTA* K_s. While the magnitude cuts introduce a possible Malmquist bias, the effect is small due to the small photometric errors. Further, a bias would only affect our results if the extinction law for the faint stars were different than that of the bright stars, which is highly unlikely since they are part of the same cluster.

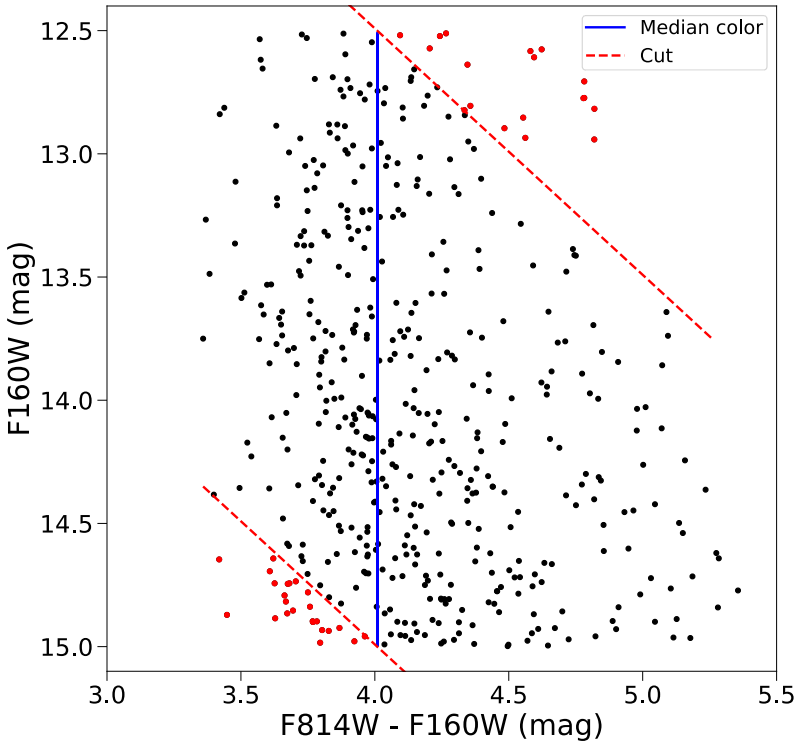

Figure 3.5 Cut applied to the Wd1 sample to eliminate intrinsically brighter/fainter stars that have scattered into the target magnitude range due to differential extinction. Bright (i.e. high mass) interlopers can be scattered into the sample redward of the median cluster sequence while faint (i.e. low mass) interlopers can be scattered blueward. The median cluster sequence is shown by the blue line, the applied cuts by the red dotted lines, and the stars removed by this cut by the red points.

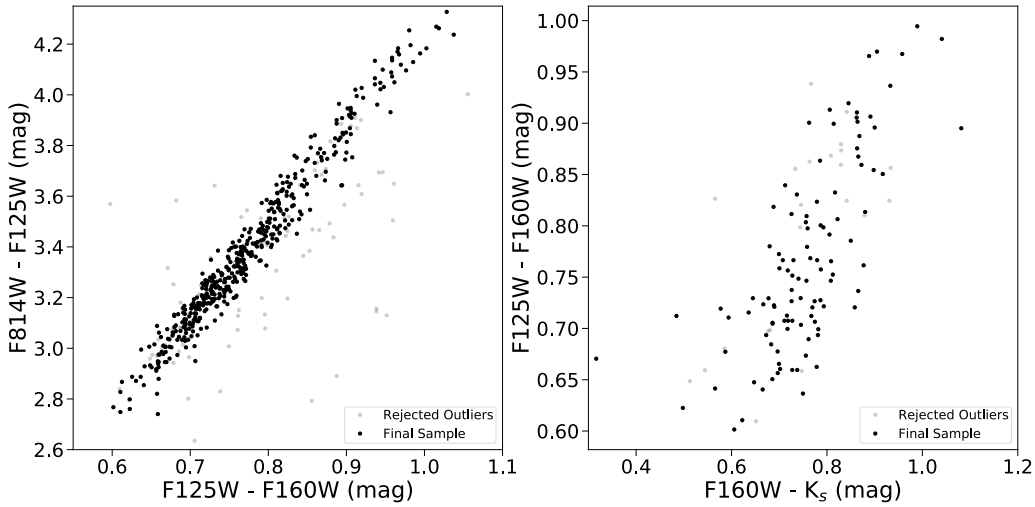

Figure 3.6 Two-color diagrams of final Wd1 sample, with the *HST*-only 2CD on the left and *HST*-*VISTA* 2CD to the right. Stars rejected as photometric outliers or scattered stars are shown in gray, while the final sample is shown in black. The high photometric precision of *HST* relative to *VISTA* is evident by the scatter introduced by the *VISTA* photometry in the *HST*-*VISTA* 2CD.

3.3.3 Arches sample: Red Clump Stars

RC stars are low-mass giants that are in the core helium-burning stage of their evolution. Exhibiting a narrow range of T_{eff} and $\log(g)$ values, these stars form a well defined clump in the CMD that spreads along the reddening vector in the presence of differential extinction (Girardi 2016, for review). While no significant RC star population is found in the Wd1 observations, H15 found a large RC field population in NIR *HST* observations of the Arches cluster. These stars are associated with the Galactic Bulge and have a distance distribution that peaks close to the GC along this sight-line. Since the GC distance is known to 2% (Boehle et al. 2016), the normalization of the extinction law to these stars can be constrained to a much higher precision than is possible with Wd1.

RC stars are visible in the Arches field CMD as a high-density "bar" (Figure 3.7). To identify the RC stars we use the unsharp-masking technique described by De Marchi et al. (2016). This method increases the contrast of high-frequency features while reducing the contrast of low-frequency ones. First, we convert the F153M vs. F127M - F153M CMD into a Hess diagram (i.e., a 2D histogram of stellar density), treating the position of each star as a Gaussian probability distribution with

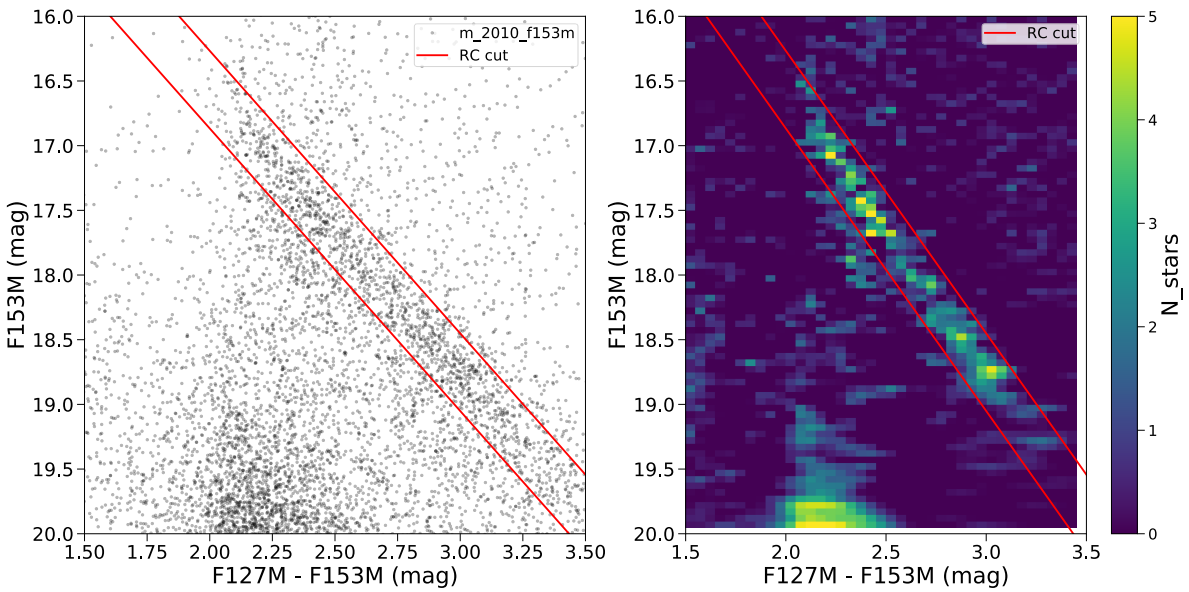

Figure 3.7 The selection criterion used to identify RC stars in the Arches cluster field. Following De Marchi et al. (2016), we convert the observed CMD (left) into a Hess diagram and perform unsharp-masking to identify the high-density ridge corresponding to the RC population. The resulting unsharp-masked density histogram is shown to the right. RC stars are identified as those falling within +/- 0.3 mags of a linear fit to the RC density histogram. This selection criterion is shown by the red lines.

a width corresponding to the photometric error. A bin size of 0.05 mags in both both color and mag space is used. Next, we create the unsharp mask by convolving the Hess diagram with a 2D Gaussian kernel having a width of 0.2 mags. The mask is then subtracted from the original Hess diagram to create the unsharp-masked diagram. We calculate a linear fit to the high-density "ridge" created by the RC population and identify RC stars as those that fall within F153M +/- 0.3 mags of the best-fit line (Figure 3.7). A total of 1119 RC stars are identified in this manner.

Similar to the Wd1 sample, we adopt a series of cuts to ensure the quality of the RC sample for the extinction law analysis. We require each star to have a photometric error less than 0.05 mag in both filters and perform a 3σ iterative outlier rejection in the CMD. The final RC sample contains 819 stars with typical photometric uncertainties of 0.015 mags.

The expected distance distribution of the sample is calculated using the RC density profiles of Wegg & Gerhard (2013), which are measured for the major, intermediate, and minor axes of the

Galactic bar. These profiles are rotated by 28° (the measured angle of the Galactic bar relative to the GC; Wegg & Gerhard 2013) to determine the density profile of the Arches LOS. The expected number of RC stars is then calculated as a function of distance by multiplying the solid angular area of the observations by the LOS density profile. The resulting distribution is nearly Gaussian with a peak at 96 pc beyond the GC and a width of 630 pc (Figure 3.8). The peak in the observed counts is not centered at the GC due to the increase in projected field area with LOS distance.

The RC star distance distribution is robust against uncertainties in the Galactic bar rotation angle (α) and the RC density profiles. Varying α between 25° – 33° (the possible range reported by Wegg & Gerhard 2013 and Wegg et al. 2015) only shifts the peak of the distribution by 12 pc. Redrawing the RC density profiles of Wegg & Gerhard (2013) while applying the reported uncertainty of 10% on each measurement results in a typical shift in the distribution of just ±20 pc. Both sources of error are well within the uncertainty in the GC distance itself (140 pc) and are not considered in the analysis.

In the CMD, we expect the distribution of F153M residuals relative to the RC ridge to be driven by the variation in stellar distance across the population. To test this, we compare the observed residuals to those calculated for a synthetic RC population created with the predicted distance distribution in Figure 3.8. Details on how the synthetic population is created is provided in Appendix 3.8. The observed F153M residual distribution is wider than the residual distribution for the synthetic data by ∼0.03 mag (Figure 3.9). This indicates that either the RC distance distribution is slightly wider than expected or that there is an additional source of magnitude dispersion among the RC stars. Given that the synthetic RC population assumes a single age and metallicity, it is likely that variations in stellar age or metallicity within the bulge are also impacting the observed F153M residual distribution (e.g. Salaris & Girardi 2002; Chen et al. 2017).

3.3.4 Extinction Law Fitter

Extinction Law Model and Priors

To construct the extinction law, we define A_λ / A_{Ks} at 5 specific wavelengths and use a cubic B-spline to interpolate the law across all wavelengths. The extinction law is thus a continuous function that can be adjusted by changing the A_λ / A_{Ks} values at the wavelength points, which

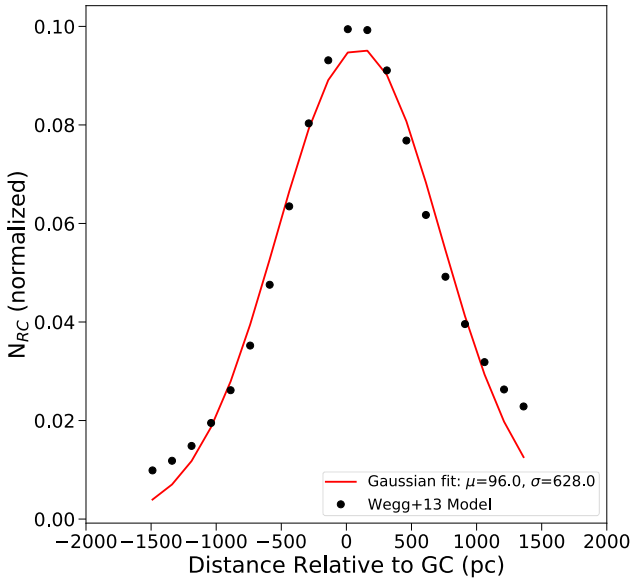

Figure 3.8 The expected distribution of RC stars as a function of distance in the Arches field based on RC density curves of Wegg & Gerhard (2013). The distribution (black points) is approximated by a Gaussian (red line) centered 96 pc beyond the GC itself with a width of 630 pc.

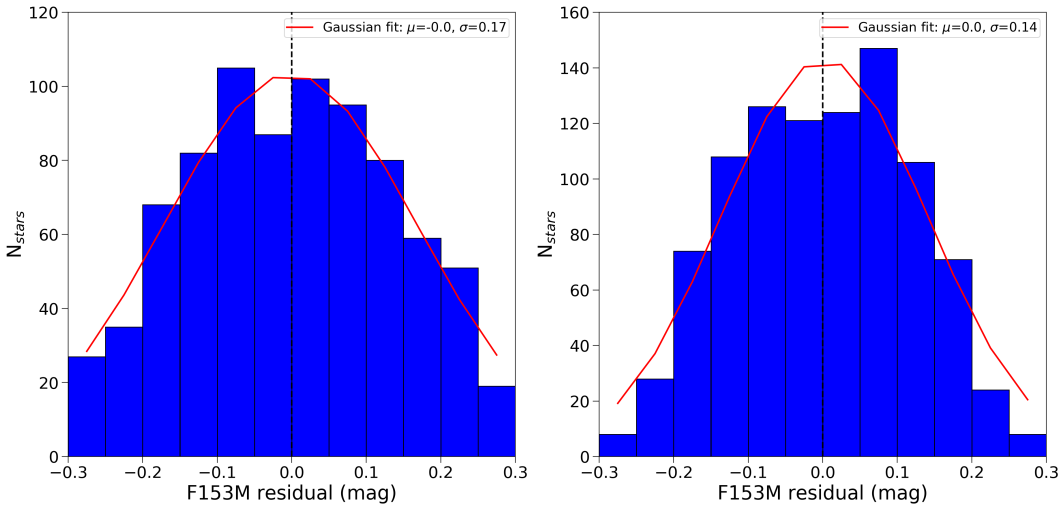

Figure 3.9 The distribution of F153M residuals in CMD space for the observations (left) and synthetic RC stars with $\sigma_d = 630$ pc (right). The observed distribution is wider, likely caused by intrinsic magnitude variations within the observed RC population due to differences in stellar age and/or metallicity.

are free parameters in our model. There are 10 additional free parameters in the model: 4 for the global Wd1 and RC population parameters (Wd1 total extinction A_{Ks}; Wd1 distance d_{wd1}; average RC distance d_{rc}; Gaussian width of F153M residuals around the reddening vector σ_{rc}), and 6 for systematic offsets in the photometric zeropoints of the filters (ΔZP_{λ}). The parameters and adopted priors are discussed below and summarized in Table 3.3.

In the extinction law, a wavelength point is assigned to the pivot wavelength (Tokunaga & Vacca 2005) of each Wd1 filter (F814W, F125W, and F160W). The A_{λ} / A_{Ks} values at these points are given uniform priors. Two additional wavelength points are added for the SST/IRAC [3.6] and PanSTARRS y filters, though no observations at these wavelengths are used. Our analysis revealed that the y-band point is required to capture the needed curvature in the extinction law between the F125W and F814W filters (§3.5.3). We adopt a uniform prior for A_{λ} / A_{Ks} at this point, as well. The [3.6] point is included to enforce reasonable behavior through the red-edge of the extinction law. We adopt a gaussian prior using the value of Nishiyama et al. (2009) with a conservative uncertainty of 10% ($A_{3.5}$ / $A_{Ks} = 0.5 \pm 0.05$). The cubic B-spline interpolation is calculated using the *scipy.interpolate.splrep* function in python between 0.8 μm – 2.2 μm. The exact function call is provided in the stand-alone python code referenced in §3.4.3. This is converted into a *pysynphot* custom reddening law for the synthetic photometry. Since each A_{λ} / A_{Ks} point is allowed to vary independently, no assumption regarding the functional form of the extinction law is made.

For the global Wd1 population parameters, we adopt a uniform prior for A_{Ks} and a Gaussian prior of 3900 $\pm$ 700 pc for d_{wd1}. The distance constraint is derived from the kinematics of HI gas associated with the cluster (Kothes & Dougherty 2007). Though additional distance measurements exist from an eclipsing binary analysis (Koumpia & Bonanos 2012), spectrally-typed evolved stars (e.g. Negueruela et al. 2010), and CMD fitting of pre-MS stars (e.g. Andersen et al. 2017), these analyses must correct for extinction and thus depend on the extinction law.

For the RC stars, we adopt a Gaussian prior of 7960 $\pm$ 140 pc for d_{rc}. This is 100 pc beyond the GC distance measurement of Boehle et al. (2016), matching the predicted average population distance in §3.3.3. For σ_{rc}, we adopt a prior of 0.17 $\pm$ 0.01 mags, corresponding to the measured width found in Figure 3.9.

The zeropoint offsets are included in the model since errors in the zeropoints would propagate through the analysis as a systematic error rather than as a random one. The offsets are assigned

Table 3.3. Model Parameters and Priors

Parameter[a]	λ[b](μm)	Prior[c]	Units	Prior Reference
A_{F814W} / A_{K_s}	0.806	U(4, 14)	—	—
A_y / A_{K_s}	0.962	U(4, 14)	—	—
A_{F125W} / A_{K_s}	1.25	U(1, 6)	—	—
A_{F160W} / A_{K_s}	1.53	U(1, 6)	—	—
$A_{[3.6]}$ / A_{K_s}	3.545	G(0.5, 0.05)	—	Nishiyama et al. (2009)
A_{K_s}	2.14	U(0.3, 1.3)	mag	—
d_{wd1}	—	G(3900, 700)	pc	Kothes & Dougherty (2007)
d_{rc}	—	G(7960, 140)	pc	Boehle et al. (2016), §3.3.3
σ_{rc}	—	G(0.17, 0.01)	mag	§3.3.3
ΔZP_{Ks}	—	G(0, 0.012)	mag	§3.2.2
ΔZP_{F160W}	—	G(0, 0.01)	mag	§3.2.1
ΔZP_{F153M}	—	G(0, 0.01)	mag	§3.2.1
ΔZP_{F127M}	—	G(0, 0.01)	mag	§3.2.1
ΔZP_{F125W}	—	G(0, 0.01)	mag	§3.2.1
ΔZP_{F814W}	—	G(0, 0.01)	mag	§3.2.1

[a] A_λ / A_{Ks}: extinction law in filter; A_{Ks}: total extinction of Wd1; d_{wd1}: distance to Wd1; d_{rc}: average RC star distance; σ_{rc}: gaussian width of the RC F153M residuals around the reddening vector; ΔZP_λ: zeropoint offset in filter

[b] HST + PanSTARRS filters: Pivot wavelengths of filter; IRAC [3.6] filter: isophotal wavelength from Nishiyama et al. (2009)

[c] Uniform distributions: U(min, max), where min and max are bounds of the distribution; Gaussian distributions: G(μ, σ), where μ is the mean and σ is the standard deviation

Gaussian priors centered at zero with a width corresponding to the uncertainty in the zeropoint derivation in §3.2.1.

Wd1 Star Likelihood

For the Wd1 component of the likelihood, the observed sample is compared to the theoretical isochrone produced by the model in terms of the F160W magnitude and F160W - F814W, F160W - F125W, and F160W - K_s colors. The full sample is used for the *HST* colors and the *HST*-*VISTA* subsample is used for F160W - K_s. Since a smaller number of stars have *VISTA* photometry, the *HST* colors have larger weight in the extinction law fit. However, this is desirable as the K_s observations have larger scatter than the *HST* observations.

Initially, the observed photometric errors are smaller than the magnitude sampling of the isochrone. We address this by performing a cubic spline interpolation of the isochrone magnitudes as a function of stellar luminosity and resample in steps of $2.5\text{x}10^{-3}$ in log luminosity. This results

in a magnitude spacing of 3.7x10^{-3} mags on the isochrone, which is more than 2 times smaller than the typical magnitude error (0.01 mag). However, there are a handful of stars with mag errors below this threshold. Since finer isochrone sampling significantly increases the computation time of the analysis, we instead add an error floor of 3.7x10^{-3} mags in quadrature to the observations to avoid this problem.

A single isochrone is insufficient to reproduce the data due to the differential extinction (dA$_{K_s}$) in the field. Instead, we generate a grid of isochrones with a range of extinction values ± 0.6 mags from the input A$_{K_s}$ in steps of 5x10^{-4} mags. This ensures that the color sampling between isochrones is at least 2 times smaller than the photometric uncertainty for each color in the model.

For each observed Wd1 MS star, we identify the nearest-neighbor synthetic star in the multi-dimensional magnitude-color space described above. We define the set of observed magnitudes and colors as $\boldsymbol{m}$ and their associated errors $\boldsymbol{\sigma}$. The likelihood is:

$$\mathcal{L}_{Wd1}(\boldsymbol{m}, \boldsymbol{\sigma}) = \prod_{j=1}^{4} \mathcal{L}_j(\boldsymbol{m_j}, \boldsymbol{\sigma_j}) \tag{3.2}$$

where $\boldsymbol{m_j}$ and $\boldsymbol{\sigma_j}$ are the measurements and errors in the jth dimension, with the dimensions corresponding to F160W, F160W - F814W, F160W - F125W, and F160W - K$_s$. For each observed star, the nearest neighbor synthetic star across all dimensions is found. The likelihood for each dimension is then calculated by comparing the observed sample to their corresponding nearest neighbors:

$$\mathcal{L}_j(\boldsymbol{m_j}, \boldsymbol{\sigma_j}) = \prod_{i=0}^{N_{s,j}} \frac{1}{\sigma_{j,i}\sqrt{2\pi}} e^{\frac{(m_{j,i} - NN_{mod}(m_{j,i}))^2}{2\sigma^2_{j,i}}} \tag{3.3}$$

where $N_{s,j}$ is the number of stars in the jth dimension, $m_{j,i}$ and $\sigma_{j,i}$ are the mag/color and corresponding error of the ith star in the jth dimension, and $NN_{mod}(m_{j,i})$ is the mag/color of the ith star's nearest neighbor synthetic star in the model. The full sample is used for the F160W, F160W - F814W, and F160W - F125W dimensions, while only the *HST-VISTA* subsample is used for the F160W - K$_s$ dimension.

RC Star Likelihood

We calculate the RC star likelihood component in a similar manner, comparing the observed sample to the reddening vector from the extinction law model in color-magnitude space (F153M and F127M - F153M). With $\boldsymbol{m_r}$ and $\boldsymbol{c_r}$ representing the set of F153M magnitudes and F127M - F153M colors with errors $\boldsymbol{\sigma_{m_r}}$ and $\boldsymbol{\sigma_{c_r}}$:

$$\mathcal{L}_{RC} = \mathcal{L}_{m_r}(\boldsymbol{m_r}, \boldsymbol{\sigma_{m_r}}, \sigma_{rc}) * \mathcal{L}_{c_r}(\boldsymbol{c_r}, \boldsymbol{\sigma_{c_r}}) \tag{3.4}$$

where σ_{RC} is the free parameter in the model corresponding to the Gaussian width of the F153M residuals around the reddening vector. Each component of the likelihood is defined as:

$$\mathcal{L}_{m_r}(\boldsymbol{m_r}, \boldsymbol{\sigma_{m_r}}, \sigma_{rc}) = \prod_{i=0}^{N_r} \frac{1}{\sqrt{\sigma^2_{m_r,i} + \sigma^2_{rc}}\sqrt{2\pi}} e^{\frac{(m_{m_r,i} - NN_{mod}(c_r,i))^2}{2(\sigma^2_{m_r,i} + \sigma^2_{rc})}} \tag{3.5}$$

$$\mathcal{L}_{c_r}(\boldsymbol{c_r}, \boldsymbol{\sigma_{c_r}}) = \prod_{i=0}^{N_r} \frac{1}{\sigma^2_{c_r,i}\sqrt{2\pi}} e^{\frac{(c_{r,i} - NN_{mod}(c_r))^2}{2\sigma^2_{c_r,i}}} \tag{3.6}$$

where $NN_{mod}(c_r, i)$ is the nearest neighbor model star in color space for the ith star and N_r is the total number of RC stars in the sample. Note that the nearest neighbor is only calculated for color space, due to the extra dispersion in the magnitudes as discussed in §3.3.3. The extra dispersion is captured by the σ_{rc} parameter in the F153M dimension of the likelihood, which manifests as an extra error term in addition to the photometric errors. Since the dispersion is primarily driven by individual RC distance variation, it is not included in the color likelihood term.

Final Likelihood

The final likelihood combines the Wd1 and RC likelihood components. For each to have an equal weight we must account for the fact that the RC sample is significantly larger than the Wd1 sample, which causes $\mathcal{L}_{rc} > \mathcal{L}_{wd1}$ regardless of the quality of the fit. After converting to log-likelihood, we scale the RC likelihood component to the same number of stars as the Wd1 sample (N_{wd1}):

$$\log \mathcal{L}_{tot} = \log \mathcal{L}_{wd1} + \log \mathcal{L}_r * \frac{N_{wd1}}{N_{rc}} \tag{3.7}$$

With the likelihood function defined, we determine the best-fit extinction law model using Bayes' Theorem:

$$P(\boldsymbol{M}|\Theta) = \frac{\mathcal{L}_{tot} * P(\boldsymbol{M})}{P(\Theta)} \tag{3.8}$$

where $\boldsymbol{M}$ is the model with the set of free parameters $[\boldsymbol{A_\lambda/A_{Ks}}, \boldsymbol{\Delta ZP}, A_{Ks}, d_{wd1}, d_{rc}, \sigma_{rc}]$(with $\boldsymbol{A_\lambda/A_{Ks}}, \boldsymbol{\Delta ZP}$ representing the set values at 5 and 6 different wavelengths, respectively) and $\Theta = [\boldsymbol{m}, \boldsymbol{\sigma}, \boldsymbol{m_r}, \boldsymbol{\sigma_r}, \boldsymbol{c_r}, \boldsymbol{\sigma_{c_r}}]$ is the set of observations. $P(\boldsymbol{M}|\boldsymbol{\Theta})$ is the posterior probability of the model given the data, and P($\boldsymbol{M}$) is the prior probability on $\boldsymbol{M}$.

The posterior probability distributions are calculated using *Multinest*, a nested sampling algorithm shown to be more efficient than Markov Chain Monte Carlo algorithms in complex parameter spaces with multiple modes or pronounced degeneracies (Feroz & Hobson 2008; Feroz et al. 2009). This iterative technique calculates the posterior probability at a fixed number of points in the parameter space and identifies possible peaks, restricting subsequent sampling to the regions around these peaks until the change in evidence drops below a user-defined tolerance level. An evidence tolerance of 0.5 and sampling efficiency of 0.8 are adopted for 400 active points. To run the sampler we use *Pymultinest*, a convenient wrapper module in python (Buchner et al. 2014).

Testing the Analysis

To test the performance of the extinction law fitter, we simulate a set of Wd1 MS and Arches RC star observations with known extinction properties and run it through the analysis. A detailed description of the process used to generate the simulated data and the subsequent results are provided in Appendix 3.8. In summary, a large degeneracy between d_{wd1}, A_{Ks}, and the extinction law is obtained when the analysis is limited to the Wd1 MS stars, due to the uncertainty in the extinction law normalization. However, when the Wd1 and RC samples are combined, the fitter successfully recovers all of the model parameters to within 1σ. The fitter is also able to extract the correct extinction law when just the RC star sample is used. These tests validate our methodology.

3.4 Results

We present three fits of the extinction law: one using only the Wd1 MS sample (§3.4.1), one using only the Arches RC sample (§3.4.2), and one using the combined Wd1 and RC samples (§3.4.3). The Wd1-only fit constrains the shape of the extinction law, leveraging the large wavelength coverage of the observations. The RC-only fit constrains A_{F125W} / A_{F160W}, which defines the normalization. The Wd1 + RC fit combines the strengths of both data sets to produce the final extinction law.

To quantify the extinction law shape we introduce the parameter $\mathcal{S}_{1/\lambda}$, which is the ratio of the derivative of the B-spline interpolated extinction law with respect to $1/\lambda$ to the derivative of the law with respect to $1/2.14$ μm:

$$S_{1/\lambda} = \frac{\frac{\partial(A_\lambda/A_{Ks})}{\partial(1/\lambda)}}{\frac{\partial(A_\lambda/A_{Ks})}{\partial(1/\lambda)}|_{\lambda=2.14\mu m}} \tag{3.9}$$

The advantage of this quantity over a color excess ratio is that it is continuous as a function of wavelength (as the derivative of a cubic B-spline must be continuous if the knots are distinct; de Boor 1978), making it easier to compare extinction laws measured in different filters. Further discussion of $\mathcal{S}_{1/\lambda}$ and its relationship to the color excess ratio can be found in Appendix 3.7. A summary of the results are presented in Table 3.4 and selected posterior distributions are shown in Appendix 4.9. Unless otherwise specified, we report two errors for the parameters in the text below, the first being the statistical error and the second being the systematic error.

Table 3.4. Extinction Law Results

Parameter	This study[a]				Literature[b]					
	Wd1 only	RC only	Wd1 + RC	σ_{sys}[c]	C89	D16	N09	F09	$S16_1$	$S16_2$
A_{Ks} (mag)	0.78 ± 0.16	—	0.611 ± 0.024	0.02	—	0.74 ± 0.08	0.87 ± 0.01[d]	—	—	—
d_{wd1} (pc)	4428 ± 309	—	4780 ± 76	48	—	—	—	—	—	—
d_{rc} (pc)	—	7938 ± 78	7926 ± 87	68	—	—	—	—	—	—
σ_d (mag)	—	0.192 ± 0.004	0.187 ± 0.005	$1x10^{-4}$	—	—	—	—	—	—
A_{F814W} / A_{Ks}	7.81 ± 1.5	—	9.66 ± 0.32	0.33	5.09	8.14	7.30	8.98	5.86	9.71
A_y / A_{Ks}	5.13 ± 0.91	—	6.29 ± 0.19	0.24	3.72	5.87	5.05	6.31	4.16	6.71
A_{F125W} / A_{Ks}	3.01 ± 0.43	—	3.56 ± 0.10	0.11	2.44	3.42	2.93	3.57	2.56	3.81
A_{F160W} / A_{Ks}	2.05 ± 0.23	—	2.33 ± 0.06	0.04	1.76	2.17	1.95	2.24	1.75	2.39
$A_{[3.6]}$ / A_{Ks}	0.50 ± 0.03	—	0.50 ± 0.03	0.002	—	0.36	0.50	—	0.54	0.18
A_{F125W} / A_{F160W}	1.468 ± 0.047	1.527 ± 0.006	1.525 ± 0.004	0.01	1.385	1.576	1.498	1.595	1.459	1.616
ΔZP_{Ks} (mag)	0.0024 ± 0.008	—	0.0025 ± 0.008	0.00014	—	—	—	—	—	—
ΔZP_{F160W} (mag)	-0.0037 ± 0.006	—	-0.005 ± 0.006	0.0024	—	—	—	—	—	—
ΔZP_{F153M} (mag)	—	0.0013 ± 0.007	0.002 ± 0.006	0.0057	—	—	—	—	—	—
ΔZP_{F127M} (mag)	—	-0.0011 ± 0.007	-0.0012 ± 0.007	0.0031	—	—	—	—	—	—
ΔZP_{F125W} (mag)	0.0016 ± 0.006	—	0.0022 ± 0.006	0.0014	—	—	—	—	—	—
ΔZP_{F1814W} (mag)	0.0001 ± 0.0047	—	0.000 ± 0.007	0.00042	—	—	—	—	—	—
$\mathcal{S}_{1/0.806\mu m}$	3.49 ± 0.26	—	3.50 ± 0.28	0.18	15.79	16.52	20.14	18.58	19.48	19.48
$\mathcal{S}_{1/0.962\mu m}$	2.82 ± 0.16	—	2.84 ± 0.16	0.12	8.03	10.95	11.67	11.96	13.52	13.52
$\mathcal{S}_{1/1.25\mu m}$	1.64 ± 0.09	—	1.66 ± 0.08	0.04	4.06	5.52	5.00	5.66	5.65	5.65

Table 3.4—Continued

Parameter	This study[a]				Literature[b]					
	Wd1 only	RC only	Wd1 + RC	σ_{sys}[c]	C89	D16	N09	F09	$S16_1$	$S16_2$
$\mathcal{S}_{1/1.53\mu m}$	1.54 ± 0.10	—	1.56 ± 0.10	0.07	2.39	3.04	2.73	3.01	3.40	3.40
$\mathcal{S}_{1/2.14\mu m}$	1.0	—	1.0	0	1.0	1.0	1.0	1.0	1.0	1.0

[a]Assuming a Wd1 cluster age of 5 Myr

[b]C89: Cardelli et al. (1989); D16: Damineli et al. (2016); N09: Nishiyama et al. (2009); F09: Fitzpatrick & Massa (2009), with α=2.5; $S16_1$: Schlafly et al. (2016), rhk = 1.55; $S16_2$: Schlafly et al. (2016), rhk = 2.0

[c]Systematic error, see §3.5.4

[d]From Andersen et al. (2017) using N09 law

3.4.1 Wd1 MS Only

To fit the Wd1 MS sample, we set $\mathcal{L}_{tot} = \mathcal{L}_{wd1}$ in Equation 3.8 and do not consider the model parameters related to the RC stars (d_{rc}, σ_{rc}, ZP_{F127M}, and ZP_{F153M}). A cluster age of 5 Myr is assumed. As with the simulated cluster tests in Appendix 3.8, a large degeneracy is found between d_{wd1}, A_{K_s} and the extinction law due to the uncertainty in the normalization, though the shape of the law is well constrained (Figure 3.10). d_{wd1} is constrained to 4428 ± 309 ± 48 pc, consistent with the result from (Kothes & Dougherty 2007), and A_{K_s} is found to be 0.78 ± 0.16 ± 0.02 mag, also broadly consistent with the literature. No statistically significant zeropoint offsets are obtained for any of the filters, indicating that the zeropoints presented in in Figure 3.3 are accurate to 0.006 mag for the *HST* filters and 0.008 mag for the *VISTA* K_s filter. The extinction law provides a good fit to the observations, with reduced chi-square (χ^2_{red}) values of 0.38 for the *HST* CCD and 0.77 for the *HST*-*VISTA* CCD (Figure 3.11). That the χ^2_{red} values are less than 1.0 suggests that the photometric errors are conservative.

The shape of the extinction law is inconsistent with a single power law, which would produce a straight line in $S_{1/\lambda}$ vs. $\log(1/\lambda)$ plot in Figure 3.10. We will examine this further in the final extinction law fit (§3.4.3).

We test the impact of assuming an age for Wd1 by performing identical analyses with cluster ages of 4 Myr and 6 Myr, the range of possible ages suggested by the evolved star population (Crowther et al. 2006; Negueruela et al. 2010). Since the stellar mass of the pre-MS bridge decreases with age, changing the age affects the mass range of the MS sample. Using the selection criteria described in §3.3.1, the MS mass range becomes 4.83 $M_\odot$ – 16.0 $M_\odot$ for a 4 Myr cluster and 3.95 $M_\odot$ – 12.50 $M_\odot$ for a 6 Myr cluster. This affects the normalization of the extinction law, with the law generally becoming steeper (i.e., larger A_λ / A_{Ks} values) with increasing age, but the shape of the law remains almost identical (Figure 3.12).

3.4.2 Arches RC stars only

Since the distance distribution of the Arches RC population is known to significantly higher precision than Wd1, the normalization of the extinction law can be much better constrained. We perform an extinction law fit using just the RC sample, setting $\mathcal{L}_{tot} = \mathcal{L}_{rc}$ in Equation 3.8

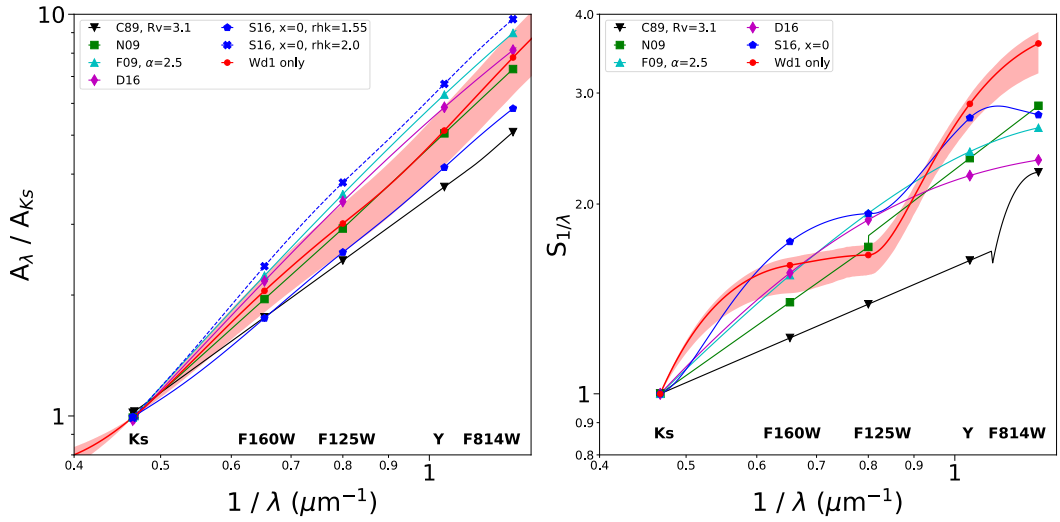

Figure 3.10 Extinction law fit to the Wd1-only sample, with the extinction law to the left and the shape of the law (in terms of $\mathcal{S}_{1/\lambda}$, see Equation 3.9) to the right. The best-fit model is represented by the solid red line, with the 1σ statistical errors represented by the red shaded region. Several extinction laws from the literature are included for comparison: Cardelli et al. (1989, C89), Nishiyama et al. (2009, N09), Damineli et al. (2016, D16), Schlafly et al. (2016, S16) and De Marchi et al. (2016, DM16). A cluster age of 5 Myr is assumed.

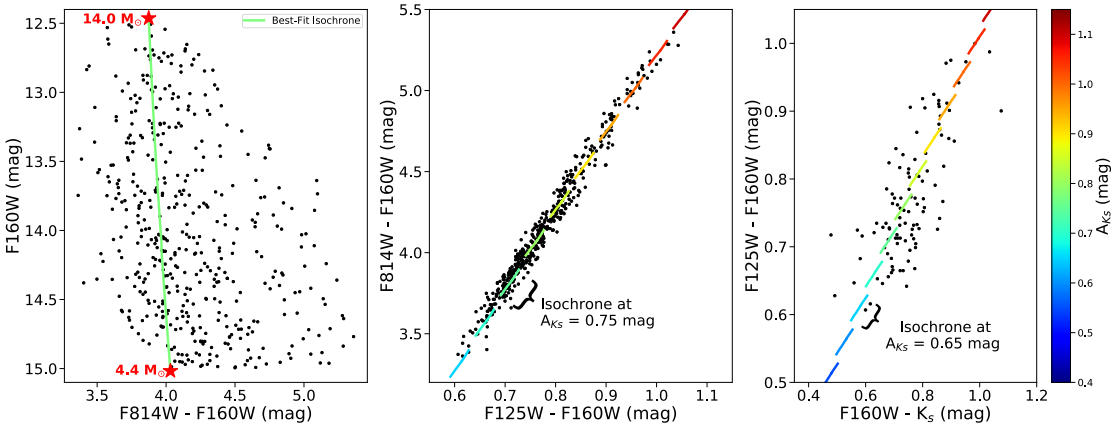

Figure 3.11 A comparison between the model isochrones and the observed Wd1 sample for the best-fit extinction law in the Wd1-only analysis. In each plot, the observed sample is shown by the black points and the model isochrones are shown as lines with a color corresponding to their total extinction. The left plot shows the best-fit isochrone in the CMD ($A_{Ks} = 0.78$ mag) with the highest and lowest masses labeled by red stars. The middle and right plot show individual isochrones at different total extinctions in the *HST* and *HST*-*VISTA* 2CD, respectively. These isochrones trace the reddening vector of the population.

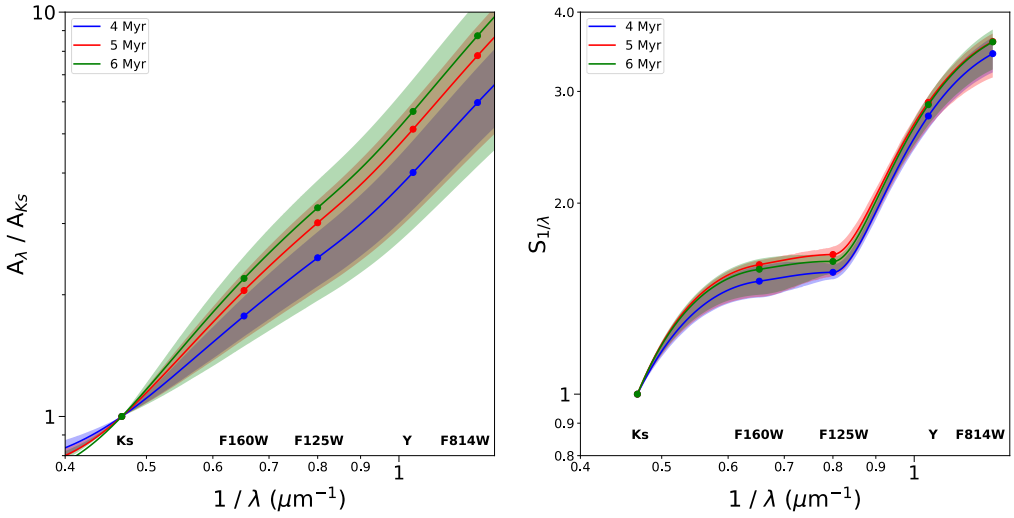

Figure 3.12 Extinction law fits to the Wd1 sample assuming cluster ages of 4 Myr (blue), 5 Myr (red), and 6 Myr (green). The best-fit model is represented by the solid lines, with the 1σ statistical limits represented by the shaded regions. While the extinction law degeneracy increases when different ages are considered (left plot), the extinction law shape is effectively unchanged (right plot).

and removing the free parameters related to Wd1 (i.e. d_{wd1}, A_{K_s}). Only the extinction law ratios A_{F125W} / A_{K_s} and A_{F160W} / A_{K_s} are included in the model, approximately matching the wavelengths of the F127M and F153M observations. We present the ratio A_{F125W} / A_{F160W}, which combines the information from both filters.

The best-fit recovers A_{F125W} / A_{F160W} = 1.527 ± 0.006 ± 0.01 and d_{rc} = 7938 ± 87 ± 68 pc. The statistical uncertainty in A_{F125W} / A_{F160W} is a factor of ∼8 smaller than the value obtained for the Wd1-only fit (1.468 ± 0.047 ± 0.01), eliminating much of the uncertainty in the normalization. Statistically, d_{rc} is constrained to ∼1.1%, which is better than the input prior and in principle places a constraint on the GC distance. However, we have adopted a simplified description of the RC (assuming an average age and metallicity for the population) and are susceptible to possible systematic uncertainties in the RC star model (§3.5.4). A careful analysis of the GC distance is beyond the scope of this paper.

3.4.3 Wd1 MS and Arches RC Combined Fit

The final extinction law derived using the combined Wd1 MS + Arches RC sample is shown in Figure 3.13. Once again, a Wd1 age of 5 Myr is assumed. The law is well constrained with combined uncertainties (statistical and systematic added in quadrature) better than ∼5% in A_λ / A_{K_s} and ∼10% in $\mathcal{S}_{1/\lambda}$ (Table 3.4). There is no significant change in the shape of the law relative to the Wd1-only fit, which supports the assumption that the shape is the same for both populations. Fitting a power law to the A_λ /A_{Ks} values results in a reduced chi-squared (χ^2_{red}) value of 3.7, indicating that the difference between the best-fit law and a power law are statistically significant (Figure 3.14). This is in agreement with previous studies of the OIR extinction law (e.g. Fitzpatrick & Massa 2009). Interestingly, we find that the NIR portion of the law (K_s, F160W, F125W) is also statistically inconsistent with a power law with $\chi^2_{red} = 3.3$, in contrast to what is often assumed in the literature. We only consider the statistical errors on A_λ / A_{Ks} in the χ^2_{red} calculations. Extinction law analyses with various systematics applied (§3.5.4) also show statistically significant deviations from a power law, and so the systematics do not affect this conclusion. A stand-alone python code to calculate the Wd1+RC extinction law at all wavelengths between 0.8 μm – 2.2 μm is available online[3].

A comparison of the best-fit model and Wd1 and Arches RC observations is shown in Figure 3.15. The law is able to reproduce the photometry of both populations well, with χ^2_{red} values for the Wd1 CCDs are nearly identical to the Wd1-only fit (0.38 and 0.77, respectively) and $\chi^2_{red} =$ 0.83 for the RC CMD.

Repeated analyses of the extinction law assuming Wd1 ages of 4 Myr, 6 Myr, and 7 Myr show that the extinction law is not impacted by changing the cluster age. However, d_{wd1} is found to systematically decrease with increasing cluster age. We explore this trend further in §3.4.4.

3.4.4 The Age and Distance of Wd1

To demonstrate of the impact of the extinction law, we show how the new extinction law changes the distance and age of the cluster. In the Wd1+RC extinction law fit, d_{wd1} varies from 5222 ± 113 pc for a Wd1 age of 4 Myr to 4133 ± 66 pc for a Wd1 age of 7 Myr (statistical and systematic

[3]https://doi.org/10.5281/zenodo.1063708

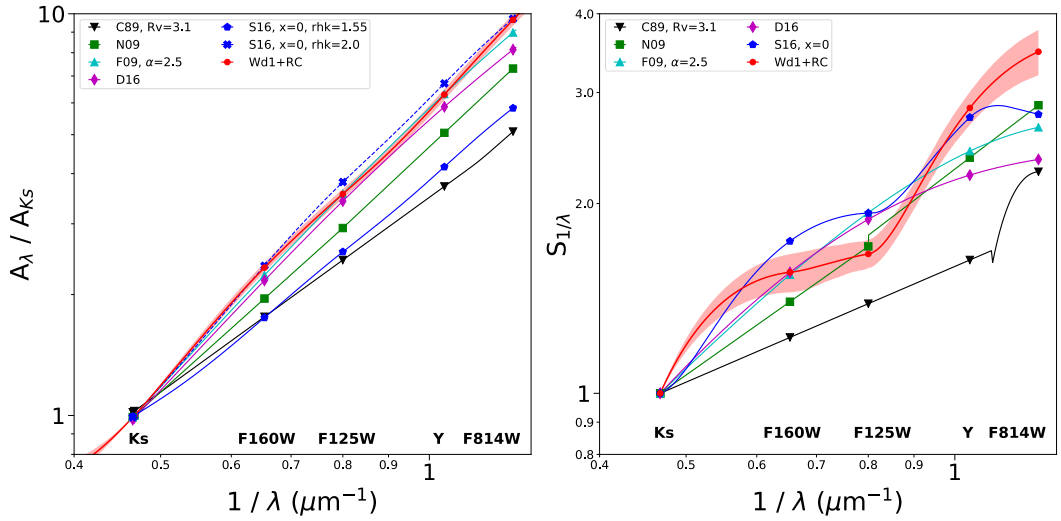

Figure 3.13 Extinction law fit to the Wd1+RC sample, with the extinction law to the left and the shape of the law (in terms of $\mathcal{S}_{1/\lambda}$) to the right. The best-fit model is represented by the solid red line, with the 1σ errors represented by the red shaded region. The observed law is inconsistent with a power law (which would appear as a straight line in both plots) and is most similar to the F09 law (with $\alpha = 2.5$) and S16 law (with rhk = 2.0) from the literature. A Wd1 age of 5 Myr is assumed, though this assumption has no significant effect on either the law or $S_{1/\lambda}$.

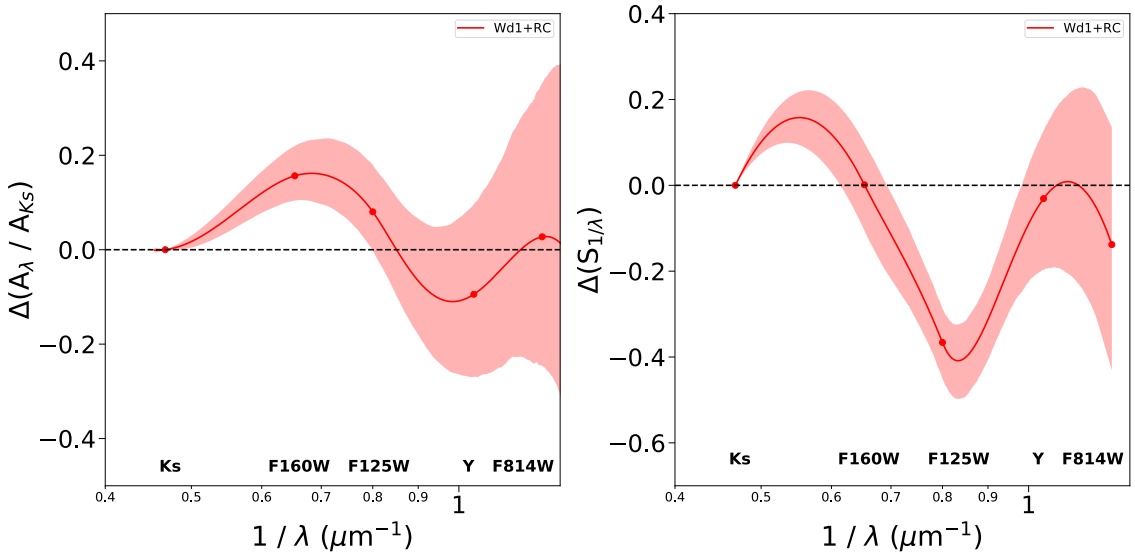

Figure 3.14 The deviation of the Wd1+RC extinction law from a power law, both in terms of A_λ / A_{Ks} (left) and $S_{1/\lambda}$ (right). The residuals between the best-fit law and a power law are shown by the red points and lines, while the uncertainties are represented by the red shaded regions. The Wd1+RC extinction law is statistically inconsistent with a power law, even in the NIR.

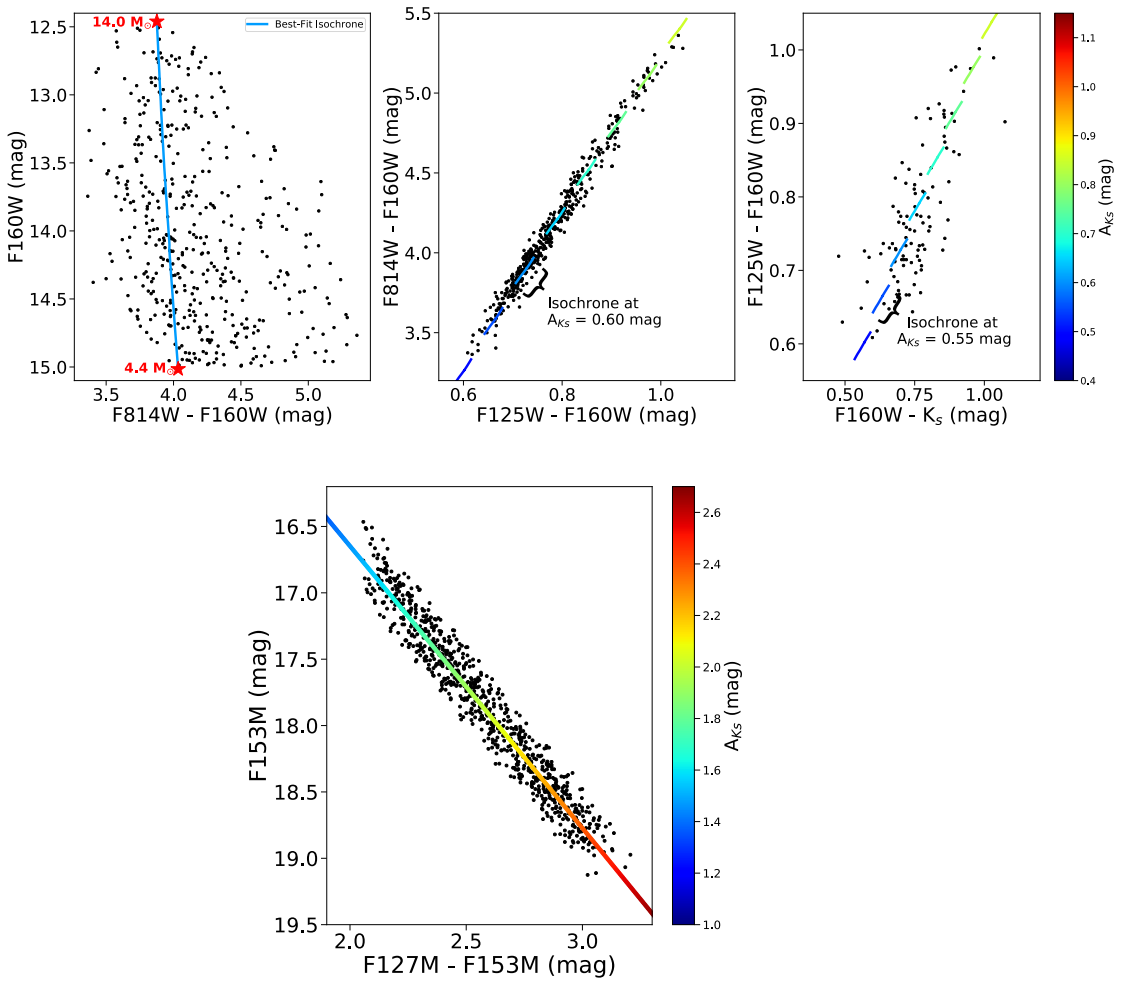

Figure 3.15 A comparison between the model isochrones and the data for the best-fit extinction law in the Wd1+RC analysis. *Top:* The Wd1 sample and cluster isochrones plotted in CMD space (left) and the *HST* and *HST* - *VISTA* 2CD (middle and right, respectively), using the same conventions as Figure 3.11. *Bottom:* The Arches RC stars (black points) compared to the best-fit reddening vector (colored line, where the color at each point corresponds to the total extinction) in the CMD. The model provides a good match to the data for both the Wd1 and RC samples.

errors added in quadrature). Thus, an independent estimate of d_{wd1} offers a constraint on the cluster's age. This is especially valuable given the diverse population of evolved stars in Wd1, which include yellow hypergiants (Clark et al. 2005), red supergiants (Clark et al. 2010), WR stars (Crowther et al. 2006), luminous blue variables (Clark & Negueruela 2004; Dougherty et al. 2010), and a magnetar (Muno et al. 2006). The presence of these objects provides a strong test of stellar evolution models, which struggle to reproduce such a sizable population of cool supergiants and WR stars simultaneously (Clark et al. 2010; Ritchie et al. 2010).

We obtain an independent estimate of d_{wd1} from published measurements of W13, a 9.2 day eclipsing binary within the cluster (Bonanos 2007). Koumpia & Bonanos (2012, hereafter K12) combine the optical (VRI) lightcurves from Bonanos (2007) with multi-epoch spectroscopy to derive the physical properties of the system, found to be a near-contact binary composed of a B0.5Ia+/WNVL and O9.5-B0.5I star. From the derived effective temperatures and stellar radii, they calculate a total system luminosity of $\log L/L_{\odot} = 5.54 \pm 0.11$. K12 correct for extinction by adopting A_J / $A_{Ks} = 2.50 \pm 0.15$ (Indebetouw et al. 2005), ultimately reporting a distance of 3710 ± 550 pc. We redo this calculation using the Wd1+RC extinction law, which is steeper than the Indebetouw value (A_J / $A_{Ks} = 3.56 \pm 0.15$, with statistical and systematic errors added in quadrature). This does not bias the Wd1 distance calculation since the law is independent of cluster age and thus not tied to the value of d_{wd1} derived in the extinction law analysis.

Following K12, we calculate a distance to W13 using its 2MASS J-band apparent magnitude, a theoretical bolometric correction (BC_{λ}) for O9.5I stars, and an extinction correction based on the NIR colors of nearby WR stars. The 2MASS J-band magnitude is 9.051 ± 0.16 mags, with the uncertainty set by the depth of the primary eclipse since the phase of the measurement is unknown. From Martins & Plez (2006) we adopt BC_J = -3.24 ± 0.08 mags, with the uncertainty based on the scatter in the BC_{λ} - T_{eff} relation. The total extinction (A_{Ks}) of W13 is calculated from the J - K color excesses of the Wolf-Rayet stars "R" and "U" reported in Crowther et al. (2006), both of which are ∼6" away from W13. Using our extinction law, these stars have $A_{Ks} = 0.55 \pm 0.05$ mags and 0.52 ± 0.05 mags, respectively, and so we adopt $A_{Ks} = 0.535 \pm 0.035$ mag for W13.

With all the pieces in place, we can calculate a distance to W13:

$$\mu = m_J - M_J - A_J \tag{3.10}$$

where μ is the distance modulus, m_J is the 2MASS J-band apparent magnitude, A_J is the total extinction at J-band, and M_J is the J-band absolute magnitude. The J-band absolute magnitude is calculated from the luminosity using the bolometric correction:

$$M_J = M_{\odot}^{bol} - BC_J - 2.5 \log \left(\frac{L}{L_{\odot}} \right) \tag{3.11}$$

where $M_{\odot}^{bol} = 4.75$ is the bolometric magnitude of the sun and $L_{\odot}$ is the solar luminosity. Plugging in the values and propagating the errors, we find $\mu = 12.958 \pm 0.235$ mag, or 3905 ± 422 pc. The major source of remaining uncertainty is the 2MASS photometry, since the phase of the system was unknown at the time of measurement. New multi-epoch OIR photometry of W13 would dramatically increase the precision of the derived distance. Unfortunately W13 is saturated in the *HST* observations and so our observations are not helpful in this regard.

A comparison between the W13 distance and the d_{wd1} from the extinction law analysis is shown in Figure 3.16. The eclipsing binary distance is consistent with an older cluster age, being discrepant from the 4 Myr and 5 Myr extinction fit distances by 3.0σ and 2.0σ, respectively. The 6 Myr and 7 Myr distances are only discrepant by 1.2σ and 0.5σ, respectively. An older cluster age for Wd1 is not unreasonable, given that the constraint of 4 – 5 Myr from Crowther et al. (2006) is based stellar evolution models of the Wolf-Rayet star population, which are not yet well understood. Negueruela et al. (2010) find that the HR diagram of OB supergiants is consistent with a cluster age greater than 5 Myr, though this analysis relies on the Rieke & Lebofsky (1985) extinction law (A_J /A_{Ks} = 2.35). Unfortunately their observations are primarily shortward of I-band, and so we cannot recreate their HR diagram using our extinction law. We leave a detailed analysis of the age and distance of Wd1 to a future paper.

3.5 Discussion

3.5.1 Comparison with Previous Extinction Laws

We compare our result with several extinction laws in the literature. These include Cardelli et al. (1989, hereafter C89), assuming $R_V = 3.1$ as is often adopted for the interstellar medium (however, changing R_V has little effect on the extinction law in this wavelength range); Nishiyama et al.

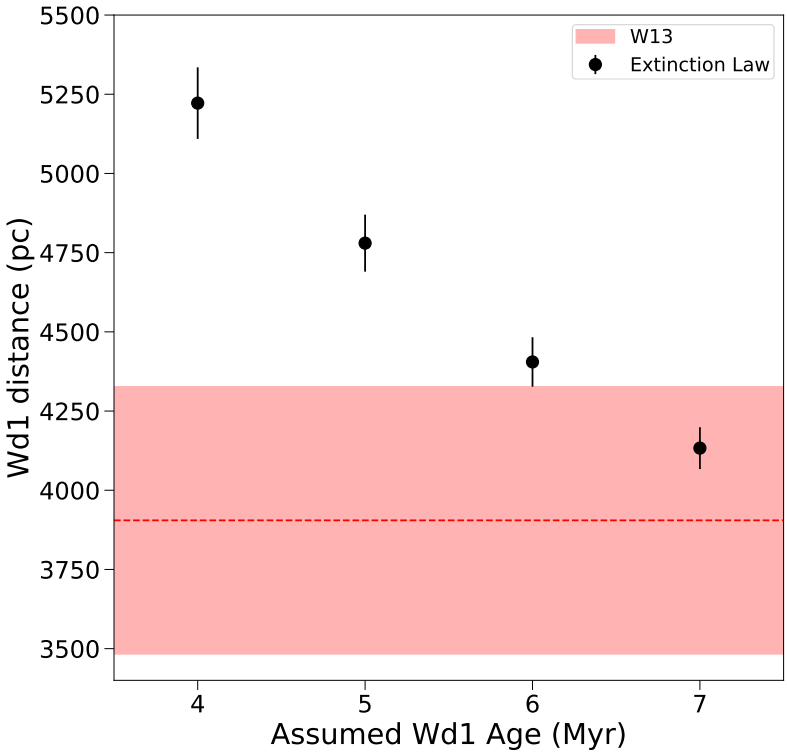

Figure 3.16 Wd1 distance as a function of the assumed cluster age in the Wd1+RC extinction law analysis. No other parameter shows statistically significant variations. The red dotted line shows the independent distance estimate from the eclipsing binary W13 using the best-fit law, with the 1σ error represented by the red shaded region. A cluster age of 6 – 7 Myr is favored over an age of 4 – 5 Myr.

(2009, hereafter N09), often used for the GC and Galactic bulge; Damineli et al. (2016, hereafter D16), derived specifically for Wd1; Fitzpatrick & Massa (2009, hereafter F09), assuming $\alpha = 2.5$ and $R_V = 3.1$; and Schlafly et al. (2016, hereafter S16), assuming A_H / A_{Ks} ("rhk") values of 1.55 (consistent with Indebetouw et al. 2005) and 2.0. To construct the C89, D16, and F09 laws we use the functional forms reported by the authors, and for S16 we use the python code referenced in their Appendix[4]. For N09 we adopt a power law with $\beta = 2.0$ between 1.25 μm – 2.14 μm and then use a linear interpolation in $\log(A_\lambda$ / $A_{Ks})$ vs. $\log(1$ / $\lambda)$ space to extend from A_J / A_{Ks} to the A_V / A_{Ks} value reported in Nishiyama et al. (2008). This method was adopted to have minimal impact on the shape of the N09 law shortward of J-band, where no functional form is provided.

Theoretical cluster isochrones using the published extinction laws are unable to reproduce the observed colors of the Wd1 MS (Figure 3.17). This is especially evident in the *HST* 2CD, where the model reddening vectors are offset between 0.29 mag – 0.72 mag to the blue in F814W - F125W (about 9% and 22%, respectively), and between 0.08 mag – 0.19 mag to the red in F125W - F160W (about 12% and 25%, respectively). These offsets are huge relative to the *HST* photometric errors, which is typically 0.02 mag for both colors. In the *HST*-*VISTA* 2CD, most literature extinction laws produce reddening vectors that are 0.07 mag – 0.10 mag too blue in F160W - K_s (about 12%), which is significant but not as large relative to the typical color uncertainty of ∼0.06 mags. The exception is C89, which reproduces the observed sequence in this 2CD well. These isochrones assume a cluster age of 5 Myr, though changing the age has little to no effect on the colors. Note that the discrepancies in color-color space are due to differences in the shape of the extinction law, rather than the normalization.

In Figures 3.10, 3.13 and Table 3.4 we compare our extinction law results to the published laws. The Wd1+RC extinction law is generally steep (i.e. has large A_λ / A_{Ks} values), being most similar to F09 law with $\alpha = 2.5$ and the S16 law with A_H / $A_{Ks} = 2.0$. Notably, we find A_{F125W} / A_{Ks} to be 18% larger and A_{F814W} / A_{Ks} to be 24% larger than the N09 law commonly used for the inner Milky Way. The shape of the law also differs from those in the literature, which is expected given the inability of the published laws to reproduce the observations in Figure 3.17. In particular, S_{F814W} / S_{Ks} is significantly larger than any of the published laws, indicating a steeper derivative

[4]http://faun.rc.fas.harvard.edu/eschlafly/apored/extcurve_s16.py

through the F814W filter relative to the K_s filter. However, our data calls for such steepness as discussed in §3.5.3.

Our extinction law differs from the one previously derived for Wd1 by D16, who describe the law as a power law with a slope $\beta = 2.13 \pm 0.08$ between 0.8 μm – 4.0 μm. Our Wd1+RC law is 4% larger at A_{F125W} / A_{Ks} and 16% larger at A_{F814W} / A_{Ks}. The D16 law is derived from ground-based photometry of 105 evolved stars and a sample of RC stars in the Wd1 field, using color excess ratios and requiring a power law functional form between the JHK$_s$ filters. We believe our study offers several key advantages: 1) space-based photometry with higher precision (∼0.01 mag) than is generally possible for ground-based observations; 2) a sample of kinematically-selected Wd1 members that is ∼4x larger than the D16 sample and is composed of main sequence stars, where stellar models are better understood relative to evolved stars; and 3) our forward-modeling technique makes no assumption regarding the functional form of the extinction law. However, D16 does have the advantage of using RC stars in the Wd1 field, while we rely on RC stars toward the Arches cluster. Unfortunately, the *HST* data does not stretch as far to the red as the D16 observations, and so we do not observe a significant RC population in the Wd1 field. That said, only our law is able to reproduce the observed MS colors of the cluster, indicating its effectiveness.

3.5.2 Extinction Law at the Galactic Center

Schödel et al. (2010, hereafter S10) measure the total extinction of the GC in the H and K$_s$ filters using observations of RC stars in the region. Adopting a K$_s$ absolute magnitude M_{Ks} = -1.54 mag (Groenewegen 2008), an intrinsic H - K$_s$ color (H - K$_s$)$_0$ = 0.07 mag, and a GC distance of 8.03 kpc, they calculate absolute extinction values of $A_H = 4.48 \pm 0.13$ mag and $A_{Ks} = 2.54 \pm 0.12$ mag. This results an extinction ratio A_H / $A_{Ks} = 1.76 \pm 0.18$, providing an independent test of the normalization of the extinction law.

We calculate A_H / A_{Ks} for the Wd1+RC extinction law as well as the N09 law, which is often adopted for the GC/Galactic Bulge. Calculating A_H and A_{Ks} at effective wavelengths of 1.677 μm and 2.168 μm, respectively, the Wd1+RC law produces A_H / $A_{Ks} = 1.936 \pm 0.08$ (statistical and systematic combined in quadrature). This is 10% higher than the S10 result but within 1σ given the uncertainties. The N09 law predicts a value of 1.68 ± 0.03, which is 5% lower than the S10 value (0.4σ difference). However, it is important to note that the A_H / A_{Ks} value in S10 and

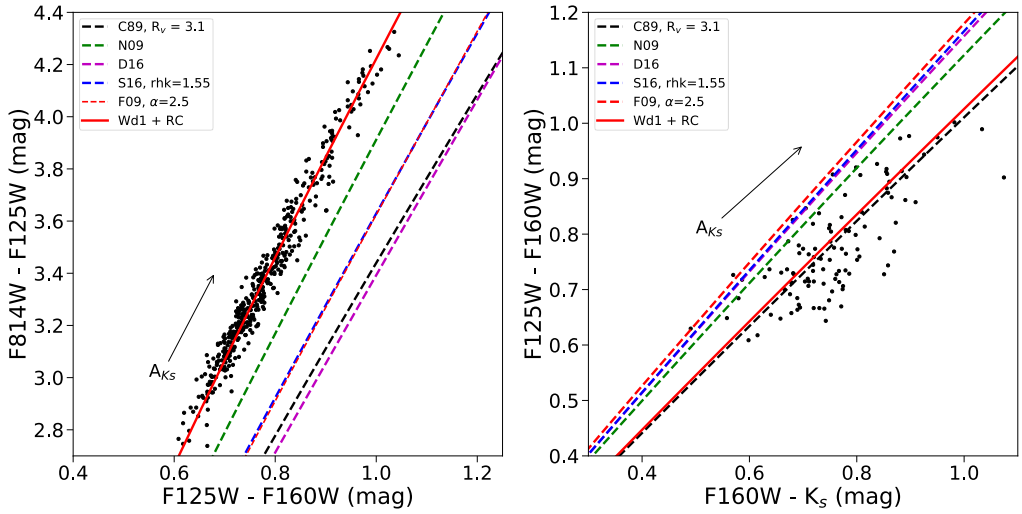

Figure 3.17 Color-color diagrams comparing the observed Wd1 MS to the reddening vectors predicted by Wd1 + RC extinction law (red solid line) and several extinction laws in the literature (dashed lines). The literature laws show significant differences between the reddening vector and observations, especially in the *HST* colors where the photometric errors are typically 0.02 mag. These discrepancies are caused by differences in the extinction law shape. Note that all reddening vectors trace back to the un-reddened main sequence (approximately at the origin of these plots), but diverge at the high extinction of Wd1 due to varying degrees of curvature in the vector.

the extinction laws from this work and N09 rely on knowing the absolute magnitude, colors, and distance of RC stars in the filters of interest. This can lead to systematic errors in the extinction law, as discussed in §3.5.4. We conclude that our law is in acceptable agreement with the S10 measurement.

The Wd1+RC law is also broadly consistent with the most recent measurement of the GC NIR extinction law, which reports a power law with $\beta = 2.31 \pm 0.03$ (Nogueras-Lara et al. 2017). A power-law fit to the NIR filters in our law results in $\beta = 2.38 \pm 0.15$. However, we reiterate our result in §3.4.3 that the Wd1+RC law is inconsistent with a power law in the NIR regime. Non-power law behavior is hinted in Nogueras-Lara et al. (2017) as small differences between power law exponents derived in the JH vs. HK_s filters, though they conclude a single power law is sufficient within the sensitivity of their study.

3.5.3 Curvature in the Reddening Vector

By forward modeling the Wd1 photometry we can account for nonlinearity in the reddening vector. This can occur in regions of high extinction, where the extinction-weighted central wavelength of a filter (i.e., the flux-weighted average wavelength of the extinguished stellar energy distribution convolved with the filter function) changes relative to another filter. Differences in the filter width (e.g. Kim et al. 2005, 2006) or slope of the extinction law between filters can cause this effect. Both processes are captured by the synthetic photometry in our extinction law analysis.

We observe reddening vector curvature in the *HST* 2CD, where a simple linear fit to the MS sample does not trace back to the origin at $A_{Ks} = 0$ as expected for these stars (Figure 3.18). Two extinction law fits to the data are shown: one with the PanStarrs y point (0.962 μm) included and another without. Both vectors have significant curvature and are thus able to broadly match the data and trace back to the origin in the zero extinction case. However, the model with the y point has more curvature and is able to better fit to the data. This is because adding A_y / A_{Ks} increases the flexibility of the extinction curve between the F125W and F814W filters, allowing for a steeper slope through the F814W filter as is called for by the data.

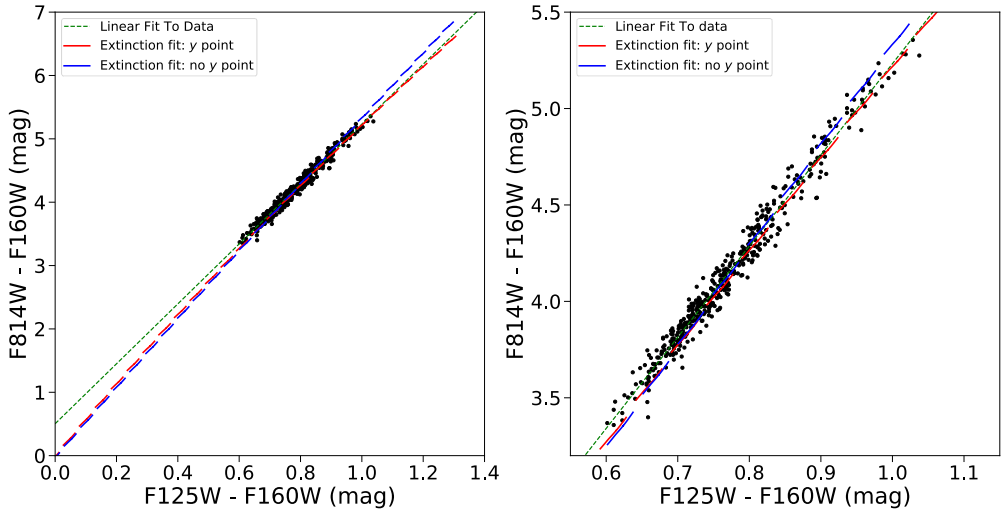

Figure 3.18 The *HST* 2CD compared to an orthogonal linear regression fit to the data (green dashed line) and the extinction law models derived with (red) and without (blue) the PanStarrs y point included. The right plot a zoomed-in version of the left plot. The fact that the linear fit does not trace back to the origin shows that there is significant curvature in the reddening vector. The model with the y point, which allows for a steeper extinction law slope through the F814W filter, provides the best match to the data.

3.5.4 Sources of Systematic Error

Here we explore potential sources of systematic error and quantify their impact on the extinction law analysis.

RC Star Model

A possible source of systematic error is the RC stellar model, which is adopted from a 10 Gyr Parsec isochone at solar metallicity. The absolute F153M magnitude of the RC star model is used in combination with the GC distance to derive the overall extinction of the RC stellar population, which in turn sets the normalization of the Wd1+RC extinction law. If we use an intrinsic RC star model that is brighter than our current model, then the extinction law becomes systematically more shallow (i.e., smaller A_λ /A_{Ks} values), and vice versa.

Since there are no empirical calibrations of the RC absolute magnitude in either F127M or F153M, we must rely on the stellar models in our analysis. However, several measurements of the RC absolute magnitude exist for the 2MASS K_s filter. The RC model we adopt is a 1.03 $M_\odot$ star

with an absolute magnitude of K_s = -1.43 mag. An initial K_s calibration from RC stars in the *Hipparcos* catalog found an absolute magnitude of K_s = -1.61 ± 0.03 mag (Alves 2000), though this has been revised faintward to K_s = -1.54 ± 0.04 mag (Groenewegen 2008) and K_s = -1.51 ± 0.01 (Francis & Anderson 2014) based on updated *Hipparcos* parallaxes (van Leeuwen 2007) and correcting for selection biases.

While the revised RC magnitudes are ∼0.1 mag brighter than our RC model, some or all of the discrepancy could be attributed to an age difference between the RC stars in our sample and those in the *Hipparcos* sample. The Arches field RC stars are primarily located in the Galactic Bulge, which has been shown to be dominated by ∼10 Gyr stars (Zoccali et al. 2003; Clarkson et al. 2008; Schultheis et al. 2017), though a spread of ages are present (e.g. Bensby et al. 2013). However, *Hipparcos* sample reflects the star formation history of the local solar neighborhood. Studies of the solar neighborhood have suggested a generally increasing star formation rate since ∼10 Gyr (Bertelli & Nasi 2001), perhaps with a peak of activity around 3 Gyr (Cignoni et al. 2006; Rowell 2013), though these results are model-dependent and are debated (Aumer & Binney 2009). RC models (e.g. Salaris & Girardi 2002) and observations (e.g. Chen et al. 2017) both indicate that RC stars become fainter with increasing age, with a K_s difference of ∼0.1 mags between a 3 Gyr and 10 Gyr population. Thus, while our RC model is reasonable, this remains a source of systematic error potentially at the ∼0.1 mag level.

We estimate the systematic uncertainty of the Parsec evolution models themselves by comparing the 10 Gyr Parsec RC model a 10 Gyr MIST isochrone RC model, which is built on the MESA stellar evolution models (Choi et al. 2016). The MIST RC model is found to be 0.06 mags brighter in F153M and 0.01 mags larger (i.e., more red) in F127M - F153M color. Further, if one weights the MIST isochrone by a standard Kroupa initial mass function (Kroupa 2001) and calculates the average magnitudes of stars in the RC portion of the F153M vs. F127M - F153M CMD, the RC model becomes an additional 0.04 mags brighter and 0.003 mags redder. So, the total difference between the adopted Parsec RC model and the IMF-weighted MIST RC model is 0.10 mag in F153M and 0.013 mag in F127M - F153M color. This represents the widest range of systematic error in both color and magnitude from uncertainties in the stellar evolution models themselves.

An error in the average metallicity in the RC sample could impact the absolute magnitudes as well. We have adopted solar metallicity for our RC model, consistent with what has been reported

for the Bulge near the Galactic Plane (Zoccali et al. 2003; Clarkson et al. 2008; Gonzalez et al. 2013). However, evidence of a bimodal metallicity distribution in the bulge has been found with peaks around [Fe/H] $\sim$ -0.3 dex and [Fe/H] $\sim$ 0.3 dex (Hill et al. 2011; Bensby et al. 2013; Schultheis et al. 2017). RC models for at 10 Gyr population at -0.38 dex $<$ [Fe/H] $<$ 0.2 dex show a $\pm\sim$0.1 mag variation relative to the solar metallicity model (Salaris & Girardi 2002). With these sources of error, we adopt a total systematic error of $\pm$0.1 mags on the RC absolute magnitude due to the uncertainties in the RC star model.

GC Distance

An additional source of systematic error is the GC distance, which we've adopted to be 7860 $\pm$ 140 pc from Boehle et al. (2016). However, a recent compilation and analysis of literature GC distance measurements by de Grijs & Bono (2016) recommends a distance of 8300 $\pm$ 200 (statistical) $\pm$ 400 (systematic) pc. If the GC distance is indeed 8300 pc, then the average RC distance prior is underestimated by $\sim$400 pc. In our analysis, this is equivalent to our RC model being too bright by $\sim$0.1 mags. As a conservative estimate, we adopt an additional systematic error of $\pm$0.1 mags on the RC absolute magnitude due to the GC distance uncertainty.

Total Systematic Error

We add the individual sources of systematic error in quadrature for a total systematic error of $\pm$0.14 mags on the RC star absolute magnitude. To assess the impact of this systematic, we change the RC model F153M magnitude by 0.14 mags relative to the model used in §3.4.3 and redo the extinction law analysis. We adopt the difference between the extinction law parameters in the new analysis and the original analysis as an estimate of the systematic error and report them in Table 3.4. The systematic errors are are approximately equal to or less than the 1σ statistical errors.

3.5.5 Other Applications and Future Work

The Wd1+RC law can be applied to stellar populations that similar foreground dust as the Wd1 and Arches field RC stars, namely the spiral arms of the Galaxy in the Galactic Plane. Examples of future applications include studies of stellar populations near the GC, such as the Quintuplet cluster and Young Nuclear Cluster, and the structure and kinematics of the inner Bulge at low

Table 3.5. Wd1+RC Extinction Law in Different Filters

Filter	λ_{pivot} (μm)[a]	A_λ / A_{Ks}	Filter Ref [b]
2MASS J	1.239	3.69	1
2MASS H	1.648	1.99	1
2MASS K_s	2.189	0.95	1
NIRC2 J	1.245	3.66	4
NIRC2 H	1.618	2.09	4
NIRC2 K_s	2.130	1.01	4
PS1 i	0.752	11.65	2
PS1 z	0.866	8.33	2
PS1 y	0.962	6.41	2
VISTA Z	0.880	8.00	3
VISTA Y	1.022	5.53	3
VISTA J	1.253	3.61	3
VISTA H	1.644	2.01	3
VISTA K_s	2.145	0.99	3

[a] As defined by (Tokunaga & Vacca 2005)

[b] 1: Cohen et al. (2003), 2: Tonry et al. (2012), 3: Saito et al. (2012), 4: https://www2.keck.hawaii.edu/inst/nirc2/filters.html

galactic latitudes. To aid future use, the Wd1+RC extinction law in several commonly-used filters is provided in Table 3.5. In addition, a python code to generate the law at any wavelength between 0.8 μm – 2.2 μm is available online (see §3.4.3). The law can also be accessed through the astropy-affiliated package *PopStar*, which will soon be released in a beta test.

While a detailed analysis of the dust properties is beyond the scope of this study, the measurement of significant non-power law behavior in the OIR extinction law suggests that there are subtle features that can be used to constrain dust models. The steepness of the law presents a challenge as well, as the classic silicate+graphite grain models (e.g. Mathis et al. 1977; Weingartner & Draine 2001) struggle to produce NIR laws steeper than the canonical C89 law (Moore et al. 2005; Fritz et al. 2011). Models that incorporate composite grains with organic refractory material and water ice (e.g. Zubko et al. 2004) and porous dust structures (e.g. Voshchinnikov et al. 2017) are promising in this regard.

A major caveat of this analysis is that it relies on the assumption that the extinction law is the same for Wd1 and the RC stars. While this is supported by our analysis and the literature, future studies are needed to confirm this assumption, especially at shorter wavelengths (e.g.

A_{F814W} / A_{Ks}) where R_V-like variations might begin to have an effect. Currently, the law normalization is set almost entirely by the RC stars, due to the relatively large uncertainty in the Wd1 cluster distance. A reanalysis of the Wd1 data when the distance is known to higher precision would allow for a constraint on the normalization from the Wd1 stars directly. Similarly, the shape of the extinction law is dominated by the Wd1 data, since the RC observations are limited to just the F127M and F153M filters. Additional observations of the RC stars in filters across a larger wavelength range would confirm that the shape of the law toward the RC stars.

In §3.5.4 we show that the systematic errors, mainly coming from uncertainties in the intrinsic RC star properties and GC distance, are roughly the size of the presented error bars in the Wd1+RC extinction law. As a result, a more precise measurement of the extinction law (at least those that use RC stars) is not possible until these uncertainties are addressed. In particular, observational calibrations of RC star models at older ages (∼10 Gyr) are needed to correctly represent the Bulge population, using multiple filters to test the stellar evolution and atmosphere models. Continued progress in understanding the Bulge age/metallicity distribution as well as the GC distance will also decrease the systematics in the extinction law analysis.

3.6 Conclusions

We use *HST* and *VISTA* photometry to measure the OIR (0.8 μm – 2.2 μm) extinction law toward two highly reddened stellar populations: Wd1 and RC stars in the Arches cluster field. The Wd1 sample contains 453 proper-motion selected main sequence stars, a sample 4x larger than previous studies of the extinction law in the cluster. The RC sample contains 813 stars identified in the Arches field CMD. We combine these data sets using a forward modeling Bayesian analysis that simultaneously fits the extinction law and distance of both populations while allowing for systematic offsets in the photometric zeropoints. By combining the samples we measure both the shape and normalization of the extinction law, without making any assumptions regarding its function form.

The best-fit Wd1+RC extinction law is well constrained with typical uncertainties of ∼5% on A_λ / A_{Ks}. The law is able to reproduce the observed colors of the Wd1 MS stars, where previous extinction laws produce colors that are typically off by 10% – 30%. Contrary to what is often assumed for the OIR, the Wd1+RC law is statistically inconsistent with a single power law, even

when only the NIR filters are considered. It is generally steeper (i.e. has larger A_λ / A_{Ks} values) than many extinction laws in the literature, being most similar to the Fitzpatrick & Massa (2009) law with $\alpha = 2.5$ and the Schlafly et al. (2016) law with A_H / $A_{Ks} = 2.0$. Notably, A_{F125W} / A_{Ks} and A_{F814W} / A_{Ks} are 18% and 24% larger, respectively, than the Nishiyama et al. (2009) law often adopted for the GC/Galactic Bulge, and 4% and 16% larger than the previous extinction law derived for Wd1 by Damineli et al. (2016). The new law produces A_H / $A_{Ks} = 1.936 \pm 0.08$, which is 10% higher than has been previously measured for RC stars at the GC but is consistent within uncertainties.

Throughout the extinction law analysis we assume an age of 5 Myr for Wd1. We show that varying the cluster age only impacts the cluster distance in the Wd1+RC extinction law fit. We calculate an independent distance to Wd1 using published observations of the eclipsing binary W13 and the new extinction law. The resulting distance of 3937 ± 332 pc favors an older cluster age of 6 Myr – 7 Myr, deviating from the cluster distances in the 4 Myr and 5 Myr extinction law models by 3.7σ and 2.5σ, respectively. A detailed analysis of the age and distance of Wd1 is left to a future paper.

This analysis probes the OIR extinction law toward Wd1 (ℓ = -20.451°, b = -0.404°) and the Arches cluster (ℓ = 0.121°, b = 0.017°). By necessity, we have assumed that the law is the same for both LOS in this wavelength range, which is supported by our analysis and the literature. Physically, this assumption asserts that the dust causing the extinction for these population have similar properties (in this case, material from foreground spiral arms in the Galactic plane). While future studies of Wd1 and the RC stars are required to verify this assumption, the Wd1+RC law is the best available for highly reddened stellar populations with similar foreground material, such as the Quintuplet cluster and Young Nuclear Cluster. For ease of use, the extinction law in several commonly-used filter sets is provided in Table 3.5 and a python code to generate the law is available online (see § 3.4.3).

We demonstrate that the methodology developed in this paper allows for a highly detailed measurement of the extinction law. Such measurements will become critical in light of upcoming space-based infrared observatories such as the James Web Space Telescope (JWST) and Wide Field Infrared Survey Telescope (WFIRST), which will push infrared observations into increasingly extinguished regions with high precision.

Acknowledgments

The authors thanks the anonymous referee for their helpful comments that greatly improved the clarity of the paper. M.W.H. and J.R.L. acknowledge support from NSF AAG (AST-1518273) and HST GO-13809. This work is based on observations made with the NASA/ESA Hubble Space Telescope, obtained at the Space Telescope Science Institute, which is operated by the Association of Universities for Research in Astronomy, Inc., under NASA contract NAS 5-26555. The Arches field observations observations are associated with programs 11671, 12318, and 12667, and the Westerlund 1 observations are associated with programs 10172, 11708, and 13044. It also uses data products from observations made with ESO Telescopes at the La Silla or Paranal Observatories under ESO programme ID 179.B-2002. This research has made extensive use of the NASA Astrophysical Data System.

References

Alves, D. R. 2000, ApJ, 539, 732

Andersen, M., Gennaro, M., Brandner, W., et al. 2017, A&A, 602, A22

Anderson, J., Sarajedini, A., Bedin, L. R., et al. 2008, AJ, 135, 2055

Aumer, M., & Binney, J. J. 2009, MNRAS, 397, 1286

Bensby, T., Yee, J. C., Feltzing, S., et al. 2013, A&A, 549, A147

Bertelli, G., & Nasi, E. 2001, AJ, 121, 1013

Boehle, A., Ghez, A. M., Schödel, R., et al. 2016, ApJ, 830, 17

Bonanos, A. Z. 2007, AJ, 133, 2696

Bovy, J., Rix, H.-W., Schlafly, E. F., et al. 2016, ApJ, 823, 30

Brandner, W., Clark, J. S., Stolte, A., et al. 2008, A&A, 478, 137

Bressan, A., Marigo, P., Girardi, L., et al. 2012, MNRAS, 427, 127

Buchner, J., Georgakakis, A., Nandra, K., et al. 2014, A&A, 564, A125

Cardelli, J. A., Clayton, G. C., & Mathis, J. S. 1989, ApJ, 345, 245

Castelli, F., & Kurucz, R. L. 2004, ArXiv Astrophysics e-prints, astro-ph/0405087

Chen, Y. Q., Casagrande, L., Zhao, G., et al. 2017, ApJ, 840, 77

Choi, J., Dotter, A., Conroy, C., et al. 2016, ApJ, 823, 102

Cignoni, M., Degl'Innocenti, S., Prada Moroni, P. G., & Shore, S. N. 2006, A&A, 459, 783

Clark, J. S., & Negueruela, I. 2004, A&A, 413, L15

Clark, J. S., Negueruela, I., Crowther, P. A., & Goodwin, S. P. 2005, A&A, 434, 949

Clark, J. S., Ritchie, B. W., & Negueruela, I. 2010, A&A, 514, A87

Clarkson, W., Sahu, K., Anderson, J., et al. 2008, ApJ, 684, 1110

Cohen, M., Wheaton, W. A., & Megeath, S. T. 2003, AJ, 126, 1090

Crowther, P. A., Hadfield, L. J., Clark, J. S., Negueruela, I., & Vacca, W. D. 2006, MNRAS, 372, 1407

Damineli, A., Almeida, L. A., Blum, R. D., et al. 2016, MNRAS, 463, 2653

de Boor, C. 1978, A practical guide to splines

de Grijs, R., & Bono, G. 2016, ApJS, 227, 5

De Marchi, G., Panagia, N., Sabbi, E., et al. 2016, MNRAS, 455, 4373

Diolaiti, E., Bendinelli, O., Bonaccini, D., et al. 2000, in Proc. SPIE, Vol. 4007, Adaptive Optical Systems Technology, ed. P. L. Wizinowich, 879–888

Dolphin, A. E. 2000, PASP, 112, 1383

Dougherty, S. M., Clark, J. S., Negueruela, I., Johnson, T., & Chapman, J. M. 2010, A&A, 511, A58

Draine, B. T. 1989, in ESA Special Publication, Vol. 290, Infrared Spectroscopy in Astronomy, ed. E. Böhm-Vitense

Draine, B. T. 2003, ARA&A, 41, 241

Ekström, S., Georgy, C., Eggenberger, P., et al. 2012, A&A, 537, A146

Feldmeier-Krause, A., Neumayer, N., Schödel, R., et al. 2015, A&A, 584, A2

Feroz, F., & Hobson, M. P. 2008, MNRAS, 384, 449

Feroz, F., Hobson, M. P., & Bridges, M. 2009, MNRAS, 398, 1601

Fierro, C. R., Borissova, J., Zsargó, J., et al. 2015, PASP, 127, 428

Fitzpatrick, E. L. 1999, PASP, 111, 63

Fitzpatrick, E. L., & Massa, D. 2009, ApJ, 699, 1209

Francis, C., & Anderson, E. 2014, MNRAS, 441, 1105

Fritz, T. K., Gillessen, S., Dodds-Eden, K., et al. 2011, ApJ, 737, 73

Gennaro, M., Brandner, W., Stolte, A., & Henning, T. 2011, MNRAS, 412, 2469

Girardi, L. 2016, ARA&A, 54, 95

Gonzalez, O. A., Rejkuba, M., Zoccali, M., et al. 2013, A&A, 552, A110

Groenewegen, M. A. T. 2008, A&A, 488, 935

Habibi, M., Stolte, A., Brandner, W., Hußmann, B., & Motohara, K. 2013, A&A, 556, A26

Hill, V., Lecureur, A., Gómez, A., et al. 2011, A&A, 534, A80

Hosek, Jr., M. W., Lu, J. R., Anderson, J., et al. 2018, ApJ, 855, 13

Husser, T.-O., Wende-von Berg, S., Dreizler, S., et al. 2013, A&A, 553, A6

Indebetouw, R., Mathis, J. S., Babler, B. L., et al. 2005, ApJ, 619, 931

Kalirai, J. S., MacKenty, J., Bohlin, R., et al. 2009, WFC3 SMOV Proposal 11451: The Photometric Performance and Calibration of WFC3/IR, Tech. rep.

Kim, S. S., Figer, D. F., & Lee, M. G. 2006, PASP, 118, 62

Kim, S. S., Figer, D. F., Lee, M. G., & Oh, S. 2005, PASP, 117, 445

Kothes, R., & Dougherty, S. M. 2007, A&A, 468, 993

Koumpia, E., & Bonanos, A. Z. 2012, A&A, 547, A30

Krist, J. E., Hook, R. N., & Stoehr, F. 2011, in Proc. SPIE, Vol. 8127, Optical Modeling and Performance Predictions V, 81270J

Kroupa, P. 2001, MNRAS, 322, 231

Majaess, D., Turner, D., Dékány, I., Minniti, D., & Gieren, W. 2016, A&A, 593, A124

Martin, P. G., & Whittet, D. C. B. 1990, ApJ, 357, 113

Martins, F., & Plez, B. 2006, A&A, 457, 637

Mathis, J. S., Rumpl, W., & Nordsieck, K. H. 1977, ApJ, 217, 425

Messineo, M., Habing, H. J., Menten, K. M., et al. 2005, A&A, 435, 575

Minniti, D., Lucas, P. W., Emerson, J. P., et al. 2010, , 15, 433

Mishenina, T. V., Bienaymé, O., Gorbaneva, T. I., et al. 2006, A&A, 456, 1109

Moore, T. J. T., Lumsden, S. L., Ridge, N. A., & Puxley, P. J. 2005, MNRAS, 359, 589

Muno, M. P., Clark, J. S., Crowther, P. A., et al. 2006, ApJ, 636, L41

Nataf, D. M., Gonzalez, O. A., Casagrande, L., et al. 2016, MNRAS, 456, 2692

Negueruela, I., Clark, J. S., & Ritchie, B. W. 2010, A&A, 516, A78

Nishiyama, S., Nagata, T., Tamura, M., et al. 2008, ApJ, 680, 1174

Nishiyama, S., Tamura, M., Hatano, H., et al. 2009, ApJ, 696, 1407

Nogueras-Lara, F., Gallego-Calvente, A. T., Dong, H., et al. 2017, ArXiv e-prints, arXiv:1709.09094

Rieke, G. H., & Lebofsky, M. J. 1985, ApJ, 288, 618

Ritchie, B. W., Clark, J. S., Negueruela, I., & Langer, N. 2010, A&A, 520, A48

Rowell, N. 2013, MNRAS, 434, 1549

Saito, R. K., Hempel, M., Minniti, D., et al. 2012, A&A, 537, A107

Salaris, M., & Girardi, L. 2002, MNRAS, 337, 332

Schlafly, E. F., Meisner, A. M., Stutz, A. M., et al. 2016, ApJ, 821, 78

Schödel, R. 2010, A&A, 509, A58

Schödel, R., Najarro, F., Muzic, K., & Eckart, A. 2010, A&A, 511, A18

Schultheis, M., Kordopatis, G., Recio-Blanco, A., et al. 2015, A&A, 577, A77

Schultheis, M., Rojas-Arriagada, A., García Pérez, A. E., et al. 2017, A&A, 600, A14

STScI Development Team. 2013, pysynphot: Synthetic photometry software package, Astrophysics Source Code Library, , , ascl:1303.023

Tognelli, E., Prada Moroni, P. G., & Degl'Innocenti, S. 2011, A&A, 533, A109

Tokunaga, A. T., & Vacca, W. D. 2005, PASP, 117, 421

Tonry, J. L., Stubbs, C. W., Lykke, K. R., et al. 2012, ApJ, 750, 99

van Leeuwen, F. 2007, A&A, 474, 653

Voshchinnikov, N. V., Henning, T., & Il'in, V. B. 2017, ApJ, 837, 25

Wang, S., & Jiang, B. W. 2014, ApJ, 788, L12

Wegg, C., & Gerhard, O. 2013, MNRAS, 435, 1874

Wegg, C., Gerhard, O., & Portail, M. 2015, MNRAS, 450, 4050

Weingartner, J. C., & Draine, B. T. 2001, ApJ, 548, 296

Williams, B. F., Lang, D., Dalcanton, J. J., et al. 2014, ApJS, 215, 9

Witzel, G., Lu, J. R., Ghez, A. M., et al. 2016, in Proc. SPIE, Vol. 9909, Adaptive Optics Systems V, 99091O

Zoccali, M., Renzini, A., Ortolani, S., et al. 2003, A&A, 399, 931

Zubko, V., Dwek, E., & Arendt, R. G. 2004, ApJS, 152, 211

3.7 Appendix A: Extinction Law Definitions

In this appendix we describe the extinction law terms used in the paper. The parameter A_λ is the amount of extinction (in magnitudes) observed toward a source at wavelength λ:

$$m_{obs} = M_0 + \mu + A_\lambda \tag{3.12}$$

where m_{obs} and M_0 are the observed and absolute magnitudes of a source, respectively, and μ is the distance modulus. We present the extinction law as the ratio A_λ/A_{K_s}, which can be generally written as:

$$A_\lambda/A_{K_s} = bf(\lambda) + c \tag{3.13}$$

where $f(\lambda)$ is the wavelength-dependent shape of the extinction law and b and c together comprise the normalization factors. The shape of the extinction law is often constrained via stellar color-excess ratios, where the normalization factors conveniently cancel out:

$$\frac{E(\lambda_1 - \lambda_2)}{E(\lambda_2 - \lambda_3)} = \frac{A_{\lambda_1} - A_{\lambda_2}}{A_{\lambda_2} - A_{\lambda_3}} = \frac{f(\lambda_1) - f(\lambda_2)}{f(\lambda_2) - f(\lambda_3)} \tag{3.14}$$

While being directly observed quantities, color excess ratios are not continuous as a function of wavelength and depend on the filters used. This makes comparing color-excess ratios across different studies difficult. We present an alternative approach based on the derivative of the extinction law with respect to $1/\lambda$:

$$\nabla_{1/\lambda} = \frac{\partial(A_\lambda/A_{Ks})}{\partial(1/\lambda)} = -b * \lambda^2 * f'(\lambda) \tag{3.15}$$

where $f'(\lambda) = \frac{\partial(f(\lambda))}{\partial(\lambda)}$. We define the parameter $S_{1/\lambda}$ such that it only depends on the extinction law shape and the ratio of λ to 2.14 μm, which we use as a reference wavelength:

$$S_{1/\lambda} = \frac{\nabla_{1/\lambda}}{\nabla_{1/2.14\mu m}} = \frac{f'(\lambda)}{f'(2.14\mu m)} * \left(\frac{\lambda}{2.14}\right)^2 \tag{3.16}$$

To see the relationship between $S_{1/\lambda}$ and the color excess ratio, we evaluate Equation 3.14 in the limit where λ_2 - $\lambda_1 = \Delta\lambda_1$ and λ_3 - $\lambda_2 = \Delta\lambda_2$ are small and set $\lambda_2 = 2.14$ μm:

$$\frac{E(\lambda_1 - \lambda_2)}{E(\lambda_2 - \lambda_3)} = \frac{f(\lambda_1) - f(\lambda_1 + \Delta\lambda_1)}{f(\lambda_2) - f(\lambda_2 + \Delta\lambda_2)} = \frac{f'(\lambda_1)}{f'(\lambda_2)} \frac{\Delta\lambda_1}{\Delta\lambda_2} = S_{1/\lambda} \left(\frac{\lambda_2}{\lambda_1}\right)^2 \frac{\Delta\lambda_1}{\Delta\lambda_2} \tag{3.17}$$

3.8 Appendix B: Simulated Data Tests

We simulate a set of Wd1 MS and Arches RC star observations with known extinction properties in order to test the extinction law analysis. The synthetic photometry is constructed from stellar models as described in §3.3.1. A total of 400 stars are randomly drawn from this isochrone (the approximate size of the Wd1 sample) and extinction is applied using a Nishiyama et al. (2009) extinction law. To replicate differential extinction, the total extinction for each star is drawn from a Gaussian distribution centered at $A_{Ks} = 0.7$ mags with a width of $dA_{Ks} = 0.15$ mags. This distribution was found to broadly reproduce the spread of the real observations in CMD and 2CD space. Finally, realistic photometric errors are applied to the simulated measurements based on the median photometric error calculated as a function of magnitude for the observations in each filter. The photometry of each star is perturbed by a value drawn from a Gaussian distribution with $\mu = 0$ and standard deviation equal to the appropriate photometric error at that star's magnitude in the given filter (typically $\sim$0.01 mag).

The synthetic RC stars are generated in a similar manner, adopting the RC stellar model from §3.3.1 and creating a sample of 900 stars with extinction values uniformly distributed between 2.7 mag $< A_{Ks} <$ 3.5 mag using a Nishiyama et al. (2009) law. This dA_{Ks} was found to reproduce the color range of the observed RC sequence in CMD space. Initially, the stars are generated at the same distance, namely the d_{rc} value defined by the user. Then, the photometry of each star is perturbed by a value drawn from a Gaussian distribution with a width equal σ_{rc}, also defined by the user. This perturbation, which is the same in both filters, represents the impact of the unknown distance of the particular star as discussed in §3.3.3. Like Wd1, realistic photometric errors are also added to the photometry. The RC sample is then restricted to stars that fall within $\pm$0.3 mag of the reddening vector in both of CMDs, matching the criteria adopted for the observed RC sample.

First, we test the extinction law fitter using the simulated Wd1 MS sample only; that is, $\mathcal{L}_{tot} = \mathcal{L}_{wd1}$ in equation 3.8. The synthetic star catalog is subjected to the same set of cuts as the observed catalog discussed in §3.3.2. We adopt the same priors as is used for the real data except

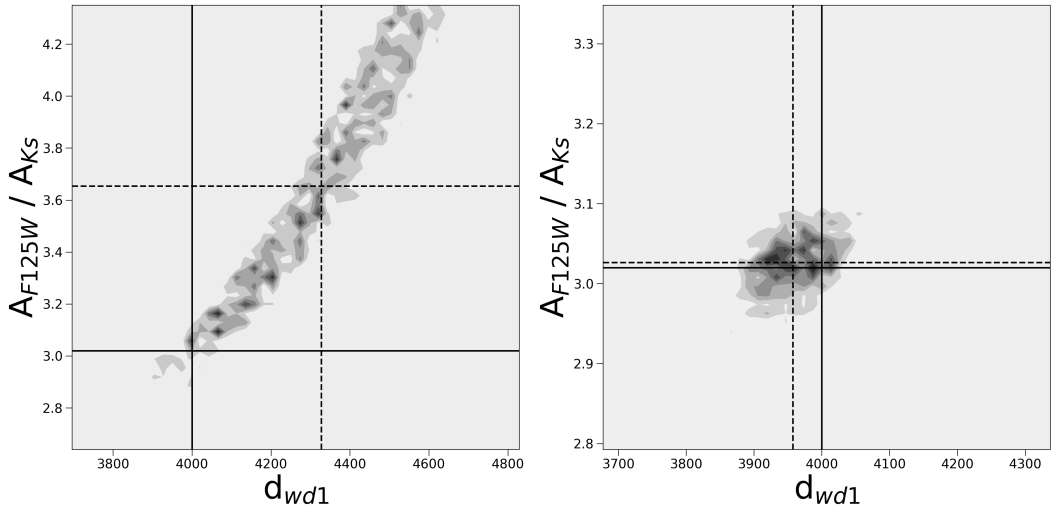

Figure 3.19 The marginalized two-dimensional posterior probability distributions for A_{F125W} / A_{Ks} vs. d_{wd1} in the simulated cluster tests. These posteriors show the degeneracy between the extinction law and cluster parameters (d_{wd1} in this case). The solid black lines denote the input value for the simulated cluster while the dotted black lines denote the best-fit value from the fit. *Left:* The posterior for the Wd1-only simulated analysis, which has a large degeneracy due to the uncertainty in the cluster distance and thus normalization of the law. *Right:* The posterior for the Wd1+RC simulated analysis, where the extinction law normalization is constrained by the RC stars and thus the degeneracy is broken.

for the RC parameters which aren't used in the model. The resulting posterior distributions show a large degeneracy as a wide range of extinction laws are allowed for different combinations of A_{Ks} and d_{wd1} (Figure 3.19). Generally, the synthetic observations can be reproduced by a more distant cluster model with a lower A_{Ks} and steeper extinction law, or a closer cluster with a higher A_{Ks} and shallower law. This degeneracy caused by the uncertainty in the normalization.

Next, we test the fitter using only the simulated RC sample, such that $\mathcal{L}_{tot} = \mathcal{L}_{RC}$ in equation 3.8. We similarly subject the stars to the same cuts as the observed sample and adopt the same priors. None of the Wd1 cluster parameters are used, and the extinction law itself is limited to A_{F125W} / A_{F160W}, where the RC data has constraining power. The resulting posterior distributions show that all input parameters are recovered to within 1σ.

Finally, we test the fitter using both the simulated Wd1 MS and Arches RC data sets. The advantage of the RC sample is that the distance distribution is known to much higher precision than that of Wd1, allowing for a tighter constraint on the normalization of the extinction law

Table 3.6. Simulated Data Results

Parameter	Input	Prior[a]	Wd1-only	Wd1+RC
A_{F814W} / A_{Ks}	8.87	U(4, 14)	11.31 ± 1.82	8.86 ± 0.12
A_y / A_{Ks}	6.00	U(4, 14)	7.34 ± 1.13	5.98 ± 0.09
A_{F125W} / A_{Ks}	3.02	U(1, 6)	3.65 ± 0.47	3.03 ± 0.03
A_{F160W} / A_{Ks}	1.93	U(1, 6)	2.22 ± 0.21	1.93 ± 0.02
A_{Ks}	0.70	U(0.3, 1.4)	0.53 ± 0.10	0.71 ± 0.02
$A_{[3.6]}$ / A_{Ks}	0.50	G(0.50, 0.05)	0.50 ± 0.03	0.50 ± 0.04
d_{wd1}	4000	G(4000, 700)	4328 ± 193	3958 ± 45
d_{rc}	8000	G(8000, 160)	–	8009 ± 105
σ_{rc}	0.2	G(0.2, 0.01)	–	0.2 ± 0.006
ZP_{Ks}	0	G(0, 5x10^{-3})	-8x10^{-4} ± 4x10^{-3}	-1.3x10^{-3} ± 3x10^{-3}
ZP_{F160W}	0	G(0, 8.8x10^{-4})	0.0 ± 1x10^{-3}	-1x10^{-4} ± 1x10^{-3}
ZP_{F153M}	0	G(0, 7.2x10^{-4})	–	0.0 ± 1x10^{-4}
ZP_{F127M}	0	G(0, 7.1x10^{-4})	–	0.0 ± 1x10^{-4}
ZP_{F125W}	0	G(0, 1.2x10^{-3})	1x10^{-4} ± 1x10^{-3}	0.0 ± 1x10^{-3}
ZP_{F1814W}	0	G(0, 5.2x10^{-4})	0.0 ± 1x10^{-4}	0.0 ± 1x10^{-4}

[a]Uniform distributions: U(min, max), where min and max are bounds of the distribution; Gaussian distributions: G(μ, σ), where μ is the mean and σ is the standard deviation

(Figure 3.19). The RC sample distribution is anchored to the GC, which has a distance that is known to within ∼2% (Boehle et al. 2016), compared to the Wd1 distance uncertainty of ∼18%. The fit recovers the input extinction law parameters to within 1σ, with an uncertainty in A_λ / A_{Ks} ranging from 0.14 at F814W to 0.02 at F160W. The remaining parameters in the model (A_{Ks}, d_{wd1}, d_{rc}, σ_{rc}, and the zeropoint offsets) are also recovered within 1σ. The set of simulated cluster results is provided in Table 3.6.

3.9 Appendix C: Extinction Law Fit Posteriors

In this appendix we present a representative example of the posterior distributions for the extinction law fits, specifically the A_{F125W} / A_{Ks} two-dimensional posterior distributions. Figure 3.20 shows the posteriors for the Wd1-only fit (§3.4.1) and the Wd1 + RC fit (§3.4.3).

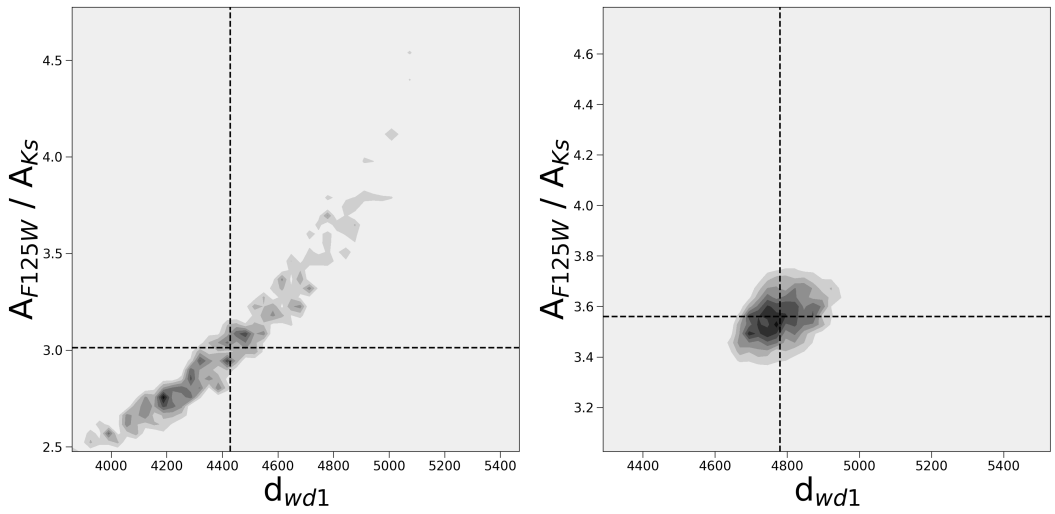

Figure 3.20 The marginalized two-dimensional posterior probability distributions for A_{F125W} / A_{Ks} vs. d_{wd1} in the extinction law analysis. The dotted black lines denote the best-fit value from the fit. *Left:* The posterior for the Wd1-only analysis, which suffers from a large degeneracy due to the uncertainty in the extinction law normalization. *Right:* The posterior for the Wd1+RC analysis, where the law normalization has been constrained by the RC stars. The posteriors for the real cluster analyses are similar to what we expect based on the simulated cluster analyses.

References

Alves, D. R. 2000, ApJ, 539, 732

Andersen, M., Gennaro, M., Brandner, W., et al. 2017, A&A, 602, A22

Anderson, J., Sarajedini, A., Bedin, L. R., et al. 2008, AJ, 135, 2055

Aumer, M., & Binney, J. J. 2009, MNRAS, 397, 1286

Bensby, T., Yee, J. C., Feltzing, S., et al. 2013, A&A, 549, A147

Bertelli, G., & Nasi, E. 2001, AJ, 121, 1013

Boehle, A., Ghez, A. M., Schödel, R., et al. 2016, ApJ, 830, 17

Bonanos, A. Z. 2007, AJ, 133, 2696

Bovy, J., Rix, H.-W., Schlafly, E. F., et al. 2016, ApJ, 823, 30

Brandner, W., Clark, J. S., Stolte, A., et al. 2008, A&A, 478, 137

Bressan, A., Marigo, P., Girardi, L., et al. 2012, MNRAS, 427, 127

Buchner, J., Georgakakis, A., Nandra, K., et al. 2014, A&A, 564, A125

Cardelli, J. A., Clayton, G. C., & Mathis, J. S. 1989, ApJ, 345, 245

Castelli, F., & Kurucz, R. L. 2004, ArXiv Astrophysics e-prints, astro-ph/0405087

Chen, Y. Q., Casagrande, L., Zhao, G., et al. 2017, ApJ, 840, 77

Choi, J., Dotter, A., Conroy, C., et al. 2016, ApJ, 823, 102

Cignoni, M., Degl'Innocenti, S., Prada Moroni, P. G., & Shore, S. N. 2006, A&A, 459, 783

Clark, J. S., & Negueruela, I. 2004, A&A, 413, L15

Clark, J. S., Negueruela, I., Crowther, P. A., & Goodwin, S. P. 2005, A&A, 434, 949

Clark, J. S., Ritchie, B. W., & Negueruela, I. 2010, A&A, 514, A87

Clarkson, W., Sahu, K., Anderson, J., et al. 2008, ApJ, 684, 1110

Cohen, M., Wheaton, W. A., & Megeath, S. T. 2003, AJ, 126, 1090

Crowther, P. A., Hadfield, L. J., Clark, J. S., Negueruela, I., & Vacca, W. D. 2006, MNRAS, 372, 1407

Damineli, A., Almeida, L. A., Blum, R. D., et al. 2016, MNRAS, 463, 2653

de Boor, C. 1978, A practical guide to splines

de Grijs, R., & Bono, G. 2016, ApJS, 227, 5

De Marchi, G., Panagia, N., Sabbi, E., et al. 2016, MNRAS, 455, 4373

Diolaiti, E., Bendinelli, O., Bonaccini, D., et al. 2000, in Proc. SPIE, Vol. 4007, Adaptive Optical Systems Technology, ed. P. L. Wizinowich, 879–888

Dolphin, A. E. 2000, PASP, 112, 1383

Dougherty, S. M., Clark, J. S., Negueruela, I., Johnson, T., & Chapman, J. M. 2010, A&A, 511, A58

Draine, B. T. 1989, in ESA Special Publication, Vol. 290, Infrared Spectroscopy in Astronomy, ed. E. Böhm-Vitense

Draine, B. T. 2003, ARA&A, 41, 241

Ekström, S., Georgy, C., Eggenberger, P., et al. 2012, A&A, 537, A146

Feldmeier-Krause, A., Neumayer, N., Schödel, R., et al. 2015, A&A, 584, A2

Feroz, F., & Hobson, M. P. 2008, MNRAS, 384, 449

Feroz, F., Hobson, M. P., & Bridges, M. 2009, MNRAS, 398, 1601

Fierro, C. R., Borissova, J., Zsargó, J., et al. 2015, PASP, 127, 428

Fitzpatrick, E. L. 1999, PASP, 111, 63

Fitzpatrick, E. L., & Massa, D. 2009, ApJ, 699, 1209

Francis, C., & Anderson, E. 2014, MNRAS, 441, 1105

Fritz, T. K., Gillessen, S., Dodds-Eden, K., et al. 2011, ApJ, 737, 73

Gennaro, M., Brandner, W., Stolte, A., & Henning, T. 2011, MNRAS, 412, 2469

Girardi, L. 2016, ARA&A, 54, 95

Gonzalez, O. A., Rejkuba, M., Zoccali, M., et al. 2013, A&A, 552, A110

Groenewegen, M. A. T. 2008, A&A, 488, 935

Habibi, M., Stolte, A., Brandner, W., Hußmann, B., & Motohara, K. 2013, A&A, 556, A26

Hill, V., Lecureur, A., Gómez, A., et al. 2011, A&A, 534, A80

Hosek, Jr., M. W., Lu, J. R., Anderson, J., et al. 2018, ApJ, 855, 13

Husser, T.-O., Wende-von Berg, S., Dreizler, S., et al. 2013, A&A, 553, A6

Indebetouw, R., Mathis, J. S., Babler, B. L., et al. 2005, ApJ, 619, 931

Kalirai, J. S., MacKenty, J., Bohlin, R., et al. 2009, WFC3 SMOV Proposal 11451: The Photometric Performance and Calibration of WFC3/IR, Tech. rep.

Kim, S. S., Figer, D. F., & Lee, M. G. 2006, PASP, 118, 62

Kim, S. S., Figer, D. F., Lee, M. G., & Oh, S. 2005, PASP, 117, 445

Kothes, R., & Dougherty, S. M. 2007, A&A, 468, 993

Koumpia, E., & Bonanos, A. Z. 2012, A&A, 547, A30

Krist, J. E., Hook, R. N., & Stoehr, F. 2011, in Proc. SPIE, Vol. 8127, Optical Modeling and Performance Predictions V, 81270J

Kroupa, P. 2001, MNRAS, 322, 231

Majaess, D., Turner, D., Dékány, I., Minniti, D., & Gieren, W. 2016, A&A, 593, A124

Martin, P. G., & Whittet, D. C. B. 1990, ApJ, 357, 113

Martins, F., & Plez, B. 2006, A&A, 457, 637

Mathis, J. S., Rumpl, W., & Nordsieck, K. H. 1977, ApJ, 217, 425

Messineo, M., Habing, H. J., Menten, K. M., et al. 2005, A&A, 435, 575

Minniti, D., Lucas, P. W., Emerson, J. P., et al. 2010, , 15, 433

Mishenina, T. V., Bienaymé, O., Gorbaneva, T. I., et al. 2006, A&A, 456, 1109

Moore, T. J. T., Lumsden, S. L., Ridge, N. A., & Puxley, P. J. 2005, MNRAS, 359, 589

Muno, M. P., Clark, J. S., Crowther, P. A., et al. 2006, ApJ, 636, L41

Nataf, D. M., Gonzalez, O. A., Casagrande, L., et al. 2016, MNRAS, 456, 2692

Negueruela, I., Clark, J. S., & Ritchie, B. W. 2010, A&A, 516, A78

Nishiyama, S., Nagata, T., Tamura, M., et al. 2008, ApJ, 680, 1174

Nishiyama, S., Tamura, M., Hatano, H., et al. 2009, ApJ, 696, 1407

Nogueras-Lara, F., Gallego-Calvente, A. T., Dong, H., et al. 2017, ArXiv e-prints, arXiv:1709.09094

Rieke, G. H., & Lebofsky, M. J. 1985, ApJ, 288, 618

Ritchie, B. W., Clark, J. S., Negueruela, I., & Langer, N. 2010, A&A, 520, A48

Rowell, N. 2013, MNRAS, 434, 1549

Saito, R. K., Hempel, M., Minniti, D., et al. 2012, A&A, 537, A107

Salaris, M., & Girardi, L. 2002, MNRAS, 337, 332

Schlafly, E. F., Meisner, A. M., Stutz, A. M., et al. 2016, ApJ, 821, 78

Schödel, R. 2010, A&A, 509, A58

Schödel, R., Najarro, F., Muzic, K., & Eckart, A. 2010, A&A, 511, A18

Schultheis, M., Kordopatis, G., Recio-Blanco, A., et al. 2015, A&A, 577, A77

Schultheis, M., Rojas-Arriagada, A., García Pérez, A. E., et al. 2017, A&A, 600, A14

STScI Development Team. 2013, pysynphot: Synthetic photometry software package, Astrophysics Source Code Library, , , ascl:1303.023

Tognelli, E., Prada Moroni, P. G., & Degl'Innocenti, S. 2011, A&A, 533, A109

Tokunaga, A. T., & Vacca, W. D. 2005, PASP, 117, 421

Tonry, J. L., Stubbs, C. W., Lykke, K. R., et al. 2012, ApJ, 750, 99

van Leeuwen, F. 2007, A&A, 474, 653

Voshchinnikov, N. V., Henning, T., & Il'in, V. B. 2017, ApJ, 837, 25

Wang, S., & Jiang, B. W. 2014, ApJ, 788, L12

Wegg, C., & Gerhard, O. 2013, MNRAS, 435, 1874

Wegg, C., Gerhard, O., & Portail, M. 2015, MNRAS, 450, 4050

Weingartner, J. C., & Draine, B. T. 2001, ApJ, 548, 296

Williams, B. F., Lang, D., Dalcanton, J. J., et al. 2014, ApJS, 215, 9

Witzel, G., Lu, J. R., Ghez, A. M., et al. 2016, in Proc. SPIE, Vol. 9909, Adaptive Optics Systems V, 99091O

Zoccali, M., Renzini, A., Ortolani, S., et al. 2003, A&A, 399, 931

Zubko, V., Dwek, E., & Arendt, R. G. 2004, ApJS, 152, 211

Chapter 4

The Initial Mass Function of the Arches Cluster

Note: This chapter will be submitted for publication this shortly with co-authors Jessica R. Lu, Jay Anderson, Francisco Najarro, Andrea M. Ghez, Mark R. Morris, William I. Clarkson, and Saundra M. Albers.

Abstract

As a young massive cluster in the Central Molecular Zone, the Arches cluster is a valuable probe of the stellar Initial Mass Function (IMF) in the extreme Galactic Center environment. We use multi-epoch Hubble Space Telescope observations to obtain high-precision proper motion and photometric measurements of the cluster, calculating cluster membership probabilities for stars down to $\sim$1.8 $M_\odot$ between cluster radii of 0.25 pc – 3.0 pc. We achieve a cluster sample with just $\sim$8% field contamination, a significant improvement over photometrically-selected samples due to the severe differential extinction across the field. Combining this sample with K-band spectroscopy of 5 cluster members, we forward model the Arches cluster to simultaneously constrain its IMF and other properties (such as age and total mass) while accounting for observational uncertainties, completeness, mass segregation, and stellar multiplicity. We find that the Arches IMF is best described by a 1-segment power law that is significantly top-heavy ($\alpha = 1.76 \pm 0.03 \pm 0.05$, where $dN/dm \propto m^{-\alpha}$), though we cannot discount a 2-segment power law model with a high-mass slope only slightly shallower than local star forming regions ($\alpha = 2.11 \pm 0.11$) with a break at $5.16^{+1.25}_{-0.65}$ $M_\odot$. In either case, the Arches IMF is significantly different than the standard IMF. Comparing

the Arches to other young massive clusters in the Milky Way, we find tentative evidence for a systematically top-heavy IMF at the Galactic Center.

4.1 Introduction

A fundamental quantity in star formation is the Initial Mass Function (IMF), which describes the distribution of stellar masses created during star formation. Though its functional form is debated (e.g. Chabrier 2005), the IMF is often represented as a multi-part power-law given by dN/dm $\propto$ $m^{-\alpha}$, where:

$$\alpha = \begin{cases} 0.3 \pm 0.4, & \text{for } 0.01 < m/M_{\odot} \lesssim 0.08 \\ 1.3 \pm 0.3, & \text{for } 0.08 < m/M_{\odot} \leq 0.5 \\ 2.3 \pm 0.36, & \text{for } 0.5 < m/M_{\odot} \leq 150 \end{cases} \tag{4.1}$$

as discussed in Kroupa (2002). Stellar populations in the Milky Way and nearby galaxies have been found to be consistent with this "local IMF", leading to the suggestion that it may be a universal property of star formation (see reviews by Bastian et al. 2010; Offner et al. 2014, and references therein). Thus, the local IMF is often used to describe stellar populations throughout the universe.

However, it is unknown whether the local IMF is applicable to environments other than those found in local star formation regions. Of particular interest are starburst environments, which exhibit extremely high gas densities and temperatures, radiation fields, and turbulence (e.g. Swinbank et al. 2011). Some studies predict that the increased thermal Jeans mass results in an overabundance of high-mass stars and a "top-heavy" IMF (e.g. Larson 2005; Bonnell et al. 2006; Klessen et al. 2007; Bonnell & Rice 2008; Papadopoulos et al. 2011; Narayanan & Davé 2013). Alternatively, others claim that the IMF is set by the mass distribution of pre-stellar cores within a molecular cloud (the core mass function, or CMF), which itself is set by turbulence (e.g. Padoan & Nordlund 2002; Hopkins 2012). These theories predict that the increased turbulence in starburst environments would favor the formation of low-mass stars and a "bottom-heavy" IMF (Hopkins 2013; Chabrier et al. 2014). However, recent simulations suggest that CMF cannot be directly mapped to the IMF (e.g. Bertelli Motta et al. 2016; Liptai et al. 2017). A third set of studies contend that the IMF is driven by local processes such as radiative feedback (e.g. Bate 2009; Offner

et al. 2009; Krumholz 2011; Krumholz et al. 2012), and is largely independent of environment (e.g. Guszejnov et al. 2016). Thus, understanding how the IMF behaves in starburst environments yields critical insight to the underlying physics driving star formation (e.g. Krumholz 2014).

There is some observational evidence that the IMF changes in starburst environments, though these results are debated. Studies of massive elliptical galaxies have found that the IMF becomes increasingly bottom-heavy with increasing velocity dispersion and/or α-element enhancement, conditions that reflect starburst-like conditions (e.g. Conroy & van Dokkum 2012; Conroy et al. 2013; Cappellari et al. 2012, 2013; La Barbera et al. 2013; Spiniello et al. 2014; Li et al. 2017). Further studies suggest that the cores of massive galaxies, which are thought to have formed rapidly in starburst-like environments at high redshift (e.g. Oser et al. 2010), are systematically bottom-heavy relative to the rest of the galaxy (e.g. Martín-Navarro et al. 2015; van Dokkum et al. 2017; Conroy et al. 2017; Parikh et al. 2018). However, these results rely on modeling stellar populations from unresolved stellar spectra, which is prone to systematic effects such as elemental abundance gradients (e.g. McConnell et al. 2016; Zieleniewski et al. 2015, 2017; Vaughan et al. 2018). Overall, the consistency of IMF determinations for a single galaxy using spectroscopic, kinematic, and lensing methods has not yet been established, with some galaxies showing agreement and others showing significant discrepancies (Lyubenova et al. 2016; Newman et al. 2017). This highlights the difficulty of measuring the IMF from these complex and unresolved stellar populations.

Massive star clusters in starburst galaxies (also known as super star clusters, or starburst clusters) also offer a probe into starburst environments. Still unresolved with current observing facilities, their mass functions are inferred from the light-to-mass ratios (e.g. Ho & Filippenko 1996). This analysis also faces many challenges, including the need for virial equilibrium, uncertainties in stellar models and extinction corrections, the impact of mass segregation and multiplicity, and anisotropy in the velocity dispersion (e.g. Bastian et al. 2007). A range of both bottom-heavy and top-heavy IMFs have been reported for these clusters, perhaps as a result of these difficulties (Larsen et al. 2004; McCrady et al. 2005; Bastian et al. 2006).

Ideally, one would directly measure the IMF of starburst environments using resolved stellar populations. Such investigations are possible at the Milky Way Galactic Center (GC), which has been shown exhibit similar densities, temperatures, and kinematics to those in starburst galaxies (Kruijssen & Longmore 2013; Ginsburg et al. 2016). The GC contains several young massive clusters

whose youth and high mass make them ideal tools for measuring the IMF (Morris & Serabyn 1996). The Young Nuclear Cluster (YNC; ∼2.5 – 5.8 Myr, M $\gtrsim$ 2x10^4 M$_\odot$), which lies within the central parsec of the galaxy, has been found to have a top-heavy IMF with $\alpha = 1.7 \pm 0.2$ (Lu et al. 2013). The Arches cluster (2 – 4 Myr, M ∼ 4–6 x 10^4 M$_\odot$; Martins et al. 2008; Clarkson et al. 2012), located within the Central Molecular Zone (CMZ) and at a projected distance of ∼26 pc from the central supermassive black hole, offers an additional opportunity to probe the IMF in this extreme environment.

Despite many efforts, the IMF of the Arches cluster has not yet been established. This is due to two significant challenges: mass segregation and differential extinction. As a result of mass segregation, the *present-day mass function* (PDMF) of the inner region (r $\lesssim$ 0.5 pc) has been measured to be top-heavy (Figer et al. 1999; Stolte et al. 2002, 2005; Kim et al. 2006), while the outer regions (r $\gtrsim$ 0.5 pc) have been found to be either consistent with the local IMF or bottom-heavy (Espinoza et al. 2009; Habibi et al. 2013). Dynamical modeling is required to determine whether the observed PDMF is consistent with the IMF (e.g. Kim et al. 2000; Harfst et al. 2010; Park et al. 2018), though the uncertainty in cluster orbit (Stolte et al. 2008) and initial conditions requires that a large parameter space must be considered.

In addition, inferring the IMF from the PDMF depends heavily on the PDMF at large cluster radii, where the differences between dynamical models are the largest (e.g., Figure 13 of Habibi et al. 2013). However, significant differential extinction ($\Delta A_V \sim 15$ mag; Habibi et al. 2013) makes it challenging to separate the cluster from field populations via photometry, especially at large radii where field star contamination can be high (e.g. Stolte et al. 2005). Measurements of the internal velocity dispersion of the cluster indicate that its mass function is top-heavy and/or truncated at low masses (Clarkson et al. 2012), but this has yet to be confirmed by direct star counts.

In this paper, we combine multi-epoch *Hubble Space Telescope* (*HST*) WFC3-IR observations with Keck OSIRIS K-band spectroscopy to measure the IMF of the Arches cluster for M > 1.8 M$_\odot$. We describe our observations in §4.2 and our methods for calculating cluster membership probabilities, correcting for extinction, and measuring observational completeness in §4.3. In §4.4 we detail our forward modeling technique for constraining the IMF, and in §4.5 we present our result that the Arches cluster IMF is inconsistent with the local IMF. We compare this to past

Arches IMF measurements and discuss in the context of other young massive clusters in the Milky Way in §4.6, and conclude in §4.7.

4.2 Observations and Measurements

4.2.1 HST Photometry and Astrometry

Astrometry and photometry of the Arches cluster were obtained from observations with the infrared channel of the Wide Field Camera 3 (WFC3-IR) on the Hubble Space Telescope (*HST*) for 4 epochs between 2010 and 2016. The 2010 epoch contains images in the F127M, F139M, and F153M filters (GO-11671, PI: Ghez, A.M.), while the 2011, 2012, and 2016 epochs only have images in the F153M filter (GO-12318, GO-12667, PI: Ghez, A.M.; GO-14613, PI: Lu., J.R.). A detailed description of the 2010 – 2012 observations is provided in (Hosek et al. 2015, hereafter H15). The 2016 observations were designed to mimic the earlier F153M epochs in order to maximize the astrometric precision between the data sets. These observations have a field of view (FOV) of 120" x 120", providing coverage of at least 30% of the cluster area within annuli out to ∼3 pc (Figure 4.1).

We extract high-precision astrometry and photometry using the `FORTRAN` codes `img2xym_wfc3ir`, a version of the `img2xym_WFC` package for WFC3-IR (Anderson & King 2006), and `KS2`, a generalization of the software developed for the Globular Cluster Treasury Program (Anderson et al. 2008, see also Bellini et al. 2018). A detailed description of this procedure and the analysis of the subsequent astrometric and photometric errors is provided in Appendix A of H15. In short, point-spread function (PSF) fit astrometry and photometry is extracted using a grid of spatially-varying PSF models across the field. No significant differences in measurement precision were found for the 2016 epoch compared to the previous epochs, with average astrometric and photometric errors of 0.15 mas and 0.008 mag, respectively, for the brightest non-saturated stars. The photometry is calibrated to the Vega magnitude system using the improved `KS2` zero-points derived in Hosek et al. (2018, hereafter H18), which uses significantly more stars than the original zero-point derivation in H15.

The stellar positions in each epoch are transformed into a master astrometric reference frame using a 2nd-order polynomial transformation in both X and Y (12 free parameters). The master frame is constructed such that there is no net motion of the cluster, as only high-probability cluster

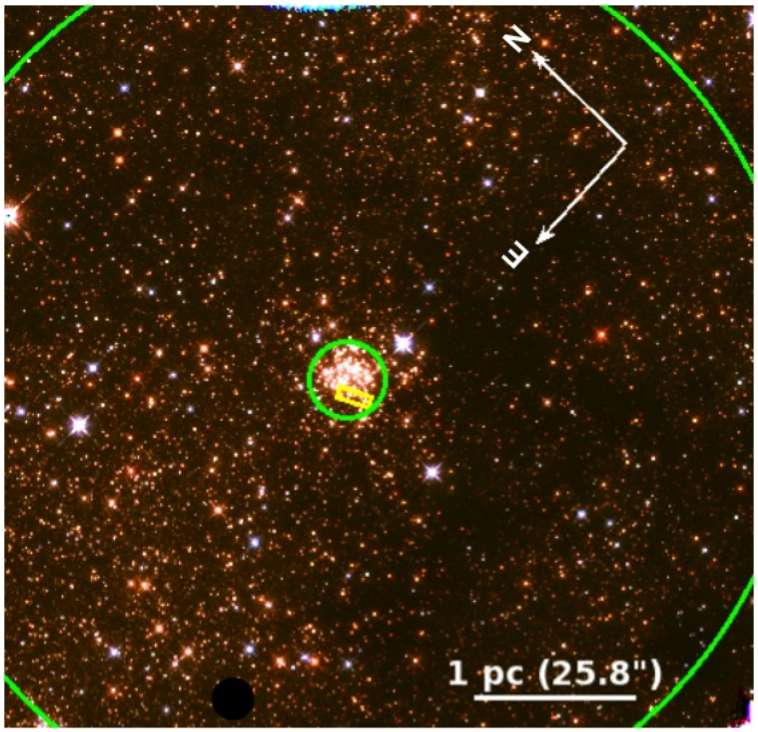

Figure 4.1 Three color *HST* image of the Arches Cluster, with F127M = blue, F139M = green, and F153M = red. The inner and outer green circles represent cluster radii of 0.25 pc and 3.0 pc, which define the boundaries of our *HST* sample. The yellow box near the center of the cluster corresponds to the Keck OSIRIS field, where K-band spectroscopy of 5 cluster members were obtained. The hole in the lower left side of the image is due to a known defect in the WFC3IR chip.

members ($\geq$0.7) in the H15 catalog are used as reference stars. An iterative process is used to match stars, calculate initial proper motions, and then rematch stars using those proper motions to identify stars across the epochs. The star matching is done by position, using a search radius of 0.5 pix (0.06"). Proper motions are calculated for stars detected in at least 3 F153M epochs using a linear fit to the X and Y positions as a function of time, weighted by their astrometric errors. The final star catalog contains $\sim$45,000 stars with proper motion errors 3 times smaller than H15 due to the increased time baseline, reaching a precision of $\sim$0.03 mas yr^{-1} at the bright end (Figure 4.2).

4.2.2 Keck OSIRIS Spectroscopy

K-band spectroscopy of a sample of Arches cluster members was obtained using the OH-Suppressing Infrared Integral Field Spectrograph (OSIRIS; Larkin et al. 2006) with Laser Guide Star Adaptive

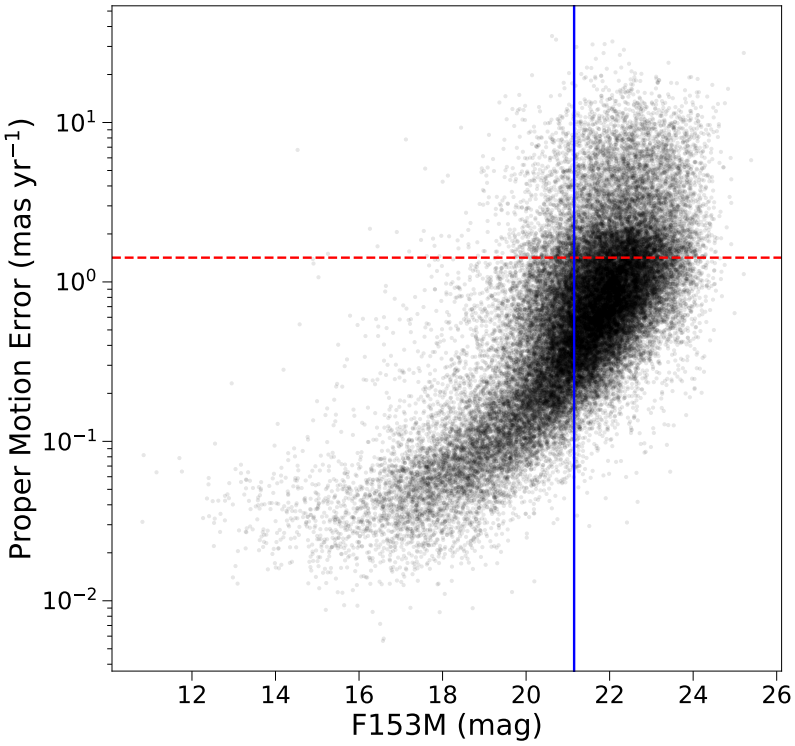

Figure 4.2 Proper motion error as a function of F153M magnitude in the final star catalog. For each star, the error shown is the average between the X and Y directions. The red dotted line denotes the proper motion error limit of 1.42 mas yr^{-1} required for membership analysis (§4.3.1). The solid blue line shows the completeness limit of F153M = 21.15 mag, which corresponds to ∼1.8 $M_{\odot}$ (§4.3.3). These errors are $\sim 3\times$ lower than those reported in H15 due to the increased time baseline.

Optics (Wizinowich et al. 2006) on the Keck I telescope on 2014 May 16. The Kbb filter was used with the 0.10" spatial scale, which provides a spectral coverage of 1.965 μm – 2.381 μm at R $\sim$ 3800 over a 1.6" x 6.4" FOV. A single field was observed near the core of the cluster (J2000: α = 17:45:50.7, δ = -28:49:23.4; Figure 4.1) at a position angle of 28°, using 10 dithered exposures of 900 s for a total integration time of 9000 s. This field was chosen to maximize the number of non-WR stars (F153M $\geq$ 14.5 mag, see §4.3.4) while avoiding the densest inner region of the cluster. The spectroscopic sample contains five stars, as described in Table 4.1.

Table 4.1. OSIRIS Spectroscopic Sample

Name[a]	RA[b] (J2000)	DEC[b] (J2000)	Spectral Type[c] (literature)	F127M (mag)	F153M (mag)	A_{Ks}[d] (mag)	T_{eff} (K)	log g (cgs)
47	17:45:50.68	-28:49:24.39	O4-5 Ia	17.01 ± 0.01	14.85 ± 0.01	2.12	34750^{+3000}_{-1500}	$3.50^{+0.30}_{-0.15}$
44	17:45:50.62	-28:49:24.77	–	17.18 ± 0.01	14.91 ± 0.01	2.13	34500^{+3000}_{-1500}	$3.75^{+0.15}_{-0.25}$
53	17:45:50.64	-28:49:24.14	O4-5 Ia	17.10 ± 0.01	14.91 ± 0.01	2.12	37000^{+2000}_{-2000}	$3.50^{+0.30}_{-0.10}$
55	17:45:50.73	-28:49:24.54	O5.5-6 I-III	17.09 ± 0.01	14.97 ± 0.01	2.09	34500^{+3000}_{-1500}	$3.85^{+0.25}_{-0.15}$
60	17:45:50.74	-28:49:21.08	O4-5 Ia	17.20 ± 0.01	15.03 ± 0.01	2.09	36000^{+2500}_{-1500}	$3.60^{+0.20}_{-0.15}$

[a] As defined in the catalog from Figer et al. (2002)

[b] Measured in 2010 F153M epoch

[c] From Clark et al. (2018)

[d] Derived using the extinction map in §4.3.2

The OSIRIS data cubes were reduced using version 4.1.0 of the OSIRIS data reduction pipeline[1] (ODRP; Krabbe et al. 2004). The ODRP corrects for dark current, electronic biases and crosstalk, and cosmic rays, and properly extracts the wavelength-calibrated spectrum at each spaxel (spatial pixel). The science data cubes were averaged together using the "Mosaic Frames" module to create the master science data cube. One-dimensional science spectra were extracted using a 3x3 aperture box centered on the spaxel with the highest integrated flux for the star. This aperture size was chosen to maximize the signal-to-noise while minimizing contamination from nearby stars.

After extraction, the raw science spectra need to be corrected for contamination from sky features such as continuum, OH emission lines, and telluric absorption lines. The standard set of calibration observations (sky frames and telluric standards) were obtained at the telescope, but we found that the sky features were better corrected using the `Skycorr`[2] (Noll et al. 2014) and `molecfit`[3] (Smette et al. 2015; Kausch et al. 2015) software packages. `Skycorr` removes sky emission lines by fitting physically-related OH line groups in a reference sky spectrum and scaling them to match the science spectrum (e.g. Davies 2007). The sky continuum is measured by a linear interpolation of the wavelength channels without line emission, and then combined with the OH line model to produce the final sky spectrum that is subtracted from the science spectrum. In this case, a reference sky spectrum for each star is extracted using a box annulus formed by a 5x5 and 7x7 spaxel box centered on the star itself, and then rescaled to science spectrum aperture size. Once `Skycorr` has removed the sky emission and continuum, the telluric absorption lines are modeled using `molecfit`, which uses a radiative transfer code and an atmospheric profile based on the date and location of the observations to predict atmospheric lines caused by molecules such as H_2O, CO_2, and CH_4. The telluric model is then divided out of the science spectrum to produce the final reduced science spectrum.

However, as discussed by Lockhart et al. (2017), OSIRIS introduces a shape to the stellar continuum due to its varying sensitivity as a function of wavelength that cannot be modeled by `molecfit`. This requires an extra step of creating an OSIRIS "flat" free of sky, telluric, and stellar flux contributions. We construct this flat using the observed telluric standards, empirically subtracting the sky and using `molecfit` to remove the telluric lines. In the A0 V spectrum, the

[1] https://github.com/Keck-DataReductionPipelines/OsirisDRP/releases
[2] http://www.eso.org/sci/software/pipelines/skytools/skycorr
[3] https://www.eso.org/sci/software/pipelines/skytools/molecfit

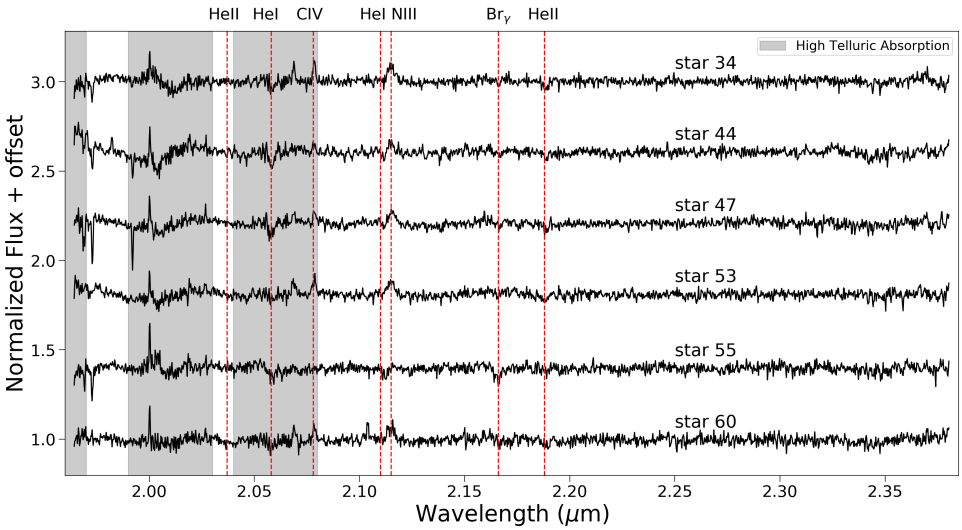

Figure 4.3 Reduced OSIRIS spectra of Arches cluster members. The gray regions mark wavelengths with high telluric absorption, while the red dotted lines denote several useful spectral features.

only remaining feature is the Br-γ line. To remove this line, we combine the A0 V and GII V spectra using the technique described in Do et al. (2009), replacing the A0 V spectrum between 2.155 μm and 2.175 μm with the spectrum of the GII V star after it has been divided by the solar spectrum. Finally, we smooth the resulting spectrum using a median filter (kernel size = 51 pix) to create the OSIRIS flat. The science spectra are divided by this flat and normalized to produce the final science spectra (Figure 4.3).

4.3 Methods

4.3.1 Proper-Motion Based Cluster Membership

Cluster membership probabilities are calculated using the proper motions derived in §4.2.1 and the Gaussian Mixture Model technique described in H15. This approach provides the flexibility to fit the complex kinematics of the cluster and field populations while taking the proper motion errors into account. To reduce outliers, an error cut of 1.42 mas yr^{-1} (1/3 of the difference between the average cluster and field population proper motions in H15) is adopted, resulting in a membership catalog of 29,895 stars. This is significantly larger than the sample analyzed in H15 (∼6000 stars) because we adopt a proper motion error cut that is 2.2x larger, do not impose a magnitude error

cut, and generally have improved proper motion errors due to the extra epoch of data. As a result, a 5-gaussian mixture model is required to fit the cluster and field populations (Figure 4.4), as opposed to the 4-gaussian model used in H15.

Individual cluster membership probabilities are calculated as

$$P^i_{pm} = \frac{\pi_c P^i_c}{\pi_c P^i_c + \sum_k^K \pi_k P^i_k} \tag{4.2}$$

where π_c and π_k are the fraction of total stars in the cluster and kth field Gaussian, respectively, and P^i_c and P^i_k are the probability of ith star being part of the cluster and kth field Gaussian, respectively. A table describing the parameters of the Gaussian Mixture Model fit is provided in Appendix 4.8. A Monte Carlo simulation reveals that the uncertainty in the cluster membership probabilities is less than 3% across the sample, and so it is ignored in the following analysis.

4.3.2 Extinction Correction

Red Clump (RC) stars are used to correct for differential extinction across the field. The intrinsic magnitude and colors of these stars do not vary significantly with age or metallicity, making them useful "standard crayons" with which to measure extinction (Girardi 2016). While not associated with the Arches cluster itself, RC stars are numerous in the Galactic bulge and have a density distribution that is sharply peaked at the GC (Wegg & Gerhard 2013). Thus, we assume that the extinction of the RC stars is similar to that of the cluster, and so an extinction map derived using RC stars can be used for cluster stars. This approach was validated in H15, who showed that an RC extinction map significantly reduced the differential extinction in proper-motion selected Arches members.

We improve the extinction map presented in H15 by using a refined sample of RC stars identified using an unsharp masking technique (e.g. De Marchi et al. 2016) and adopting the updated optical/near-infrared extinction law derived for highly reddened populations in the Galactic Plane from H18. The advantage of the unsharp masking technique is that it increases the contrast of high-density features, such as the RC population, while reducing low-frequency noise. We select RC stars using the criteria described in H18: we calculate a best-fit line to the high-density RC feature in the CMD after unsharp masking and identify stars within ΔF153M = 0.3 mags of the

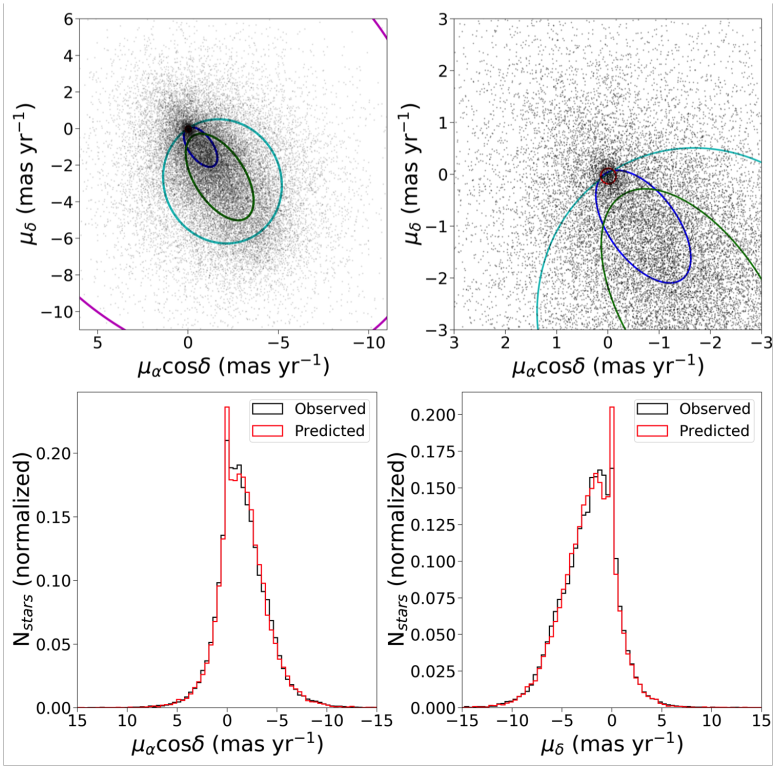

Figure 4.4 The Gaussian Mixture Model fit to the observed cluster and field proper motion distributions. Top: The vector point diagram of the proper motions with the 1σ gaussian contours overlaid. The red gaussian corresponds to the cluster, while the blue, green, cyan, and magenta Gaussians describe the field population. The right panel is a zoomed-in version of the left panel, focusing on the cluster distribution. Bottom: The observed (black) vs. predicted (red) proper motion distributions in the RA and DEC directions (left and right panels, respectively). Good agreement is found between the observations and model.

best fit line as the RC population (see Figure 7 from H18). This width is selected to encompass the RC feature, and is likely caused by the distribution of stellar distances, metallicities, and ages within the population, all of which alter their location in the CMD. In addition, we only consider stars with $P_{clust} \leq 0.02$ in order to eliminate cluster members from the sample (which is necessary since the populations overlap in CMD space), and require a photometric error better than 0.05 mags in both the F127M and F153M filters in order to remove field interlopers that scatter into the selection space. Ultimately, 869 RC stars are used in the final extinction map.

The Arches extinction map is created using a spatial interpolation of the RC star sample with a fifth-order bivariate spline[4] (Figure 4.5). All pixels with $r_{cl} < 0.25$ pc are removed from the map, since high stellar crowding prevents an adequate number of RC stars from being detected at these radii. Ignoring the extreme values at the edge of the field where the interpolation becomes invalid, the extinction map values range from 1.6 mag $< A_{Ks} <$ 2.31 mag, with a median extinction of $A_{Ks} = 2.07$ mag for stars with $P_{pm} \geq 0.5$. These extinctions are systematically lower than the ones reported in H15 (1.8 mag $< A_{Ks} <$ 3.0 mag, with a median of $A_{Ks} = 2.4$ mag for likely cluster members) due to the updated extinction law. We will adopt this as an initial estimate for the average extinction of the cluster and include a term in the IMF analysis to capture residual differential extinction in the cluster due to errors in the extinction map (§4.4).

4.3.3 Completeness

Observational completeness is determined using artificial star planting and recovery tests. We plant a total of 675,000 artificial stars and run them through the same detection pipeline as the real stars. These stars are generated in three sets. The first set contains 400,000 artificial stars with magnitudes drawn from the observed CMD, perturbed by a random amount drawn from a Gaussian distribution with a width equal to the photometric uncertainty. These stars are planted uniformly across the field. The second set contains 175,000 artificial stars that are assigned to a grid of magnitudes and colors in order to cover sparsely populated regions of the CMD (e.g., the brightest and faintest observed magnitudes), in order to improve the confidence of the completeness corrections in these regions. These stars are also given a uniform spatial distribution. The final set of 100,000 artificial stars are generated based on the brighter stars in the observed CMD (F153M $\leq$

[4]The interpolation is calculated using the *scipy.interpolate.bisplrep* routine in `python`.

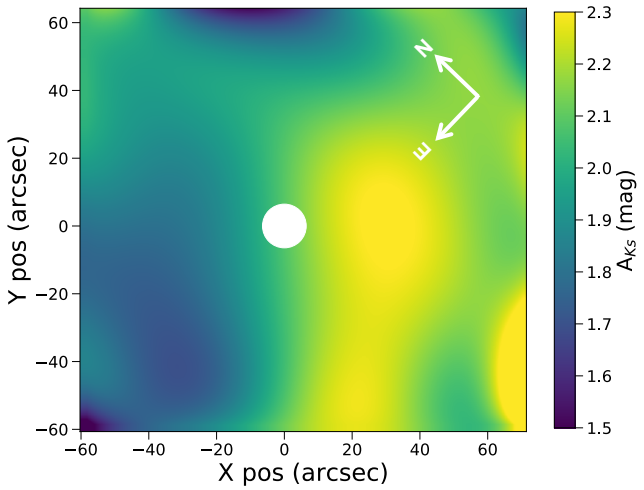

Figure 4.5 The RC-interpolated extinction map for the Arches cluster field, with the positions shown in arcseconds relative to the cluster center. No measurement is made for $r_{cl} < 0.25$ pc due to the low HST completeness in the area.

18 mag) and planted according to the radial profile of the Arches cluster from H15. This increases the confidence of the completeness correction near the cluster center, where the effects of stellar crowding are strongest.

After the artificial stars are extracted by the detection pipeline, their photometric and astrometric errors are lower than the real data errors because they don't account for PSF uncertainty. Following H15, a magnitude-dependent error term is added in quadrature to the artificial star errors so their distribution matches those of the real star errors. Proper motions are then calculated and photometry differentially de-reddened for the artificial stars in the same manner as the real stars. To be successfully recovered, an artificial star must detected within 0.5 mags of its planted magnitude and 0.5 pixels of its planted position in at least three of the four F153M epochs and the F127M epoch, and have a proper motion error ≤ 1.42 mas yr^{-1}. The resulting F127M and F153M completeness curves as a function of differentially de-reddened magnitude in different cluster radius bins (0 pc $\leq$ R $\leq$ 3 pc, in steps of 0.25 pc) are shown in Figure 4.6.

For the IMF analysis, we calculate the completeness for each star based on its cluster radius and position in the CMD. Within a given radius bin, the CMD is binned in steps of 0.15 mags in F153M (range: 24.5 mag – 12.3 mag) and 0.2 mags in F127M - F153M (range: 0 mag – 5 mags). The completeness in each bin is assigned to the lowest value from the F127M and F153M completeness

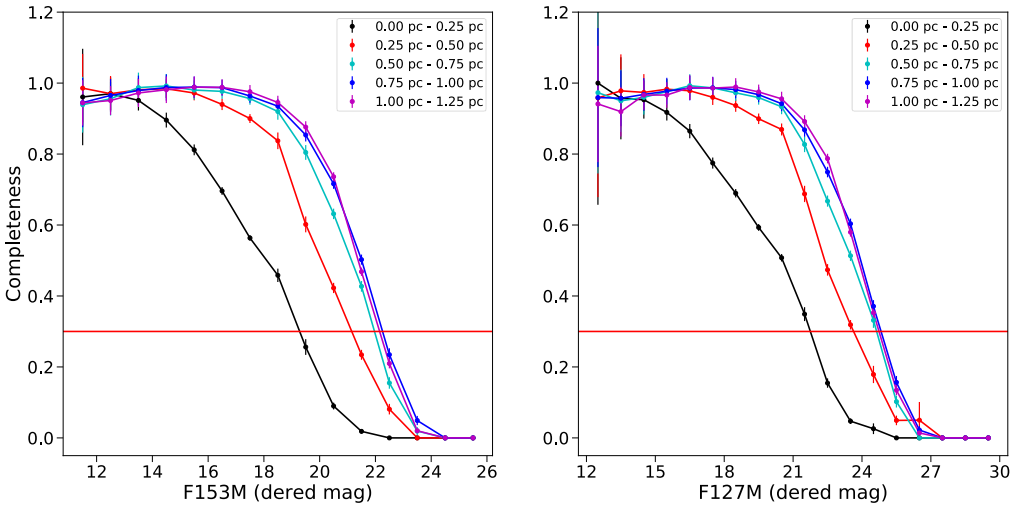

Figure 4.6 Observational completeness as a function of cluster radius and differentially de-reddened F153M (left panel) and F127M (right panel) magnitude. At the average color of the cluster in the CMD, the F153M curve sets the completeness. Due to the low completeness in the innermost radius bin (0 pc - 0.25 pc), we exclude stars at these radii from the IMF analysis. We require a minimum requirement of 30% completeness across the sample (red horizontal line), and thus adopt an F153M magnitude cut at F153M = 21.15 mag (§4.3.4).

curves at the respective F153M and F127M magnitudes at the center of the bin. At the average color of the cluster, the F153M curve sets the completeness limit.

4.3.4 Final Sample

Starting with the cluster membership catalog described in §4.3.1 (29,895 stars), we apply a series of cuts in order to produce a high-quality sample for the IMF analysis. We require:

- $P_{pm} \geq 0.3$, in an effort to reduce the number of field stars in our sample.
- A minimum of 30% completeness as determined in §4.3.3. Due to the limited HST completeness at small cluster radii, we only consider stars with 0.25 pc $\leq r_{cl} \leq$ 3.0 pc. We thus achieve a depth of F153M $\leq$ 21.15 mag, corresponding to M $\geq\sim$1.8 $M_{\odot}$.
- A minimum of 30% area coverage within the field-of-view at a given radius. As discussed in H15, this is achieved for $r_{cl} \leq$ 3.0 pc

Table 4.2. Sample Selection

Selection Description	Criterion	N_{stars}	$\sum P_{pm}$
Original Sample		**29895**	**1290.7**
	Cut from Sample		
Membership	$P_{pm} \geq 0.3$	28237	
Completeness	≥ 0.3	539	
F153M Mag Diff	≤ 0.5 mags	45	
WR stars	F153M ≥ 14.5 mag	16	
Color cut	see §4.3.4	78	
Final Sample		**980**	**636.7**

- All F153M measurements for a given star to agree with its median F153M magnitude within 0.5 mags. This was found to remove situations where a faint star is misidentified as a nearby bright star.

- WR stars will be removed from our sample, given the uncertainty in their stellar models and thus stellar masses. We use the population of spectroscopically-identified WR stars in the Arches cluster (Figer et al. 2002; Martins et al. 2008; Clark et al. 2018) determine their F153M magnitudes at the average cluster extinction of $A_{Ks} = 2.07$ mag. We find find the faintest of these stars have a differentially de-reddened magnitude of F153M = 14.1 mags (star B1 in Clark et al. 2018), and so adopt a conservative magnitude cut of F153M ≥ 14.5 mag.

Finally, a photometric color-cut is used to remove obvious field contaminants from the sample. High-probability cluster members ($P_{pm} \geq 0.6$) are corrected for differential extinction as described in §4.3.2, and a 3σ clipping algorithm is used to calculate the average F127M - F153M color and standard deviation as a function of F153M magnitude. For the entire sample, stars with differentially de-reddened colors larger than 2σ to the blue or 3σ to the red of the cluster sequence are automatically assigned $P_{pm} = 0$, while all others are unchanged. This color-cut is more conservative to the red in order to account for the fact that some stars may have intrinsic reddening due to circumstellar disk material due to the cluster's young age (e.g. Stolte et al. 2015).

After these cuts, we are left with a sample of 980 stars with $\sum P_{pm} = 636.7$. The CMD of this sample before and after the differential extinction correction is shown in Figure 4.7, and a summary of the cuts and their impact on the sample size is given in Table 2.

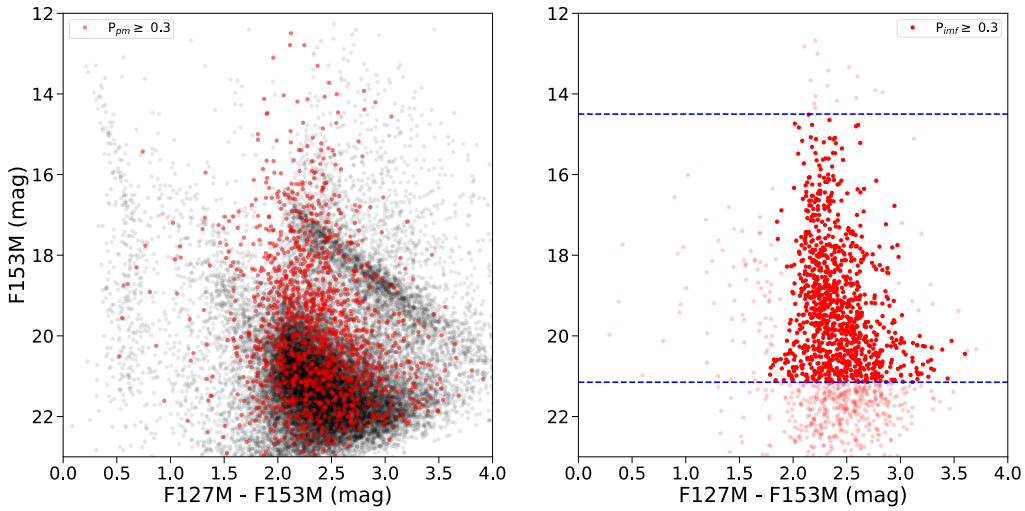

Figure 4.7 Left: The observed CMD of the proper-motion selected sample ($P_{pm} \geq 0.3$; in red) versus the field stars (black). Due to the significant overlap between the populations, proper-motion analysis is required to obtain an accurate cluster sample. Right: The differentially de-reddened CMD of the stars used in the IMF analysis. The solid red points are stars with $P_{pm} \geq 0.3$ and F153M magnitudes within the adopted magnitude limits (blue dashed line). Stars eliminated by the color or magnitude cuts are shown as the faded red points. The cluster sequence significantly tightens after the differential extinction correction, though a term for residual differential extinction is still required in the IMF analysis.

Despite these efforts, some field contamination inevitably remains in our sample. This is due to stars with similar proper motions and colors as the cluster, and so their membership probabilities are artificially inflated. In §4.5.1, we derive revised cluster membership probabilities *after* the IMF analysis using the best-fit cluster and field model in order to take full advantage of the photometric information. We find that the number of cluster stars based on P_{pm} is ∼8% larger than the number of cluster stars based on the revised membership probabilities, and thus conclude that the sample contains approximately this amount of field contamination.

4.3.5 Spectroscopic Analysis

Effective temperatures and surface gravities are derived for the spectroscopic stars by comparing the spectra to non-LTE CMFGEN model atmospheres (Hillier & Miller 1998; Hillier & Lanz 2001). Non-LTE treatment is required due to the high temperatures of the stars and the presence of significant stellar winds, as evidenced by the Br-γ emission inferred from the weak Br-γ photospheric absorption line. Uncertainties in the stellar parameters are conservatively estimated by adjusting the models until poor fits are obtained for the main diagnostic lines. Throughout the analysis we assume a terminal velocity (V_{inf}) of 2000 km s^{-1}, since this cannot be constrained from the spectra.

The best-fit model spectra are shown in Figure 4.8 and the corresponding T_{eff} and log g values are reported in Table 4.1. T_{eff} is constrained to within ±3000 K or better, and is determined primarily from the HeII/HeI line ratios as well as the absorption component of the HeI 2.113 μm line. Stars 47, 55, and 60 were recently classified as O4-5 Ia stars and star 53 as an O5.5-6 I-III star by Clark et al. (2018). Our derived temperatures are consistent with the observed T_{eff} vs. spectral type relation for galactic O-type stars within uncertainties (Martins et al. 2005). The log g values are less well constrained since they rely on the weak Brγ lines, and thus are not used in the IMF analysis.

4.4 Modeling the Cluster

We use a forward modeling approach to derive the IMF of the Arches cluster, comparing the observations to a cluster and field model within a Bayesian framework. The methodology described

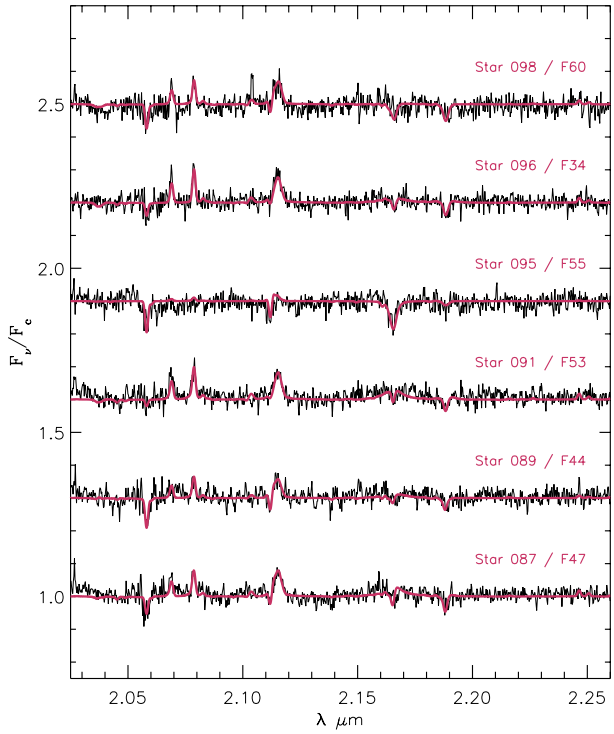

Figure 4.8 Best-fit CMFGEN models (red) compared to the observed spectra (black).

Table 4.3. IMF Model Parameters

Parameter	Description	Prior[a]	Units
α_1	High-mass IMF slope	U(1.0, 3.0)	—
dα	α_2 / α_1[b]	U(0, 1)	—
m_{break}	Break mass[b]	U(2, 14)	$M_\odot$
M_{cl}	Mass[c]	U(3000, 50000)	$M_\odot$
log t	Age	U(6.2, 7.0)	log(years)
d	Distance	G(8000, 250)	parsecs
A_{Ks}	Average extinction	U(1.5, 2.7)	A_{Ks} (mags)
ΔA_{Ks}	Differential extinction	U(0, 0.5)	A_{Ks} (mags)

[a]Uniform distributions: U(min, max), where min and max are bounds of the distribution; Gaussian distributions: G(μ, σ), where μ is the mean and σ is the standard deviation

[b]Only used in 2-segment IMF model

[c]Formally, M_{cl} is the cluster mass between m_{min} and m_{max} (0.8 $M_\odot$ and 150 $M_\odot$, respectively) since this is the mass range over which the IMF is sampled when constructing the cluster

in Lu et al. (2013) is expanded to simultaneously fit the IMF and other cluster parameters while taking into account degeneracies between cluster parameters, observational uncertainties, stellar multiplicity, and the empirical field population. Two IMF models are used: a 1-segment power law and a 2-segment power law. In the 1-segment IMF model, the free parameters are the the high-mass IMF slope α_1, the cluster mass (M_{cl}), age (log t), distance (d), average extinction (A_{Ks}), and residual differential extinction after the extinction map correction (ΔA_{Ks}). The 2-segment IMF model has additional free parameters m_{break} and dα, where m_{break} is the mass at which the IMF slope is α_2 = dα * α_1 for m $\leq$ m_{break} and α_1 for m > m_{break}. We require that $0 \leq$ dα ≤ 1 to enforce that $\alpha_2 <= \alpha_1$ (i.e., the low-mass IMF slope is more shallow than the high-mass IMF slope). The model parameters and their adopted priors are presented in Table 4.3.

To create a synthetic cluster, a population of stellar masses is stochastically generated based on the input IMF and the total cluster mass. We use the numerical formulation described by Pflamm-Altenburg & Kroupa (2006) to efficiently generate masses from the IMF between 0.8 $M_\odot$ and 150 $M_\odot$. Note that this is the mass range over which M_{cl} is valid, since masses above and below these values are not generated in the synthetic cluster. The multiplicity of each star is determined using the mass-dependent multiplicity fraction, companion star fraction, and mass ratio empirically derived by Lu et al. (2013) from studies of nearby young clusters in the literature. Stars and their

companions are generated in batches until the cumulative stellar mass is larger than the designated mass of the cluster. Then, the population is trimmed to the star at which the cumulative mass is closest to the overall cluster mass, and then 1 additional star is drawn from the IMF and added to the sample.

Stellar evolution models are used to determine the physical properties of each star in the population. For a given age, a stellar evolution model provides the effective temperature (T_{eff}) and surface gravity ($\log g$) at each stellar mass. We use two sets of stellar evolution models: the Pisa evolution models (Tognelli et al. 2011) for the pre-main sequence stars and the most recent Geneva models with rotation (Ekström et al. 2012) for the main sequence and evolved stars. The Pisa models have been shown to be consistent with observations of eclipsing binaries (Stassun et al. 2014) and nearby moving groups (Herczeg & Hillenbrand 2015) for stars above 1 $M_{\odot}$, and are advantageous in that they model pre-main sequence stars to high masses ($\sim$7 $M_{\odot}$). High mass pre-main sequence stars are necessary due to the young age of the Arches cluster. The Geneva models have been shown to match observations for all but the most massive stars ($M > 60$ $M_{\odot}$; Martins & Palacios 2013), where stellar evolution models become uncertain.

The physical properties are fed into a stellar atmosphere model, which returns a spectral energy distribution (SED) for each star. We assume solar metallicity, consistent with spectroscopic studies of the bright WR stars which find the Arches metallicity to be solar (Najarro et al. 2004) or slightly super-solar (Z = 1.3 - 1.4 $Z_{\odot}$; Martins et al. 2008). Two sets of atmosphere models are used: an ATLAS9 grid (Castelli & Kurucz 2004) for $T_{eff} > 5500$ K and a PHOENIX grid (version 16; Husser et al. 2013) for $T_{eff} < 5000$ K. An average between the two model grids is used in the transition region between 5000 K – 5500 K. Both model grids assume local thermodynamic equilibrium (LTE), an assumption that begins to fail for massive stars. However, synthetic photometry calculated with ATLAS9 models compared to non-LTE CMFGEN models (Fierro et al. 2015) show differences of $\leq\sim$0.017 mags in F153M up to temperatures of 31,000 K.

The choice of stellar evolution and atmosphere models is an unavoidable source of systematic uncertainty in our analysis. To assess the impact of our model selections, we also run our IMF analysis using the recent MIST v1.0 evolution models (Choi et al. 2016; Dotter 2016), which are computed using the Modules for Experiments in Stellar Astrophysics (MESA) code (Paxton et al. 2011, 2013, 2015). These analysis are discussed in §4.6.4.

We use *Pysynphot* (STScI Development Team 2013) to calculate synthetic photometry for the individual stars in the cluster population. The SEDs are reddened to the model A_{Ks} according to the extinction law from H18 and then convolved with the WFC3IR F127M and F153M filter transmission functions. Multiple systems are treated as unresolved, with the total flux in each filter calculated as the sum of the system components. To simulate differential extinction, the photometry of each star system is perturbed by a random amount drawn from a Gaussian distribution centered at 0 with a width corresponding to the given ΔA_{Ks} in that particular filter.

Finally, the synthetic stars are assigned cluster radii based on the observed radial density profile of the Arches. We combine the radial profile for R < 0.25 pc from (Espinoza et al. 2009) with the magnitude-dependent profiles between 0.25 pc ≤ R ≤ 3.0 pc from H15 (F153M > 17 mag, F153M ≤ 17 mag) for complete radial coverage over our data range. The stellar radii are drawn from the following probability density distribution:

$$P(r) = \begin{cases} \frac{1}{c_b}\Sigma_b(r) 2\pi r\ a(r)\ dr, & F153M \leq 17 \text{ mag} \\ \frac{1}{c_f}\Sigma_f(r) 2\pi r\ a(r)\ dr, & F153M > 17 \text{ mag} \end{cases} \tag{4.3}$$

where $\Sigma_b(r)$ and $\Sigma_f(r)$ are the bright-star (F153M ≤ 17 mag) and faint-star (F153M > 17 mag) radial profiles, respectively, c_b and c_f are constants such that $\int_{r=0pc}^{r=3pc} P(r) = 1$, and a(r) is the fraction of the observed area at radius r relative to that of an infinitely large field of view ($a(r) = 1.0$ for $0 < r \leq 2.3$ pc, $A_i < 1.0$ for $r > 2.3$ pc). Thus we are able to simulate mass segregation in the synthetic cluster, and can properly account for the fact that all stars with $r <$ 0.25 pc are removed from the observed sample due to low completeness. The synthetic cluster stars are then binned using the same radius, color, and magnitude bins as the completeness calculations (§4.3.3) in preparation for the IMF analysis.

4.4.1 Bayesian Analysis

For a cluster model Θ, we adopt a likelihood function with four components:

$$\mathcal{L}(\boldsymbol{k_{obs}}, N_{cl}, N_{WR}, T_{eff}|\Theta) = p(\boldsymbol{k_{obs}}|\Theta) \cdot p(N_{cl}|\Theta) \cdot p(N_W|\Theta) \cdot p(\{T_{eff}, m_{obs}\}|\Theta) \tag{4.4}$$

where $p(\boldsymbol{k_{obs}}|\Theta)$ is the probability of obtaining the observed distribution of stars in CMD space, with $\boldsymbol{k_{obs}}$ representing the set of observed F153M magnitudes and F127M - F153M colors; $p(N_{cl}|\Theta)$ is the probability of detecting the number of observed cluster stars N_{cl}; $p(N_W|\Theta)$ is the probability of the detecting the observed number of WR stars; and $p(\{T_{eff}, m_{obs}\}|\Theta)$ is the probability of measuring the observed T_{eff} values for the spectroscopic stars given their F153M magnitudes m_{obs}.

To calculate $p(\boldsymbol{k_{obs}}|\Theta)$ we must first calculate the CMD probability distribution for the cluster model and the field. The intrinsic CMD distribution of cluster stars generated by the model Θ, $p(\boldsymbol{k_{int}}|\Theta)_{cl}$, is calculated according to the procedure described in §4.4. Here, $\boldsymbol{k_{int}}$ is the distribution of synthetic star mags and colors in the model cluster. To reduce the impact of stochastic effects in the synthetic CMD, the model cluster is generated with a total mass of 5x10^6 $M_\odot$ ($\sim$500 times more massive than the expected mass of the Arches), regardless of the M_{cl} designated by the model. To calculate CMD probability distribution we would "observe" for the model cluster, we apply the observational completeness and make the same magnitude cuts as the observed sample (§4.3.4):

$$p(\boldsymbol{k_{int}}|\Theta)_{cl,obs} = \frac{\sum_{r=0}^{N_r} p(\boldsymbol{k_{int,r}}|\Theta)_{cl} * C(r)}{\sum_{k=0}^{N_k} \sum_{r=0}^{N_r} p(\boldsymbol{k_{int,r}}|\Theta)_{cl} * C(r)} \tag{4.5}$$

where $p(\boldsymbol{k_{int,r}}|\Theta)_{cl}$ and $C(r)$ are the intrinsic model cluster CMD and observational completeness at a cluster radius r, N_r is the number of radius bins, and N_k is the total number of magnitude-color bins in the CMD itself.

In addition to the synthetic cluster, we construct a CMD probability distribution for the field stars. We select all stars with $P_{pm} \leq 0.03$ and then apply the same differential extinction correction, magnitude, and color cuts as the IMF analysis sample and then normalize their CMD distribution:

$$p(\boldsymbol{k_{obs,f}}) = \frac{\boldsymbol{k_{obs,f}}}{\sum_{k=0}^{N_k} \boldsymbol{k_{obs,f}}} \tag{4.6}$$

where $\boldsymbol{k_{obs,f}}$ is the observed field CMD and $p(\boldsymbol{k_{obs,f}})$ is the field CMD probability distribution. Note that we do not apply a completeness correction since the CMD is already "observed" and thus it is already inherently included, and that $p(\boldsymbol{k_{obs,f}})$ is not dependent on the cluster model.

With the cluster and field CMD probability distributions in place, we can calculate the probability of observing the ith star given its color and magnitude ($p(k_{obs,i}|\Theta)$). We infer that the field membership probability for a given star is P_f = 1 - P_{pm}. To incorporate observational

error, we assume that $k_i = k'_i + \epsilon$, where ϵ is drawn from a normal distribution centered at zero and with standard deviation drawn from the set of observational errors $\sigma_{k,i}$. Thus:

$$p(k_{obs,i}|\Theta) = \int_{-\infty}^{\infty} (P_{pm} * p(\boldsymbol{k_{int}}|\Theta)_{cl,obs} + P_f * p(\boldsymbol{k_{obs,f}})) * \frac{1}{\sqrt{2\pi\sigma_{k,i}}} e^{\frac{-(k'_i - k_i)^2}{2\sigma^2_{k,i}}} dk'_i \tag{4.7}$$

The final CMD likelihood is calculated by multiplying the individual likelihoods for the observed stars together:

$$p(\boldsymbol{k_{obs}}|\Theta) = \prod_{i=1}^{N_{obs}} p(k_{obs,i}|\Theta) \tag{4.8}$$

where N_{obs} is the number of stars in the sample.

The second component of the likelihood, $p(N_{cl}|\Theta)$, is calculated from the number of cluster stars we would predict to observe given the cluster model. Returning to the intrinsic synthetic cluster CMD $\boldsymbol{k_{int}}$, we perturb the photometry of each star by a random amount drawn from the photometric error of the observations at its magnitude and then apply the magnitude cuts and observational completeness. Following Lu et al. (2013), we linearly scale the number of stars in the simulated cluster after it is convolved with the observational completeness (N_{sim}) to the cluster model mass in order to obtain the expected number of observed stars N_e:

$$N_e = N_{sim} * \left(\frac{M_{cl}}{5 * 10^6}\right) \tag{4.9}$$

where M_{cl} is the cluster model mass. The probability of obtaining the observed number of cluster stars $N_{cl} = \sum P_{pm}$ is calculated from a Poisson distribution:

$$p(N_{cl}|\Theta) = \frac{N_e^{N_{cl}} e^{-N_e}}{N_{cl}!} \tag{4.10}$$

The purpose of applying the observational errors to $\boldsymbol{k_{int}}$ for this calculation to account for any potential Malquist bias that is introduced by our magnitude cuts. Note that this is not done in Equation 4.5 for the CMD component of the likelihood since the observational errors are already accounted for in Equation 4.7.

The third component of the likelihood is based on the predicted number of WR stars in the cluster model, which serves as a constraint on the cluster age (e.g. Lu et al. 2013). The brightest stars in the inner region of the cluster ($r_{cl} < 0.75$ pc) were cataloged by Figer et al. (2002), and later spectroscopic studies identified 13 WR stars among this sample (Martins et al. 2008; Clark et al. 2018). In the cluster model, we calculate the number of predicted WR stars within this radius range and, similarly scaling that number to cluster model mass, calculate the probability of obtaining the observed number of WR stars:

$$p(N_W|\Theta) = \frac{N_{W_0}^{N_W} e^{-N_{W_0}}}{N_W!} \tag{4.11}$$

where $N_W = 13$ and is the number of WR stars in the observations within $r_{cl} < 0.75$ pc, and N_{W_0} is the number of WR stars predicted by the scaled cluster model in that same radius range.

The final component of the likelihood comes from from the T_{eff} measurements from the spectroscopic sample. For each star, we calculate $\overline{T_{eff_0}}$ and σ_{Teff_0}, which represent the median T_{eff} and its standard deviation for all stars in the cluster model with (m_{obs} - $\sigma_{m_{obs}}$) $\leq m \leq$ (m_{obs} + $\sigma_{m_{obs}}$) and (col_{obs} - $\sigma_{col_{obs}}$) $\leq col \leq$ (col_{obs} + $\sigma_{col_{obs}}$) where m_{obs}, $\sigma_{m_{obs}}$, col_{obs}, $\sigma_{col_{obs}}$ are the F153M magnitude and F127M - F153M color of the observed star and its respective errors. The likelihood of measuring T_{eff} for the star is then:

$$p(T_{eff}, m_{obs}|\Theta) = \frac{1}{\sigma_{tot}\sqrt{2\pi}} * e^{-(T_{eff}-T_{eff_0})^2/(2\sigma_{tot}^2)} \tag{4.12}$$

where T_{eff} and $\sigma_{T_{eff}}$ is the measured effective temperature and associated error of the star and $\sigma_{tot} = \sqrt{\sigma_{T_{eff}}^2 + \sigma_{Teff_0}^2}$. The likelihood of the spectroscopic sample is calculated by multiplying the individual likelihoods together:

$$p(\{T_{eff}, m_{obs}\}|\Theta) = \prod_{i=1}^{N_{spec}} p(T_{eff_i}, m_{obs_i}|\Theta) \tag{4.13}$$

where N_{spec} is the number of stars in the spectroscopic sample.

We derive the best-fit cluster model using Bayes theorem:

$$P(\Theta|\boldsymbol{k_{obs}}, N_{cl}, N_{WR}, T_{eff}) = \frac{\mathcal{L}(\boldsymbol{k_{obs}}, N_{cl}, N_{WR}, T_{eff}|\Theta)P(\Theta)}{P(\boldsymbol{k_{obs}}, N_{cl}, N_{WR}, T_{eff})} \tag{4.14}$$

where $P(\Theta|\boldsymbol{k_{obs}}, N_{cl}, N_{WR}, T_{eff})$ is the posterior probability for the given model Θ, $\mathcal{L}(\boldsymbol{k_{obs}}, N_{cl}, N_{WR}, T_{eff}|\Theta)$ is the likelihood equation, $P(\Theta)$ is the priors on the model free parameters, and $P(\boldsymbol{k_{obs}}, N_{cl}, N_{WR}, T_{eff})$ is the sample evidence. To sample the parameter space to find the best-fit model we use *Multinest*, a publicly available multimodal sampling algorithm shown to be more efficient that Markov Chain Monte Carlo algorithms when exploring complex parameter spaces (Feroz et al. 2009). We adopt an evidence tolerance of 0.5, a sampling efficiency of 0.8, and 1000 live points to run the analysis. The algorithm is run using the python wrapper module *PyMultinest* (Buchner et al. 2014).

We test the accuracy of this procedure by running the analysis on simulated clusters of known properties. A discussion of how the simulated clusters are created and the results of the tests is provided in Appendix 4.10. We find that the analysis is able to recover the input values to within 1σ for all parameters for both the 1-segment and 2-segment IMF models.

4.4.2 Model-Dependent Membership Probabilities and Stellar Properties

After the best-fit cluster model is determined, we calculate a revised cluster membership probability for each star that takes full advantage of the available kinematic and photometric information. The cluster model provides the distribution of cluster stars in CMD space, from which stars with proper motions similar to the cluster but with photometry similar to the field can be de-weighted. First, we take the model cluster CMD probability distribution (after observational effects are applied) and field star CMD probability distribution and scale them by the total number of cluster stars and field stars in our sample:

$$\begin{aligned} \boldsymbol{k_{\Theta,cl}} &= \sum_{i=0}^{N_{obs}} P_{pm,i} * p(\boldsymbol{k_{int}}|\Theta)_{cl,obs} \\ \boldsymbol{k_f} &= \sum_{i=0}^{N_{obs}} P_{f,i} * p(\boldsymbol{k_{obs,f}}) \end{aligned} \tag{4.15}$$

where $\boldsymbol{k_{\Theta,cl}}$ and $\boldsymbol{k_f}$ are the scaled cluster and field CMDs, respectively, and $p(\boldsymbol{k_{int}}|\Theta)_{cl,obs}$ and $p(\boldsymbol{k_{obs,f}})$ are as defined in Equations 4.5 and 4.6. The revised membership probability for a given star then becomes:

$$P_{clust,i} = \int_{-\infty}^{\infty} \left(\frac{\boldsymbol{k_{\Theta,cl}}}{(\boldsymbol{k_{\Theta,cl}} + \boldsymbol{k_f})} \right) * \frac{1}{\sqrt{2\pi\sigma_{k,i}}} e^{\frac{-(k'_i - k_i)^2}{2\sigma^2_{k,i}}} dk'_i \tag{4.16}$$

P_{clust} is thus a combination of the proper motion membership, which sets the relative scale of cluster and field CMD components, and the CMD of the cluster model $\boldsymbol{k_{\Theta,cl}}$.

We also use the best-fit cluster model to infer the intrinsic properties (e.g. mass) for each star in the observed sample. These values are often estimated by tracing the star to a theoretical cluster isochrone along the reddening vector, but this approach is challenging near the pre-main sequence turn-on where multiple intersections between the reddening vector and isochrone can occur. Instead, we calculate a probability distribution for the desired stellar property from $\boldsymbol{k_{int}}$, based on the stars located at the observed star's location in the CMD. For example, the mass probability distribution within a given CMD bin k is:

$$p(m|\Theta)_k = \frac{\sum_i^{N_i} m_{i,b,k}}{\sum_b^{N_b} \sum_i^{N_i} m_{i,b,k}} \tag{4.17}$$

where $m_{i,b,k}$ is the mass of the ith star in mass bin b in the CMD bin k. N_i is the number of stars in mass bin b, and N_b is the total number of mass bins. The mass bins are chosen to be 20 equal log-space bins between 0.8 $M_\odot$ and 70 $M_\odot$, which are the minimum and maximum masses in the cluster model[5].

For a given star, we calculate its mass probability distribution by multiplying $p(m|\Theta)_k$ by the position of the star in the CMD convolved with its photometric error:

$$\phi(m)_i = \int_{-\infty}^{\infty} p(m|\Theta)_k * \frac{1}{\sqrt{2\pi\sigma_{k,i}}} e^{\frac{-(k'_i - k_i)^2}{2\sigma^2_{k,i}}} dk'_i \tag{4.18}$$

We construct the observed initial mass function Φ_{obs} by multiplying the mass probability distributions by each star's revised cluster membership probability, observational completeness as a function of CMD position and radius, $C(k, r)$, and area completeness $A(r)$ and summing over the sample:

[5]Though the IMF is sampled from 0.8 $M_\odot$ –150 $M_\odot$ to create the cluster, only synthetic stars within the F153M magnitude limits are considered in this analysis. This corresponds to a mass range between 1.8 $M_\odot$ – 51 $M_\odot$ for the best-fit isochrone, but differential extinction scatters lower- and higher-mass stars into the sample.

$$\Phi_{obs} = \sum_{i}^{N_i} \phi(m)_i * \frac{P_{clust,i}}{C(r) * A(r)} \tag{4.19}$$

We reiterate that Φ_{obs} is dependent on the synthetic cluster and is calculated *after* the best-fit model is found. It thus serves as a check that the IMF derived in the analysis is indeed a good match to the observations.

4.5 Results

We find that the Arches cluster is best described by a 1-segment IMF model that is top-heavy (α = 1.76 $\pm$ 0.03 (stat) $\pm$ 0.05 (sys). However, we cannot discount a 2-segment IMF model with a high-mass slope closer to the local IMF value (α = 2.1 $\pm$ 0.12) but with a break at $5.16^{+1.25}_{-0.65}$ $M_{\odot}$. This section is organized as follows: we describe the best-fit IMF model in §4.5.1 and compare the 1-segment and 2-segment IMF model solutions in §4.5.2. In §4.5.3 we discuss the impact of our assumptions regarding stellar evolution models and stellar multiplicity.

4.5.1 The Arches Cluster IMF: Best-fit Model

The best-fit cluster models for each of the different cases examined in this analysis (1-segment vs. 2-segment IMF, Pisa/Esktrom vs. MIST evolution models, with vs. without multiplicity) are given in Table 4.4 and a breakdown of the corresponding likelihoods in Table 4.5. A detailed comparison of these cases is presented in §4.5.2 and §4.5.3, but in summary: 1) we do not find significant evidence that the 2-segment IMF model is favored over the 1-segment IMF model; 2) we cannot distinguish between the Pisa/Geneva and MIST evolution models; and 3) the fits without multiplicity are strongly disfavored. So, we adopt the 1-segment IMF fit using Pisa/Geneva evolution models and with multiplicity applied as the best-fit IMF model, and use the MIST model atmosphere solution used to estimate the systematic uncertainty.

Table 4.4. Best-fit Cluster Models

Parameter[a]	1-Segment IMF				2-Segment IMF	
	Pisa/Geneva[b]		MIST v1.0[c]		Pisa/Geneva[b]	MIST v1.0[c]
	mode 1	mode 2	mode 1	mode 2		
α_1	1.76 ± 0.03	1.75 ± 0.03	1.66 ± 0.04	1.67 ± 0.03	2.1 ± 0.11	2.06 ± 0.12
α_2	—	—	—	—	0.74 ± 0.41	0.81 ± 0.42
m_{break}	—	—	—	—	$5.16^{+1.25}_{-0.65}$	$5.32^{+1.70}_{-0.81}$
M_{cl}	25600 ± 1400	24600 ± 1200	29200 ± 2000	28000 ± 1600	20000^{+2000}_{-1800}	20800^{+2400}_{-2200}
log t	6.57 ± 0.01	6.48 ± 0.01	6.56 ± 0.01	6.4 ± 0.01	6.55 ± 0.05	6.52 ± 0.04
d	7695 ± 100	7869 ± 100	7702 ± 107	8181 ± 100	7991 ± 160	8042 ± 160
A_{Ks}	2.12 ± 0.01	2.11 ± 0.01	2.12 ± 0.01	2.11 ± 0.01	2.13 ± 0.01	2.13 ± 0.01
ΔA_{Ks}	0.13 ± 0.01	0.12 ± 0.01	0.13 ± 0.01	0.12 ± 0.01	0.13 ± 0.01	0.13 ± 0.01

[a]Priors and units are the same as described in Table 4.3

[b]Pisa: Tognelli et al. (2011); Geneva: Ekström et al. (2012)

[b]Choi et al. (2016); Dotter (2016)

Table 4.5. IMF Model Likelihoods

Component	1-Segment IMF					2-Segment IMF		
	Pisa/Geneva[a]		MIST v1.0[b]		No Multiples	Pisa/Geneva[a]	MIST v1.0[b]	No Multiples
	mode 1	mode 2	mode 1	mode 2				
CMD	-4977.7	-4978.0	-4978.4	-4978.6	-4988.0	-4969.8	-4968.4	-4974.0
N_{stars}	-4.3	-4.2	-4.2	-4.3	-4.2	-4.2	-4.2	-4.16
N_{WR}	-3.9	-4.2	-2.7	-2.3	-2.3	-2.3	-2.6	-2.6
Spectroscopy	-19.5	-19.9	-19.5	-20.6	-22.0	-19.5	-19.6	-20.0
log($\mathcal{L}$)	**-5023.4**	**-5023.5**	**-5022.3**	**-5023.1**	**-5034.2**	**-5015.4**	**-5015.3**	**-5020.3**
BIC	**10088.1**	**10088.3**	**10085.9**	**10087.5**	**10109.7**	**10085.9**	**10085.7**	**10095.7**

[a]Pisa: Tognelli et al. (2011); Geneva: Ekström et al. (2012)

[b]Choi et al. (2016); Dotter (2016)

The set of posteriors for the best-fit IMF model is provided in Appendix 4.9. Two distinct models are present that are primarily distinguished by cluster age; all other parameters are consistent to well within 1σ, except for the cluster distance which differs by 1.2σ. The component of the likelihood driving the two modes is the number of WR stars, which is not monotonic with age and thus multiple solutions are possible (e.g., Figure 3 of Lu et al. 2013). The fact that the total likelihood of the two modes are nearly identical indicates that they fit the data equally well (see Table 4.5). A comparison between the observed and model CMD for mode 1 is shown in Figure 4.9 and the subsequent F153M luminosity function shown in Figure 4.10. Good agreement is generally found between the observations and model, though perhaps with a slight excess of model stars at the bright end of the sample (F153M $\gtrsim$ 16 mag). Agreement is also found between the spectroscopic T_{eff} measurements and those predicted by the model is shown in a Hertzsprung-Russell Diagram (HRD), where the (model-dependent) luminosity for each of the observed stars has been derived in the manner described in §4.4.2 (Figure 4.11). The T_{eff} vs. log g diagram shows less agreement, with the log g values favoring an older cluster population of $\sim$5 Myr (Figure 4.12). However, there are limited gravity indicators in the K-band (e.g. Hanson et al. 2005) and so future observations are required to see if a discrepancy truly exists. The total number of cluster stars predicted by the model (626.6 $\pm$ 33) in good agreement with the observed value ($\sum P_{pm}$ = 636.7), though the expected number of WR stars is $\sim 1.7\sigma$ higher than observed (20.1 $\pm$ 1.75, compared to N_{wr} = 13).

We obtain a high-mass power law slope of $\alpha = 1.76 \pm 0.03$, which is 1.5σ lower than the local IMF value and $\sim 11\sigma$ lower than the measured IMF of young clusters in M31 ($\alpha = 2.45^{+0.03}_{-0.06}$; Weisz et al. 2015). A comparison of these values and their statistical errors is shown in Figure 4.13. This suggests that the Arches has a top-heavy IMF, with an overabundance of high-mass stars relative to low-mass stars for M > $\sim$1.8 $M_\odot$. The α we derive does depend somewhat on which stellar evolution model we adopt, as the best-fit cluster with the MIST models has $\alpha = 1.66 \pm 0.04$. We thus add a systematic error term of 0.05 to our α measurement (the difference in the parameter value minus the statistical uncertainties of each measurement summed in quadrature), and so the final constraint becomes $\alpha = 1.76 \pm 0.03$ (stat) $\pm$ 0.05 (sys).

The cluster ages of the two best-fit modes are log $t = 6.57 \pm 0.01$ (negligible systematic error) and log $t = 6.48 \pm 0.01 \pm 0.066$ (3.7 $\pm$ 0.1 Myr and 3.0 $\pm$ 0.1 $\pm$ 0.5 Myr, respectively). These values are consistent with previous ages reported in the literature. Past estimates come primarily

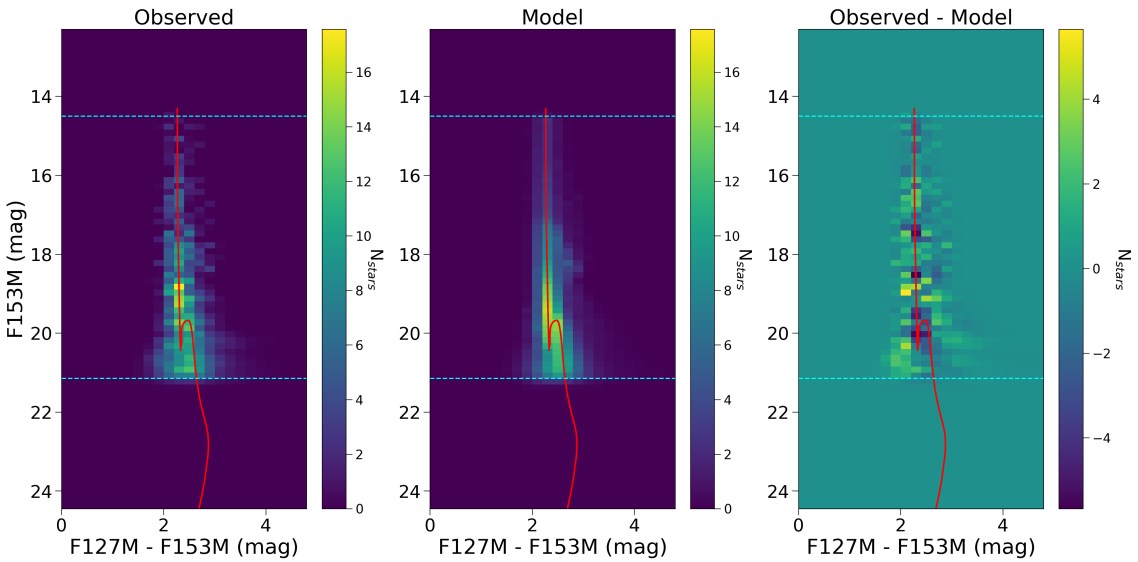

Figure 4.9 A comparison between the observed CMD and the predicted CMD from the best-fit cluster model (mode 1). The left panel shows the hess diagram for the observed cluster, the middle panel shows the hess diagram of the best-fit cluster model, and the right panel shows the residuals between the two. The cluster model has been convolved with observational uncertainties in this comparison. In all panels the isochrone associated with the best-fit model is plotted as a red line and the F153M magnitude limits are represented by the cyan dashed lines. Note that the cluster model contains both cluster and field components; the impact of the red clump is particularly evident by the slight high-density diagonal feature near F153M $\sim$ 18 mag.

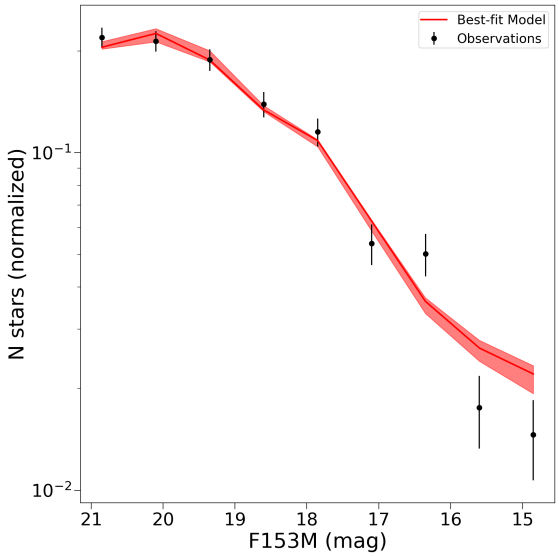

Figure 4.10 A comparison of the observed F153M luminosity function (black points) versus the mode 1 best-fit model (red line). The 1σ envelope of possible models, sampled from the posterior distribution, is shown by the red envelope. Good agreement is found with the exception of a possible excess of model stars in the brightest magnitude bins (F153M $\gtrsim$ 16 mag).

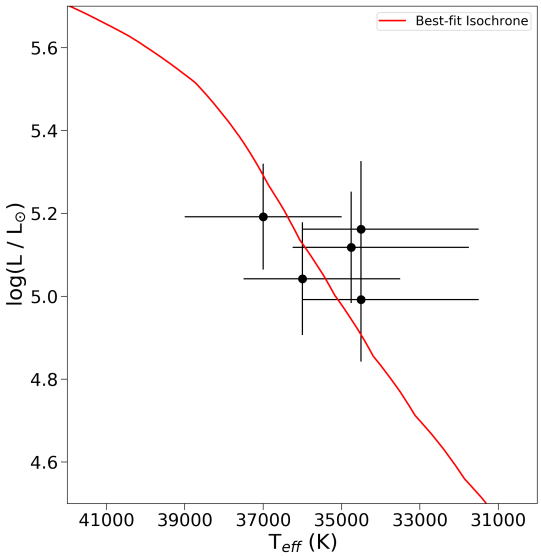

Figure 4.11 The measured T_{eff} and inferred luminosity of the spectroscopic stars (black points) compared to mode 1 of the best-fit model (red line).

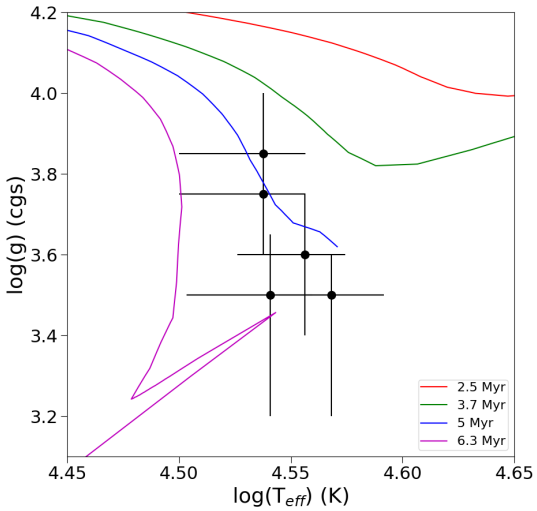

Figure 4.12 T_{eff} vs log g for the spectrosopic stars, compared to theoretical cluster isochrones at different ages. Though the IMF analysis has a best-fit cluster age of 3.7 Myr (green line), the log g values seem to favor an age of $\sim$ 5 Myr. However, there are limited gravity indicators in the K-band wavelength range and so these measurements must be treated with caution.

from spectroscopic studies of the massive stars, with values of 2 - 2.5 Myr based on the observed Nitrogen abundances of WR stars (Najarro et al. 2004), 2 - 4 Myr based on the locations of WR + O stars on the HR diagram (Martins et al. 2008), 2 - 3.3 Myr based on the spectral types of candidate main-sequence stars (Clark et al. 2018), and $2.6^{+0.4}_{-0.2}$ Myr based on the properties of an eclipsing binary in the cluster (Lohr et al. 2018). An additional age constraint of 3.7 $\pm$ 0.7 was obtained by Schneider et al. (2014) based on the shape of the PDMF relative to stellar population models with binary star evolution. Unfortunately, the degeneracy of our solution prevents us from differentiating between the younger ($\lesssim$3 Myr) and older ($\gtrsim$3 Myr) age estimates.

We infer a cluster mass of M_{cl} = 2.56 $\pm$ 0.14 $\pm$ 0.12 x 10^4 $M_\odot$, which represents the intrinsic mass between 0.8 $M_\odot$ – 150 $M_\odot$ out to a cluster radius of 3 pc. This assumes that the 1-segment IMF model is valid over the entire mass range and that the radial profile is adequately modeled for r $<$ 0.25 pc, which is beyond the observed sample (§4.6.4). However, the advantage of this result is that it is jointly constrained with the IMF, while previous photometric mass estimates of the cluster needed to adopt and IMF and extrapolate it to achieve a similar depth (e.g. Serabyn et al. 1998; Figer et al. 1999; Espinoza et al. 2009).

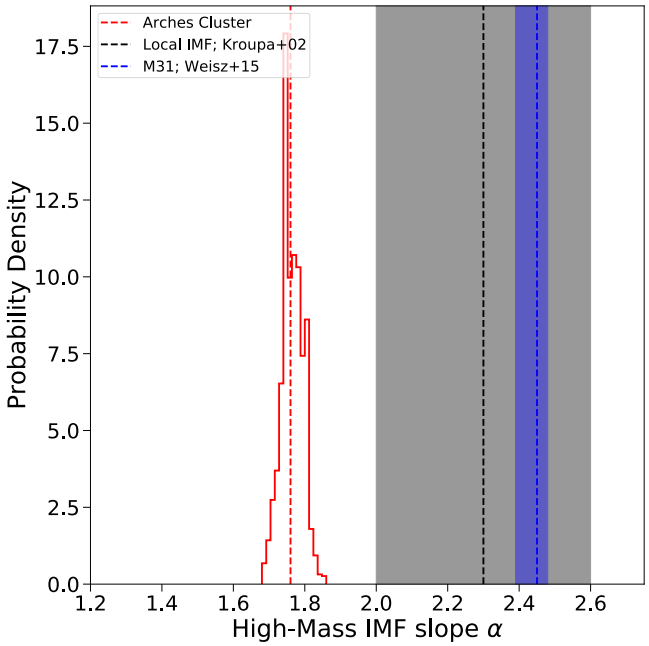

Figure 4.13 The posterior probability distribution for the high-mass IMF slope α in the Arches cluster (red) compared to the local IMF (black dotted line; Kroupa 2002) and the IMF of young clusters in M31 (blue dotted line Weisz et al. 2015), with the 1σ uncertainties shown by the respective shaded regions. The Arches IMF slope is significantly lower than the Milky Way or M31, indicating that the cluster has a top-heavy IMF. Note that the uncertainties shown in this figure are statistical in nature. We estimate a systematic uncertainty of ± 0.05 in our measurement of α.

As a consistency check, we compare the best-fit cluster mass model to dynamical mass estimates of the cluster by Clarkson et al. (2012). Using the velocity dispersion of the cluster core region, they estimate the dynamical mass of the cluster to be $0.9^{+0.40}_{-0.35}$ x 10^4 $M_\odot$ for $r_{cl} < 0.4$ pc and $1.5^{+0.74}_{-0.60}$ x 10^4 $M_\odot$ for $r_{cl} < 1.0$ pc. Since the mass range of our model is truncated, we would expect the enclosed mass at these radii to be lower than the dynamical estimate. This is indeed the case, with model enclosed masses of (0.78 ± 0.08) x 10^4 $M_\odot$ and (1.3 ± 0.1) x 10^4 $M_\odot$ for $r_{cl} < 0.4$ pc and $r_{cl} < 1.0$ pc, respectively.

Using mode 1 of the best-fit cluster model, we use the procedure outlined in §4.4.2 to calculate revised membership probabilities and Φ_{obs}. Figure 4.14 shows P_{pm} and P_{clust} for the individual stars in the CMD. A comparison of the panels reveals the regions where $P_{pm} > P_{clust}$, suggesting P_{pm} is overestimated due to field contamination, which is especially evident near the Red Clump (the diagonal distribution of stars to the red of the cluster sequence at F153M ∼ 18 mag) and faint field star distribution (the stars to the blue of the cluster sequence at F153M ≥ 20 mag). The total number of cluster stars based on P_{clust} is 583.1 stars, which is ∼8% smaller than what is calculated from P_{pm}. Thus, we estimate that P_{pm} (which was used in the IMF analysis) contains ∼8% field contamination.

The observed initial mass function Φ_{obs} is shown in Figure 4.15. Also plotted is the Φ_{obs} we would obtain if we adopted a cluster model identical to the best-fit but with the local IMF. The mass function obtained with the local IMF is significantly inconsistent with the observations, while the mass function obtained from the best-fit model is a good match to the observations.

4.5.2 1-segment vs. 2-segment IMF Model

The best-fit 2-segment cluster model (which has a unimodal solution) is also significantly different than the local IMF, but in a different manner than the 1-segment IMF model. While the high-mass IMF slope is perhaps slightly shallow ($\alpha_1 = 2.1 \pm 0.11$), the real discrepancy is in the detection of a significant m_{break} at $5.15^{+1.25}_{-0.65}$ $M_\odot$, which is an order of magnitude larger than the local IMF ($m_{break} = 0.5$ $M_\odot$). The power law slope below m_{break} is $\alpha_2 = 0.74 \pm 0.41$, which is ∼3.2σ lower than α_1, and roughly in-between the local IMF values of 1.3 ± 0.3 for 0.08 $M_\odot \leq M < 0.5$ $M_\odot$ and 0.3 ± 0.4 for 0.01 $M_\odot \leq M < 0.08$ $M_\odot$ (Kroupa 2002). As a result of the high m_{break}, the Arches 2-segment IMF could be characterized as "bottom-light", with an deficit of low-mass stars relative

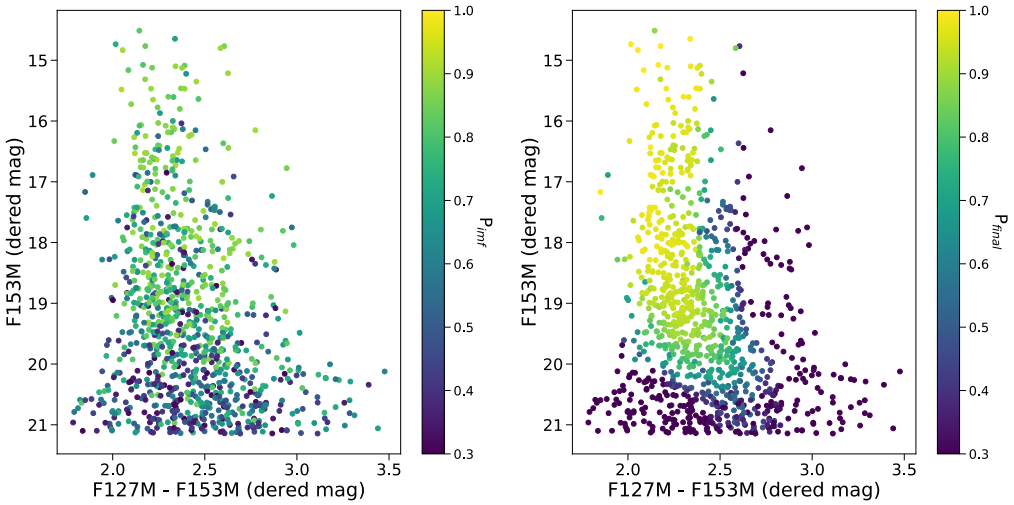

Figure 4.14 P_{pm} (left) and P_{final} (right) for the observed sample, plotted in the CMD. P_{final} is a more accurate determination of the cluster membership probability since it uses both proper motion and photometric information, but is dependent on the best-fit cluster model from the IMF analysis. Regions where $P_{pm} > P_{final}$ reveal field contamination in the proper motion memberships, in particular around the Red Clump (F153M $\sim$ 18 mag, F127M - F153M $>$ $\sim$2.5 mag) and faint field stars (F153M $\geq$ 20 mag, F127M - F153M $<$ $\sim$2.5 mag). All magnitudes have been differentially de-reddened to $A_{Ks} = 2.07$ mag using the extinction map.

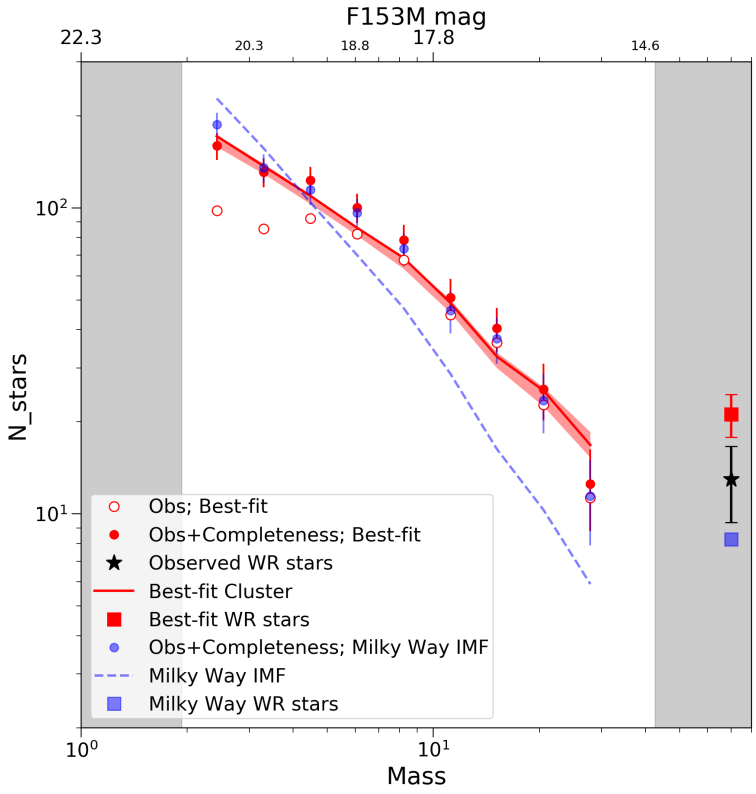

Figure 4.15 The IMF of the Arches cluster constructed using P_{final} and the stellar mass probability distributions derived using the cluster model. The red points represent the IMF constructed using the stellar masses calculated with the best-fit cluster model, while the red line is the IMF of the best-fit cluster itself. The 1σ uncertainty in the best-fit cluster model is represented by the red shaded region, which is calculated by drawing different sets parameter values from the joint posterior distribution. The red box represents the number of WR stars predicted by the best-fit model, compared to the observed number (black star). A good agreement is found between the observed IMF and the cluster model. On the other hand, the blue points represent the IMF constructed using stellar masses derived from a cluster identical to the best-fit but with a Milky Way IMF ($\alpha = 2.3$), with the intrinsic cluster IMF shown by the blue dotted line. The Milky Way IMF is a poor fit to the data, as it significantly underestimates the number of high-mass stars and overestimates the number of low-mass stars.

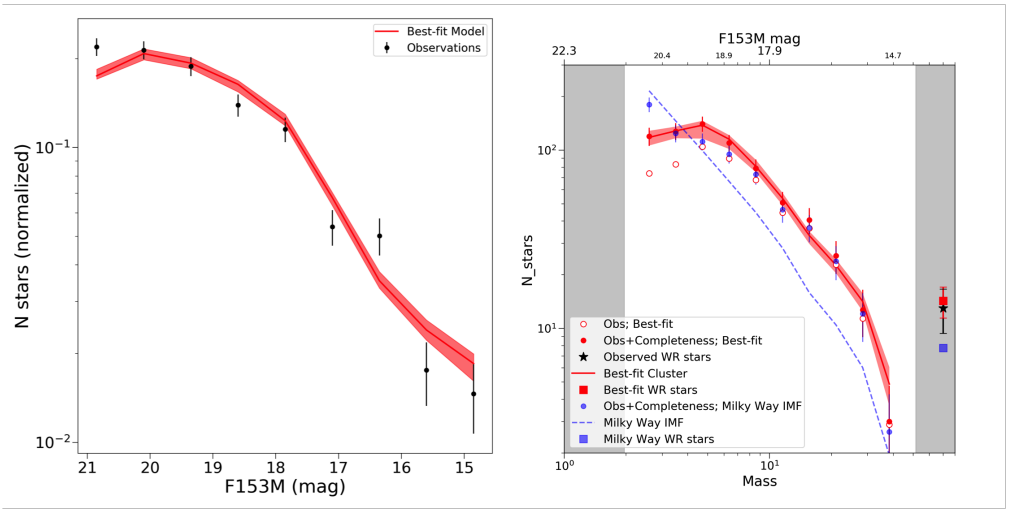

Figure 4.16 A comparison of the best-fit 2-segment IMF model with the observed luminosity function (left) and Φ_{obs} (right). The features of the plots are the same as described for Figures 4.10 and 4.15. The 2-segment IMF solution is not significantly favored over the 1-segment IMF solution, and so we adopt the 1-segment IMF solution as the best-fit Arches cluster IMF. Additional studies are required to distinguish between these two models.

to the local IMF. Figure 4.16 shows the 2-segment model compared to the observed luminosity function and the derived Φ_{obs}.

One of the advantages of the bayesian framework is that we can distinguish between 1-segment and 2-segment IMF models by comparing the likelihoods of the best-fit solutions. We use the Bayesian Information Criterion (BIC; Schwarz 1978) for this comparison:

$$\mathrm{BIC} = \ln(n) * k - 2 * \ln(\mathcal{L}) \tag{4.20}$$

where n is the total number of stars in the sample (980, in this case), k is the number of free parameters in the model (i.e., 6 for 1-segment model and 8 for the 2-segment model), and $\mathcal{L}$ is the best-fit likelihood of the model. When comparing the two models, the model with the lowest BIC is preferred, and the absolute value of the difference between the BIC values (ΔBIC) is a measure of how significant that preference is. Table 4.5 contains the likelihoods and BIC values for the 1-segment and 2-segment IMF fits. For the 1-segment model we will use the mode 1 solution to calculate the ΔBIC.

The 2-segment IMF model is slightly preferred over the 1-segment IMF model in both Pisa/Ekstrom and MIST cases, with ΔBIC = 2.2 and 0.2, respectively. To assess the significance of this preference, we generate artificial clusters with 1-segment and 2-segment IMFs as described in Appendix 4.10 (adopting the best-fit values in the Arches solutions) and fit them in both the 1-segment and 2-segment cases, and the calculate the corresponding ΔBIC values. For a cluster with an intrinsic 1-segment IMF, we find that the 1-segment IMF model is always preferred with ΔBIC = 17.1 $\pm$ 4.2. Similarly, for a cluster with an intrinsic 2-segment IMF, the 2-segment IMF model is always preferred with ΔBIC = 17.6 $\pm$ 3.9. These ΔBIC values are significantly higher than the ones we calculate for the real data fits. Thus, we conclude that the preference for the 2-segment IMF model is not significant and adopt the 1-segment IMF model as the overall best-fit model. That said, we also cannot definitively rule out the 2-segment IMF model solution. In either case, our results show that the Arches cluster IMF is significantly different from the local IMF.

4.5.3 The Impact of Stellar Evolution Models and Stellar Multiplicity

Table 4.4 reveals that the best-fit model parameters are only weakly dependent on the choice of stellar evolution model. In the 2-segment IMF case, the parameters obtained with the Pisa/Ekstrom and MIST models are consistent to well within 1σ, whereas in the 1-segment IMF case there is a systematic difference of $\alpha \pm 0.05$ and $M_{cl} \pm 0.12$ x 10^4 $M_\odot$ (after the statistical errors have been accounted for). There is also a systematic difference of $\log t \pm 0.066$ for the mode 2 solution, while the mode 1 solution ages agree within the statistical errors. Similar to §4.5.2, we use the BIC test to determine if our analysis prefers one set of evolution models over the other.

Both the 2-segment and 1-segment IMF cases slightly favor the MIST evolution models, with ΔBIC values of 0.2 and 2.2, respectively. Table 4.5 reveals that the primary cause for the difference is the predicted number of WR stars N_{WR}, with the MIST models showing slightly better agreement with the data. However, artificial cluster tests show that these ΔBIC values are not significant: in the 2-segment IMF case, the typical ΔBIC between evolution models is 2.1 $\pm$ 1.2, while in the 1-segment IMF case ΔBIC = 5.39 $\pm$ 2.56. We conclude that we cannot distinguish between the Pisa/Ekstrom and MIST models with our observations, and adopt the Pisa/Ekstrom results while using the MIST results to estimate the systematic error.

Whether stellar multiplicity is accounted for in the cluster model is found to significantly impact the quality of the best-fit model. The BIC analysis strongly favors the models that include stellar multiplicity, with ΔBIC values of 21.6 and 9.8 for the 1-segment and 2-segment IMF model cases, respectively. As seen in Table 4.5, this difference is primarily driven by the CMD likelihood component. Artificial cluster tests show that the observed ΔBIC values are significant; for artificial clusters that have intrinsic multiplicity, $\Delta\text{BIC} = 12.2 \pm 0.5$ in favor of the fit with multiplicity in the 1-segment IMF case and $\Delta\text{BIC} = 8.8 \pm 0.5$ in the 2-segment IMF case. Thus, we adopt the model fits with multiplicity included over those without.

4.6 Discussion

4.6.1 Past IMF Measurements of the Arches Cluster

Our result that the high-mass slope of the Arches IMF is significantly top-heavy differs from previous photometric studies of the cluster which have found the IMF to be largely consistent with the local IMF (Kim et al. 2006; Espinoza et al. 2009; Habibi et al. 2013; Shin & Kim 2015). However, a key advantage of this study is that we use proper motions to calculate cluster membership probabilities, which produces a significantly more accurate sample of cluster members than is possible through photometry alone. For example, Figure 4.17 shows a comparison between cluster samples obtained using proper motions versus a photometric color-cut similar to Habibi et al. (2013). Even when limited to r $<$ 1.5 pc and M $>$ 10 $M_\odot$ (the range PDMF was measured by Habibi et al. 2013), the photometric sample is systematically larger than the proper motion selection due to field contamination. On the other hand, adopting stricter color-cuts can be problematic as well, as Espinoza et al. (2009) note that the color-cuts they adopt forces them to eliminate stars that could be high-mass (M $>$ 16 $M_\odot$) cluster members.

An alternative approach is to statistically subtract the field from the cluster based on the photometric properties of the field population in nearby control fields (e.g. Kim et al. 2006; Shin & Kim 2015). However, differential extinction not only alters the average extinction between fields, but can also change the distribution of extinction values within a field (e.g., note the detailed extinction structures in Figure 4.5). As a result, it is challenging to obtain a sufficiently detailed model of the field stars in the cluster field itself. In addition, care must be taken that the control

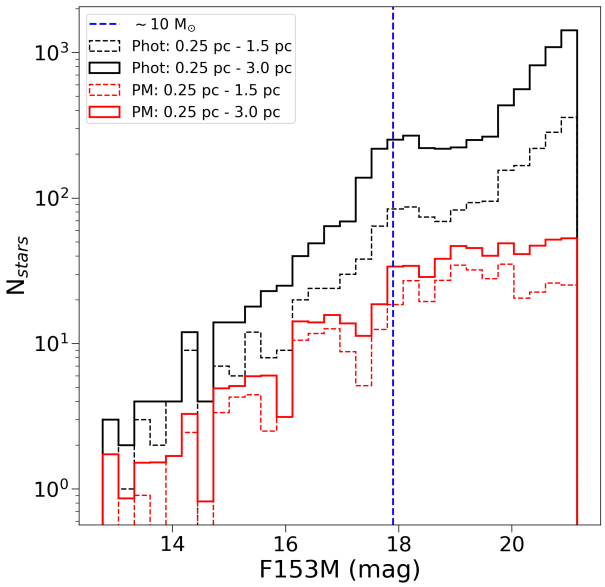

Figure 4.17 A comparison between Arches cluster members selected via proper motion versus a photometric color cut. The proper motion sample, shown as the red solid and dashed lines, contains all stars with $P_{pm} > 0.3$, where each star is weighted by its membership probability for radius ranges of 0.25 pc $<$ r $<$ 3.0 pc and 0.25 pc $<$ r $<$ 1.5 pc, respectively. The photometric sample is selected as all stars with differentially de-reddened F127M - F153M colors within $\pm$ 0.3 mag of the average color on the main sequence, similar to Habibi et al. (2013). The photometric sample is larger than the proper motion due to field contamination, even at high masses (blue dashed line represents 10 $M_{\odot}$).

field are beyond the extent of the cluster, which H15 shows extends to a radius of at least 75" ($\sim$3 pc).

It is interesting to note that several previous studies have reported evidence of an enhancement in the PDMF at $\sim$6 $M_{\odot}$, whether it be evidence of a turnover (Stolte et al. 2005) or a localized "bump" in the mass function (Kim et al. 2006). The presence of such a feature may be driving the 2-segment IMF model solution. Future studies are needed to extend the proper-motion selected sample to lower masses in order to definitively distinguish between the 1-segment and 2-segment IMF models and determine if an enhancement at 5-6 $M_{\odot}$ truly exists.

4.6.2 A Top-Heavy IMF Near the GC?

The top-heavy IMF we obtain for the Arches cluster ($\alpha = 1.76 \pm 0.03 \pm 0.05$) is in good agreement with YNC ($\alpha = 1.7 \pm 0.2$ for M > 10 $M_\odot$; Lu et al. 2013). This suggests that this atypical IMF extends beyond the central parsec of the Galaxy and into the CMZ, which spans a galactocentric radius of ∼200 pc (Morris & Serabyn 1996). Unfortunately, the exact birth location of the Arches is not well constrained due to the range of possible orbits allowed by the three-dimensional motion of the cluster (Stolte et al. 2008; Kruijssen et al. 2015). Further, the proper motion of the cluster *in the galactocentric reference frame* is not yet well determined, as current estimates are based on the relative proper motion between the cluster and a single-gaussian kinematic model for the field (e.g. Clarkson et al. 2012). In reality, the field exhibits a more complex kinematic structure (see H15 and Appendix 4.8), and so the measured cluster motion may need to be revised. This is left to a future paper.

However, this result raises the question of whether the top-heavy IMF is truly due to the GC environment or if it is a general property of young massive clusters (YMCs; see review by Portegies Zwart et al. 2010). Figure 4.18 compares IMF measurements of YMCs in the Milky Way disk to the YNC and Arches cluster at the GC. The YMC sample includes Westerlund 1 (Wd1; Gennaro et al. 2011; Lim et al. 2013; Andersen et al. 2017), Westerlund 2 (Wd2; Zeidler et al. 2017), NGC 3603 (Harayama et al. 2008; Pang et al. 2013), Trumpler 14 and 16 (Hur et al. 2012), and h and χ Persei (Slesnick et al. 2002).

Figure 4.18 shows that the YMCs in the Galactic disk are generally consistent with the local IMF, though potential discrepancies exist. In particular, NGC 3603 has been found to be potentially top-heavy ($\alpha = 1.74^{+0.62}_{-0.47}$, 1.88 ± 0.15; Harayama et al. 2008; Pang et al. 2013, respectively). However, these results may be biased due to mass segregation, which both studies find to be significant in the cluster. Indeed, the uncertainty in the Harayama et al. (2008) measurement is quite large in order to account for this (as well as other) systematic uncertainties, while Pang et al. (2013) acknowledge that their IMF measurement is restricted to the inner 60" of the cluster. The IMF of Westerlund 1 is potentially discrepant as well, with reported high-mass IMF slopes that are near-standard ($\alpha = 2.44^{+0.08}_{-0.20}$; Gennaro et al. 2011, via near-infrared photometry) and top-heavy ($\alpha = 1.8 \pm 0.1$; Lim et al. 2013, via optical photometry). However, the low-mass stellar content

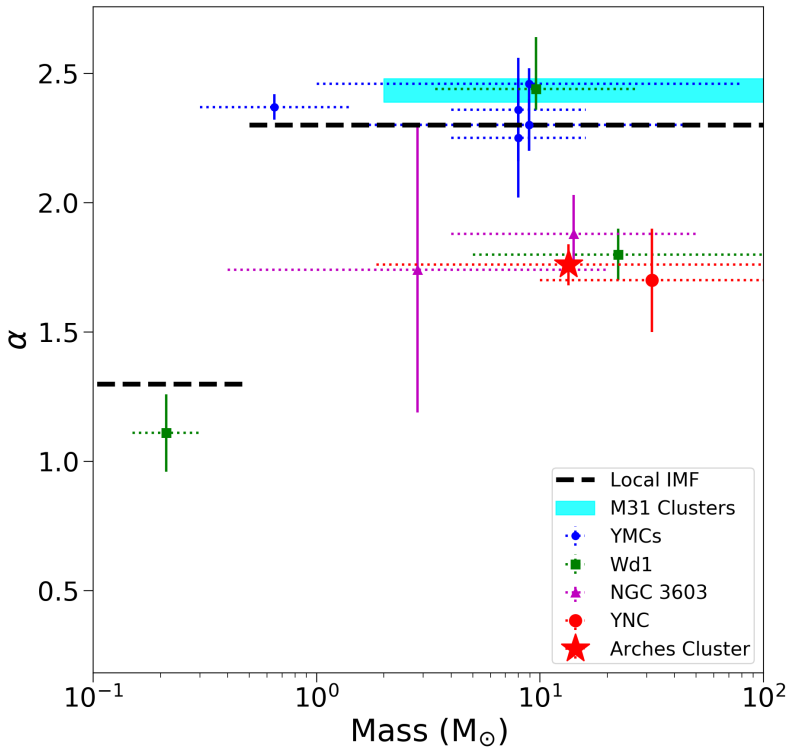

Figure 4.18 A plot of IMF slope α versus mass for YMCs in the Galactic disk (blue points: Wd2, Trumpler 14, Trumpler 16, h and χ Persei), green squares: Wd1, magneta triangles: NGC 3603) and the GC (red circle: YNC, red star: Arches cluster). The dotted error bars in the X-direction show the mass range over which the measurement was made, while the solid error bars in the Y-direction show the measurement uncertainty. The references are provided in the text; Wd1 and NGC 3603 have their own symbols to show the multiple values reported in the literature. Also shown is the local IMF (black dashed line) and IMF measured for young cluster in M31 from Weisz et al. (2015, cyan box)

of the cluster has been found to be consistent with the local IMF (Andersen et al. 2017). These cases highlight the difficulty of these measurements, as differences in cluster membership selection, stellar models, and methodology may significantly impact results.

Given the uncertainties surrounding the NGC 3603 and Wd1 measurements, the fact that the YMCs in the Galactic disk have been found to be consistent with the local IMF while the Arches and YNC are top-heavy provides tentative evidence that the top-heavy IMF is indeed caused by the extreme GC environment. We discuss the implications of a top-heavy IMF at the GC in §4.6.3 and the caveats of our Arches IMF measurement in §4.6.4.

The Quintuplet cluster, a third YMC in the CMZ that is often considered a slightly older version of the Arches cluster, provides another probe of the IMF at the GC. A previous proper motion-based analysis of the Quintuplet mass function was carried out by Hußmann et al. (2012), who found a top-heavy PDMF ($\alpha = 1.68^{+0.13}_{-0.09}$) for the inner 0.5 pc of the cluster. However, it is uncertain whether this is due to mass segregation or a top-heavy IMF. A study of the Quintuplet IMF using a similar approach as this work is currently in progress.

4.6.3 Implications for Star Formation

At first, a top-heavy IMF at the GC appears to favor star formation models where the increased thermal Jeans mass leads to the formation of more high-mass stars (e.g. Larson 2005; Bonnell et al. 2006; Klessen et al. 2007; Bonnell & Rice 2008; Papadopoulos et al. 2011; Narayanan & Davé 2013). However, the main prediction of these models is that the turn-over mass of the IMF should increase, leading to a deficit of low-mass stars, rather than a shallow high-mass slope. This behavior is similar to the "bottom-light" 2-segment IMF solution, but we do not yet have enough evidence to conclude that this is preferred over the top-heavy 1-segment IMF solution.

However, our result is inconsistent with models where the IMF is set by the CMF (e.g. Padoan & Nordlund 2002; Hopkins 2012). Though the combination of turbulence and gravity naturally produces a CMF with a shape similar to the local IMF, these models predict a steeper mass slope and a bottom-heavy IMF near the GC (Hopkins 2013; Chabrier et al. 2014). This suggests that the CMF cannot be directly mapped to the IMF and that additional processes are involved. Simulations have shown that radiative feedback (e.g. Bate 2009; Offner et al. 2009; Krumholz 2011), protostellar

outflows (e.g. Krumholz et al. 2012; Federrath et al. 2014), and magnetic fields (e.g. Hennebelle et al. 2011; Myers et al. 2013) can impact the IMF.

Only recently have star formation simulations begun to incorporate all of these processes simultaneously (Myers et al. 2014; Krumholz et al. 2016; Li et al. 2018; Cunningham et al. 2018). However, these simulations have been limited to molecular clouds with initial masses $\leq$1000 $M_\odot$, and thus have been limited to low mass stars in environmental conditions similar to local star forming regions. Future simulations of higher masses molecular clouds in starburst-like environments are needed in order to determine what physics is behind a shallow high-mass IMF slope in the GC.

4.6.4 Caveats

A caveat of our IMF measurement is that we do not take the potential effects of tidal stripping into account. Tidal stripping might be expected to play a significant role in the evolution of the Arches cluster given the strength of the Galactic tidal field near the GC. Since tidal stripping preferentially removes low-mass stars from a cluster, especially in cases where that cluster is initially mass segregated (e.g. Kruijssen 2009; Lamers et al. 2013), it could bias the mass function to appear top-heavy. However, it is unclear from current dynamical models of the Arches whether tidal stripping would significantly impact the mass range examine in this study ($M \gtrsim 1.8$ $M_\odot$). N-body simulations by Habibi et al. (2014) predict the formation to tidal tail structures out to 20 pc from the cluster core primarily composed of stars with $M < 40$ $M_\odot$. Additional simulations by Park et al. (2018) also predict the formation of tidal tails, but find that $\sim$96% of the tidally stripped stars have masses less than 2.5 $M_\odot$ and that the impact on the mass function above this limit is minor. This is consistent with the observations of H15 that find no evidence of tidal tails down to $\sim$2.5 $M_\odot$ and to a cluster radius of 3 pc. Thus, we assume that the effects of tidal stripping can be ignored for the mass range in our sample.

It should be noted that the dynamical models discussed above require assumptions regarding the initial conditions and orbit of the Arches cluster, both of which are quite uncertain. In addition, only stars are considered in the simulations, though presumably gas loss has had a significant impact on the evolution of the cluster as well (e.g. Goodwin & Bastian 2006; Farias et al. 2015). Thus, future work is required to assess the potential impact of tidal stripping on the IMF.

Another caveat is that this analysis does not contain data for r < 0.25 pc, where the observational completeness is low due to stellar crowding. We have adopted the radial profile of Espinoza et al. (2009) for this region when modeling the cluster (§4.4), but it should be noted that this profile was derived only using stars with M > 10 $M_{\odot}$. In other words, while we use magnitude dependent radial profiles for 0.25 pc < r < 3.0 pc in order to account for mass segregation, the profile for all stars within the cluster core is the same. Combining the *HST* data set from this study with higher resolution ground-based observations of the cluster core will be the topic of a future paper.

4.7 Conclusions

We use multi-epoch *HST* WFC3-IR observations and Keck OSIRIS K-band spectroscopy to measure the IMF of the Arches cluster. Critically, we use proper motions to calculate cluster membership probabilities for stars down to ∼1.8 $M_{\odot}$ with cluster radii 0.25 pc ≤ r_{cl} ≤ 3.0 pc, obtaining a sample with just ∼8% field contamination. This is a significant improvement over past studies that have been limited to identifying cluster members photometrically, which is challenging due to the severe differential extinction across the field. Our proper motion sample contains $\sum P_{pm}$ = 636.7 cluster members, which we combine with K-band spectra of 5 O-type giants and supergiants in order to measure the IMF.

We forward model the Arches cluster to simultaneously constrain its IMF with the cluster distance, total mass, average extinction, and residual differential extinction (after a spatially-dependent extinction correction). This approach allows us to account for observational uncertainties, completeness, mass segregation, and stellar multiplicity. We generate synthetic clusters of varying parameters and compare them to the observations using a likelihood equation with four components: the distribution of stars in the color-magnitude diagram, the total number of observed stars, the total total number of Wolf-Rayet stars with r_{cl} < 0.75 pc (taken from spectroscopic surveys in the literature), and a comparison of the measured T_{eff} of the spectroscopic stars versus those predicted by the cluster model.

We find that the Arches IMF is best described by a 1-segment power law with a slope of α = 1.76 ± 0.03 ± 0.05, which is significantly more shallow than the local IMF and thus making it "top-heavy." However, we cannot discount a 2-segment power law model that has a high-mass

slope only slightly shallower than local star forming regions ($\alpha = 2.1 \pm 0.11$) but exhibits a break at $5.16^{+1.25}_{-0.65}$ $M_\odot$, making the Arches IMF deficient in low-mass stars and thus "bottom-light." In either case, the Arches IMF is significantly different than the local IMF common throughout the Milky Way and nearby galaxies.

The unusual nature of the Arches IMF, combined with the top-heavy IMF observed for the Young Nuclear Cluster ($\alpha = 1.7 \pm 0.2$; Lu et al. 2013) suggests that the starburst-like environment at the GC induces variations in the IMF. Other YMCs in the Galactic disk have been found to be generally consistent with the local IMF, indicating that these variations are truly due to the GC environment rather than an intrinsic property of YMCs. However, several disk YMCs (NGC 3603, Westerlund 1) have been found to be potentially discrepant with the local IMF, and so future studies must clarify the nature of their IMFs in order to strengthen this conclusion.

We note that the potential impact of tidal stripping is not included in our analysis. Measurements of the stellar radial density profile (Hosek et al. 2015) and the N-body simulations of the Arches (Park et al. 2018) suggest that tidal stripping has not significantly impacted the mass function over the mass ranged examined in this study. However, better constraints on the cluster orbit (e.g. Stolte et al. 2008) and full dynamical modeling of the stars and primordial gas is needed to fully explore the effects of tidal stripping. This is beyond the scope of the current study.

The authors thank Kelly Lockhart and Tuan Do for help with OSIRIS data reduction.

References

Andersen, M., Gennaro, M., Brandner, W., et al. 2017, A&A, 602, A22

Anderson, J., & King, I. R. 2006, PSFs, Photometry, and Astronomy for the ACS/WFC, Tech. rep.

Anderson, J., Sarajedini, A., Bedin, L. R., et al. 2008, AJ, 135, 2055

Bastian, N., Covey, K. R., & Meyer, M. R. 2010, ARA&A, 48, 339

Bastian, N., Konstantopoulos, I., Smith, L. J., et al. 2007, MNRAS, 379, 1333

Bastian, N., Saglia, R. P., Goudfrooij, P., et al. 2006, A&A, 448, 881

Bate, M. R. 2009, MNRAS, 392, 1363

Bellini, A., Libralato, M., Bedin, L. R., et al. 2018, ApJ, 853, 86

Bertelli Motta, C., Clark, P. C., Glover, S. C. O., Klessen, R. S., & Pasquali, A. 2016, MNRAS, 462, 4171

Bonnell, I. A., Clarke, C. J., & Bate, M. R. 2006, MNRAS, 368, 1296

Bonnell, I. A., & Rice, W. K. M. 2008, Science, 321, 1060

Buchner, J., Georgakakis, A., Nandra, K., et al. 2014, A&A, 564, A125

Cappellari, M., McDermid, R. M., Alatalo, K., et al. 2012, Nature, 484, 485

—. 2013, MNRAS, 432, 1862

Castelli, F., & Kurucz, R. L. 2004, ArXiv Astrophysics e-prints, astro-ph/0405087

Chabrier, G. 2005, in Astrophysics and Space Science Library, Vol. 327, The Initial Mass Function 50 Years Later, ed. E. Corbelli, F. Palla, & H. Zinnecker, 41

Chabrier, G., Hennebelle, P., & Charlot, S. 2014, ApJ, 796, 75

Choi, J., Dotter, A., Conroy, C., et al. 2016, ApJ, 823, 102

Clark, J. S., Lohr, M. E., Najarro, F., Dong, H., & Martins, F. 2018, ArXiv e-prints, arXiv:1803.09567

Clarkson, W. I., Ghez, A. M., Morris, M. R., et al. 2012, ApJ, 751, 132

Conroy, C., Dutton, A. A., Graves, G. J., Mendel, J. T., & van Dokkum, P. G. 2013, ApJ, 776, L26

Conroy, C., & van Dokkum, P. G. 2012, ApJ, 760, 71

Conroy, C., van Dokkum, P. G., & Villaume, A. 2017, ApJ, 837, 166

Cunningham, A. J., Krumholz, M. R., McKee, C. F., & Klein, R. I. 2018, MNRAS, 476, 771

Davies, R. I. 2007, MNRAS, 375, 1099

De Marchi, G., Panagia, N., Sabbi, E., et al. 2016, MNRAS, 455, 4373

Do, T., Ghez, A. M., Morris, M. R., et al. 2009, ApJ, 703, 1323

Dotter, A. 2016, ApJS, 222, 8

Ekström, S., Georgy, C., Eggenberger, P., et al. 2012, A&A, 537, A146

Espinoza, P., Selman, F. J., & Melnick, J. 2009, A&A, 501, 563

Farias, J. P., Smith, R., Fellhauer, M., et al. 2015, MNRAS, 450, 2451

Federrath, C., Schrön, M., Banerjee, R., & Klessen, R. S. 2014, ApJ, 790, 128

Feroz, F., Hobson, M. P., & Bridges, M. 2009, MNRAS, 398, 1601

Fierro, C. R., Borissova, J., Zsargó, J., et al. 2015, PASP, 127, 428

Figer, D. F., Kim, S. S., Morris, M., et al. 1999, ApJ, 525, 750

Figer, D. F., Najarro, F., Gilmore, D., et al. 2002, ApJ, 581, 258

Gennaro, M., Brandner, W., Stolte, A., & Henning, T. 2011, MNRAS, 412, 2469

Ginsburg, A., Henkel, C., Ao, Y., et al. 2016, A&A, 586, A50

Girardi, L. 2016, ARA&A, 54, 95

Goodwin, S. P., & Bastian, N. 2006, MNRAS, 373, 752

Guszejnov, D., Krumholz, M. R., & Hopkins, P. F. 2016, MNRAS, 458, 673

Habibi, M., Stolte, A., Brandner, W., Hußmann, B., & Motohara, K. 2013, A&A, 556, A26

Habibi, M., Stolte, A., & Harfst, S. 2014, A&A, 566, A6

Hanson, M. M., Kudritzki, R.-P., Kenworthy, M. A., Puls, J., & Tokunaga, A. T. 2005, ApJS, 161, 154

Harayama, Y., Eisenhauer, F., & Martins, F. 2008, ApJ, 675, 1319

Harfst, S., Portegies Zwart, S., & Stolte, A. 2010, MNRAS, 409, 628

Hennebelle, P., Commerçon, B., Joos, M., et al. 2011, A&A, 528, A72

Herczeg, G. J., & Hillenbrand, L. A. 2015, ApJ, 808, 23

Hillier, D. J., & Lanz, T. 2001, in Astronomical Society of the Pacific Conference Series, Vol. 247, Spectroscopic Challenges of Photoionized Plasmas, ed. G. Ferland & D. W. Savin, 343

Hillier, D. J., & Miller, D. L. 1998, ApJ, 496, 407

Ho, L. C., & Filippenko, A. V. 1996, ApJ, 472, 600

Hopkins, P. F. 2012, MNRAS, 423, 2037

—. 2013, MNRAS, 433, 170

Hosek, Jr., M. W., Lu, J. R., Anderson, J., et al. 2015, ApJ, 813, 27

—. 2018, ApJ, 855, 13

Hur, H., Sung, H., & Bessell, M. S. 2012, AJ, 143, 41

Husser, T.-O., Wende-von Berg, S., Dreizler, S., et al. 2013, A&A, 553, A6

Hußmann, B., Stolte, A., Brandner, W., Gennaro, M., & Liermann, A. 2012, A&A, 540, A57

Kausch, W., Noll, S., Smette, A., et al. 2015, A&A, 576, A78

Kim, S. S., Figer, D. F., Kudritzki, R. P., & Najarro, F. 2006, ApJ, 653, L113

Kim, S. S., Figer, D. F., Lee, H. M., & Morris, M. 2000, ApJ, 545, 301

Klessen, R. S., Spaans, M., & Jappsen, A.-K. 2007, MNRAS, 374, L29

Krabbe, A., Gasaway, T., Song, I., et al. 2004, in Proc. SPIE, Vol. 5492, Ground-based Instrumentation for Astronomy, ed. A. F. M. Moorwood & M. Iye, 1403–1410

Kroupa, P. 2002, Science, 295, 82

Kruijssen, J. M. D. 2009, A&A, 507, 1409

Kruijssen, J. M. D., Dale, J. E., & Longmore, S. N. 2015, MNRAS, 447, 1059

Kruijssen, J. M. D., & Longmore, S. N. 2013, MNRAS, 435, 2598

Krumholz, M. R. 2011, ApJ, 743, 110

—. 2014, Phys. Rep., 539, 49

Krumholz, M. R., Klein, R. I., & McKee, C. F. 2012, ApJ, 754, 71

Krumholz, M. R., Myers, A. T., Klein, R. I., & McKee, C. F. 2016, MNRAS, 460, 3272

La Barbera, F., Ferreras, I., Vazdekis, A., et al. 2013, MNRAS, 433, 3017

Lamers, H. J. G. L. M., Baumgardt, H., & Gieles, M. 2013, MNRAS, 433, 1378

Larkin, J., Barczys, M., Krabbe, A., et al. 2006, in Proc. SPIE, Vol. 6269, Society of Photo-Optical Instrumentation Engineers (SPIE) Conference Series, 62691A

Larsen, S. S., Brodie, J. P., & Hunter, D. A. 2004, AJ, 128, 2295

Larson, R. B. 2005, MNRAS, 359, 211

Li, H., Ge, J., Mao, S., et al. 2017, ApJ, 838, 77

Li, P. S., Klein, R. I., & McKee, C. F. 2018, MNRAS, 473, 4220

Lim, B., Chun, M.-Y., Sung, H., et al. 2013, AJ, 145, 46

Liptai, D., Price, D. J., Wurster, J., & Bate, M. R. 2017, MNRAS, 465, 105

Lockhart, K. E., Lu, J. R., Peiris, H. V., et al. 2017, ArXiv e-prints, arXiv:1710.01394

Lohr, M. E., Clark, J. S., Najarro, F., et al. 2018, ArXiv e-prints, arXiv:1804.05607

Lu, J. R., Do, T., Ghez, A. M., et al. 2013, ApJ, 764, 155

Lyubenova, M., Martín-Navarro, I., van de Ven, G., et al. 2016, MNRAS, 463, 3220

Martín-Navarro, I., Barbera, F. L., Vazdekis, A., Falcón-Barroso, J., & Ferreras, I. 2015, MNRAS, 447, 1033

Martins, F., Hillier, D. J., Paumard, T., et al. 2008, A&A, 478, 219

Martins, F., & Palacios, A. 2013, A&A, 560, A16

Martins, F., Schaerer, D., & Hillier, D. J. 2005, A&A, 436, 1049

McConnell, N. J., Lu, J. R., & Mann, A. W. 2016, ApJ, 821, 39

McCrady, N., Graham, J. R., & Vacca, W. D. 2005, ApJ, 621, 278

Morris, M., & Serabyn, E. 1996, ARA&A, 34, 645

Myers, A. T., Klein, R. I., Krumholz, M. R., & McKee, C. F. 2014, MNRAS, 439, 3420

Myers, A. T., McKee, C. F., Cunningham, A. J., Klein, R. I., & Krumholz, M. R. 2013, ApJ, 766, 97

Najarro, F., Figer, D. F., Hillier, D. J., & Kudritzki, R. P. 2004, ApJ, 611, L105

Narayanan, D., & Davé, R. 2013, MNRAS, 436, 2892

Newman, A. B., Smith, R. J., Conroy, C., Villaume, A., & van Dokkum, P. 2017, ApJ, 845, 157

Noll, S., Kausch, W., Kimeswenger, S., et al. 2014, A&A, 567, A25

Offner, S. S. R., Clark, P. C., Hennebelle, P., et al. 2014, Protostars and Planets VI, 53

Offner, S. S. R., Klein, R. I., McKee, C. F., & Krumholz, M. R. 2009, ApJ, 703, 131

Oser, L., Ostriker, J. P., Naab, T., Johansson, P. H., & Burkert, A. 2010, ApJ, 725, 2312

Padoan, P., & Nordlund, Å. 2002, ApJ, 576, 870

Pang, X., Grebel, E. K., Allison, R. J., et al. 2013, ApJ, 764, 73

Papadopoulos, P. P., Thi, W.-F., Miniati, F., & Viti, S. 2011, MNRAS, 414, 1705

Parikh, T., Thomas, D., Maraston, C., et al. 2018, MNRAS, arXiv:1803.08515

Park, S.-M., Goodwin, S. P., & Kim, S. S. 2018, ArXiv e-prints, arXiv:1804.08869

Paxton, B., Bildsten, L., Dotter, A., et al. 2011, ApJS, 192, 3

Paxton, B., Cantiello, M., Arras, P., et al. 2013, ApJS, 208, 4

Paxton, B., Marchant, P., Schwab, J., et al. 2015, ApJS, 220, 15

Pflamm-Altenburg, J., & Kroupa, P. 2006, MNRAS, 373, 295

Portegies Zwart, S. F., McMillan, S. L. W., & Gieles, M. 2010, ARA&A, 48, 431

Schneider, F. R. N., Izzard, R. G., de Mink, S. E., et al. 2014, ApJ, 780, 117

Schwarz, G. 1978, The Annals of Statistics, 6, 461

Serabyn, E., Shupe, D., & Figer, D. F. 1998, Nature, 394, 448

Shin, J., & Kim, S. S. 2015, MNRAS, 447, 366

Slesnick, C. L., Hillenbrand, L. A., & Massey, P. 2002, ApJ, 576, 880

Smette, A., Sana, H., Noll, S., et al. 2015, A&A, 576, A77

Spiniello, C., Trager, S., Koopmans, L. V. E., & Conroy, C. 2014, MNRAS, 438, 1483

Stassun, K. G., Feiden, G. A., & Torres, G. 2014, , 60, 1

Stolte, A., Brandner, W., Grebel, E. K., Lenzen, R., & Lagrange, A.-M. 2005, ApJ, 628, L113

Stolte, A., Ghez, A. M., Morris, M., et al. 2008, ApJ, 675, 1278

Stolte, A., Grebel, E. K., Brandner, W., & Figer, D. F. 2002, A&A, 394, 459

Stolte, A., Hußmann, B., Olczak, C., et al. 2015, A&A, 578, A4

STScI Development Team. 2013, pysynphot: Synthetic photometry software package, Astrophysics Source Code Library, , , ascl:1303.023

Swinbank, A. M., Papadopoulos, P. P., Cox, P., et al. 2011, ApJ, 742, 11

Tognelli, E., Prada Moroni, P. G., & Degl'Innocenti, S. 2011, A&A, 533, A109

van Dokkum, P., Conroy, C., Villaume, A., Brodie, J., & Romanowsky, A. J. 2017, ApJ, 841, 68

Vaughan, S. P., Davies, R. L., Zieleniewski, S., & Houghton, R. C. W. 2018, MNRAS, 475, 1073

Wegg, C., & Gerhard, O. 2013, MNRAS, 435, 1874

Weisz, D. R., Johnson, L. C., Foreman-Mackey, D., et al. 2015, ArXiv e-prints, arXiv:1502.06621

Wizinowich, P. L., Chin, J., Johansson, E., et al. 2006, in Proc. SPIE, Vol. 6272, Society of Photo-Optical Instrumentation Engineers (SPIE) Conference Series, 627209

Zeidler, P., Nota, A., Grebel, E. K., et al. 2017, AJ, 153, 122

Zieleniewski, S., Houghton, R. C. W., Thatte, N., & Davies, R. L. 2015, MNRAS, 452, 597

Zieleniewski, S., Houghton, R. C. W., Thatte, N., Davies, R. L., & Vaughan, S. P. 2017, MNRAS, 465, 192

4.8 Appendix A: Gaussian Mixture Model

The Gaussian Mixture Model used to describe the cluster and field kinematics is described in Table 4.6. Cluster membership probabilities are calculated using this model as discussed in §4.3.1.

Table 4.6. Cluster and Field Population Model: Free Parameters, Priors, and Results

Parameter[a]	Cluster Gaussian		Field Gaussian 1		Field Gaussian 2		Field Gaussian 3		Field Gaussian 4	
	Prior[b]	Result	Prior	Result	Prior	Result	Prior	Result	Prior	Result
π_k	U(0, 1)	0.047 ± 0.003	U(0, 1)	0.182 ± 0.019	U(0, 1)	0.467 ± 0.026	U(0, 1)	0.296 ± 0.023	U(0, 1)	0.008 ± 0.001
$\mu_{\alpha,k}$ (mas yr^{-1})	G(0, 0.2)	-0.01 ± 0.014	U(-7, 4)	-0.69 ± 0.05	U(-7, 4)	-1.75 ± 0.07	U(-7, 4)	-1.90 ± 0.08	U(-7, 4)	-0.76 ± 1.36
$\mu_{\delta,k}$ (mas yr^{-1})	G(0, 0.2)	-0.34 ± 0.014	U(-7, 4)	-1.01 ± 0.06	U(-7, 4)	-2.65 ± 0.10	U(-7, 4)	-2.89 ± 0.10	U(-7, 4)	-0.20 ± 1.44
$\sigma_{a,k}$ (mas yr^{-1})	U(0, 4)	0.15 ± 0.01	U(0, 20)	1.27 ± 0.08	U(0, 20)	2.68 ± 0.05	U(0, 20)	3.46 ± 0.09	U(0, 20)	14.41 ± 1.24
$\sigma_{b,k}$ (mas yr^{-1})	$\sigma_b = \sigma_a$	0.15 ± 0.01	U(0, $\sigma_{a,k}$)	0.66 ± 0.05	U(0, $\sigma_{a,k}$)	1.39 ± 0.06	U(0, $\sigma_{a,k}$)	3.21 ± 0.09	U(0, $\sigma_{a,k}$)	11.24 ± 1.01
θ_k (rad)	—	0	U(0, π)	0.93 ± 0.04	U(0, π)	0.99 ± 0.02	U(0, π)	1.01 ± 0.14	U(0, π)	0.79 ± 0.21

[a]Description of parameters: π_k = fraction of stars in Gaussian; $\mu_{\alpha,k}$ = RA-velocity centroid of Gaussian; $\mu_{\delta,k}$ = DEC-velocity centroid of Gaussian; $\sigma_{a,k}$ = semi-major axis of Gaussian; $\sigma_{b,k}$ = semi-minor axis of Gaussian; θ_k = angle between $\sigma_{a,k}$ and the RA-axis

[b]Uniform distributions: U(min, max), where min and max are bounds of the distribution; Gaussian distributions: G(μ, σ), where μ is the mean and σ is the standard deviation

4.9 Appendix B: Arches Cluster Model Posteriors

In this appendix we show the posterior probability distributions for the 1-segment IMF and 2-segment IMF analyses. For the 1-segment IMF fit, we show the joint posterior distribution for α_1 and M_{cl} in Figure 4.19 and the 1D posteriors for each model parameter in Figure 4.20. The corresponding posteriors for the 2-segment IMF fit posteriors are shown in Figures 4.21 and 4.22.

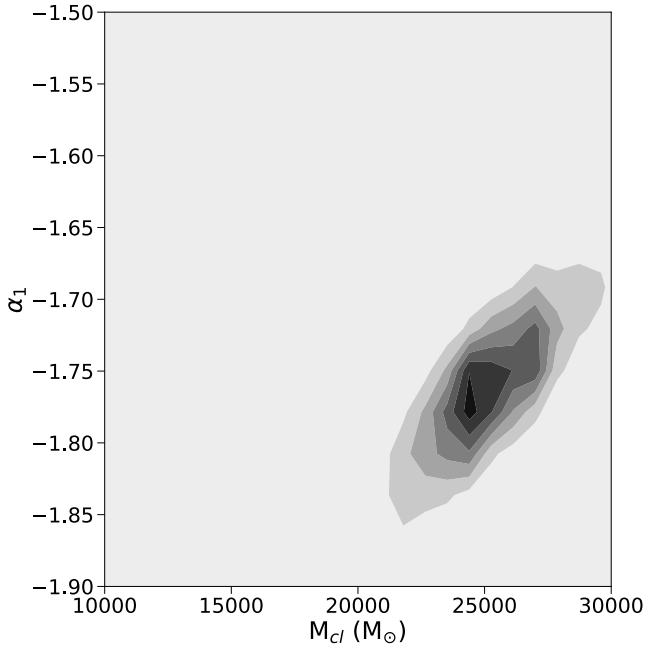

Figure 4.19 The joint posterior probability distribution for -α_1 and M_{cl} for the 1-segment IMF analysis for the Arches cluster.

4.10 Appendix C: Testing the IMF Analysis with Synthetic Clusters

To verify the accuracy of the IMF analysis, we apply it to simulated observations of a synthetic cluster and compare the output best-fit parameters with the input ones. The synthetic cluster is created as described in §4.4 and observational completeness applied as a function of position in the CMD and cluster radius. To simulate observational errors, the synthetic photometry for each star is perturbed by a random amount drawn from a normal distribution with a width equal to the median photometric error of the observed stars at the synthetic star's magnitude. These stars are

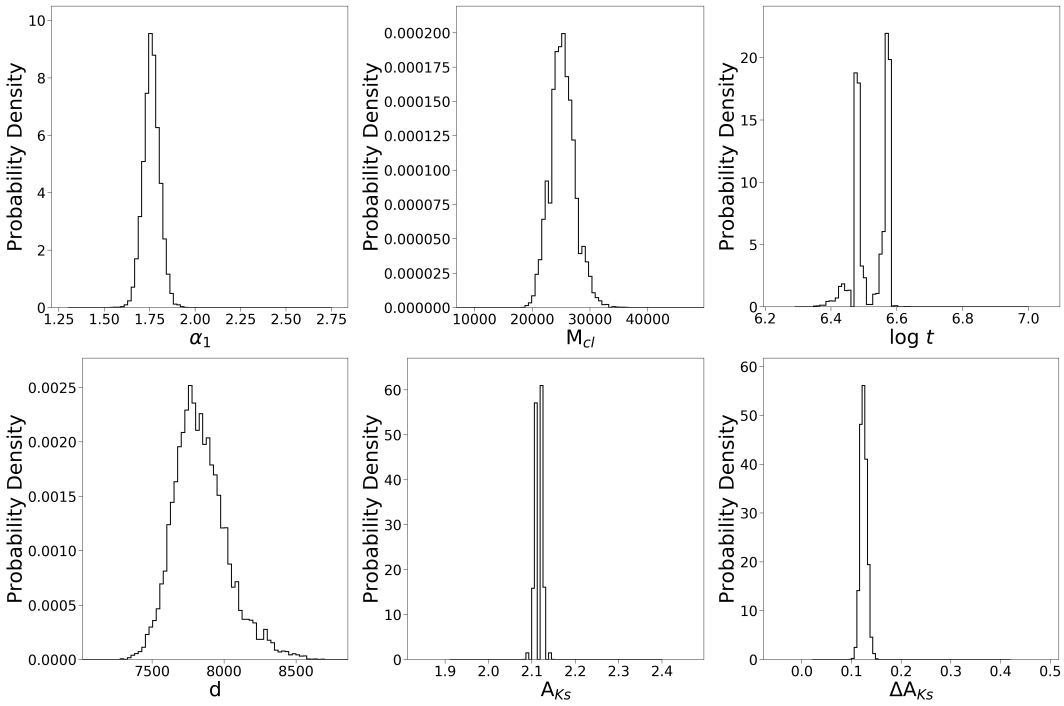

Figure 4.20 The 1D posterior probability distributions for the 1-segment IMF model for the Arches cluster.

assigned $P_{pm} = 1$. To simulate field stars, a number of stars are drawn from the observed field star population used to calculate $p(k|\Theta)_{f,obs}$ in Equation 4.6 and are assigned $P_{pm} = 0$. The number of field stars drawn is chosen such that the combined sample contains 80% cluster stars and 20% field stars. The spectroscopic sample is simulated by selecting 6 random stars with 14.5 mag $\leq$ F153M $\leq$ 15.0 mag and assigning them T_{eff} uncertainties similar to those found in §4.3.5.

The combined synthetic catalog is run through the Bayesian analysis in §4.4.1 in the same way as the real observed catalog, with two exceptions: no differential de-reddening correction is applied, since the cluster is already generated with a realistic value of ΔA_{Ks}, and no minimum P_{pm} value is enforced. The number of WR stars within $r_{cl} < 0.75$ pc is calculated and input to the fitter, mimicking the information gained from the real spectroscopic surveys of the Arches. The priors are the same as the real analysis, as described in Table 4.3.

The results of the tests are shown in Table 4.7, which found the output values to match the input values to within 1σ. The joint posterior probability distributions for α_1 and M_{cl} in the 1-

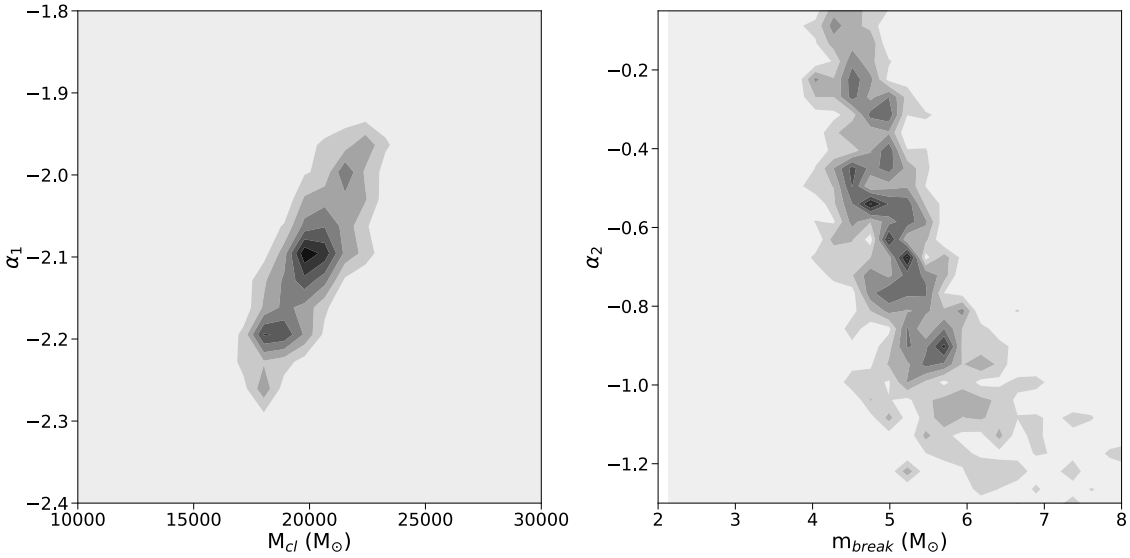

Figure 4.21 The joint posterior probability distribution for -α_1 and M_{cl} and -α_2 and m_{break} for the 2-segment IMF analysis for the Arches cluster.

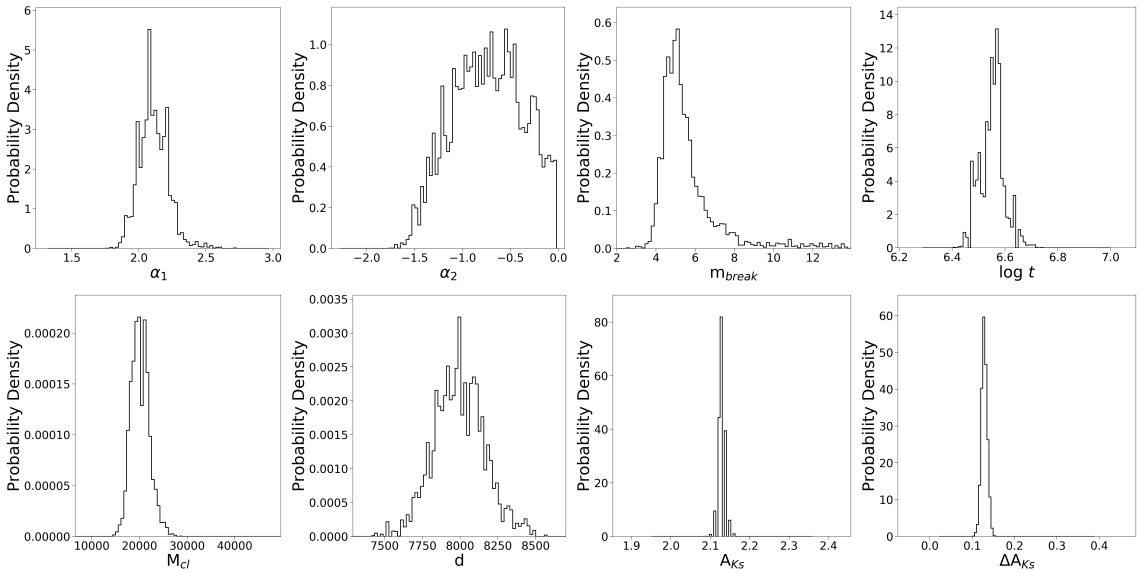

Figure 4.22 The 1D posterior probability distributions for the 2-segment IMF model for the Arches cluster.

Table 4.7. Simulated Cluster Analyses[a]

	1-segment IMF		2-segment IMF	
Parameter	Input Value	Recovered Value	Input Value	Recovered Value
α_1	1.7	1.7 ± 0.06	2.1	1.99 ± 0.13
α_2	—	—	0.7	0.74 ± 0.27
m_{break}	—	—	5.0	4.43 ± 0.91
M_{cl}	20000	21400 ± 1900	20000	20400 ± 2300
log t	6.40	6.41 ± 0.03	6.40	6.39 ± 0.01
d	8000	7865 ± 146	8000	8101 ± 139
A_{Ks}	2.07	2.07 ± 0.01	2.07	2.06 ± 0.01
ΔA_{Ks}	0.15	0.13 ± 0.01	0.15	0.14 ± 0.01

[a]Parameter priors and units are the same as Table 4.3

segment IMF fit is shown in Figure 4.23, while the joint posterior probability distributions for α_1 and M_{cl} and α_2 and m_{break} in the 2-segment IMF fit is shown in Figure 4.24.

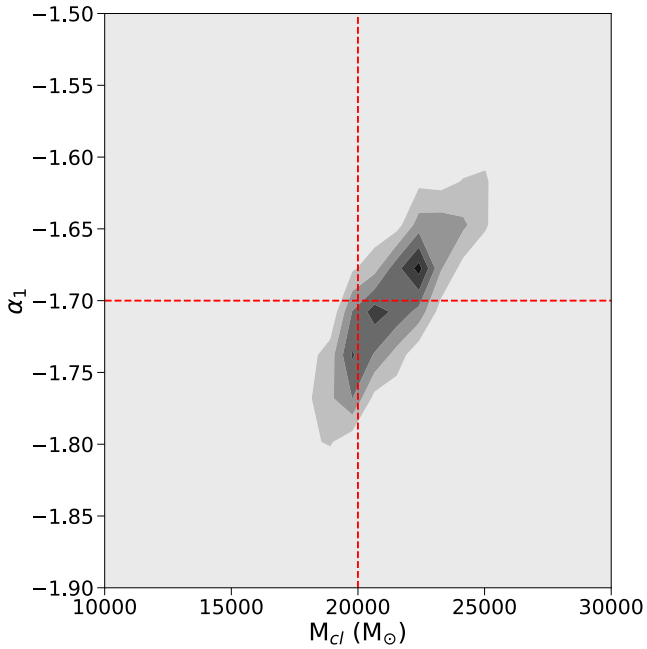

Figure 4.23 The 2D posterior probability distribution for -α_1 and M_{cl} for the 1-segment IMF simulated cluster analysis. The input values are represented by the red dotted lines.

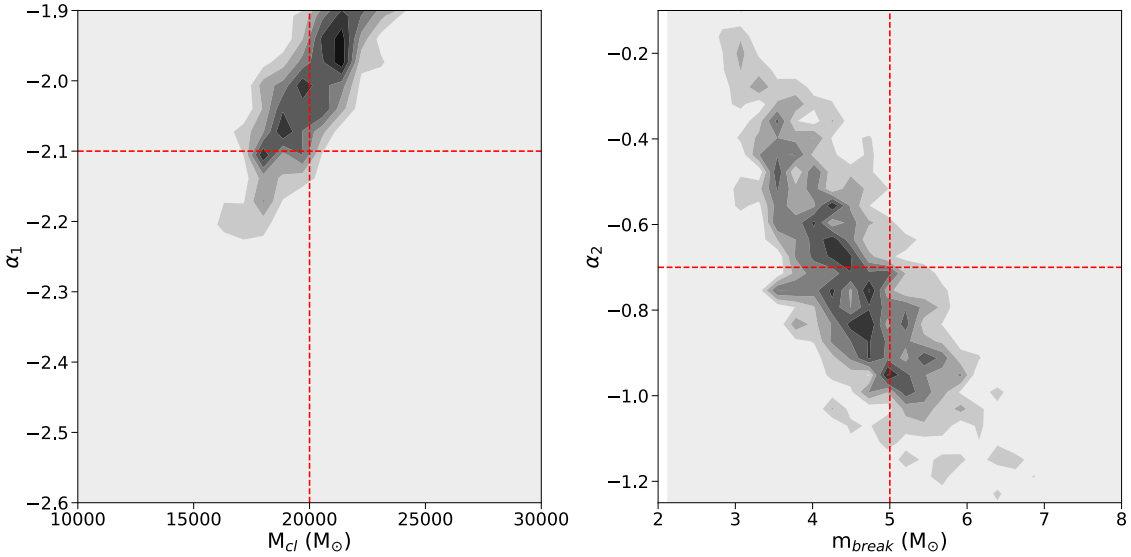

Figure 4.24 The joint posterior probability distribution for α_1 and M_{cl} (left) and α_2 and m_{break} (right) for the 2-segment IMF simulated cluster analysis. The input values are represented by the red dotted lines.

References

Andersen, M., Gennaro, M., Brandner, W., et al. 2017, A&A, 602, A22

Anderson, J., & King, I. R. 2006, PSFs, Photometry, and Astronomy for the ACS/WFC, Tech. rep.

Anderson, J., Sarajedini, A., Bedin, L. R., et al. 2008, AJ, 135, 2055

Bastian, N., Covey, K. R., & Meyer, M. R. 2010, ARA&A, 48, 339

Bastian, N., Konstantopoulos, I., Smith, L. J., et al. 2007, MNRAS, 379, 1333

Bastian, N., Saglia, R. P., Goudfrooij, P., et al. 2006, A&A, 448, 881

Bate, M. R. 2009, MNRAS, 392, 1363

Bellini, A., Libralato, M., Bedin, L. R., et al. 2018, ApJ, 853, 86

Bertelli Motta, C., Clark, P. C., Glover, S. C. O., Klessen, R. S., & Pasquali, A. 2016, MNRAS, 462, 4171

Bonnell, I. A., Clarke, C. J., & Bate, M. R. 2006, MNRAS, 368, 1296

Bonnell, I. A., & Rice, W. K. M. 2008, Science, 321, 1060

Buchner, J., Georgakakis, A., Nandra, K., et al. 2014, A&A, 564, A125

Cappellari, M., McDermid, R. M., Alatalo, K., et al. 2012, Nature, 484, 485

—. 2013, MNRAS, 432, 1862

Castelli, F., & Kurucz, R. L. 2004, ArXiv Astrophysics e-prints, astro-ph/0405087

Chabrier, G. 2005, in Astrophysics and Space Science Library, Vol. 327, The Initial Mass Function 50 Years Later, ed. E. Corbelli, F. Palla, & H. Zinnecker, 41

Chabrier, G., Hennebelle, P., & Charlot, S. 2014, ApJ, 796, 75

Choi, J., Dotter, A., Conroy, C., et al. 2016, ApJ, 823, 102

Clark, J. S., Lohr, M. E., Najarro, F., Dong, H., & Martins, F. 2018, ArXiv e-prints, arXiv:1803.09567

Clarkson, W. I., Ghez, A. M., Morris, M. R., et al. 2012, ApJ, 751, 132

Conroy, C., Dutton, A. A., Graves, G. J., Mendel, J. T., & van Dokkum, P. G. 2013, ApJ, 776, L26

Conroy, C., & van Dokkum, P. G. 2012, ApJ, 760, 71

Conroy, C., van Dokkum, P. G., & Villaume, A. 2017, ApJ, 837, 166

Cunningham, A. J., Krumholz, M. R., McKee, C. F., & Klein, R. I. 2018, MNRAS, 476, 771

Davies, R. I. 2007, MNRAS, 375, 1099

De Marchi, G., Panagia, N., Sabbi, E., et al. 2016, MNRAS, 455, 4373

Do, T., Ghez, A. M., Morris, M. R., et al. 2009, ApJ, 703, 1323

Dotter, A. 2016, ApJS, 222, 8

Ekström, S., Georgy, C., Eggenberger, P., et al. 2012, A&A, 537, A146

Espinoza, P., Selman, F. J., & Melnick, J. 2009, A&A, 501, 563

Farias, J. P., Smith, R., Fellhauer, M., et al. 2015, MNRAS, 450, 2451

Federrath, C., Schrön, M., Banerjee, R., & Klessen, R. S. 2014, ApJ, 790, 128

Feroz, F., Hobson, M. P., & Bridges, M. 2009, MNRAS, 398, 1601

Fierro, C. R., Borissova, J., Zsargó, J., et al. 2015, PASP, 127, 428

Figer, D. F., Kim, S. S., Morris, M., et al. 1999, ApJ, 525, 750

Figer, D. F., Najarro, F., Gilmore, D., et al. 2002, ApJ, 581, 258

Gennaro, M., Brandner, W., Stolte, A., & Henning, T. 2011, MNRAS, 412, 2469

Ginsburg, A., Henkel, C., Ao, Y., et al. 2016, A&A, 586, A50

Girardi, L. 2016, ARA&A, 54, 95

Goodwin, S. P., & Bastian, N. 2006, MNRAS, 373, 752

Guszejnov, D., Krumholz, M. R., & Hopkins, P. F. 2016, MNRAS, 458, 673

Habibi, M., Stolte, A., Brandner, W., Hußmann, B., & Motohara, K. 2013, A&A, 556, A26

Habibi, M., Stolte, A., & Harfst, S. 2014, A&A, 566, A6

Hanson, M. M., Kudritzki, R.-P., Kenworthy, M. A., Puls, J., & Tokunaga, A. T. 2005, ApJS, 161, 154

Harayama, Y., Eisenhauer, F., & Martins, F. 2008, ApJ, 675, 1319

Harfst, S., Portegies Zwart, S., & Stolte, A. 2010, MNRAS, 409, 628

Hennebelle, P., Commerçon, B., Joos, M., et al. 2011, A&A, 528, A72

Herczeg, G. J., & Hillenbrand, L. A. 2015, ApJ, 808, 23

Hillier, D. J., & Lanz, T. 2001, in Astronomical Society of the Pacific Conference Series, Vol. 247, Spectroscopic Challenges of Photoionized Plasmas, ed. G. Ferland & D. W. Savin, 343

Hillier, D. J., & Miller, D. L. 1998, ApJ, 496, 407

Ho, L. C., & Filippenko, A. V. 1996, ApJ, 472, 600

Hopkins, P. F. 2012, MNRAS, 423, 2037

—. 2013, MNRAS, 433, 170

Hosek, Jr., M. W., Lu, J. R., Anderson, J., et al. 2015, ApJ, 813, 27

—. 2018, ApJ, 855, 13

Hur, H., Sung, H., & Bessell, M. S. 2012, AJ, 143, 41

Husser, T.-O., Wende-von Berg, S., Dreizler, S., et al. 2013, A&A, 553, A6

Hußmann, B., Stolte, A., Brandner, W., Gennaro, M., & Liermann, A. 2012, A&A, 540, A57

Kausch, W., Noll, S., Smette, A., et al. 2015, A&A, 576, A78

Kim, S. S., Figer, D. F., Kudritzki, R. P., & Najarro, F. 2006, ApJ, 653, L113

Kim, S. S., Figer, D. F., Lee, H. M., & Morris, M. 2000, ApJ, 545, 301

Klessen, R. S., Spaans, M., & Jappsen, A.-K. 2007, MNRAS, 374, L29

Krabbe, A., Gasaway, T., Song, I., et al. 2004, in Proc. SPIE, Vol. 5492, Ground-based Instrumentation for Astronomy, ed. A. F. M. Moorwood & M. Iye, 1403–1410

Kroupa, P. 2002, Science, 295, 82

Kruijssen, J. M. D. 2009, A&A, 507, 1409

Kruijssen, J. M. D., Dale, J. E., & Longmore, S. N. 2015, MNRAS, 447, 1059

Kruijssen, J. M. D., & Longmore, S. N. 2013, MNRAS, 435, 2598

Krumholz, M. R. 2011, ApJ, 743, 110

—. 2014, Phys. Rep., 539, 49

Krumholz, M. R., Klein, R. I., & McKee, C. F. 2012, ApJ, 754, 71

Krumholz, M. R., Myers, A. T., Klein, R. I., & McKee, C. F. 2016, MNRAS, 460, 3272

La Barbera, F., Ferreras, I., Vazdekis, A., et al. 2013, MNRAS, 433, 3017

Lamers, H. J. G. L. M., Baumgardt, H., & Gieles, M. 2013, MNRAS, 433, 1378

Larkin, J., Barczys, M., Krabbe, A., et al. 2006, in Proc. SPIE, Vol. 6269, Society of Photo-Optical Instrumentation Engineers (SPIE) Conference Series, 62691A

Larsen, S. S., Brodie, J. P., & Hunter, D. A. 2004, AJ, 128, 2295

Larson, R. B. 2005, MNRAS, 359, 211

Li, H., Ge, J., Mao, S., et al. 2017, ApJ, 838, 77

Li, P. S., Klein, R. I., & McKee, C. F. 2018, MNRAS, 473, 4220

Lim, B., Chun, M.-Y., Sung, H., et al. 2013, AJ, 145, 46

Liptai, D., Price, D. J., Wurster, J., & Bate, M. R. 2017, MNRAS, 465, 105

Lockhart, K. E., Lu, J. R., Peiris, H. V., et al. 2017, ArXiv e-prints, arXiv:1710.01394

Lohr, M. E., Clark, J. S., Najarro, F., et al. 2018, ArXiv e-prints, arXiv:1804.05607

Lu, J. R., Do, T., Ghez, A. M., et al. 2013, ApJ, 764, 155

Lyubenova, M., Martín-Navarro, I., van de Ven, G., et al. 2016, MNRAS, 463, 3220

Martín-Navarro, I., Barbera, F. L., Vazdekis, A., Falcón-Barroso, J., & Ferreras, I. 2015, MNRAS, 447, 1033

Martins, F., Hillier, D. J., Paumard, T., et al. 2008, A&A, 478, 219

Martins, F., & Palacios, A. 2013, A&A, 560, A16

Martins, F., Schaerer, D., & Hillier, D. J. 2005, A&A, 436, 1049

McConnell, N. J., Lu, J. R., & Mann, A. W. 2016, ApJ, 821, 39

McCrady, N., Graham, J. R., & Vacca, W. D. 2005, ApJ, 621, 278

Morris, M., & Serabyn, E. 1996, ARA&A, 34, 645

Myers, A. T., Klein, R. I., Krumholz, M. R., & McKee, C. F. 2014, MNRAS, 439, 3420

Myers, A. T., McKee, C. F., Cunningham, A. J., Klein, R. I., & Krumholz, M. R. 2013, ApJ, 766, 97

Najarro, F., Figer, D. F., Hillier, D. J., & Kudritzki, R. P. 2004, ApJ, 611, L105

Narayanan, D., & Davé, R. 2013, MNRAS, 436, 2892

Newman, A. B., Smith, R. J., Conroy, C., Villaume, A., & van Dokkum, P. 2017, ApJ, 845, 157

Noll, S., Kausch, W., Kimeswenger, S., et al. 2014, A&A, 567, A25

Offner, S. S. R., Clark, P. C., Hennebelle, P., et al. 2014, Protostars and Planets VI, 53

Offner, S. S. R., Klein, R. I., McKee, C. F., & Krumholz, M. R. 2009, ApJ, 703, 131

Oser, L., Ostriker, J. P., Naab, T., Johansson, P. H., & Burkert, A. 2010, ApJ, 725, 2312

Padoan, P., & Nordlund, Å. 2002, ApJ, 576, 870

Pang, X., Grebel, E. K., Allison, R. J., et al. 2013, ApJ, 764, 73

Papadopoulos, P. P., Thi, W.-F., Miniati, F., & Viti, S. 2011, MNRAS, 414, 1705

Parikh, T., Thomas, D., Maraston, C., et al. 2018, MNRAS, arXiv:1803.08515

Park, S.-M., Goodwin, S. P., & Kim, S. S. 2018, ArXiv e-prints, arXiv:1804.08869

Paxton, B., Bildsten, L., Dotter, A., et al. 2011, ApJS, 192, 3

Paxton, B., Cantiello, M., Arras, P., et al. 2013, ApJS, 208, 4

Paxton, B., Marchant, P., Schwab, J., et al. 2015, ApJS, 220, 15

Pflamm-Altenburg, J., & Kroupa, P. 2006, MNRAS, 373, 295

Portegies Zwart, S. F., McMillan, S. L. W., & Gieles, M. 2010, ARA&A, 48, 431

Schneider, F. R. N., Izzard, R. G., de Mink, S. E., et al. 2014, ApJ, 780, 117

Schwarz, G. 1978, The Annals of Statistics, 6, 461

Serabyn, E., Shupe, D., & Figer, D. F. 1998, Nature, 394, 448

Shin, J., & Kim, S. S. 2015, MNRAS, 447, 366

Slesnick, C. L., Hillenbrand, L. A., & Massey, P. 2002, ApJ, 576, 880

Smette, A., Sana, H., Noll, S., et al. 2015, A&A, 576, A77

Spiniello, C., Trager, S., Koopmans, L. V. E., & Conroy, C. 2014, MNRAS, 438, 1483

Stassun, K. G., Feiden, G. A., & Torres, G. 2014, , 60, 1

Stolte, A., Brandner, W., Grebel, E. K., Lenzen, R., & Lagrange, A.-M. 2005, ApJ, 628, L113

Stolte, A., Ghez, A. M., Morris, M., et al. 2008, ApJ, 675, 1278

Stolte, A., Grebel, E. K., Brandner, W., & Figer, D. F. 2002, A&A, 394, 459

Stolte, A., Hußmann, B., Olczak, C., et al. 2015, A&A, 578, A4

STScI Development Team. 2013, pysynphot: Synthetic photometry software package, Astrophysics Source Code Library, , , ascl:1303.023

Swinbank, A. M., Papadopoulos, P. P., Cox, P., et al. 2011, ApJ, 742, 11

Tognelli, E., Prada Moroni, P. G., & Degl'Innocenti, S. 2011, A&A, 533, A109

van Dokkum, P., Conroy, C., Villaume, A., Brodie, J., & Romanowsky, A. J. 2017, ApJ, 841, 68

Vaughan, S. P., Davies, R. L., Zieleniewski, S., & Houghton, R. C. W. 2018, MNRAS, 475, 1073

Wegg, C., & Gerhard, O. 2013, MNRAS, 435, 1874

Weisz, D. R., Johnson, L. C., Foreman-Mackey, D., et al. 2015, ArXiv e-prints, arXiv:1502.06621

Wizinowich, P. L., Chin, J., Johansson, E., et al. 2006, in Proc. SPIE, Vol. 6272, Society of Photo-Optical Instrumentation Engineers (SPIE) Conference Series, 627209

Zeidler, P., Nota, A., Grebel, E. K., et al. 2017, AJ, 153, 122

Zieleniewski, S., Houghton, R. C. W., Thatte, N., & Davies, R. L. 2015, MNRAS, 452, 597

Zieleniewski, S., Houghton, R. C. W., Thatte, N., Davies, R. L., & Vaughan, S. P. 2017, MNRAS, 465, 192

Chapter 5

Moving Forward

5.1 The Initial Mass Function of the Quintuplet Cluster: Current Status

The natural next step in understanding the IMF at the Galactic Center is to measure the IMF of the Quintuplet cluster. With an identical set of *Hubble Space Telescope* observations (GO-11671, GO-12318, GO-12667, PI: Ghez, A.M.; GO-14613, PI: Lu., J.R.), the analysis techniques developed in chapters 2 and 4 (as well as the extinction law in chapter 3) can be applied to the Quintuplet data. In this section I describe the progress that has been made in this analysis, which I will continue to work on over the summer.

5.1.1 The Quintuplet Cluster: Extended Structure and Tidal Radius

In order to constrain the Quintuplet IMF, we must first measure the stellar radial density profile of the cluster and to determine if it exhibits mass segregation or tidal tails. I have mentored UC Berkeley undergraduate Nicholas Rui since Fall 2016 on a project analyzing the dynamical structure of the Quintuplet cluster in a similar manner as the Arches cluster in chapter 2. This work is nearly ready for submission with the following authors: Nicholas Z. Rui, Matthew W. Hosek Jr, Jessica R. Lu, Jay Anderson, Mark R. Morris, Andrea M. Ghez, and William I. Clarkson. I summarize several of the key results here.

Since the Quintuplet is less centrally concentrated than the Arches, we can use our *HST* data to measure the cluster core as well as the outer regions. Our proper motion catalog spans from 0

pc < r < 3.2 pc, covering a radius range six times larger than previous proper motion studies of the cluster (r < 0.5 pc; Hußmann et al. 2012). The CMD of the field is shown in Figure 5.1, along with stars with $P_{pm} > 0.3$. Adopting the same error cuts as H15, the completeness limit is 153M = 17.7 mag (∼8.2 $M_\odot$) for the entire sample and F153M = 18.7 mag (∼5.1 $M_\odot$) for r > 0.3 pc. The completeness is lower than the Arches profile analysis, where we achieved a depth of ∼2.5 $M_\odot$ with only 3 epochs of *HST* observations. This is likely due to the increased density of stars in the Quintuplet field, which has a lower average extinction and smaller range of differential extinction than the Arches field (see Figure 1.1).

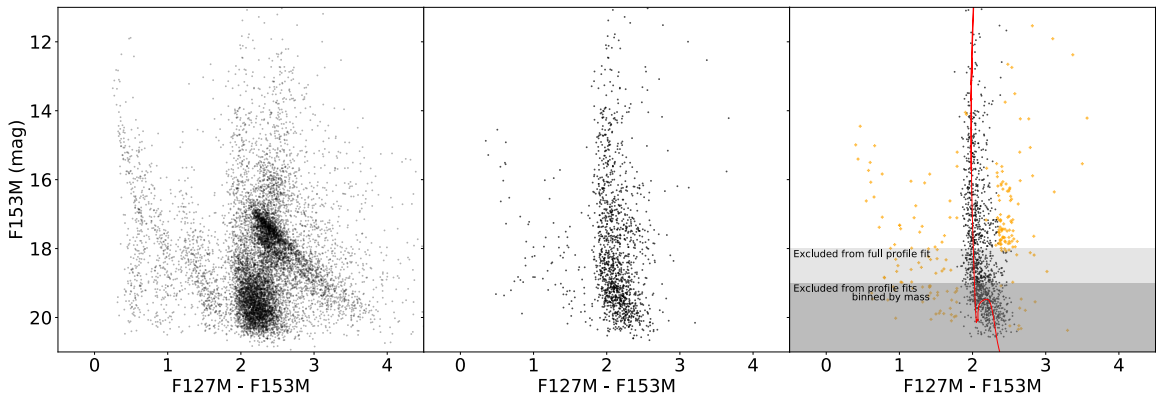

Figure 5.1 The CMD of proper motion-selected Quintuplet cluster stars. The left panel shows the CMD of the entire field (with proper motion error less than 0.65 mas yr^{-1}), the middle panel shows stars with $P_{pm} > 0.3$, and the right panel shows the stars with $P_{pm} > 0.3$ after a differential extinction correction. Stars eliminated by a color cut are shown by the orange points. Overall, the Quintuplet sequence has less spread than the Arches, indicating that the field has less differential extinction.

We find that the Quintuplet radial profile is well described by an Elson et al. (1987) profile with a constant term added for the background (see Equation 2.7). The corresponding best-fit parameters are $\gamma = 2.8^{+1.1}_{-0.6}$, $a = 0.7^{+0.3}_{-0.2}$ pc, and $b = 1.9^{+1.7}_{-1.3}$. Similar to the Arches, no evidence of tidal truncation is found, and we place a 3σ lower limit of 3.2 pc on the tidal radius. A comparison of the Arches and Quintuplet radial profiles is shown in Figure 5.2. The Quintuplet is larger, with a half-light radius more than 2x larger than the Arches (1.1 pc vs. 0.48 pc). This may be the result of star cluster evolution in the strong tidal field near the GC, as the Quintuplet is the older of the two clusters (4.8 ± 1.1 Myr; Schneider et al. 2014). Future measurement of the velocity dispersion profiles of these clusters will provide further insight into their dynamical state.

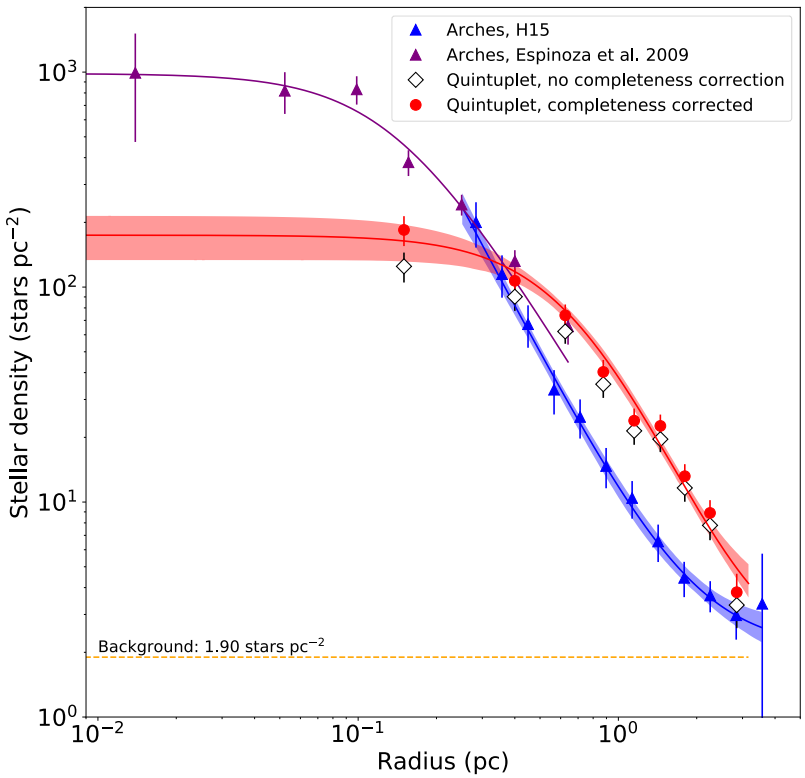

Figure 5.2 A comparison of the radial profiles of the Arches cluster (purple and blue points from Espinoza et al. 2009; Hosek et al. 2015, respectively) and the Quintuplet cluster (black open diamonds: without completeness, red solid points: with completeness). The Quintuplet is the larger of the two clusters, perhaps due to its longer exposure to the strong tidal field near the GC.

Similar to the Arches, we find no evidence for tidal tails in the Quintuplet cluster, but do find evidence of mass segregation. The power-law slope of the outer portion of the profile is found to become steeper as a function of mass, indicating that the high-mass stars are more centrally concentrated (Figure 5.3). Efforts are underway to determine if the Quintuplet is mass segregated over the entire observed mass range, or if there is a critical mass below which the radial profile shows no mass dependence.

5.1.2 Next Step: The Quintuplet IMF

Once the mass-dependent radial profile of the Quintuplet profile is finalized, we can use the methodology described in chapter 4 to measure the IMF of the Quintuplet cluster. We will again use the magnitude-dependent radial profiles to model mass segregation and assume that tidal stripping has not significantly impacted the mass function for our sample. We do not have spectroscopy of

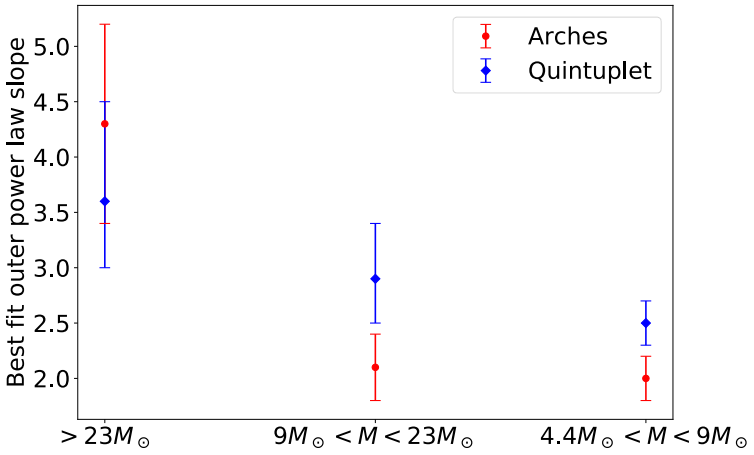

Figure 5.3 The power law slope of the outer portion of the radial profile as a function of mass for both the Arches (red) and Quintuplet (blue) clusters. For both clusters, the profile of high-mass stars is steeper than the lower-mass stars, indicating the presence of mass segregation.

cluster members, though can rely on previous spectroscopic surveys to obtain the number of WR star in the cluster (e.g. Liermann et al. 2009). Preliminary efforts to retool the IMF analysis for the Quintuplet cluster have begun.

5.2 The Arches and Quintuplet Clusters in the Age of JWST

Scheduled to launch in May 2020, the *James Webb Space Telescope* (JWST) will herald a new era of space-based near-infrared astronomy. With a 6.5m primary mirror, the increased light-gathering power and resolution of JWST will provide tremendous new opportunities to study star formation and stellar populations across different environments, including the Arches and Quintuplet clusters. We will propose for parallel observations with NIRCam and NIRSpec to:

1. Combine with existing Hubble Space Telescope observations to directly measure the IMF of the clusters down to at least 1 $M_\odot$, in order to distinguish between possible 1-segment and 2-segment IMF models.

2. Obtain the first of three astrometric JWST observations required to characterize the low-mass IMF down to $\sim$0.12 $M_\odot$, nearly the brown dwarf limit.

3. Measure the circumstellar disk fraction of as a function of both mass and radius in order to study disk evolution in a young massive cluster (YMC) environment. This will be the first such measurement for low-mass stars in a YMC, allowing for a direct comparison to disk populations in nearby star forming regions.

As discussed below, these goals can be achieved with a total exposure time of 3.05 hours, not counting overheads.

5.2.1 Measuring the IMF Over the Full Stellar Mass Range

As discussed in chapter 1, the IMF above $\sim$0.15 $M_\odot$ has been observed to generally consistent with the local IMF for star clusters across the Milky Way and nearby galaxies. However, in chapter 4 we showed that the IMF of the Arches cluster is significantly different than the local IMF for $M \gtrsim 1.8$ $M_\odot$, comprised of either a single power-law with a top-heavy slope ($\alpha = 1.76 \pm 0.03 \pm 0.05$) or a 2-segment power law with a break at $5^{+1.25}_{-0.65}$ $M_\odot$. The implications for star formation physics differ for these two scenarios. The 2-segment solution is consistent with models that predict that the peak of the IMF is set primarily by the thermal Jeans mass within a molecular cloud, and so the high gas temperatures near the GC would lead to a higher turnover mass but the high-mass slope would remain largely unaffected (e.g. Larson 2005; Bonnell et al. 2006; Klessen et al. 2007; Bonnell & Rice 2008; Papadopoulos et al. 2011; Narayanan & Davé 2013). On the other hand, the 1-segment solution contradicts theories where the high-mass slope of the IMF directly maps to the core mass function (CMF) created by the turbulent properties of the molecular cloud (e.g. Hopkins 2012, 2013; Chabrier et al. 2014). These models predict that the mass function slope should become steeper to create a bottom-heavy IMF in the highly-turbulent GC environment rather than shallower and top-heavy. Unfortunately, it is not possible to distinguish between these two solutions with current data, likely because the completeness limit is close to the potential break mass.

JWST allows us to extend our IMF measurements of the Arches and Quintuplet clusters to very low stellar masses. As detailed in §5.2.3, three epochs of astrometry over the 5-year lifetime of the mission will provide proper motion-based cluster membership probabilities nearly down to the brown dwarf limit, reaching $\sim$0.15 $M_\odot$ in the Arches cluster and $\sim$0.34 $M_\odot$ in the Quintuplet

cluster. This will allow us to characterize the IMF over the full stellar mass range, establishing both the turnover mass and high-mass IMF slope. Even a single *JWST* epoch, when combined with our existing multi-epoch *HST* star catalogs, will extend our IMF measurement to at least 1 $M_{\odot}$, which will allow us to better distinguish between the 1-segment and 2-segment IMF models.

5.2.2 Protoplanetary Disk Evolution in Young Massive Clusters

Characterizing the evolution of circumstellar disks and the mechanisms by which they are destroyed is critical to understanding how planet formation occur (e.g. Kley & Nelson 2012; Morbidelli & Raymond 2016). Though it has been established that disks dissipate within the first few million years of their host star's life (e.g. Haisch et al. 2001), the interplay between the mechanisms driving this process is not well understood. In general, nearby star forming regions have been found to have disk frequencies that decrease with stellar mass (e.g. Hernández et al. 2007; Luhman & Mamajek 2012; Ribas et al. 2015) and close proximity to massive stars (e.g. Mann et al. 2014), presumably due to increased photoevaporation from stellar winds and UV radiation (e.g. Alexander et al. 2014). However, the relative importance of stellar interactions in this process is less understood; dynamical simulations predict that these interactions can truncate or even destroy a large fraction of stellar disks in high-density environments (e.g. Olczak et al. 2012; Vincke et al. 2015), perhaps even before photoevaporation processes begin to take effect (Portegies Zwart 2016).

Young massive clusters are expected to be hazardous environments for circumstellar disks, with strong UV radiation fields from massive stars as well as high stellar densities. Previous studies have found significantly lower disk fractions for the Arches cluster (Stolte et al. 2010), Quintuplet cluster (Stolte et al. 2015), 30 Dor (Maercker & Burton 2005), and NGC 3603 (Stolte et al. 2004; Harayama et al. 2008) compared to nearby star forming regions of the same age (e.g., Figure 21 of Stolte et al. 2015). However, the disk fractions of these YMCs have only been measured for OBA-type stars, while the disk fractions for nearby star forming regions are dominated by low mass stars. Thus, it is unclear if this discrepancy is truly due to the YMC environment or if it is simply a result of increased disk destruction around high-mass stars.

With *JWST*, we will measure the circumstellar disk fraction of the Arches and Quintuplet clusters to low masses in order to characterize disk survival in YMCs relative to lower mass star forming regions. We will leverage the high-quality cluster samples provided by our proper

motion-based cluster membership catalogs to minimize field contamination and get an accurate measurement of the disk fraction. We also avoid potential selection biases against disk-free young stellar objects (as is possible in photometrically-selected samples) or high-mass stars (as is possible with X-ray selected samples). In addition, the spatial coverage provided by our *HST* + *JWST* observations is more than 2x greater than the previous studies by Stolte et al. (2010) and Stolte et al. (2015), resulting in a larger sample and better statistics at the high-mass end.

The high spatial coverage also allows us to measure the disk fraction as a function of radius within the Arches and Quintuplet clusters, revealing how the changing environment *within* a cluster affects disk evolution. No significant trend of disk fraction with radius has been found for the Quintuplet cluster, with a constant disk fraction of 4.0 ± 0.7% out to r < 1.5 pc (Stolte et al. 2015). On the other hand, the Arches disk fraction has been observed to increase from 2.7% for r < 0.16 pc to 9.7% for r > 0.3 pc (Stolte et al. 2010). Our proposed study offers a larger radius range and better spatial coverage than past work, plus the sensitivity to probe low-mass stars.

5.2.3 Observation Plan

NIRCam is an imaging camera composed of two co-aligned 2'x2' fields, each allowing for simultaneous observations in both a short wavelength (0.8 μm – 2.3 μm) and long wavelength (2.4 μm – 5.0 μm) channel. Thus, a single NIRCam field is similar to the HST WFC3-IR field and is well situated to study the Arches and Quintuplet clusters. NIRSpec is a spectrograph offering spectral coverage from 0.6 μm – 5.3 μm with multi-object and integral field capabilities with up to R∼2700. Our observations will use the multi-object mode, which offers a 3.6' x 3.4' field of view with 0.4" spatial resolution. The positions of these instruments on the JWST focal plane is fortuitous in that the clusters can be observed simultaneously, with one cluster in a NIRCam field and the other in the NIRSpec field (Figure 5.4). This allows for a very efficient observing program where spectroscopic followup of cluster members is obtained "for free."

To measure the low-mass IMF of the Arches and Quintuplet clusters, we will obtain observations in the F212N (2.121 μm) and F140M (1.405 μm) filters. The F212N observations will be used for astrometry, since it is at the shortest wavelength where JWST will be diffraction limited and thus provides the best resolution (FWHM = 0.077"). Though slightly better resolutions may be possible shortward of F212N, the corresponding increase in total extinction due to the steep extinction law

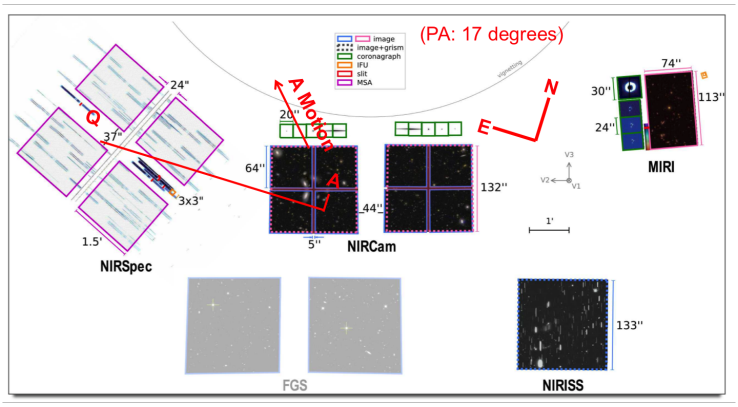

Figure 5.4 The JWST focal plane with the locations of the different instruments, adopted from https://jwst.stsci.edu/. At a position angle of 17°, the Arches cluster (denoted by the "A") and Quintuplet cluster (denoted by the "Q") can be observed in parallel with both NIRCam and NIRSpec. The proper motion vector of the Arches cluster is also shown for reference.

reduces the depth of the observations. We use the narrow-band filter to minimize saturation for the bright stars in the clusters. The F140M observations are necessary to obtain color information for the stars as required in the IMF analysis (see the CMD modeling described in chapter 4) and for the extinction correction. The medium-band filter is a compromise between avoiding saturation for the brightest stars while maintaining sensitivity to lower-mass stars due to high extinction.

To identify circumstellar disks we will use the F323N (3.237 μm) and F470N (4.708 μm) filters. The F323N filter similar to the ground-based L-band filter, which is commonly used to identify circumstellar disks via infrared excess (e.g. Lada et al. 2000; Haisch et al. 2001). By adopting similar techniques, we can directly compare the numbers of disks we identify to studies of local star forming regions. The F470N filter is the longest wavelength narrow-band filter available for NIRCam, which is advantageous because the excess emission caused by a circumstellar disk increases as a function of wavelength (e.g. Chiang & Goldreich 1997), making stars with disks easier to identify. Therefore the F470N observations are valuable in two ways: 1) we can obtain a more accurate census of stars with circumstellar disks, and 2) we can identify non-disk bearing stars falsely identified as having disks by the F323N selection criteria, characterizing this potential source of error in studies that use the L-band to identify circumstellar disks.

For the NIRSpec observations, we will use the multi-object spectroscopic mode (MSA) with the G235H/F170LP grating. This setup provides continuous spectral coverage between 1.7 μm –

3.0 μm, the conventional H-band and K-band regions, at a resolution of R$\sim$2700. Obtained in parallel with the NIRCam observations, these spectra will be used to test our cluster membership probabilities (e.g. by separating young stars from old field stars, as in Do et al. 2013) and derive stellar properties in order to further constrain the mass-luminosity relationship and test stellar evolution models (e.g. chapter 4, Repolust et al. 2005; Clark et al. 2018). While these spectra are lower resolution than previous ground-based studies, they offer wider spectral coverage and avoid systematics potentially introduced by sky subtraction and telluric correction. In addition, a large sample can be obtained quickly via the multi-object capabilities.

In the sections below, I describe several technical aspects of the observations, including the confusion limits, signal-to-noise requirements, and exposure time estimates. I also discuss the expected improvement to the current proper motion sample with just a single *JWST* epoch.

Confusion Limits

Given the sensitivity of JWST, the primary factor limiting the depth of the proposed observations is stellar crowding. We define the confusion limit as the magnitude at which stars are separated by less than two resolution elements, which occurs when the cumulative stellar density reaches 1 / (2*FWHM)^2. To estimate the confusion limits for the Arches and Quintuplet fields, we use the completeness-corrected luminosity function derived from HST WFC3-IR field outside the core radii of the clusters (r = 0.2 pc and r = 0.6 pc, respectively) and extrapolate it using a power law to fainter magnitudes. We exclude the cluster core regions because the HST completeness is too low and so extrapolation becomes difficult. The cumulative density at a given magnitude is calculated as the integral of the luminosity function down to that magnitude divided by the observed area.

The confusion limit as a function of wavelength is shown in Figure 5.6, with the confusion limits of our proposed filters in Table 5.1. We assume that the NIRCam FWHM is equal to the diffraction-limit for $\lambda > 2\mu$m and equal to the diffraction limit at 2μm for $\lambda < 2\mu$m. Also included are NIRSpec confusion limits for the IFU and MSA observing modes, which have FWHM values of 0.2" and 0.4", respectively. The confusion limits for the IMF measurements (e.g. F140M and F212N observations) are $\sim$0.14 M$_\odot$ and $\sim$0.36 M$_\odot$ for the Arches and Quintuplet, respectively. The limits for the circumstellar disk study are $\sim$0.5 M$_\odot$ and $\sim$1 M$_\odot$, respectively. As discussed in

§5.1.1, the Quintuplet limits are brighter than the Arches limits because the stellar density of field stars is higher as a result of the lower average extinction.

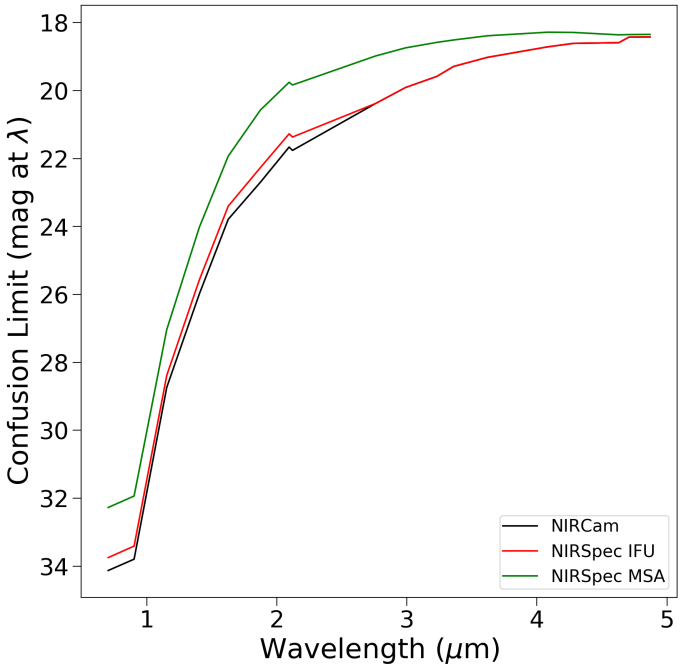

Figure 5.5 The JWST confusion limit as a function of wavelength for the Arches cluster, for NIRCam (black line), NIRSpec in MSA mode (green line), and NIRSpec in IFU mode (red line).

Signal-to-Noise Requirements

For the IMF analysis, our goal is to obtain photometric (mag, color, extinction) and cluster membership information for stars down to the confusion limit over the 5-year baseline of the JWST mission. This requirement drives the signal-to-noise ratio (SNR) needed in the F140M and F212N filters, which in turn sets the requested exposure time. In chapter 4, we demonstrated the ability to calculate proper-motion cluster memberships with just ∼8% field contamination over the sample. The median proper motion error at the faint end of the sample is 0.4 mas yr^{-1}, and so we will also require this precision at the JWST confusion limit.

Assuming three epochs of observations obtained in JWST cycles 1, 3, and 5, we calculate the astrometric precision required for a given proper motion precision as:

Table 5.1. JWST Confusion Limits

Filter	Arches Limit[a] (mag)	Mass ($M_\odot$)	Quintuplet Limit[b] (mag)	Mass ($M_\odot$)
F140M	25.98	0.14	24.50	0.36
F212N	21.67	0.14	20.71	0.36
F323N	19.58	0.28	18.84	0.63
F470N	18.42	0.48	18.18	0.98

[a]Assuming $A_{Ks} = 2.07$ mag

[b]Assuming $A_{Ks} = 1.80$ mag

$$\sigma_{ast} = \frac{\sigma_{pm} * \Delta t}{\sqrt{2}} \tag{5.1}$$

where σ_{pm} is the target proper motion error, σ_{ast} is the astrometric error, and Δt is the time baseline of the observations. From this, we find that $\sigma_{ast} = 1.4$ mas to obtain $\sigma_{pm} = 0.4$ mas yr^{-1}.

Next, we calculate what SNR is required to obtain $\sigma_{ast} = 1.4$ mas in a given epoch. Using the 3-epoch HST proper motion catalog (i.e., the catalog used in Hosek et al. 2015), we find that:

$$\sigma_{ast} = \alpha * \frac{FWHM}{SNR} \tag{5.2}$$

where $FWHM$ is the full-width half-max of the observations and $\alpha = 0.6$. For the JWST FWHM in the F212N filter, we then find that the SNR required to achieve σ_{ast}=1.4 mas is 12.1. We thus adopt this as the SNR requirement in F212N at the confusion limit.

We will model the F140M observations after the F127M observations from in chapter 4 in order to set the SNR requirement. The average F127M photometric error at the *HST* completeness limit is 0.2 mags, and so we will set this as the minimum F140M precision required over the *JWST* sample. This corresponds to SNR = 5 at the *JWST* confusion limit.

Exposure Time Calculations

We calculate the exposure times needed to meet our SNR requirements using the online JWST exposure time calculator[1]. NIRCam and NIRSpec have a range of readout patterns and observing

[1]https://jwst.etc.stsci.edu/

Table 5.2. Arches Cluster: NIRCam Observing Strategy

Filter	Readout Mode	Groups, Integrations, Exposures	t_{exp}[a] (s)	t_{tot}[b] (s)
F140M + F323N	Rapid	10, 2, 16	236	3779
F212N + F470N	Rapid	10, 1, 12	118	1417
Total				5493

[a]Time per exposure

[b]Total time of observation

strategies available which must be optimized for the given science case. For the Aches and Quintuplet, we wish to select NIRCam strategy for F140M and F212N that 1) achieves the desired SNR at the confusion limit, 2) hits hard saturation as close to the WR star magnitude limit as possible (F212 $\sim$ 12.0 mag, F140M $\sim$ 15.5 mag), so we limit information loss at the bright end of the HST sample, 3) provides acceptable SNR and saturations limits for the F323N and F470N filters, which are observed simultaneously, and 4) provide reasonable single exposure times for the NIRSpec exposures that are taken in parallel. Fortunately, the exposure time calculator provides the tools to find a suitable solution for this problem.

The available NIRCam readout patters and exposure strategies are discussed in detail in Robberto (2009, 2010). Briefly, a series of non-destructive and destructive reads are made for a given exposure. The user selects the readout pattern (which sets the frequency and grouping of the non-destructive reads), the number of non-destructive "groups" read per integration, and the number of integrations (which are destructive reads) per exposure. Table 5.2 describes the best observing strategy found for the Arches cluster, which pairs the F140M + F323N filters and F212N + F470N filters. The total exposure time for the Arches is thus 5493 s (1.53 hours), not counting overheads. With this setup, we achieve SNR $\approx$ 65 in F323N and F470N down to their respective confusion limits, thus attaining photometric precisions 0.015 mag and better over the sample. Assuming that we repeat these same observations for the Quintuplet (and again ignoring overheads), the total requested time is a modest 3.05 hours.

For the NIRSpec observations, we must select an observing strategy that produces individual exposures with exposure times less than or equal to the NIRCam exposure times, since the telescope

with dither after each NIRCam exposure. We therefore choose to obtain the NIRSpec observations in parallel with the F140M+F323N observations, which has longer individual and total exposure times. Fortunately, there is a convenient NIRSpec match for these observations: adopting a NRS IRS2 readout pattern, using 3 groups per integration, 1 integration per exposure, and 16 exposures. The individual exposure times come to 233 s with a total spectroscopic exposure time of 3735 s. This provides spectra with SNR $\gtrsim$ 70 for the main sequence stars to the pre-main sequence turn on (F153M $\sim$ 19 mag).

5.2.4 HST + JWST After One Epoch

Using the proper motion catalog in chapter 4, we predict the improvement in proper motion precision we will obtain after a single epoch of JWST astrometry. The *JWST* SNR as a function of magnitude is calculated using the online exposure time calculator and converted into σ_{ast} using Equation 5.2. Next, we add a single astrometric point for each star at t = 2020 based on its proper motion and perturb it by a random value drawn from a Gaussian with a width equal to σ_{ast}. New proper motions are calculated with the additional *JWST* point in the same manner as before. The resulting proper motion errors are $\sim$3.5 times lower than the original errors, as shown in Figure 5.6.

This analysis predicts that we will achieve typical proper motion errors better than 0.4 mas yr^{-1} over the entire HST sample, which reaches F153M = 23.5 mag (0.34 M_{odot}). However, it is important to note that we won't truly achieve this depth because we are fundamentally limited by stellar crowding in the central regions of the clusters, which significantly limit the HST observations. We use the artificial star plant and recovery tests described in chapter 4 to place an upper limit to our new 30% completeness limits after the *JWST* observation is added. We find that the Arches sample is extended to at least F153M = 21.8 mag ($\sim$1 $M_\odot$) and the Quintuplet sample is extended to at least F153M = 20.1 mag ($\sim$1.8 $M_\odot$). A more sophisticated simulation of the HST + JWST completeness is left to the actual proposal.

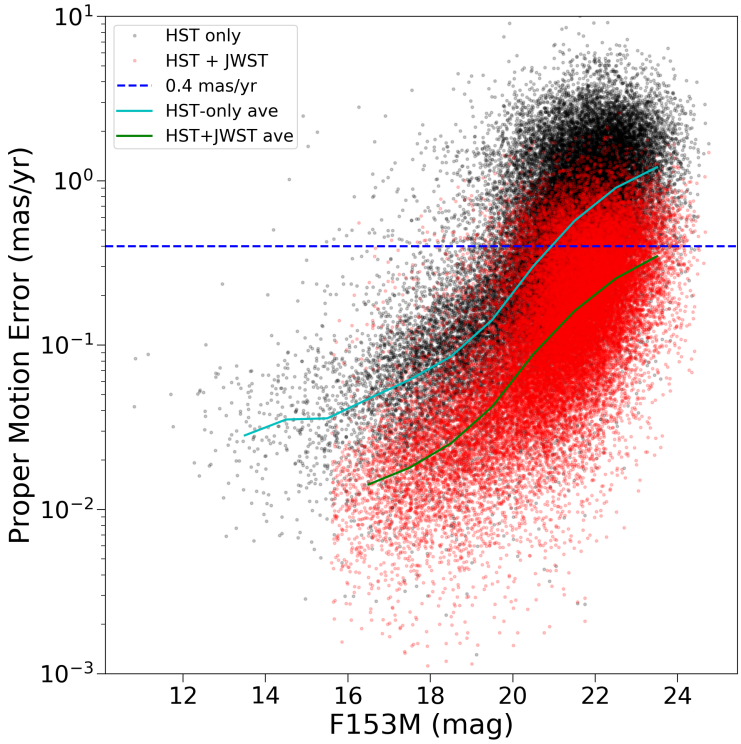

Figure 5.6 Proper motion error as a function of F153M magnitude for the current HST-only 4-epoch catalog (black points, median values shown as cyan line) and what is predicted when a single epoch of JWST astrometry is added (red points, median values shown as green line). The average error improves by a factor of ∼3.5. The blue dotted line shows an error of 0.4 mas yr^{-1}, which is required for high quality cluster membership probabilities.

References

Alexander, R., Pascucci, I., Andrews, S., Armitage, P., & Cieza, L. 2014, Protostars and Planets VI, 475

Bonnell, I. A., Clarke, C. J., & Bate, M. R. 2006, MNRAS, 368, 1296

Bonnell, I. A., & Rice, W. K. M. 2008, Science, 321, 1060

Chabrier, G., Hennebelle, P., & Charlot, S. 2014, ApJ, 796, 75

Chiang, E. I., & Goldreich, P. 1997, ApJ, 490, 368

Clark, J. S., Lohr, M. E., Najarro, F., Dong, H., & Martins, F. 2018, ArXiv e-prints, arXiv:1803.09567

Do, T., Lu, J. R., Ghez, A. M., et al. 2013, ApJ, 764, 154

Elson, R. A. W., Fall, S. M., & Freeman, K. C. 1987, ApJ, 323, 54

Espinoza, P., Selman, F. J., & Melnick, J. 2009, A&A, 501, 563

Haisch, Jr., K. E., Lada, E. A., & Lada, C. J. 2001, ApJ, 553, L153

Harayama, Y., Eisenhauer, F., & Martins, F. 2008, ApJ, 675, 1319

Hernández, J., Hartmann, L., Megeath, T., et al. 2007, ApJ, 662, 1067

Hopkins, P. F. 2012, MNRAS, 423, 2037

—. 2013, MNRAS, 433, 170

Hosek, Jr., M. W., Lu, J. R., Anderson, J., et al. 2015, ApJ, 813, 27

—. 2018, ApJ, 855, 13

Hußmann, B., Stolte, A., Brandner, W., Gennaro, M., & Liermann, A. 2012, A&A, 540, A57

Klessen, R. S., Spaans, M., & Jappsen, A.-K. 2007, MNRAS, 374, L29

Kley, W., & Nelson, R. P. 2012, ARA&A, 50, 211

Lada, C. J., Muench, A. A., Haisch, Jr., K. E., et al. 2000, AJ, 120, 3162

Larson, R. B. 2005, MNRAS, 359, 211

Liermann, A., Hamann, W.-R., & Oskinova, L. M. 2009, A&A, 494, 1137

Luhman, K. L., & Mamajek, E. E. 2012, ApJ, 758, 31

Maercker, M., & Burton, M. G. 2005, A&A, 438, 663

Mann, R. K., Di Francesco, J., Johnstone, D., et al. 2014, ApJ, 784, 82

Morbidelli, A., & Raymond, S. N. 2016, Journal of Geophysical Research (Planets), 121, 1962

Narayanan, D., & Davé, R. 2013, MNRAS, 436, 2892

Olczak, C., Kaczmarek, T., Harfst, S., Pfalzner, S., & Portegies Zwart, S. 2012, ApJ, 756, 123

Papadopoulos, P. P., Thi, W.-F., Miniati, F., & Viti, S. 2011, MNRAS, 414, 1705

Portegies Zwart, S. F. 2016, MNRAS, 457, 313

Repolust, T., Puls, J., Hanson, M. M., Kudritzki, R.-P., & Mokiem, M. R. 2005, A&A, 440, 261

Ribas, Á., Bouy, H., & Merín, B. 2015, A&A, 576, A52

Robberto, M. 2009, JWST-STScI-001721, SM-12

—. 2010, JWST-STScI-002100, SM-12

Schneider, F. R. N., Izzard, R. G., de Mink, S. E., et al. 2014, ApJ, 780, 117

Stolte, A., Brandner, W., Brandl, B., Zinnecker, H., & Grebel, E. K. 2004, AJ, 128, 765

Stolte, A., Morris, M. R., Ghez, A. M., et al. 2010, ApJ, 718, 810

Stolte, A., Hußmann, B., Olczak, C., et al. 2015, A&A, 578, A4

Vincke, K., Breslau, A., & Pfalzner, S. 2015, A&A, 577, A115

Chapter 6

Conclusions

The Galactic Center provides a unique opportunity to conduct resolved studies star formation in a starburst-like environment. In this dissertation, we use multi-epoch *HST* WFC3-IR images and Keck OSIRIS spectroscopy to examine the Arches and Quintuplet clusters, two young massive clusters in the Central Molecular Zone. Critically, we use proper motions to calculate cluster membership probabilities down to $\sim$2 $M_\odot$, obtaining significantly cleaner cluster samples ($\sim$8% field contamination) than is possible through photometry alone. In addition, we cover a field of view $\gtrsim$ 23 times larger than previous proper motion studies of the clusters, reaching the cluster outskirts at radii of $\sim$3 pc. We present the following results:

Chapter 2: The Arches Cluster: Extended Structure and Tidal Radius (Hosek et al. 2015)

We measure the stellar radial density profile of the Arches cluster from 0.25 pc $\leq$ r $\leq$ 3.0 pc for the first time, finding it to be best described by a single power-law with no tidal truncation. We place a 3σ lower limit of 2.8 pc on the tidal radius of the cluster, which is significantly larger than its predicted tidal radius of 2.5 pc. We construct magnitude dependent radial profiles to confirm the presence of mass segregation within the cluster, with a shallower radial profile for fainter low-mass stars and a steeper profile for brighter high-mass stars. However, no evidence for tidal tails is found.

Chapter 3: The Optical/Near-Infrared Extinction Law of Highly Reddened Regions (Hosek et al. 2018)

We measure the extinction law between 0.8 μm – 2.2 μm for highly reddened populations in the Galactic plane by combining observations of Red Clump stars in the Arches field with observations of main sequence stars in Westerlund 1. We develop a new methodology to forward model the extinction law of these populations while making minimal assumptions regarding its functional form. We find that the extinction law is inconsistent with a single power law, contrary to what is usually assumed for this wavelength range, and that it is significantly steeper than the Nishiyama et al. (2009) law often adopted for the GC.

Chapter 4: The Unusual Initial Mass Function of the Arches Cluster (Hosek et al., in prep)

We forward model the Arches cluster to simultaneously constrain the IMF with other cluster parameters (e.g. age, distance, extinction) while accounting for observational uncertainties, completeness, mass segregation, and stellar multiplicity. We find that the Arches IMF is significantly top-heavy ($\alpha = 1.76 \pm 0.03 \pm 0.05$, where $dN/dm \propto m^{-\alpha}$), although we cannot discount a 2-segment power law IMF with a break mass at $5.16^{+1.25}_{-0.65}$ $M_\odot$ and a high-mass slope more consistent with local star forming regions (e.g., a "bottom-light" IMF). The unusual nature of the Arches IMF, combined with past work showing that Young Nuclear Cluster IMF is also top-heavy (Lu et al. 2013) while YMCs in the Galactic disk are generally consistent with local IMF, suggests that the cause of this IMF variation is the extreme GC environment. However, further study is required to confirm this interpretation.

Chapter 5: Moving Forward (Rui et al., in prep; JWST Proposal)

We present the ongoing analysis of the radial profile of the Quintuplet cluster (led by a UC Berkeley undergraduate Nicholas Rui), which is nearly complete and will be submitted shortly (Rui, Hosek, and Lu et al., in prep). Similar to the Arches, we find that the Quintuplet cluster does not exhibit a tidal radius over our field (3σ lower limit: 3.2 pc) and shows signs of mass segregation. No evidence for tidal tails are found. The Quintuplet is more than twice the size of the Arches, possibly due to

its older age and thus longer exposure to the strong tidal field near the GC. Comparisons between the structure of the Arches and Quintuplet provide insight into the evolution of star clusters in strong tidal environments.

We also present a the foundation for a future JWST proposal to observe the Arches and Quintuplet clusters, in order to extend our proper-motion IMF measurements throughout the full stellar mass regime and to characterize their circumstellar disk populations.

6.1 Future Work

Here I describe several avenues for future work on the Arches and Quintuplet Clusters and the IMF at the Galactic Center:

1) IMF Variations: Characteristic of the GC Environment, or An Intrinsic Property of YMCs?

To strengthen the conclusion that the IMF in the GC environment is different than the Galactic disk, it would be useful to 1) measure the IMF of the Quintuplet cluster, providing another data point for the GC; and 2) improve the IMF determinations of YMCs in the Galactic disk. Analysis of the Quintuplet cluster IMF is ongoing. In addition, our group has multi-epoch *HST* observations of Westerlund 1 (one of the YMCs in the Galactic disk potentially discrepant from the local IMF), and has begun analysis to measure its IMF using the techniques developed in this thesis.

2) Is the Arches IMF Top-Heavy or Bottom Light?

As discussed in chapter 5, deeper measurements of the IMF of the Arches cluster will distinguish between a "top-heavy" 1-segment IMF model (i.e., overabundance of high-mass stars due to a shallow mass function slope) and a "bottom-light" 2-segment IMF model (i.e., a deficit of low mass stars due to a large turnover mass). These cases have different implications for the physics that set the IMF (see chapter 4).

3) Dynamical Modeling of the Arches and Quintuplet Clusters

To derive the Arches and Quintuplet IMFs for lower masses, it may become important to consider the effects of tidal stripping (e.g. Park et al. 2018). This requires detailed dynamical modeling of the evolution of these clusters, which in turn requires a better understanding of their orbits. To improve the cluster orbits, we need to better establish their motion *in the galactocentric reference frame*. This should be achievable by comparing the current proper motion catalogs to the Gaia catalogs (Gaia Collaboration et al. 2018). Though Arches and Quintuplet stars cannot be directly observed by Gaia due to the high extinction, common foreground stars between the catalogs may make it possible to convert the *HST* proper motion into the well-defined Gaia reference frame. The number of common stars between the catalogs and precision at which such a transformation can be calculated has not yet been determined.

Future measurements of the velocity dispersion profile of these clusters will give further insight into their dynamical state. In particular, the velocity dispersion profile should show break at the Jacobi radius (the point at which the cluster's gravity balances the external gravitational potential), increasing beyond this radius since the stars are no longer bound to the cluster (e.g. Küpper et al. 2010). The Jacobi radius is directly related to the current distance between the cluster and SgrA*, thus providing the last piece of information required to establish the cluster orbit. In addition, the velocity dispersion as a function of mass (which should be attainable with the JWST observations described in chapter 5) will reveal if the clusters are in energy equipartition and whether the observed mass segregation can be ascribed to dynamical evolution or is primordial in nature (e.g. Wright et al. 2016).

4) Pre-Main Sequence Stellar Evolution Models

An additional issue that will become problematic when pushing the IMF to lower masses is the uncertainty in low-mass pre-main sequence evolution models. Many studies have shown that systematic offsets appear between the observed properties of these stars and model predictions, which have led to discrepancies in cluster age determinations made using the main sequence versus the pre-main sequence (e.g. Bell et al. 2013; Kraus et al. 2015; Herczeg & Hillenbrand 2015; Choi

et al. 2016). These issues will need to be resolved in order to accurately derive the IMF in the low-mass regime.

References

Bell, C. P. M., Naylor, T., Mayne, N. J., Jeffries, R. D., & Littlefair, S. P. 2013, MNRAS, 434, 806

Choi, J., Dotter, A., Conroy, C., et al. 2016, ApJ, 823, 102

Gaia Collaboration, Brown, A. G. A., Vallenari, A., et al. 2018, ArXiv e-prints, arXiv:1804.09365

Herczeg, G. J., & Hillenbrand, L. A. 2015, ApJ, 808, 23

Hosek, Jr., M. W., Lu, J. R., Anderson, J., et al. 2015, ApJ, 813, 27

—. 2018, ApJ, 855, 13

Kraus, A. L., Cody, A. M., Covey, K. R., et al. 2015, ApJ, 807, 3

Küpper, A. H. W., Kroupa, P., Baumgardt, H., & Heggie, D. C. 2010, MNRAS, 407, 2241

Lu, J. R., Do, T., Ghez, A. M., et al. 2013, ApJ, 764, 155

Nishiyama, S., Tamura, M., Hatano, H., et al. 2009, ApJ, 696, 1407

Park, S.-M., Goodwin, S. P., & Kim, S. S. 2018, ArXiv e-prints, arXiv:1804.08869

Wright, N. J., Bouy, H., Drew, J. E., et al. 2016, MNRAS, 460, 2593